Reconstruction par acquisition compressée en imagerie ultrasonore médicale 3D et Doppler

Oana Lorintiu

To cite this version:

Oana Lorintiu. Reconstruction par acquisition compressée en imagerie ultrasonore médicale 3D et Doppler. Imagerie médicale. INSA de Lyon, 2015. Français. NNT : 2015ISAL0093 . tel-01368597

HAL Id: tel-01368597
https://theses.hal.science/tel-01368597

Submitted on 19 Sep 2016

Numéro d'ordre : 2015ISAL0093 Année 2015

THÈSE

Délivrée par

L'Institut National des Sciences Appliquées de Lyon

DIPLÔME DE DOCTORAT

(arrété du 7 aout 2006)

ÉCOLE DOCTORALE : ÉLECTRONIQUE, ÉLECTROTECHNIQUE, AUTOMATIQUE Spécialité : Traitement du Signal et de l'Image

Soutenue publiquement le 16 octobre 2015 par

Oana LORINTIU

Compressed sensing reconstruction for 3D and Doppler medical ultrasound.

Reconstruction par acquisition compressée en imagerie ultrasonore médicale 3D et Doppler.

Jury

Denis FRIBOULET	Professeur	Directeur de thèse
Hervé LIEBGOTT	Maître de Conférences HDR	Co-directeur de thèse
Mike DAVIES	Professeur	Rapporteur
Denis KOUAMÉ	Professeur	Rapporteur
Jean-Philippe THIRAN	Professeur	Examinateur

INSA Direction de la Recherche - Ecoles Doctorales – Quinquennal 2011-2015

SIGLE	ECOLE DOCTORALE	NOM ET COORDONNEES DU RESPONSABLE
CHIMIE	**CHIMIE DE LYON** **http://www.edchimie-lyon.fr** Insa : R. GOURDON	M. Jean Marc LANCELIN Université de Lyon – Collège Doctoral Bât ESCPE 43 bd du 11 novembre 1918 69622 VILLEURBANNE Cedex Tél : 04.72.43 13 95 directeur@edchimie-lyon.fr
E.E.A.	**ELECTRONIQUE, ELECTROTECHNIQUE, AUTOMATIQUE** **http://edeea.ec-lyon.fr** Secrétariat : M.C. HAVGOUDOUKIAN eea@ec-lyon.fr	M. Gérard SCORLETTI Ecole Centrale de Lyon 36 avenue Guy de Collongue 69134 ECULLY Tél : 04.72.18 60 97 Fax : 04 78 43 37 17 Gerard.scorletti@ec-lyon.fr
E2M2	**EVOLUTION, ECOSYSTEME, MICROBIOLOGIE, MODELISATION** **http://e2m2.universite-lyon.fr** Insa : H. CHARLES	Mme Gudrun BORNETTE CNRS UMR 5023 LEHNA Université Claude Bernard Lyon 1 Bât Forel 43 bd du 11 novembre 1918 69622 VILLEURBANNE Cédex Tél : 04.72.43.12.94 e2m2@biomserv.univ-lyon1.fr
EDISS	**INTERDISCIPLINAIRE SCIENCES-SANTE** **http://ww2.ibcp.fr/ediss** Sec : Safia AIT CHALAL Insa : M. LAGARDE	M. Didier REVEL Hôpital Louis Pradel Bâtiment Central 28 Avenue Doyen Lépine 69677 BRON Tél : 04.72.68 49 09 Fax :04 72 35 49 16 Didier.revel@creatis.uni-lyon1.fr
INFOMATHS	**INFORMATIQUE ET MATHEMATIQUES** http://infomaths.univ-lyon1.fr	M. Johannes KELLENDONK Université Claude Bernard Lyon 1 INFOMATHS Bâtiment Braconnier 43 bd du 11 novembre 1918 69622 VILLEURBANNE Cedex Tél : 04.72. 44.82.94 Fax 04 72 43 16 87 infomaths@univ-lyon1.fr
Matériaux	**MATERIAUX DE LYON** Secrétariat : M. LABOUNE PM : 71.70 –Fax : 87.12 Bat. Saint Exupéry Ed.materiaux@insa-lyon.fr	M. Jean-Yves BUFFIERE INSA de Lyon MATEIS Bâtiment Saint Exupéry 7 avenue Jean Capelle 69621 VILLEURBANNE Cédex Tél : 04.72.43 83 18 Fax 04 72 43 85 28 Jean-yves.buffiere@insa-lyon.fr
MEGA	**MECANIQUE, ENERGETIQUE, GENIE CIVIL, ACOUSTIQUE** Secrétariat : M. LABOUNE PM : 71.70 –Fax : 87.12 Bat. Saint Exupéry mega@insa-lyon.fr	M. Philippe BOISSE INSA de Lyon Laboratoire LAMCOS Bâtiment Jacquard 25 bis avenue Jean Capelle 69621 VILLEURBANNE Cedex Tél :04.72.43.71.70 Fax : 04 72 43 72 37 Philippe.boisse@insa-lyon.fr
ScSo	**ScSo*** M. OBADIA Lionel Sec : Viviane POLSINELLI Insa : J.Y. TOUSSAINT	M. OBADIA Lionel Université Lyon 2 86 rue Pasteur 69365 LYON Cedex 07 Tél : 04.78.69.72.76 Fax : 04.37.28.04.48 Lionel.Obadia@univ-lyon2.fr

*ScSo : Histoire, Geographie, Aménagement, Urbanisme, Archéologie, Science politique, Sociologie, Anthropologie

Acknowledgements

Abstract

This thesis is dedicated to the application of the novel compressed sensing theory to the acquisition and reconstruction of 3D US images and Doppler signals. In 3D US imaging, one of the major difficulties concerns the number of RF lines that has to be acquired to cover the complete volume. The acquisition of each line takes an incompressible time due to the finite velocity of the ultrasound wave. One possible solution for increasing the frame rate consists in reducing the acquisition time by skipping some RF lines. The reconstruction of the missing information in post processing is then a typical application of compressed sensing. Another excellent candidate for this theory is the Doppler duplex imaging that implies alternating two modes of emission, one for B-mode imaging and the other for flow estimation. Regarding 3D imaging, we propose a compressed sensing framework using learned overcomplete dictionaries. Such dictionaries allow for much sparser representations of the signals since they are optimized for a particular class of images such as US images. We also focus on the measurement sensing setup and propose a line-wise sampling of entire RF lines which allows to decrease the amount of data and is feasible in a relatively simple setting of the 3D US equipment. The algorithm was validated on 3D simulated and experimental data. For the Doppler application, we proposed a CS based framework for randomly interleaving Doppler and US emissions. The proposed method reconstructs the Doppler signal using a block sparse Bayesian learning algorithm that exploits the correlation structure within a signal and has the ability of recovering partially sparse signals as long as they are correlated. This method is validated on simulated and experimental Doppler data.

Résumé

L'objectif de cette thèse est le développement de techniques adaptées à l'application de la théorie de l'acquisition compressée en imagerie ultrasonore 3D et Doppler. En imagerie ultrasonore 3D une des principales difficultés concerne le temps d'acquisition très long lié au nombre de lignes RF à acquérir pour couvrir l'ensemble du volume. Afin d'augmenter la cadence d'imagerie une solution possible consiste à choisir aléatoirement des lignes RF qui ne seront pas acquises. La reconstruction des données manquantes est une application typique de l'acquisition compressée. Une autre application d'intérêt correspond aux acquisitions Doppler duplex où des stratégies d'entrelacement des acquisitions sont nécessaires et conduisent donc à une réduction de la quantité de données disponibles. Dans ce contexte, nous avons réalisé de nouveaux développements permettant l'application de l'acquisition compressée à ces deux modalités d'acquisition ultrasonore. Dans un premier temps, nous avons proposé d'utiliser des dictionnaires redondants construits à partir des signaux d'intérêt pour la reconstruction d'images 3D ultrasonores. Une attention particulière a aussi été apportée à la configuration du système d'acquisition et nous avons choisi de nous concentrer sur un échantillonnage des lignes RF entières, réalisable en pratique de façon relativement simple. Cette méthode est validée sur données 3D simulées et expérimentales. Dans un deuxième temps, nous proposons une méthode qui permet d'alterner de manière aléatoire les émissions Doppler et les émissions destinées à l'imagerie mode-B. La technique est basée sur une approche bayésienne qui exploite la corrélation et la parcimonie des blocs du signal. L'algorithme est validé sur des données Doppler simulées et expérimentales.

Contents

List of Symbols and abbreviations

Abbreviations

2D	Two-dimensional
3D	Three-dimensional
BO	Bound-Optimization
BSBL	Block Sparse Bayesian Learning
CS	Compressed Sensing
CT	Computerized Tomography
CW	Continuous Wave
DCT	Discrete Cosine Transform
EM	Expectation-Minimization
IQ	In phase Quadrature
IRLS	Iterative Reweighted Least-Squares
K-SVD	K Singular Value Decomposition
MP	Matching Pursuit
MRI	Magnetic Resonance Imaging
MSE	Mean Squared Erroe
NRMSE	Normalized Root Mean Squared Error
NP	Non-deterministic Polynomial-time
OMP	Orthogonal Matching Pursuit
PET	Positron Emission Tomography
PSF	Point Spread Function
PSNR	Peak to Signal Noise Ratio
PW	Pulsed Wave
RF	Radio Frequency
SBL	Sparse Bayesian Learning
SPGL1	Spectral Projected Gradient
US	Ultrasound

Mathematical symbols

$\#$	Cardinality of a set
$\lvert \cdot \rvert$	Absolute value
$\langle \cdot \rangle$	Scalar product
$\Vert \cdot \Vert_0$	l_0 norm : $\Vert x \Vert_0 = \# \{i, x_i \neq 0\}$
$\Vert \cdot \Vert_1$	l_1 norm : $\Vert x \Vert_1 = \sum_{i=1}^{n} \lvert x_i \rvert$
$\Vert \cdot \Vert_p$	l_p norm : $\Vert x \Vert_p = (\sum_{i=1}^{n} \lvert \Vert x_i \Vert^p \rvert)^{\frac{1}{p}}, 0 < p \leq 1$

Alphabet letters

x	Signal
y	Measurements
n	Signal size
m	Number of measurements
v	Vector of coefficients
R	Restriction matrix
k	Sparsity level
X	Training samples
N	Number of samples in X
D	Dictionary
K	Number of atoms
p	Patch or segment size
q	Overcompleteness
r	Overlap rate
S	Subsampling rate
b	Block size
T_0	Number of non-zero entries in Θ
R_1	Random subsampling matrix
R_2	Line-wise subsampling matrix

Greek letters

Φ	Sensing basis
Ψ	Sparsifying basis
μ	Incoherence
Θ	Coefficients of dictionary learning problem

Résume étendu de la thèse

Objectifs de la thèse et organisation générale du manuscrit

Objectifs

La récente théorie d'acquisition compressée ou échantillonnage compressé (également connue sous le nom anglais "Compressed sensing (CS)") définit un cadre théorique qui permet d'envisager une nouvelle façon d'échantillonner les signaux ou les images. En exploitant le caractère parcimonieux que présentent la plupart des données physiques, elle permet de reconstruire les données acquises avec des fréquences d'échantillonnage bien inférieures à la limite classique de Shannon. L'échantillonnage compressé peut être appliqué pour atteindre deux objectifs principaux :

- Diminuer la quantité de données nécessaires et ainsi accélérer l'acquisition.
- Améliorer la reconstruction de signaux/images dans les domaines où les contraintes liées à l'acquisition physique produit des données très parcimonieuses.

Ce travail se concentre sur l'échographie médicale, domaine dans lequel la théorie du CS a été peu étudiée, malgré le fait que certains modes d'acquisition de l'échographie représentent d'excellentes candidates pour l'application de cette théorie.

Les modalités traditionnelles d'imagerie médicale, comme l'échographie, reposent toutes sur le théorème de Shannon-Nyquist qui fixe la limite basse pour la fréquence d'échantillonnage d'un signal à deux fois sa composante de fréquence la plus élevée. Afin d'éviter des artefacts et respecter ce théorème les appareils d'échographie ultrasonore (US) utilisent un échantillonnage correspondant à quatre fois la fréquence centrale de l'impulsion émise. Par conséquent, lors d'un échantillonnage à ces fréquences, la quantité de données obtenue est importante, en particulier en imagerie 3D, rendant le temps réel et le transfert des données difficiles voire impossibles. En imagerie ultrasonore 3D les acquisitions font appel à des sondes comportant une matrice de capteurs. Pour des raisons d'encombrement physique, de connexion et de pilotage, seule une faible fraction de ces capteurs peut être pilotée simultanément. De plus, le nombre de lignes radio-fréquences (RF) qui doivent être acquises afin de balayer la totalité du volume peut être extrêmement élevé, typiquement plusieurs milliers. Le temps d'acquisition d'une ligne RF est lié à la vitesse du son et à la profondeur du milieu imagé et ne peut pas être réduit, conduisant à des temps d'acquisition longs et donc a une cadence d'acquisition faible (de l'ordre de quelques Hz) qui limitent la faisabilité de ce type d'acquisition pour les organes dynamiques, tels que le cœur. Dans ce contexte, le "compressive sensing" présente donc un intérêt majeur pour aller vers une amélioration considérable des résolutions spatiales et temporelles des acquisitions 3D.

Un autre excellent candidat pour l'application de la théorie CS est l'acquisition Doppler duplex (imagerie simultanée du flux sanguin et de l'anatomie) qui implique l'alternance entre deux modes d'émission. L'alternance aléatoire des deux modes d'émission donne des mesures contenant des échantillons manquants. Le CS peut donc nous permettre de retrouver le signal Doppler et reconstruire les échantillons manquants en contournant le théorème d'échantillonnage de Shannon.

C'est dans ce contexte que se situe ce travail de thèse qui porte sur l'application de la théorie CS pour l'acquisition compressée et la reconstruction d'images 3D ultrasonores et des signaux Doppler. Il traite les aspects méthodologiques suivants :

- Un élément clé du CS est le fait que les données doivent avoir une représentation parcimonieuse dans une base ou un dictionnaire. En conséquence, une caractéristique importante des études existantes est le choix de la représentation dans laquelle les données US sont supposées parcimonieuses. Nous proposons d'utiliser des dictionnaires redondants appris sur les signaux d'intérêt pour la reconstruction d'images 3D ultrasonores.
- Une autre caractéristique importante pour assurer une reconstruction CS correcte est la façon dont l'acquisition des données est réalisée. Ainsi, nous nous concentrons sur l'échantillonnage des lignes RF entières en imagerie 3D US ce qui permet d'augmenter la cadence d'acquisition.
- Une difficulté fréquemment rencontrée dans ce contexte est la récupération de signaux non-parcimonieux ou partiellement parcimonieux telles que les signaux Doppler. Ainsi, nous avons proposé une méthode de CS basée sur une méthode d'apprentissage bayésien exploitant la structure de corrélation des signaux qui a la particularité de pouvoir reconstruire des signaux non-parcimonieux.

Organisation générale du manuscrit

Le manuscrit est composé de trois parties.

Dans la première partie, nous présentons les bases de la formation de l'image ultrasonore et donnons les principales propriétés de ce type d'image. Nous nous concentrons sur les modalités existantes permettant l'acquisition d'images échographiques 3D, leurs limites et leurs perspectives. Nous présentons également les systèmes Doppler utilisés pour évaluer et visualiser le flux sanguin dans le corps. Une attention particulière est donnée aux différents types de systèmes Doppler et à la formation du spectrogramme Doppler. Dans le chapitre qui suit, nous résumons les principaux aspects de la théorie d'échantillonnage compressé. Nous décrivons le cadre mathématique général, les principaux théorèmes et illustrons les hypothèses associées à cette théorie. Cela nous conduit à une discussion sur les techniques de reconstruction existantes. Le problème de reconstruction CS peut également être formulé dans un cadre bayésien, que nous présentons dans cette partie. Le dernier chapitre de cette première partie se concentre sur l'utilisation des techniques d'apprentissage de dictionnaires qui seront utilisées dans cette thèse.

La deuxième partie est consacrée à l'application du CS utilisant l'apprentissage de dictionnaires redondants aux images ultrasonores. Nous proposons dans ce travail l'utilisation de dictionnaires redondants pour représenter de manière parcimonieuse nos images échographiques. Nous commençons par donner un examen détaillé des méthodes CS utilisées pour la reconstruction des images 2D et 3D . Dans ce contexte, nous montrons les résultats préliminaires de cette méthode sur des images échographiques 2D. Le chapitre suivant, présente les conditions d'application du CS sur les données 3D. Il détaille en particulier les schémas d'échantillonnage, le schéma de reconstruction et l'étude des paramètres optimaux utilisés dans cette contribution. Enfin, nous validons cet algorithme sur des données simulées et expérimentales *ex vivo* et *in vivo*. De plus, la généralité de cette approche est étudiée et évaluée.

Dans la troisième partie de cette thèse, nous proposons une méthode qui permet d'alterner de manière aléatoire les émissions de Doppler et les émissions dédiées à l'imagerie pour les systèmes d'échographie duplex Doppler. La technique proposée est basée sur une méthode de CS bayésien qui exploite la corrélation intra-blocs. Nous examinons d'abord les techniques existantes. Nous proposons ensuite une méthode qui exploite la parcimonie et la corrélation des blocs du signal dans le cadre bayésien pour reconstruire le signal Doppler segment par segment.

Contexte

Imagerie ultrasonore

L'échographie est devenue l'une des modalités d'imagerie médicale prédominantes et est actuellement le premier examen à fin de diagnostic pour la plupart des organes, excepté pour le cerveau et les poumons. Ceci est lié aux nombreux avantages de l'imagerie ultrasonore, tels que :

- Le coût relativement faible d'un échographe (comparé au prix d'autres modalités telles que le scanner à rayons X, l'IRM ou la TEP).
- Le faible encombrement et la portabilité de l'équipement et la possibilité de faire des acquisitions au lit du patient.
- La sureté du patient, un examen échographique ne présente aucun risque pour le patient (pas de rayons ionisants).
- Dans sa forme classique, l'échographie est non-invasive.
- La résolution spatiale est très bonne puisqu'elle dépend principalement de la durée de l'impulsion ultrasonore. Cependant certains aspects pratiques, tels que l'atténuation, peuvent conduire à des difficultés techniques pour de hautes fréquences.
- La résolution temporelle est excellente, faisant de l'imagerie ultrasonore la seule modalité d'imagerie non invasive et non ionisante capable d'acquérir des images en temps réel et par conséquent de visualiser et d'évaluer un processus dynamique.

L'imagerie ultrasonore repose sur l'interaction entre une onde acoustique et les tissus du corps humain. Les principales formes d'interactions avec le milieu sont l'absorption, la réfraction et la réflexion qui peut être soit spéculaire soit diffuse. Lorsque l'onde atteint une interface entre deux milieux aux propriétés acoustiques différentes, une partie de celle-ci est réfléchie vers la source. De plus, l'onde ultrasonore transfère de l'énergie au milieu traversé, laquelle est ensuite convertie en chaleur. Il est ainsi évident que, en émettant une impulsion ultrasonore dans le corps humain, les échos obtenus contiennent d'importantes informations tant sur les propriétés acoustiques des milieux traversés que sur la position spatiale des interfaces les séparant.

L'imagerie échographique est réalisée selon deux phases principales : une phase d'émission et une autre de réception. D'abord une onde acoustique est générée par un transducteur piézoélectrique excité par un signal électrique. L'onde se propage dans le milieu et la présence d'hétérogénéités conduit à la formation d'échos qui se propagent à leur tour dans le milieu. Ils sont détectés par le transducteur ultrasonore utilisé alors en mode réception. Le signal reçu par le transducteur est amplifié et démodulé. Ce signal donne une information sur la géométrie du milieu et s'appelle ligne A ou signal RF, s'il n'est pas démodulé. Si on translate le transducteur au dessus d'un milieu, on obtient une image mode B qui est l'image échographique 2D classique.

Malgré leur utilisation très fréquente, les échographes conventionnels 2D présentent 2 limitations majeures [Fenster et al., 2011] :

- Les images ultrasonores obtenues sont 2D mais l'anatomie est 3D et de ce fait l'opérateur doit considérer plusieurs images pour son diagnostic. Cette pratique est non optimale et peut conduire à de fortes variabilités entre opérateurs ainsi qu'à des erreurs de diagnostic. De plus cela nécessite de faire des hypothèses quant à la géométrie de l'organe imagé pour pouvoir estimer le volume des structures anatomiques, telles que le ventricule gauche.
- L'image ultrasonore 2D représente une coupe prise sous un angle arbitraire et il est difficile de localiser ce plan de coupe lors d'étude de suivi. Cela introduit aussi un effet de déformation qui peut conduire à une mauvaise estimation de la forme.

L'échographie 3D consiste a réaliser non pas un plan de coupe comme en échographie 2D classique mais un volume. Ce volume d'intérêt peut être imagé en étendant les techniques conventionnelles d'imagerie ultrasonore en déplaçant le plan d'acquisition 2D. L'acquisition du volume se fait soit avec des sondes classiques soit avec des sondes spécifiques volumiques. Avec des sondes classiques, le balayage est fait manuellement et le volume obtenu est approximatif, la qualité de l'acquisition dépendant de la stabilité de la vitesse de balayage et donc de l'utilisateur. Les sondes volumiques réalisent automatiquement un balayage de plan de coupes par un déplacement mécanique de la sonde. Le balayage mécanique des plans ultrasonores est une technique lente et peu précise ce qui a conduit à l'apparition de sondes échographiques matricielles a révolutionné l'application clinique de l'échographie 3D en permettant un balayage électronique du faisceau ultrasonore dans un volume 3D. Le développement de ces nouvelles sondes est bien évidement limité par le nombre de canaux, ou nombre de voies de traitement du signal de l'échographe. De plus, le nombre d'éléments piézoélectriques actifs a une influence directe sur la résolution spatiale et la qualité de l'image.

La Figure 1 présente les différents types de sondes utilisees pour les acquisitions ultrasonores 3D.

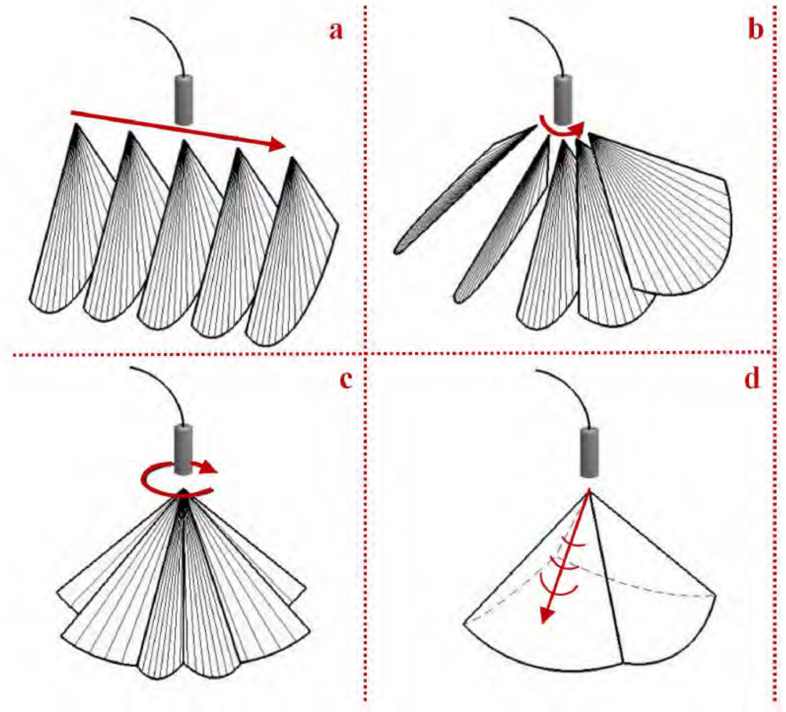

Figure 1 – Les différents types d'acquisitions 3D : (a), (b), (c) présentent les sondes volumiques mécaniques a balayage linéaire, angulaire et rotatif et (d) montre une sonde matricielle a balayage électronique.

Les échographes médicaux peuvent également être utilisés pour visualiser la vitesse et la direction du flux sanguin dans le corps à l'aide des systèmes Doppler. Ce type de système s'appuie sur le fait que la fréquence des ultrasons réfléchis par une particule en mouvement diffère de la fréquence des ultrasons émis. Cette variation de fréquence est due au mouvement de la cible (ici le sang), l'onde ultrasonore n'étant pas modifiée et donc sa longueur d'onde est conservée dans tout le milieu. La vitesse peut être alors calculée en fonction de la vitesse de propagation des ultrasons, de la longueur d'onde et de sa fréquence.

Nous distinguons deux types de systèmes Doppler : à émission continue et à émission pulsée. Le système Doppler continu est constitué d'un émetteur qui fonctionne en permanence et d'un récepteur en écoute. Dans ce cas, la vitesse des éléments en mouvement est obtenue sans résolution axiale, i.e. les information provenant de toutes les inhomogénéités en mouvement sont superposées ainsi que les vaisseaux situés sur le même axe de tir Doppler.

Dans le cas du Doppler pulsé , l'émission ultrasonore n'est plus continue mais un transducteur émet périodiquement des ondes de courte durée. Les ondes ultrasonores réfléchies pas les différentes interfaces, notamment les particules en mouvements, sont recueillis par le transducteur passé en mode réception. Le temps entre l'émission des échos reçus dépend de la distance entre la sonde et la particule qui a provoqué la réflexion. L'intérêt du Doppler pulsé est de pouvoir focaliser l'examen en profondeur, ce qui nécessite un repérage spatial donné par une image échographique mode-B. Les systèmes duplex permettent l'acquisition alternée de l'image échographique et du signal Doppler, en combinant souvent les fréquences d'émission : on utilise en Doppler une fréquence plus basse que la fréquence nécessaire à l'acquisition de l'image. L'optimisation des systèmes duplex résulte d'un compromis entre les émissions pour le Doppler et les émissions pour acquérir l'image échographique mode-B. La Figure 2 montre l'obtention d'un signal Doppler pulsé.

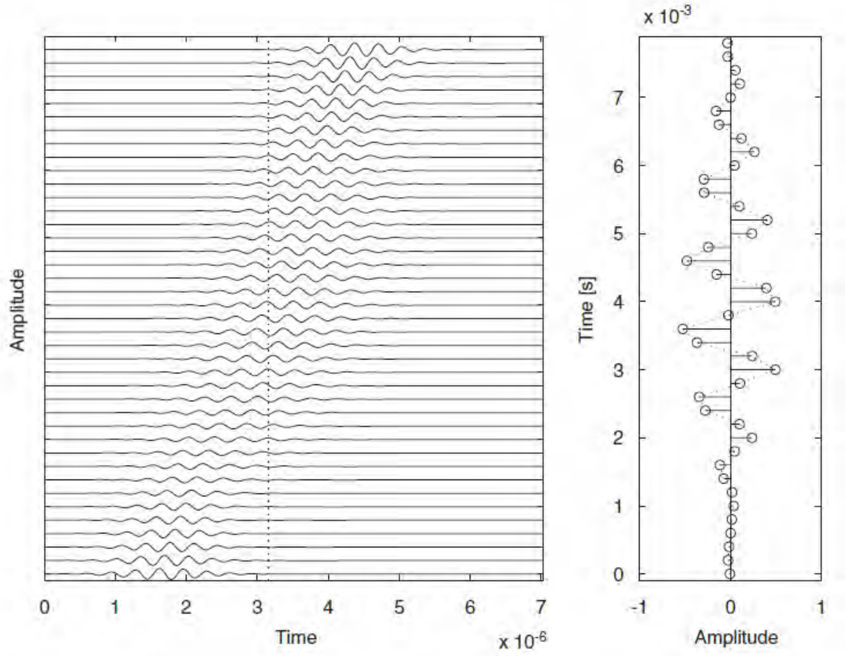

FIGURE 2 – Signal Doppler correspondant a une émission. À gauche, les lignes RF reçues par le transducteur, et à droite on trouve le signal Doppler échantillonné.

Compressed sensing

Aujourd'hui les besoins pour stocker et transmettre des volumes d'informations sont de plus en plus importants et la fréquence d'échantillonnage minimale imposée par le théorème d'échantillonnage à deux fois la fréquence maximale du signal devient une limite face à la nécessité de compresser l'information et surtout de la traiter plus rapidement. Dans de nombreuses applications émergentes, l'acquisition ou le traitement des données générées posent un énorme défi à cause de plusieurs difficultés :

- un échantillonnage trop élevé imposé par le théorème de Shannon-Nyquist,
- l'impossibilité physique de construire les dispositifs capables d'acquérir tous les échantillons nécessaires (par exemple, des capteurs sismiques, des sondes matricielles pour l'échographie 3D),

- le coût de la conception ou de l'utilisation des systèmes d'acquisition,
- le temps et les contraintes économiques imposées par les dispositifs existants,
- les risques pour la santé des utilisateurs (par exemple, l'exposition au rayonnement pendant l'acquisition d'une image CT).

Afin de relever les défis posés par le traitement des données de grande dimension, l'approche habituelle repose souvent sur la compression, survenant après l'acquisition du signal échantillonné. Il s'agit de représenter le signal dans une certaine base (ou dictionnaire) dans laquelle il se résume à un nombre limité de coefficients non nuls. Les deux étapes successives d'échantillonnage à la fréquence de Shannon puis de compression dans une base adaptée sont finalement coûteuses, puisque l'on ne conserve in fine que quelques coefficients représentatifs. L'idée novatrice du compressed sensing est d'effectuer ces deux opérations simultanément, c'est-à-dire échantillonner et compresser en même temps, grâce au caractère parcimonieux.

Formulation mathématique

Le compressed sensing (CS) [Candés and Wakin, 2008] permet de reconstruire un signal $x \in \mathbb{R}^n$ a partir de la combinaison linéaire d'un nombre restreint d'échantillons aléatoires $y \in \mathbb{R}^m$, avec $m << n$. Les observations y sont acquises avec une matrice d'échantillonnage ou de projection, appelée Φ, qui dépend du système d'acquisition et qui permet de sélectionner seulement m observations. Par exemple, en IRM, Φ est la base de Fourier et en ultrason, Φ est simplement la base de Dirac. On a alors :

$$y = R\Phi x \tag{1}$$

où $R\Phi$ est une matrice $m \times n$. Les colonnes de R modélisent la sélection aléatoire des échantillons choisis.

La théorie du CS fait l'hypothèse que x a une transformation parcimonieuse dans une matrice de mesure Ψ, qui peut être une base orthonormée, une frame ou un dictionnaire redondant, tel que :

$$x = \Psi v \tag{2}$$

ou v a uniquement $k < m < n$ coefficients non-nuls. On dit alors que le vecteur de coefficients v est k-parcimonieux. On peut alors reconstruire v si on a une faible cohérence entre les matrices Φ et Ψ [Candés and Wakin, 2008, Candés and Romberg, 2007]. Alors le problème final peut s'écrire :

$$y = R\Phi\Psi v = Av \tag{3}$$

On peut alors reconstruire v en résolvant (3) sous contrainte que v est parcimonieux. Le signal x peut alors être calculé a partir de l'équation (2).

Le problème du CS peut s'écrire sous la forme d'un problème de minimisation l_0 sousdéterminé P_0 :

$$P_0 : \quad \hat{v} = arg \min_{v \in \mathbb{R}^n} \|v\|_0 \quad \text{subject to} \quad y = Av \tag{4}$$

ou la norme l_0 de v est définie par $\|v\|_0 = \#\{i, v_i \neq 0\}$.

La norme l_0 a l'avantage de conduire à la solution exacte pour P_0 dès que $k+1 \leq m$ mais a l'inconvénient d'être très coûteuse en complexité algorithmique.

L'alternative est de remplacer la norme l_0 par la norme l_1 dans le problème P_0 et donc de considérer la relaxation convexe de (2.4). Cela nous conduit a la résolution d'un problème connu sous le nom de basis pursuit P_1 [Candés, 2008, Candés and Tao, 2005] :

$$P_1 : \quad \hat{v} = arg \min_{v \in \mathbb{R}^n} \|v\|_1 \quad \text{subject to} \quad y = Av \tag{5}$$

ou la norme l_1 de v est définie par $\|v\|_1 = \sum_{i=1}^{n} |v_i|$. Les conditions qui établissent l'équivalence des problèmes P_0 et P_1 sont basées sur la propriété d'isométrie restreinte (RIP) établie par Candès en [Candés, 2008, Candés and Wakin, 2008].

Parcimonie

Le caractère parcimonieux des signaux est déjà exploité dans les méthodes classiques de compression, survenant après l'acquisition du signal échantillonné. Il s'agit de représenter le signal dans une certaine base (ou dictionnaire) dans laquelle il se résume à un nombre limité de coefficients non nuls. C'est ainsi que la base de Fourier permet d'exprimer un signal comme somme de sinusoïdes à différentes fréquences. De même, les bases à partir d'ondelettes permettent d'obtenir une représentation du signal comme somme d'ondelettes localisées à la fois dans le domaine fréquentiel et dans le domaine temporel (ou spatial). Cette dernière décomposition est utilisée pour la représentation des images suivant le standard JPEG2000. La performance d'une base orthogonale pour traiter des signaux dépend de sa capacité à approximer ces signaux avec peu de coefficients non nuls. La Figure 3 présente un exemple de représentation parcimonieuse dans la base des ondelettes ; on observe qu'une image peut être reconstruite a partir de seulement 5% des plus grands coefficients des ondelettes.

Incohérence

On considère une paire de bases orthonormées $(\Phi, \Psi) \in \mathbb{R}^n$, correspondant respectivement aux matrices de projection et mesure. La cohérence entre Φ et Ψ est alors définie telle que :

$$\mu(\Phi, \Psi) = \sqrt{n} \cdot \max_{1 \leq k,j \leq n} |\langle \phi_k, \psi_j \rangle| \tag{6}$$

La cohérence mesure la plus grande corrélation entre les éléments de Φ et Ψ [Donoho

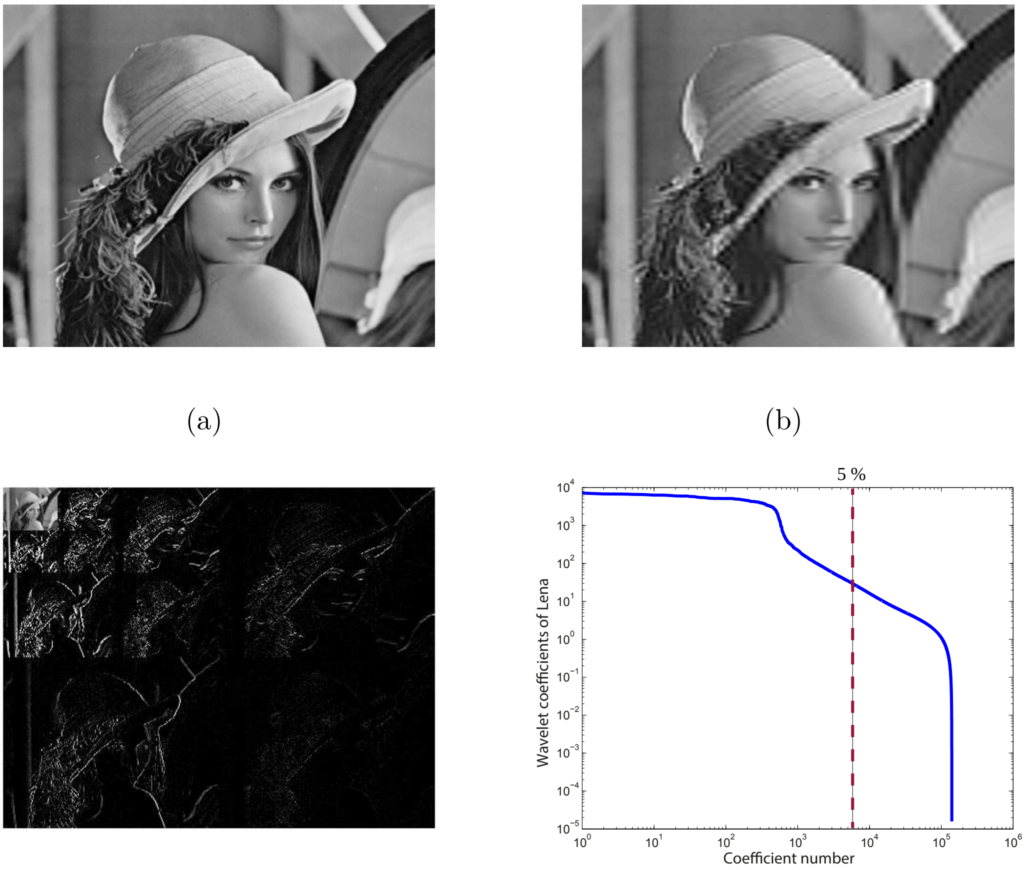

(a) (b)

(c) (d)

FIGURE 3 – (a) Image originale de Lena 512 × 512. (b) Image reconstruite a partir de 5% des plus importants coefficients d'ondelettes. (c) Décomposition en ondelettes. Les coefficients élevés sont représentés par des pixels blancs et les coefficients proches de 0 par des pixels noirs. (d) Les coefficients des ondelettes de l'image originale représentés sur une échelle logarithmique.

and Huo, 2001]. Si Φ et Ψ contiennent des éléments corrélés, la cohérence est grande, sinon, elle est faible et incluse dans $[1, \sqrt{n}]$. Le compressed sensing se base sur les paires de bases avec une faible cohérence. Cela implique que l'information est concentrée sur peu de coefficients de v en (2) et étendue sur toutes les observation de y en (3). Un exemple de bases ayant une incohérence maximale est la paire Dirac, Fourier qui a une incohérence $\mu(\Phi, \Psi) = 1$.

Le théorème lié à l'incohérence décrit dans [Candés and Romberg, 2007] montre que le nombre d'échantillons nécessaires pour une reconstruction exacte est inversement proportionnel à l'incohérence. On illustre ce théorème sur le Figure 4.

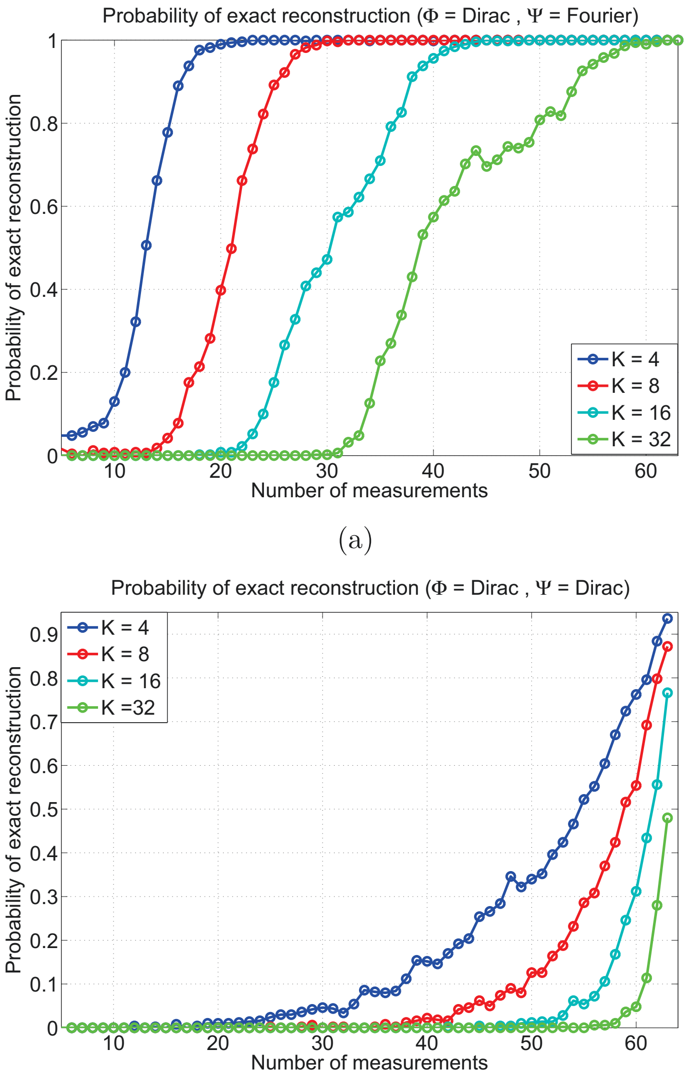

(a)

(b)

FIGURE 4 – Estimation empirique de la probabilité de reconstruction de x pour différentes valeurs de K et m (nombre d'échantillons) pour (a) Φ = Dirac, Ψ = Fourier et (b) Φ = Dirac, Ψ = Dirac.

Algorithmes de reconstruction

On trouve dans la littérature de nombreuses techniques de reconstruction pour la résolution des problèmes (4) et (5), avec des spécificités particulières en termes de rapidité et précision. Ces algorithmes de reconstruction peuvent être classifiés en 3 catégories :

- Minimisation de la norme l_0 résolue par des algorithmes dits gloutons.
- Minimisation de la norme l_1 par des algorithmes de relaxation convexe ("Basis Pursuit").
- Minimisation de norme l_p avec $0 \leq p \leq 1$ par des approches non-convexes.

Compressed sensing Bayésien

Le problème de reconstruction parcimonieuse peut être également écrit comme un problème d'estimation résolu dans un cadre Bayésien. Le bruit additif ϵ dans (2.6) dû aux erreurs provenant de l'instrumentation peut etre approximé par un bruit additif Gaussien de moyenne nulle et de variance σ^2. La vraisemblance associée s'écrit :

$$p(y|v,\sigma^2) = (\pi\sigma^2)^{-n} \exp(-\frac{1}{\sigma^2} \|y - Av\|_2^2) \tag{7}$$

La parcimonie est donc modélisée par l'introduction d'une loi a priori $p_0(v)$:

$$p_0(v) \propto \exp(-\|v\|_0) \tag{8}$$

Les approches bayésiennes transforment donc le problème du CS classique en un problème de régression linéaire avec la contrainte a priori que v est parcimonieux. Ces approches peuvent être classifiées en 3 catégories :

1. Algorithmes bayésiens gloutons [Schniter et al., 2008, Zayyani et al., 2009],
2. Algorithmes bayésiens qui remplacent la loi a priori $p_0(v)$ par une loi connue [Figueiredo and Nowak, 2001, Figueiredo, 2002, Ji et al., 2008, Tibshirani, 2011], telle que la distribution Laplace, la loi de Jeffreys ou les distributions α-stables.
3. Algorithmes bayésiens qui utilisent une loi a priori apprise à partir des données ("Sparse Bayesian learning (SBL) algortihms") [Tipping, 2001, Tan and Li, 2009, Wipf and Rao, 2007, Figueiredo, 2003].

On s'intéresse plus particulièrement, à l'algorithme proposé par Zhang [Zhang et al., 2013b, Zhang et al., 2013c] qui est une extension des algorithmes d'apprentissages bayésiens. Cet algorithme exploite la structure de la corrélation existante dans les signaux. De plus, cet algorithme a la capacité de reconstruire les signaux non-parcimonieux à condition que les signaux aient une structure de corrélation interne.

Apprentissage de dictionnaires

Les décompositions parcimonieuses décrivent un signal comme une combinaison d'un petit nombre de formes de base, appelées atomes. Le dictionnaire d'atomes, crucial pour l'efficacité de la décomposition, peut résulter d'un choix a priori (ondelettes, Fourier, ...) qui fixe la structure du dictionnaire, ou d'un apprentissage à partir d'exemples représentatifs du signal. Un dictionnaire doit être choisi en adéquation avec le signal traité. Le dictionnaire peut être choisi parmi un ensemble de dictionnaires préexistants ou alors être construit à partir d'exemples des signaux à traiter. Le problème des dictionnaires préexistants est qu'ils ne sont pas forcement adaptés à nos signaux d'intérêt et donc la représentation sera moins parcimonieuse que dans un dictionnaire fait sur mesure. Le deuxième type de dictionnaire est construit automatiquement à partir d'exemples de signaux et donc adapté à ces signaux. Il a plus de chance de représenter de manière parcimonieuse les signaux, puisque des informations sur la nature attendue des atomes a été intégrée à l'apprentissage. Les dictionnaires ainsi structurés apportent une meilleure adaptation aux propriétés du signal. Nous exposons les concepts et les outils de cette approche, notamment l'algorithme K-SVD pour l'apprentissage des dictionnaires redondants.

L'apprentissage des dictionnaires prend en entrée un ensemble d'exemples $X = \{x_i\}_{i=1}^{N}$, qui contient N exemples. On va chercher à représenter X par une combinaison linéaire Θ d'éléments de base notés D tel que $X = D\Theta$. D est le dictionnaire de taille $n \times K$ dont les vecteurs colonnes sont les K elements du dictionnaire qu'on cherche à apprendre. Afin de représenter au mieux les données, le problème consiste donc à trouver D et Θ minimisant le problème d'optimisation suivant :

$$\min_{D,\Theta} \|X - D\Theta\|_F^2 \ s.t. \ \forall i, \|\theta_i\|_0 \leq T_0 \tag{9}$$

où $\|\|_F$ est la norme de Frobenius et T_0 est le nombre de coefficients non-nuls.

L'algorithme K-SVD est un algorithme permettant de résoudre le problème d'apprentissage de dictionnaire parcimonieux formulé à l'équation (9). Il a été présenté par Aharon [Aharon et al., 2006, Smith and Elad, 2013]. Pour des raisons d'efficacité, une version optimisée de l'algorithme a récemment été proposée ici [Smith and Elad, 2013] . L'algorithme de K-SVD consiste en une optimisation alternée. On résout itérativement un problème partiel en X avec D fixe. Cette étape est appelée étape de codage parcimonieux ("sparse coding"). La seconde étape du K-SVD consiste à optimiser D avec X fixe.

Compressed sensing avec apprentissage de dictionnaires pour l'imagerie ultrasonore

Dans ce chapitre nous proposons une nouvelle approche basée sur l'utilisation des dictionnaire redondants et le compressed sensing pour la reconstruction des images ultrasonores 3D. Nous commençons par un état de l'art des techniques CS utilisées en échographie 2D et 3D. La section suivante présente les résultats préliminaires obtenus par l'utilisation des dictionnaires préalablement appris pour la reconstruction des données 2D. Ensuite, nous présentons l'application de cette technique sur des données 3D, en particulier, une analyse des paramètres utilisés, de la généralité de cette approche et les résultats de reconstruction d'images simulées et expérimentales. Nous comparons cette technique avec les approches proposées par l'état de l'art et avec un schéma de sous-échantillonnage adapté aux systèmes d'acquisition ultrasonore 3D.

État de l'art du compressed sensing en imagerie ultrasonore

Dans la partie suivante, nous allons donner un aperçu des approches récentes appliquant le CS en échographie médicale. L'application de le théorie basée sur le CS à l'imagerie ultrasonore a motivé les efforts de recherche récemment, les premiers travaux ayant été publiés en 2010 [Friboulet et al., 2010,Quinsac et al., 2010a,Achim et al., 2010] et donc peu d'études ont été consacrées à ce sujet à ce jour. Un élément clé dans le CS est la représentation parcimonieuse qui permet une meilleure reconstruction du signal. En conséquence, une caractéristique importante des études existantes est le choix de la représentation parcimonieuse des données ultrasonores. De plus, les données échographiques peuvent être considérés à différents stades de la formation de l'image. Donc, une des caractéristiques principales des études existantes est le type de signal ou image à reconstruire et le choix de la base de représentation dans laquelle les données d' ultrasons sont supposées être creuses.

Plusieurs travaux [Schiffner et al., 2012, Schiffner and Schmitz, 2011, Wagner et al., 2012, Wagner et al., 2011, Tur et al., 2011, Chernyakova and Eldar, 2014, Zhang et al.,

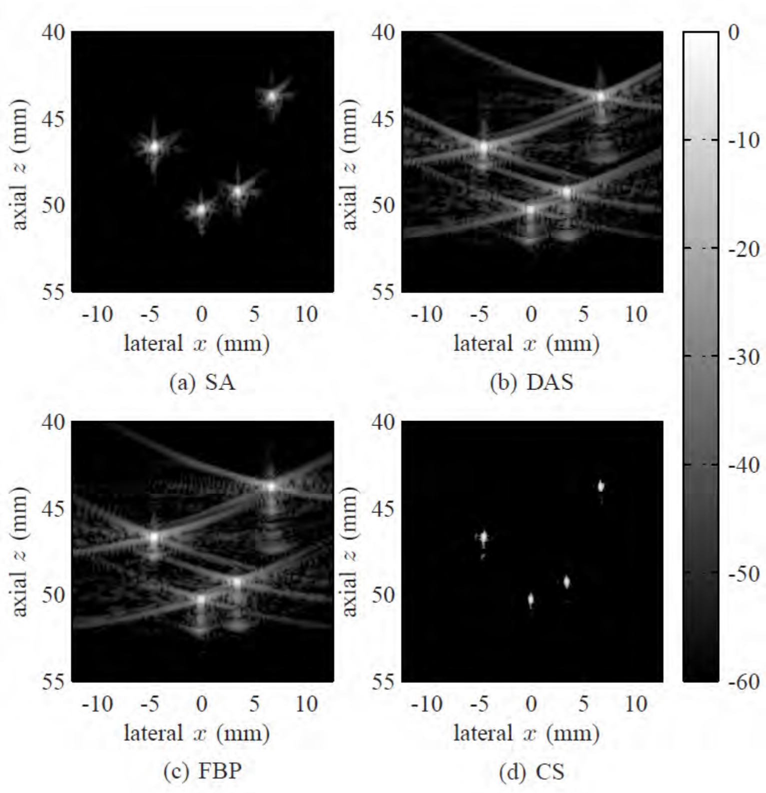

(a) SA (b) DAS (c) FBP (d) CS

FIGURE 5 – Résultat de [Schiffner et al., 2012] obtenus a partir d'un fantôme contenant quatre diffuseurs isolés. Le résultat du CS (d) est comparé avec les techniques conventionnelle de formation d'images ultrasonores (a) Ouverture synthétique, (b) Délais et sommes, (c) Rétro-propagation filtrée.

2013a, Zhuang et al., 2012] font l'hypothèse d'une distribution parcimonieuse des diffuseurs dans le domaine spatial direct. Dans [Schiffner et al., 2012, Schiffner and Schmitz, 2011], les auteurs visent à produire une image qui a la résolution spatiale d'une image US conventionnelle en utilisant une seule onde plane. L'idée à la base de cette méthode est de produire des images à une résolution temporelle plus élevée, le temps d'acquisition étant alors le temps nécessaire pour l'onde plane de faire un aller-retour à la vitesse du son. Cette approche a donné de bons résultats sur les images composées de seulement quelques diffuseurs, comme le montre la Figure 5.

La même hypothèse de parcimonie est proposée dans un contexte différent dans les travaux de [Wagner et al., 2012, Wagner et al., 2011, Tur et al., 2011, Chernyakova and Eldar, 2014], qui sont basés sur les techniques de "finite rate of innovation" et "Xampling". Ces méthodes ont le même inconvénient : elles sont à même de reconstruire correctement uniquement les diffuseurs forts et donc perdent les informations de "speckle". Ces méthodes ont été récemment étendues par une méthode plus générale [Chernyakova and Eldar, 2014] qui s'appuie sur la reconstruction avec la norme l_1 et qui préserve mieux le speckle des images ultrasonores. On peut voir les résultats dans la Figure 6.

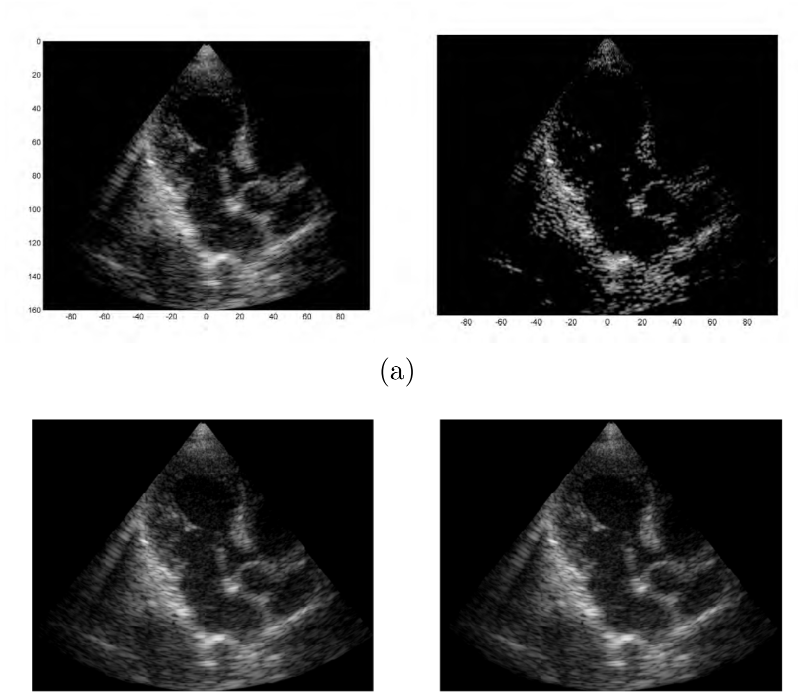

(a)

(b)

FIGURE 6 – (a) Résultats de [Wagner et al., 2012] : image originale et image obtenue par CS avec optimisation l_0. (b) Result from [Chernyakova and Eldar, 2014] : image original et image obtenue par CS avec optimisation l_1.

D'autres études considèrent la parcimonie du signal RF brut. Dans [Liebgott et al., 2013,Friboulet et al., 2010], les mesures de données brutes ont été reconstruites en utilisant la minimisation l_1 et trois bases fixes ont été testées : Fourier, ondelettes et "wave atoms". Les résultats obtenus ont montré que les "wave atoms" donnent une bonne reconstruction avec une erreur de reconstruction deux fois plus petite que la base de Fourier et les images B- mode sont obtenues en utilisant seulement 20 % des mesures originales . Cependant, cette approche utilise un échantillonnage aléatoire uniforme. Cette configuration d'acquisition est difficilement implémentable en pratique .

Une autre possibilité est de considérer que les signaux après formation de voie sont parcimonieux dans une certaine base. Dans [Chuo et al., 2013] ces signaux sont considérés comme parcimonieux dans le domaine des ondelettes, tandis que dans [Quinsac et al., 2010a, Quinsac et al., 2011, Basarab et al., 2013, Dobigeon et al., 2012] la transformée de Fourier des images 2D RF post-formation de voie est supposée être parcimonieuse. Cette hypothèse a été également appliquée dans le contexte du CS Bayésien avec de meilleurs résultats. La Figure 7 montre des résultats de cette approche.

En imagerie ultrasonore 3D il existe très peu d'études qui appliquent le CS. Dans [Quinsac et al., 2010b,Quinsac et al., 2012] des schémas d'échantillonnage par points et par lignes sont proposés et comparés à une seule image RF après formation de voie en utilisant les

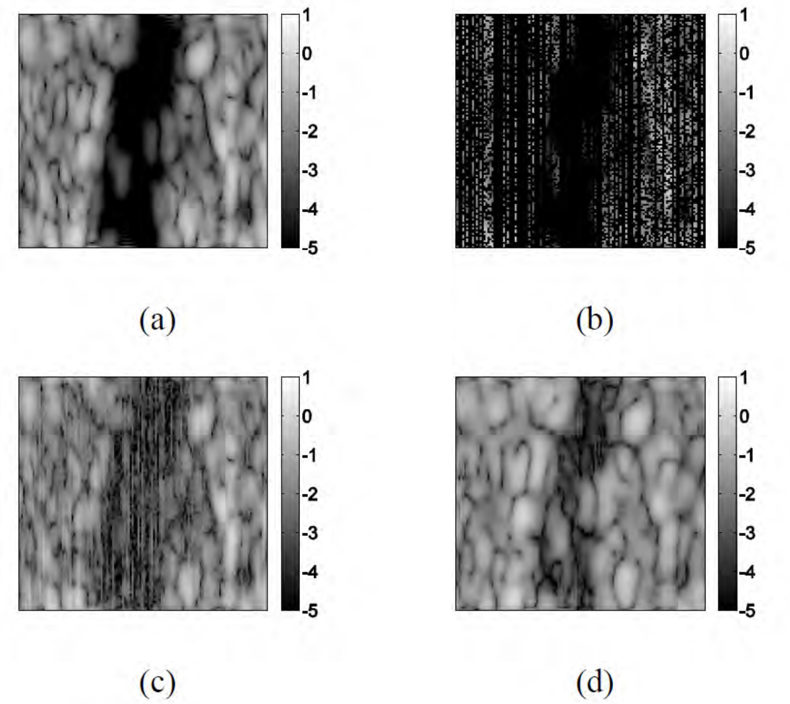

(a) (b) (c) (d)

FIGURE 7 – Résultat de [Dobigeon et al., 2012] : (a) Image US originale, (b) Échantillons mesurés, (c) Image reconstruite avec CS classique et (d) Image reconstruite avec la méthode bayésienne.

transformée en ondelettes, des différences finies et cosinus discrète. Très récemment Birk et al. [Birk et al., 2014] a étendu le mécanisme basé sur le Xampling Analogiques-Digital aux acquisitions 3D.

Contributions

L'objectif de ce chapitre est d'étudier en détail l'application du CS aux ultrasons 3D. Nous allons présenter ici quelques résultats préliminaires , mais aussi quelques nouveautés et contributions :

- Premièrement, nous proposons le cadre CS utilisant des dictionnaires redondants car ils peuvent être optimisés pour une catégorie particulière d'images telles que les images ultrasonores et permettent ainsi des représentations plus parcimonieuses que les bases fixes. Initialement, nous testons cette méthode sur des données 2D.
- Deuxièmement, nous traitons les cas de la reconstruction des données 3D et plus particulièrement, nous montrons que l'approche basée sur les dictionnaires donne de meilleures performances que les méthodes conventionnelles basées sur les transformées fixes tels que Fourier ou la transformée en cosinus discrète.
- Ensuite, nous évaluons la généralité de l'approche dictionnaire. On montre qu'il est possible de construire un dictionnaire permettant de reconstruire de manière fiable

des volumes provenant des différents organes acquis *ex vivo* et *in vivo*.

- Enfin, nous concentrons notre attention sur la configuration du système d'acquisition. Nous avons choisi de nous concentrer sur l'échantillonnage des lignes RF entières Nous étudions l'influence de la stratégie d'échantillonnage sur des données simulées, en comparant les deux modèles d'échantillonnage les plus courants, l'échantillonnage aléatoire par point et par ligne. Nous montrons en particulier que, bien que non entièrement uniforme , les résultats de l'échantillonnage par ligne en utilisant la stratégie basée sur les dictionnaires donne une précision comparable à l'échantillonnage par point classique. Cela indique que l'acquisition CS des données 3D est réalisable en pratique dans un cadre relativement simple.

Application aux images ultrasonores 2D

Les données RF expérimentales ont été acquises avec un échographe Ultrasonix MDP (Richmond, BC, Canada) en utilisant une sonde linéaire L14-5W/60 Prosonic (Korea) avec 128 éléments actifs. La fréquence centrale de la sonde est de 7 MHz et la fréquence d'échantillonnage de 40 MHz. Les images proviennent d'un fantôme de type CIRS Model 054GS (Virginia, USA). Les images acquises ont été ensuite sous-échantillonnées à des taux compris entre 25% et 75% et reconstruites en utilisant le CS.

La reconstruction CS utilisant un dictionnaire redondant a été effectuée en utilisant une approche par blocs. On considère un patch x_p de $\mathbb{R}^n, n < N$, de l'image x et D de $\mathbb{R}^{n \times K}$ un dictionnaire redondant, avec $n < K$, tel que $x_p = Dv_p$. L'application du CS implique l'apprentissage de D tel que v_p soit une représentation parcimonieuse du patch p en D. Nous pouvons ensuite récupérer les patchs de l'image originale a parti des données y. L'apprentissage du dictionnaire a été effectué avec l'algorithme proposé par Rubinstein dans [Rubinstein et al., 2006] et la reconstruction par blocs a été réalisée en utilisant l'algorithme OMP.

Afin d'appliquer la théorie du CS, on fait l'hypothèse que nos signaux sont parcimonieux dans une base Ψ. Le concept de parcimonie dans les transformées d'ondelettes, Fourier et le dictionnaire K-SVD est illustrée dans la Figure 8. Si les coefficients du signal représenté dans une base diminuent rapidement, alors le signal compressé contenant le plus grands coefficients s sera proche du signal original et ce pourcentage de coefficients sera suffisant pour obtenir des reconstructions fiables. Si en plus de la parcimonie nous satisfaisons l'hypothèse d'incohérence alors le signal original peut être reconstruit de façon fiable.

La Figure 9 présente l'erreur de reconstruction en fonction du taux d'échantillonnage pour chaque transformée utilisée dans la reconstruction CS. On remarque que l'erreur augmente avec le taux d'échantillons prélevés. La reconstruction en utilisant le dictionnaire

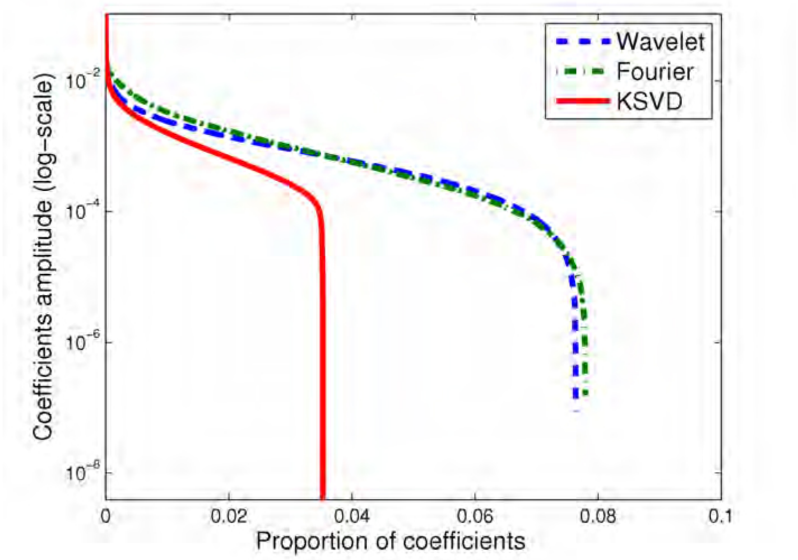

FIGURE 8 – Coefficients d'une image US dans les transformées K-SVD, Fourier et ondelettes ordonnés par ordre décroissant.

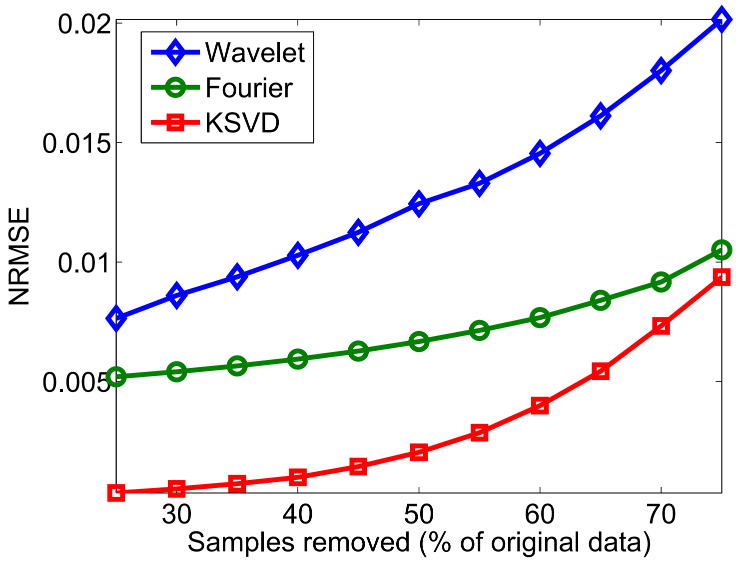

FIGURE 9 – NRMSE en fonction du taux de sous-échantillonnage.

K-SVD donne pour tous les taux de sous-échantillonnage les meilleurs résultats.

Cette étude démontre le fort potentiel des dictionnaires redondant pour la reconstruction CS en imagerie ultrasonore. Les reconstructions des données expérimentales RF utilisant le dictionnaire K-SVD et seulement 25% des échantillons initiaux ont donné des images reconstruites très proches des originales avec une perte d'information minimale.

Application aux images ultrasonores 3D

L'objectif de ce chapitre est d'étudier en détail la faisabilité du CS en échographie 3D.

Les protocoles d'échantillonnage de l'imagerie US doivent être conçus pour satisfaire à la fois les exigences du CS et des appareils échographiques. D'une part , selon la théorie du CS la base d'échantillonnage doit être incohérente avec la base de transformation. D'autre part, les appareils d'imagerie US ont un nombre limité de stratégies d'échantillonnage qui peuvent être adoptées en raison des contraintes physiques et matérielles. Bien sûr, le matériel spécifique pourrait être développé, mais cela est au-delà de la portée de ce travail qui vise à utiliser le CS avec des modifications minimes de l'équipement. Dans ce contexte, on propose l'utilisation d'un échantillonnage par ligne RF qui revient à aléatoirement sauter l'acquisition de certaines lignes RF. Ce type d'échantillonnage, qu'on va noter R_2, est présenté Figure 10. On présente aussi le schéma d'échantillonnage classique par point.

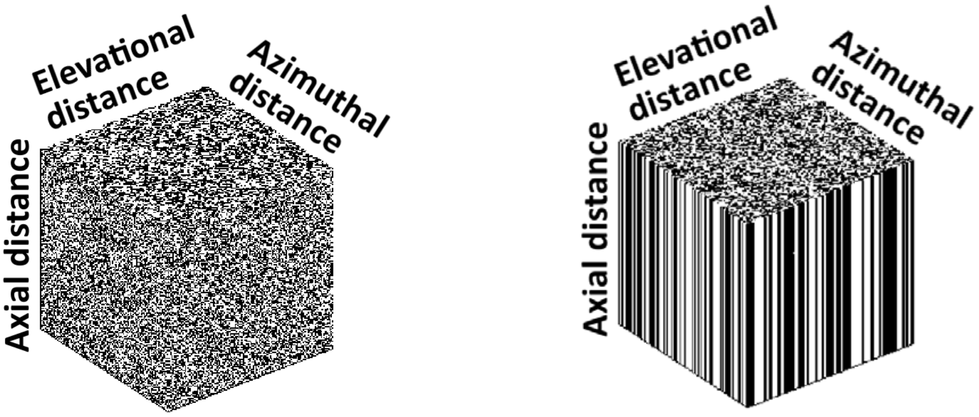

(a) R_1 : échantillonnage par point RF (b) R_2 : échantillonnage par ligne RF

FIGURE 10 – Schémas d'échantillonnage R_1 et R_2. R_1 représente un échantillonnage par point et R_2 un échantillonnage par ligne représentés sur un volume 3D.The black pixels correspond to the samples used for CS. The proportion of samples here is 50% of the original volume.

La reconstruction CS utilisant un dictionnaire redondant a été effectuée en utilisant une approche par blocs. La reconstruction 3D par blocs a été réalisé en utilisant l'algorithme SPGL1 [van den Berg and Friedlander, 2009c].

Les données test consistent dans tous les cas en un seul volume 3D qui n'a pas été inclus dans la base d'apprentissage. La reconstruction CS est ensuite effectuée à partir du volume test sous-échantillonné a des taux compris entre 20% et 80%. Étant donné que dans toutes les expériences, les données proviennent des sondes mécaniques convexes, la reconstruction est effectuée sur les images en coordonnées polaires avant conversion en

Table 1 – Paramètres

Paramètres	Valeurs par défaut value	Valeurs testées
n	**8^3**	$4^3, 6^3, 10^3, 12^3$
r (%)	**50**	0, 25, 75
q	**4**	1, 2, 3

coordonnées cartésiennes.

Résultats

Résultats sur données simulées Premièrement, nous avons testé la méthode proposée sur des données échocardiographiques 3D simulées. Ces données ont été obtenues selon la procédure décrite dans [Alessandrini et al., 2015, Craene and *et al.*, 2013].

Avant de réaliser la comparaison de plusieurs méthode basées sur le CS, nous avons effectué une étude des paramètres utilisés dans la reconstruction et l'apprentissage du dictionnaire sur des données simulées d'échocardiographie. Les paramètres étudiés sont présentés dans le tableur 1 où n est la taille du bloc, r le chevauchement des blocs et q la redondance du dictionnaire. Les paramètres donnant la meilleure performance sont les paramètres par défaut.

En utilisant ces paramètres par défaut nous avons comparé les résultats de la reconstruction utilisant le dictionnaire K-SVD avec la reconstruction utilisant la base fixe de Fourier et la transformée en cosinus discrète pour l'échantillonnage aléatoire par ligne et par point. La Figure 11 présente l'erreur de reconstruction en fonction du taux de sous-échantillonnage pour chaque type de transformée et d'échantillonnage. On observe que l'erreur augmente avec le taux de sous-échantillonnage et que le CS avec le dictionnaire K-SVD donne toujours les meilleurs résultats pour tout type de schéma d'échantillonnage.

Résultats sur données expérimentales *ex vivo* L'acquisition des volumes 3D a été effectuée avec l'échographe Ultrasonix MDP équipé d'une sonde convexe mécanique 4DC7-3/40. La fréquence centrale de la sonde est de 5 MHz et la fréquence d'échantillonnage de 40 MHz. En utilisant ce système, nous avons ensuite acquis des images expérimentales de trois organes *ex vivo* achetés dans le commerce : trois cerveaux, trois cœurs et deux reins de cochon et d'agneau. Dans une première phase nous avons appris le dictionnaire sur un type d'organe et reconstruit le même type d'organe. Les Figures 12.(a) et 12.(b) présentent les résultats obtenus en fonction du taux de sous-échantillonnage pour chaque type de transformée et d'échantillonnage. Nous observons que le CS avec le dictionnaire

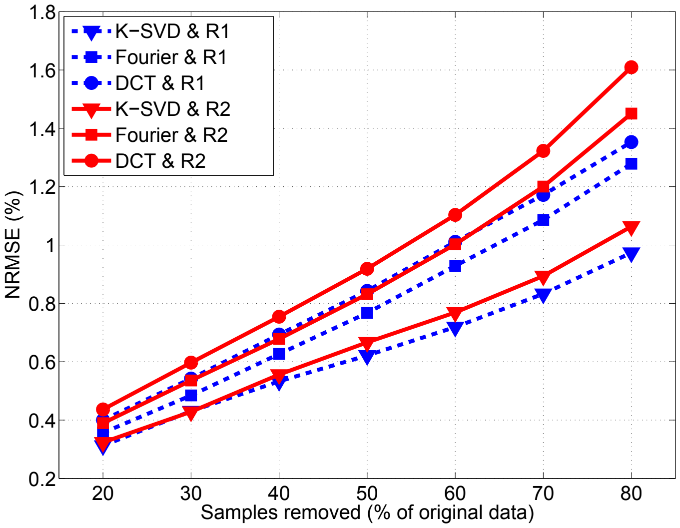

FIGURE 11 – NRMSE en fonction du taux de sous-échantillonnage pour un schéma d'échantillonnage aléatoire par point (R_1) et par ligne (R_2). L'erreur est calculée entre le volume 3D originale et le volume obtenu après reconstruction CS en utilisant le dictionnaire K-SVD, la base Fourier et la transformée en cosinus discrète.

K-SVD donne encore les meilleures résultats. La différence entre la reconstruction CS avec la base Fourier et le dictionnaire K-SVD est entre $[0.26 - 1.4] \times 10^{-2}$ pour R_1 et $[0.35 - 2.2] \times 10^{-2}$ pour R_2 pour les deux organes.

Nous avons également testé la généralité de cette approche. Le dictionnaire K-SVD a été appris sur des volumes *ex vivo* de cerveaux et cœurs et la reconstruction CS utilisant ce dictionnaire a été effectuée sur un volume de rein mais aussi sur les volumes précédents de cœur et cerveau. Les différences entre ces reconstructions et celles présentées dans les Figures 12.(a) et 12.(b) sont très faibles, de l'ordre de 10^{-4}. La reconstruction du rein donne des bons résultats équivalents aux résultats obtenus pour la reconstruction du cœur et du cerveau. La Figure 6.14 présente les images correspondantes aux reconstructions d'un volume 3D de rein en coordonnées polaires et cartésiennes. On montre uniquement les résultats obtenus avec la base de Fourier et le dictionnaire K-SVD pour les taux de sous-échantillonnage de 50% et 80% et un échantillonnage par ligne. On remarque que visuellement le CS avec le dictionnaire K-SVD donne la meilleure reconstruction même à un taux de sous-échantillonnage de 80%. Dans le cas de la reconstruction avec la base de Fourier, on remarque dès le sous-échantillonnage de 50% que les lignes manquantes se voient sur l'image reconstruite alors qu'avec le dictionnaire ce problème commence à se voir uniquement à partir de 80%.

Conclusion Cette étude démontre que la théorie CS utilisant les dictionnaires redondants peut être appliquée à l'imagerie ultrasonore 3D pour réduire le volume de données nécessaires à la reconstruction d'une image 3D. Nous avons également montré que l'ap-

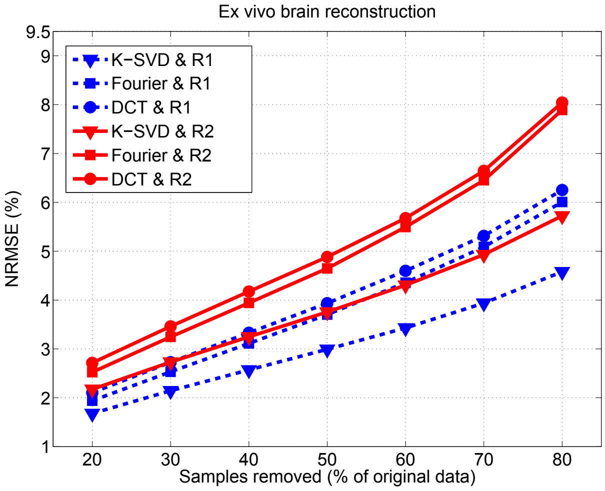

(a) Cerveau *ex vivo*

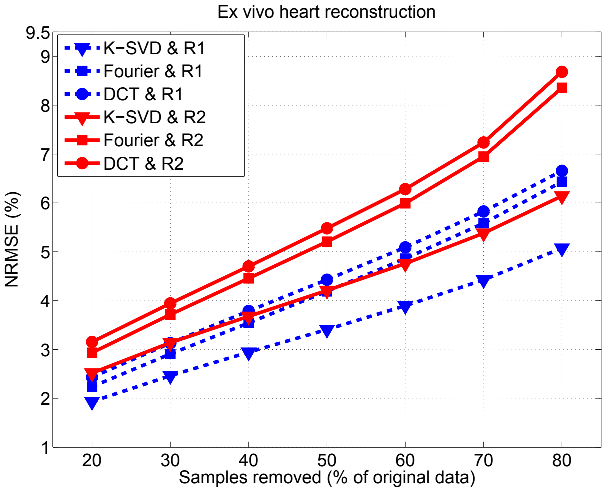

(b) Cœur *ex vivo*

FIGURE 12 – NRMSE en fonction du taux de sous-échantillonnage pour un schéma d'échantillonnage aléatoire par point (R_1) et par ligne (R_2). L'erreur est calculée entre le volume 3D originale et le volume obtenu après reconstruction CS d'un (a) cerveau et (b) cœur en utilisant le dictionnaire K-SVD, la base Fourier et la transformée en cosinus discrète.

proche basée sur l'apprentissage de dictionnaire donne des erreurs inférieures (NRMSE) à celles obtenues par les approches de reconstruction conventionnelles basées sur les transformées fixes tels que la transformée de Fourier ou cosinus discrète.

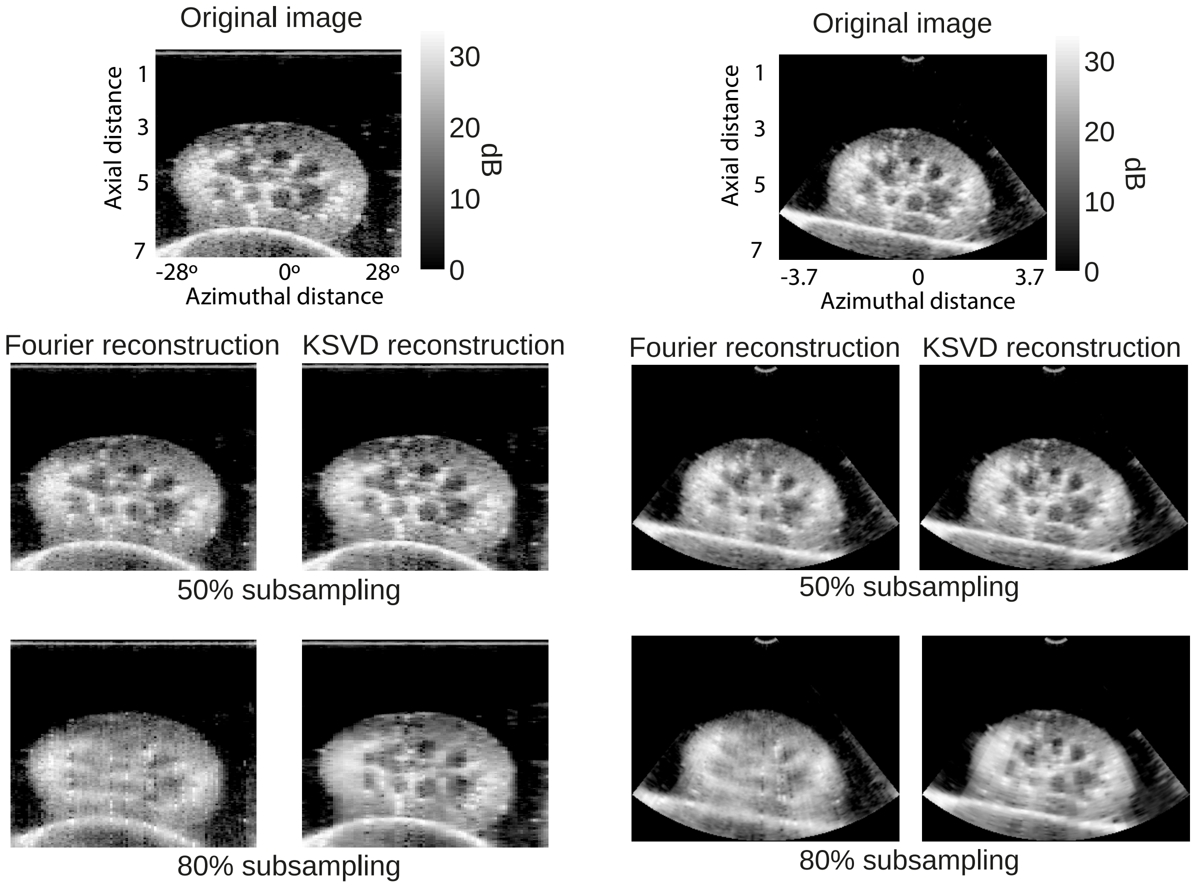

(a) Coordonnées polaires.

(b) Coordonnées cartésiennes.

Figure 13 – Reconstruction d'un volume de rein à partir de 50% et 80% des échantillons acquis avec le schéma d'échantillonnage par ligne. La reconstruction a été effectuée en utilisant la base de Fourier et le dictionnaire K-SVD.

Compressed sensing Bayésien pour l'échographie duplex Doppler

Dans cette partie, nous proposons une méthode qui permet d'alterner de manière aléatoire les émissions Doppler et les émissions d'imagerie pour les systèmes d'échographie Doppler duplex. La technique proposée est basée sur une méthode de CS bayésien qui exploite la corrélation intra-blocs. Nous examinons d'abord les techniques existantes qui utilisent le CS pour reconstruire les signaux Doppler. Nous proposons ensuite une méthode qui exploite la parcimonie et corrélation des blocs de signal dans le cadre Bayésien pour reconstruire le signal Doppler segment par segment.

État de l'art du compressed sensing en imagerie Doppler

L'imagerie duplex permet la visualisation des spectrogrammes Doppler et des images mode-B simultanément. Cependant, si ces deux modes doivent être utilisés en même temps alors une stratégie pour l'acquisition alternée de ces deux types d'images doit être mise en place.

Une première possibilité est d'alterner les deux types d'acquisition. Néanmoins, cette stratégie divise la fréquence d'acquisition des tirs (PRF) par deux et donc aussi la vitesse maximale mesurable. Une autre possibilité est d'interrompre l'émission Doppler pour acquérir une image mode-B complète. Cette approche donne un spectrogramme avec des signaux manquants. Les méthodes de Angelsen [Kristoffersen and Angelsen, 1988] et Klebaek et al. [Klebaek et al., 1995] ont été proposées pour interpoler les signaux manquants. Cependant, ces méthodes font l'hypothèse que le flux sanguin est stable et prédictible, ce qui n'est pas toujours le cas. Les seules études qui reconstruisent les données manquantes ont été proposées par Jensen dans [Jensen, 2006] et [Mollenbach and Jensen, 2008].

Dans le contexte du compressed sensing, une étude récente proposée dans [Richy et al., 2013] permet de réduire considérablement le nombre d'émissions Doppler et donne de meilleurs résultats que l'interpolation traditionnelle. La particularité de cette étude est la reconstruction du signal segment par segment et l'utilisation de la transformée de Fourier et des "wave atoms" pour représenter les signaux Doppler de façon parcimonieuse.

Application aux données Doppler

Le principe de l'acquisition compressée et de la reconstruction d'un signal Doppler à partir de ces données est présenté dans la Figure 14. Le signal d'origine est noté $x \in \mathbb{C}^N$ et un segment de ce signal x_i de $\mathbb{R}^n, n \ll N$. Donc pour ce segment, on peut écrire dans la formulation CS : $x_i = \Psi v_i$ où Ψ de $\mathbb{R}^{n \times n}$ est la transformation parcimonieuse et v_i les coefficients parcimonieux. Le signal x peut donc être reconstruit avec le schéma CS classique comme proposé dans [Richy et al., 2013] où Ψ sera la base de Fourier ou les "wave atoms" et la reconstruction sera effectuée avec l'algorithme YALL1 [Yang and Zhang, 2011a, Yang and Zhang, 2011b].

À la différence de cette dernière approche, nous proposons ici d'exploiter la corrélation interne de ce type de signal et donc d'utiliser l'approche bayésienne proposée par [Zhang and Rao, 2012, Zhang and Rao, 2013a] pour reconstruire chaque segment. Les deux méthodes bayésiennes que nous utilisons pour la reconstruction CS sont appelées "Block Sparse Bayesian Learning (BSBL)" et "Extended Block Sparse Bayesien Learning (EBSBL)". La transformation parcimonieuse sera la base de Fourier afin de pouvoir comparer nos résultats à ceux proposés dans [Richy et al., 2013].

Résultats

Résultats sur données simulées Tout d'abord nous avons simulé le flux sanguin dans une artère fémorale et l'acquisition Doppler correspondante. Premièrement, nous avons effectué une étude des paramètres des méthodes BSBL et EBSBL et de la reconstruction CS. Ensuite, nous comparons ces deux méthodes aux méthodes classiques de reconstruction CS utilisant la base de Fourier et les "wave atoms" proposées par [Richy et al., 2013]. Ces résultats ,représentés Figure 15.(a), montrent que les approches que nous proposons donnent de meilleurs résultats pour tous les taux de sous-échantillonnage allant de 20% à 80%. La différence en terme de PSNR entre les approches BSBL et EBSBL et le CS classiques sont d'environ 7 dB, ce qui représente une différence de qualité considérable. La Figure 9.10.(b) montre aussi le temps de calcul pour chaque algorithme. On remarque que les temps de calcul des algorithmes BSBL et EBSBL sont 100 fois plus élevés que ceux du CS classique basé sur la transformée de Fourier. Cependant, étant donné que la performance de l'algorithme BSBL est équivalente à celle de l'algorithme EBSBL, on utilisera en priorité le plus rapide des deux. De plus on constate que la reconstruction avec les paramètres $n = 256, r = 50\%$ est plus lente qu'avec les paramètres $n = 128, r = 25\%$.

La Figure 16 montre les spectrogrammes obtenus avec les algorithmes BSBL, EBSBL et le CS classique avec les bases Fourier et wave atome pour des taux de sous-échantillonnage

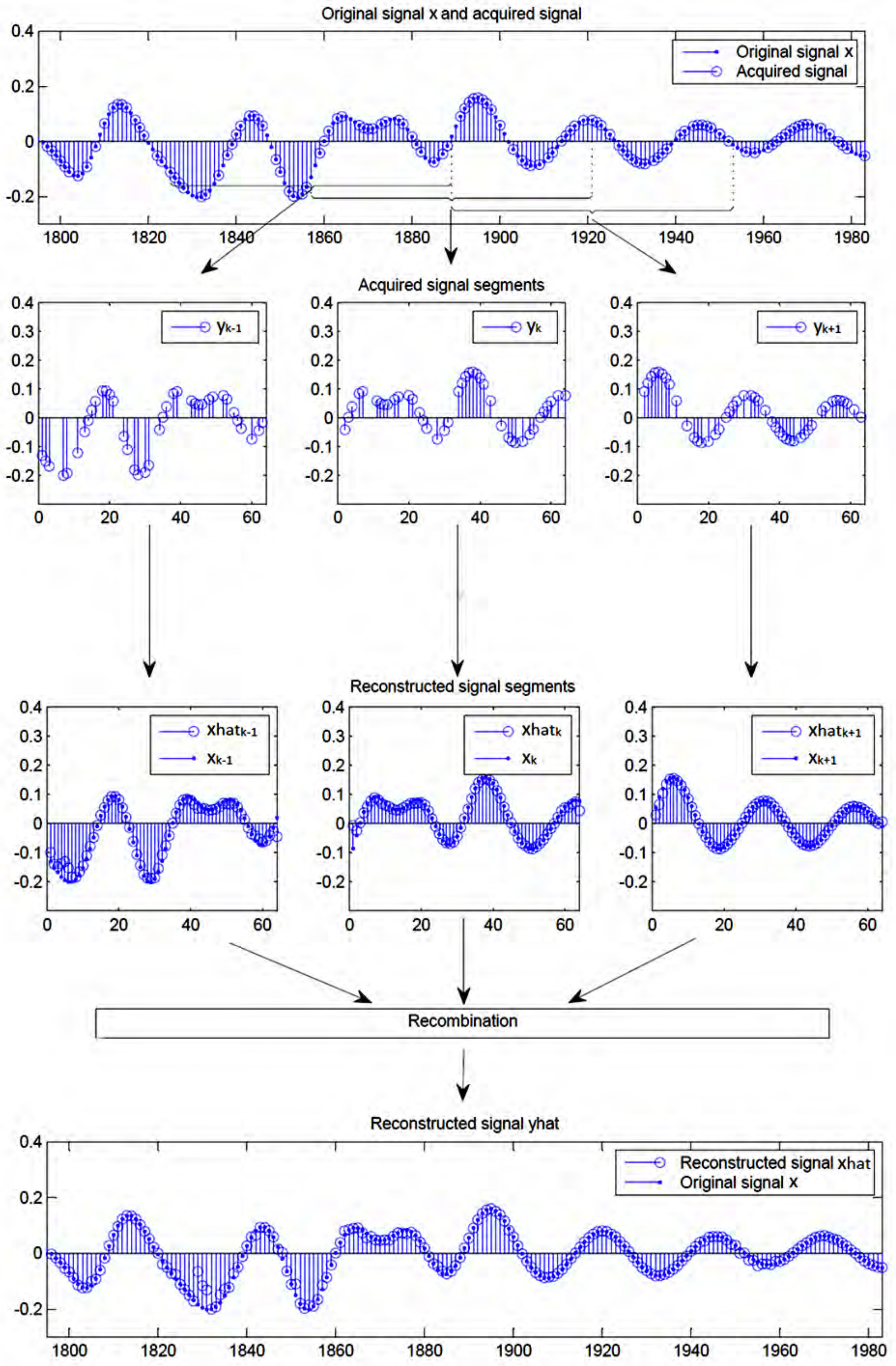
Original signal x and acquired signal

Acquired signal segments

Reconstructed signal segments

Reconstructed signal yhat

FIGURE 14 – Principe de la méthode

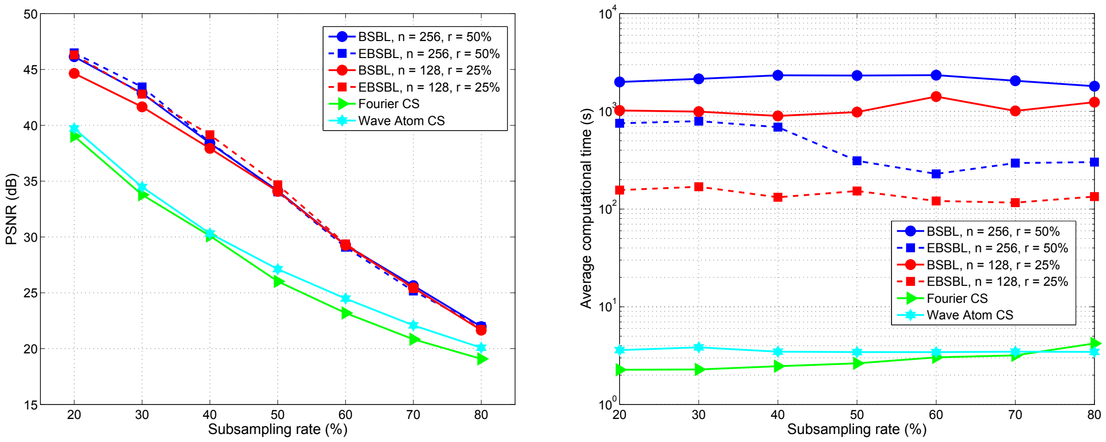

(a) (b)

FIGURE 15 – (a) PSNR et (b) temps de calcul moyen pour la reconstruction CS avec les algorithmes BSBL, EBSBL et le "Basis Pursuit" classique en fonction du taux de sous-échantillonnage (S %).

élevés, $S = 50, 60, 70, 80\%$. On remarque que la reconstruction avec l'approche CS classique est fortement perturbée par du bruit à partir de $S = 50 - 60\%$. À partir de ce seuil, le signal est fortement perturbé surtout sur le premier tiers du cycle, qui correspond à la portion la moins parcimonieuse. La partie restante étant beaucoup plus parcimonieuse est bien reconstruite même à $S = 80\%$. L'avantage des approches BSBL et EBSBL est que le signal est reconstruit même sur la portion dense et ce jusqu'à un taux de sous-échantillonnage de 80%. On gagne également un taux de compression d'au moins 10% par rapport au CS classique, car avec un taux d'échantillonnage de 70% on obtient avec BSBL et EBSBL un PSNR plus grand qu'avec le CS classique à 60%.

Résultats sur données expérimentales On propose de tester ces approches sur des données acquises *in vivo*. Le spectrogramme Doppler a été acquis sur l'artère fémorale d'un sujet sain. Le sous-échantillonnage et la reconstruction ont été effectués a posteriori.

La Figure 17 présente les résultats de la reconstruction CS avec les différentes approches proposées en fonction du taux de sous-échantillonnage. La première remarque est que le PSNR est globalement plus faible que pour les données simulées. Cependant, les méthodes BSBL et EBSBL donnent toujours des meilleurs résultats. La différence en terme de PSNR entre les approches BSBL et EBSBL et le CS classiques sont d'environ 2 dB. Dans ce cas aussi, les approches bayésiennes permettent d'augmenter le taux de compression d'environ 10%. Les temps de calcul sont équivalents aux temps obtenus sur les données simulées.

Dans la Figure 9.14 nous montrons les spectrogrammes Doppler obtenus avec les dif-

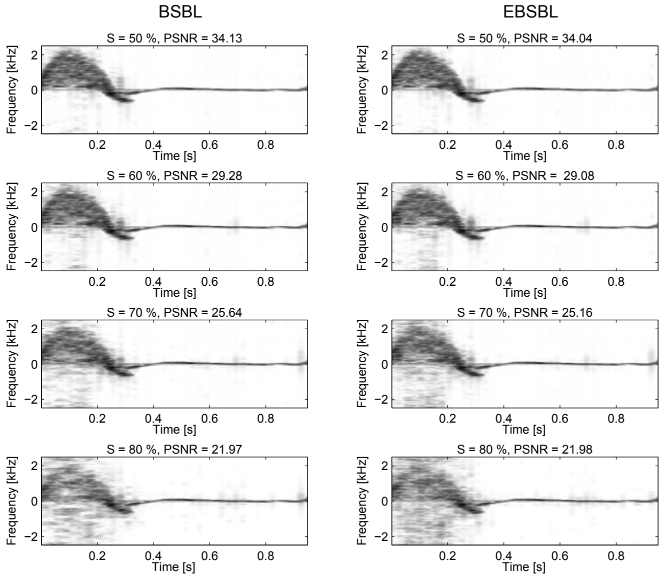

(a) BSBL and EBSBL algorithms

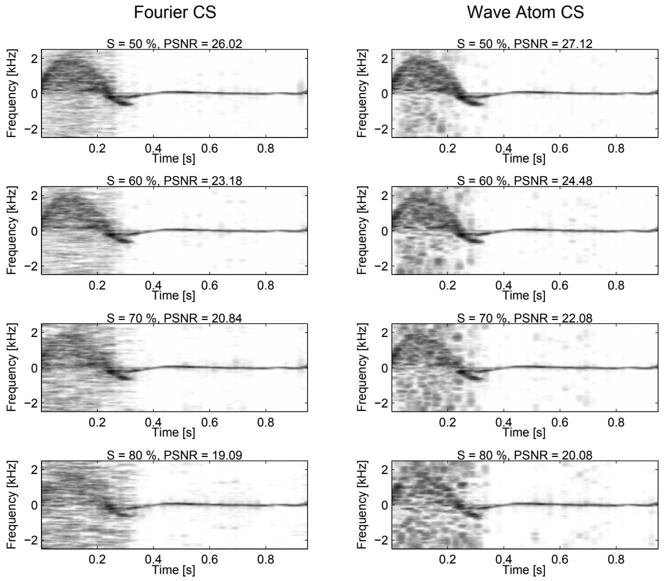

(b) Fourier and Wave atom CS

FIGURE 16 – Spectrogramme du signal reconstruit avec (a) BSBL et EBSBL et avec (B) le "Basis Pursuit" classique avec les transformées Fourier et "wave atoms" pour les taux de sous-échantillonnage : $S = 50, 60, 70, 80\%$.

férentes approches. Sur cette Figure, on remarque que sur les données expérimentales les méthodes BSBL et EBSBL donnent visuellement les meilleures reconstructions. Le bruit de fond est mal restauré par toutes les méthodes, mais avec un comportement qui dépend de la méthode de reconstruction. On constate que les méthodes bayésiennes éliminent le bruit de fond sur certaines zones qui correspondent aux partitions du signal Doppler choisies au préalable lors de la reconstruction. Cependant, pour tous les taux de sous-échantillonnage le signal Doppler est correctement reconstruit. On en déduit que ces approches allouent plus efficacement le nombre limité de fréquences disponibles de la transformée de Fourier aux composantes les plus élevées. Dans le cas de la reconstruction classique CS le bruit est plus uniformément distribué et le signal Doppler est quasi-complètement perdu pour des taux de sous-échantillonnage élevés.

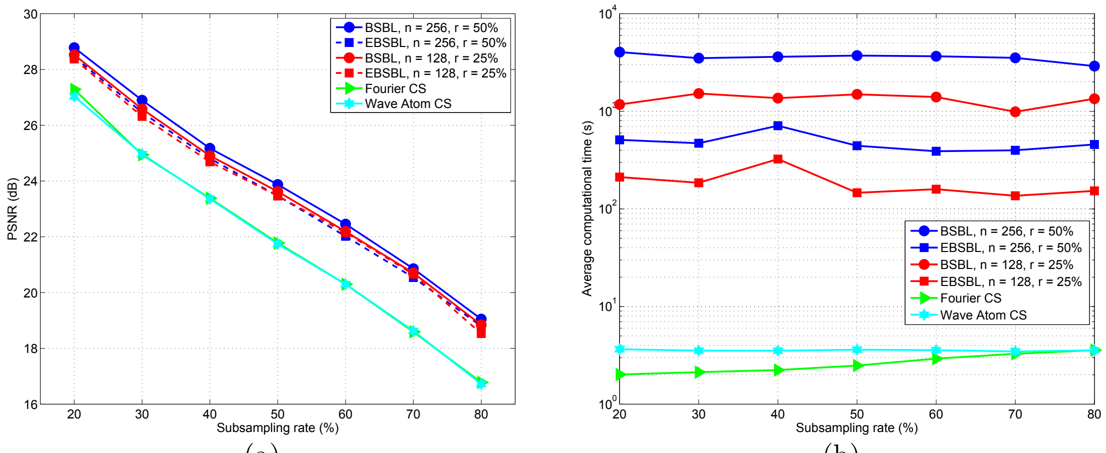

(a) (b)

FIGURE 17 – (a) (a) PSNR et (b) temps de calcul moyen pour la reconstruction CS avec les algorithmes BSBL, EBSBL et le "Basis Pursuit" classique en fonction du taux de sous-échantillonnage (S %).

Conclusion La technique proposée montre une amélioration des résultats par rapport à l'étude précédente basée sur une approche CS classique [Richy et al., 2013]. Avec les approches bayésiennes proposées les reconstruction des données simulées et expérimentales sont améliorées pour tous les taux de sous-échantillonnage et on gagne en moyenne un taux de compression de 10% par rapport aux approches classiques.

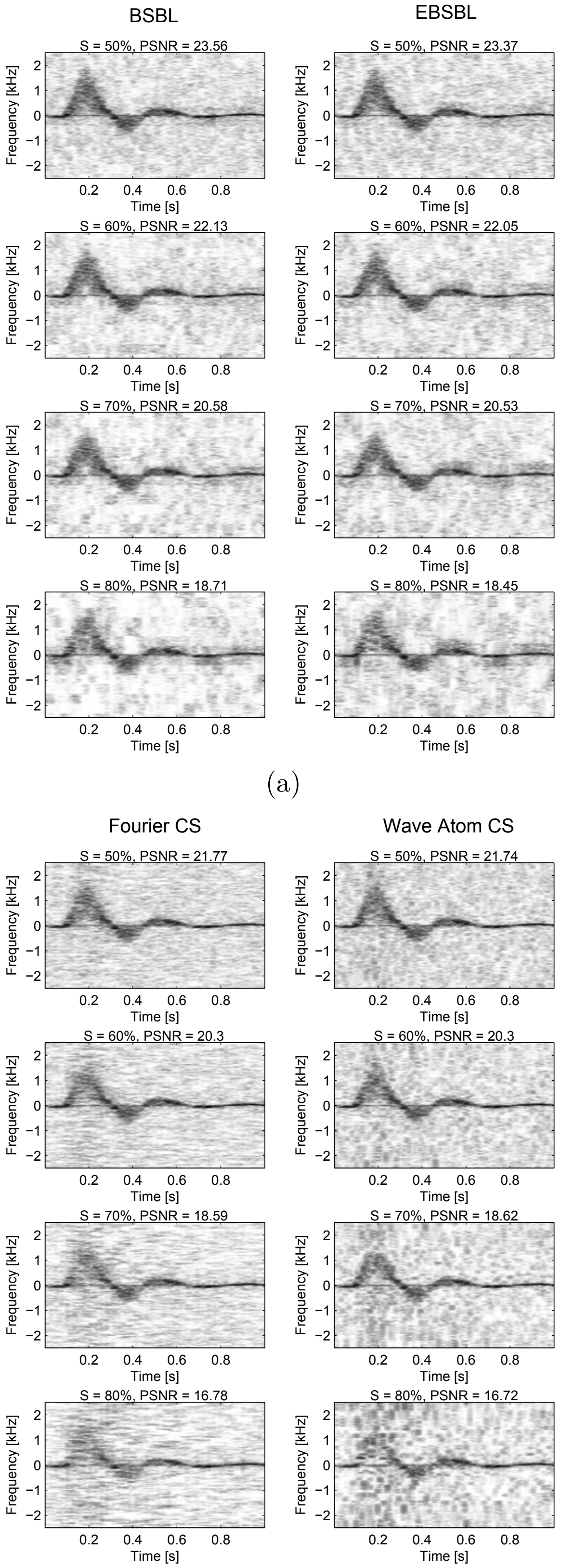

(a)

(b)

FIGURE 18 – Spectrogramme du signal reconstruit avec (a) BSBL et EBSBL et avec (B) le "Basis Pursuit" classique avec les transformées Fourier et "wave atoms" pour les taux de sous-échantillonnage : $S = 50, 60, 70, 80\%$.

Conclusions et perspectives

Notre travail de recherche sur les méthodes pour la reconstruction CS des images 3D ultrasonores en utilisant des dictionnaires redondants et des signaux Doppler basée sur une approche bayésienne a encore quelques limites et offre ainsi plusieurs perspectives de recherche.

Une des limites de cette étude provient de l'utilisation de dictionnaires préalablement appris. Bien que ceux-ci fournissent des représentations plus parcimonieuse et adaptées à nos données, leur inconvénient est qu'ils ne sont pas inversibles ou n'ont pas de transformation inverse rapide, donc pour chaque reconstruction un problème de minimisation doit être résolu. Cela augmente le temps de calcul (plusieurs heures avec notre code Matlab non optimisé), de sorte que la méthode CS basée sur l'utilisation des dictionnaires ne peut pas être utilisée actuellement pour des acquisitions 3D en temps réel. Dans le but de rendre notre algorithme utilisable en routine clinique, il est primordial de le rendre temps réel. Dans cette optique, une solution à ce problème pourrait venir de l'implémentation GPU de cette méthode. A titre d'exemple, en IRM [Li et al., 2014] ont conçu des algorithmes parallèles sur GPU pour l'algorithme d'apprentissage de dictionnaires et la reconstruction et les résultats expérimentaux ont montré une augmentation de la vitesse de plus de 325 fois par rapport aux codes non-optimisés sur CPU.

Une alternative à l'approche proposée pourrait consister à utiliser des techniques de "Deep Learning", qui permettent d'apprendre le dictionnaire mais aussi une transformation non-linéaire inverse [Qian and Shi, 2014, Gregor and LeCun, 2010]. Dans ce cas, son utilisation dans le contexte CS pourrait être intéressante car nous disposons du dictionnaire adapté pour représenter la parcimonie de nos signaux mais aussi de sa transformation inverse qui accélère l'étape de reconstruction. A notre connaissance, le seul exemple d'application de cette démarche prometteuse a été réalisé pour des données IRM par [Majumdar, 2015].

Il serait également très intéressant d'étudier la reconstruction CS des images dynamiques. En effet, dans le contexte de l'imagerie dynamique, nous pouvons supposer qu'une grande partie de l'anatomie a un mouvement lent et seules quelques portions ont un mouvement rapide. Ainsi, la différence entre deux images consécutives donne une image des différences parcimonieuse puisque les zones dont les mouvements sont lents s'annulent mutuellement et les zones avec des mouvements rapides donnent l'image des différences. L'hypothèse que la différence entre deux images consécutives est parcimonieuse représente une condition d'application idéale du CS sous une contrainte de parcimonie temporelle. Il serait intéressant de tester plusieurs algorithmes qui prennent en compte ce type de contrainte, tel que les algorithmes : Kalman Filtered Based Compressed Sensing (KF-CS) [Vaswani, 2009], Least-Squares Compressed-Sensing (LS-CS) [Vaswani, 2010] et Spatio-Temporal Sparse Bayesian Learning (STSBL) [Zhang et al., 2014] .

En imagerie duplex (imagerie Doppler associée à l'imagerie mode-B), il est important d'envisager une implémentation sur GPU ou sur CPU multi-cœur du code Matlab non-optimisé. Nous avons obtenu une reconstruction des signaux Doppler de bonne qualité sans changer le système d'acquisition. Cependant, les temps de reconstruction sont trop longs pour une acquisition en temps réel. Une implémentation GPU des approches proposées pourrait nous permettre une implémentation de ceux-ci sur les systèmes d'imagerie Doppler et un probable gain en compression à l'acquisition de jusqu'à 80%.

Une des limitations de cette étude concerne la validation qui n'a été effectuée que sur des images de sujets sains. Il serait donc important de valider aussi les performances de notre méthode sur des cas pathologiques afin de s'assurer qu'elle donne toujours des résultats corrects.

I Introduction

Objectives

The recently introduced compressed sensing (CS) theory allows, under certain assumptions, to recover a signal sampled below the Nyquist sampling limit. Compressed sensing (also known as compressive sensing or compressive sampling) can be applied for two main purposes :

- It can lower the amount of data needed and thus allows to speed up acquisition.
- It can improve the reconstruction of signals/images in fields where constraints on the physical acquisition setup yield very sparse data sets.

This work focuses on medical ultrasound, where CS theory has not been investigated deeply, yet several applications are excellent candidates.

Traditional imaging modalities, like ultrasound (US) echography, rely all on Shannon's theorem that fixes the limit for the sampling frequency of a signal to twice its highest frequency component. In order to avoid artifacts and to respect Shannon's theorem, US devices use a sampling rate that is at least four times the central frequency of the emitted pulse. Consequently, when sampling at such rates, the amount of data obtained is large, especially in 3D imaging, and can impair real-time imaging or data transfer. In 3D US imaging, the number of radiofrequency (RF) lines that must be acquired to sweep the whole volume can be extremely high, typically several thousands. The acquisition time of one RF line is related to the speed of sound and the depth of investigation and cannot be compressed, leading to long acquisition times and thus low frame rate (several Hz) which limits acquisitions for dynamic organs, such as the heart. In this context, the compressed sensing (CS) theory offers the perspective of reducing the amount of data acquired. Its application to medical ultrasound imaging is promising thanks to its capability to reduce the volume of acquired data and thus to speed up the acquisitions and increase the imaging rate of 3D US devices.

Another excellent candidate for CS theory is the Doppler duplex imaging that implies alternating between two modes of emission, one for B-mode imaging the other one for flow estimation, thus giving sparse velocity measurements. By randomly alternating the two modes of emissions, compressive sensing allows us to recover the Doppler signal using much fewer emissions.

The work presented in this thesis falls within the scopes described above and is dedicated to the application of the CS theory for the compressed acquisition and reconstruction of 3D US images and Doppler signals. It addresses the following methodological aspects :

- A key element in CS is that the data to be reconstructed should have a sparse expansion in some basis or dictionary. As a consequence, one important feature of the existing studies is the choice of the representation where the US data is assumed to be sparse. To this end, we propose using learned overcomplete dictionaries for the

CS reconstruction of 3D US images.
- Another important feature for ensuring a successful CS reconstruction is the way the measurement of the data is performed. Thus, we focus our attention on the line-wise sampling of entire RF lines in 3D US imaging which results in an increase of the frame rate.
- A difficulty often encountered in this context is the recovery of non-sparse or partially-sparse signals such as the Doppler signals. Thus, we proposed a CS framework based on the block sparse Bayesian learning that has the particularity of being able to recover non-sparse signals by exploiting their correlation structure.

Thesis overview

This manuscript is composed of three main parts.

In the first part, we present the physical basis of the ultrasound image formation and give the main properties of the echographic image. We focus on the existing modalities that allow the acquisition of 3D ultrasound images, their limitations and perspectives. We also present ourselves in the dynamic ultrasound systems that are used to estimate and visualize blood flow in the body, the Doppler systems. Particular attention is given to the existing types of Doppler systems and to the formation of the Doppler spectrogram. In the following chapter of this part, we summarize the main aspects of the compressed sensing theory. We will describe the general framework, the main theorems and illustrate and analyze the associated assumptions of the CS theory. This will lead us to a discussion on the existing reconstruction techniques. The sparse reconstruction problem of compressed sensing can also be formulated in a Bayesian framework, which we will present in this part. The last chapter focuses on the use of dictionary learning techniques in the sparse optimization context which will be used in this thesis.

The second part is dedicated to the application of compressed sensing using dictionary learning to ultrasound images. We propose in this work to use adapted learned overcomplete dictionaries to sparsely represent our ultrasound images. We begin by giving a detailed review of the compressed sensing methods used for the reconstruction of 2D and 3D images. In this context, we show preliminary results from the application of the dictionary based method to 2D ultrasound images. The next chapter, presents the conditions of application of the proposed approach to 3D data. It details in particular the sampling patterns, reconstruction scheme and the study of optimal parameters used in this contribution. Finally, we validate this algorithm on simulated, *ex vivo* and *in vivo* experimental data and we evaluate the generalization ability of the proposed approach.

In the third part of this thesis, we propose a framework for randomly interleaving in duplex Doppler ultrasound systems, where the acquisition time needs to be shared between the Doppler emissions and the B-mode imaging emissions. The proposed technique is based on a Bayesian CS framework that exploits intra-block correlation. We first review the existing techniques that use CS to reconstruct Doppler signals. We then propose a method based on the block sparse Bayesian framework to reconstruct the Doppler signal segment by segment. The performance of the algortihm is validated on simulated and experimental data and compared to a state-of-the-art method.

II Background

Chapitre 1

Ultrasound imaging

Ultrasound is a widespread medical imaging technique that relies on the propagation of ultrasound waves in biological tissues. This imaging system presents important advantages that make it one of the most popular medical modalities, among which :

- The relative low cost of the system compared to other imaging modalities such as CT, MRI, PET.
- The transportability of the equipment giving the possibility to perform bedside exams.
- The safety of this imaging type as it is non-ionizing and non-invasive.
- Lastly, echography is the only non-invasive medical imaging modality that acquires true real-time visualization of body structures by displaying their acoustic properties.

All these advantages make ultrasound imaging very attractive to the medical community and oneof the most common used techniques in medical diagnostic imaging.

1.1 Ultrasound image formation

Ultrasound imaging is based on the physical interaction between an emitted acoustical wave and the tissues of the human body. Part of the wave is reflected back in the direction of the ultrasound system whenever the wave travels through structures within the body. The intensity of the returning echoes are then used to image the tissues. Furthermore, the ultrasound wave transfers energy to the medium as it travels, which is converted to heat. The acoustic waves can have three main interaction forms with the tissues which are absorption, reflection and refraction.

1.1.1 Equipment

Transducer

An ultrasound system consists of a transducer composed of a certain number of piezoelectric elements that generate a sound wave when stimulated by an electrical signal that is transmitted into the tissue. The piezoelectric elements convert the electrical energy to acoustic energy and vice versa. Thus, usually the same transducer is used for both transmitting and receiving the ultrasound waves. The acquisition can be done with different types of transducers that sweep a rectangular area or a sectorial area (Figure 1.1). A rectangular area sweep is done with linear transducers that emit parallel beams. While the sectorial areas can be covered with two kinds of probes : convex probes or phased arrays. Convex probes use electrical sweeping to translate the activation of the elements over the convex surface to cover the sectorial zone which allows to scan deeper and wider structures. Phased arrays use electronical beam steering and are much more compact than convex probes, which makes them more useful in echocardiography as they can avoid obstacles such as the thoracic cage ribs.

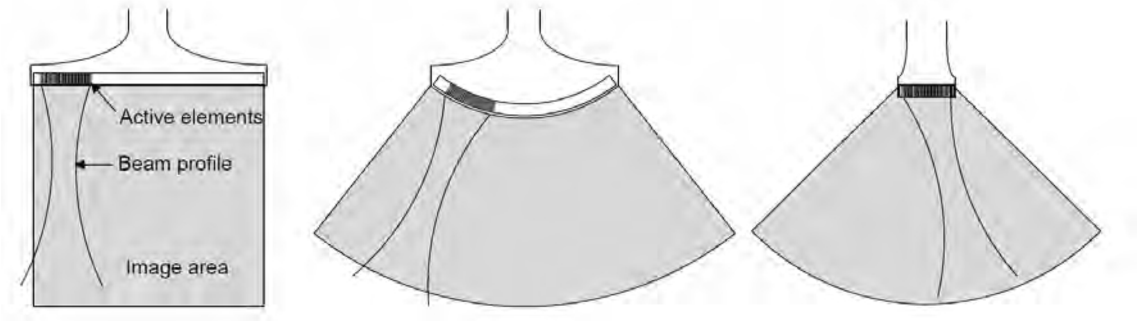

(a) (b) (c)

FIGURE 1.1 – (a) Linear array transducer. (b) Convex array transducer. (c) Phased array transducer.

Beamforming

The echographic image is built by using transducers with multiple piezoelectric elements that are activated both in emission and reception mode. The construction principle is based on the Huygens principle that states that a wavefront can be decomposed in a number of point sources, each being the center of an expanding spherical wave. Thus, any type of wavefront can be constructed using point sources. By considering the piezoelectric elements as point sources we can use this approach to focus and steer the ultrasound beam on the desired location of the medium. At transmission, the beam is formed by delaying the emission on each piezoelectric element to focus the emitted energy on a depth of interest as shown in Figure 1.2.(a). At reception, the received signals are delayed to allow focusing and then summed as in Figure 1.2.(b). In addition to focusing, the system can be improved by weighting the contribution of each element, this being called apodization. For more details on beamforming methods, one may refer to [Angelsen, 2000, Liebgott, 2005].

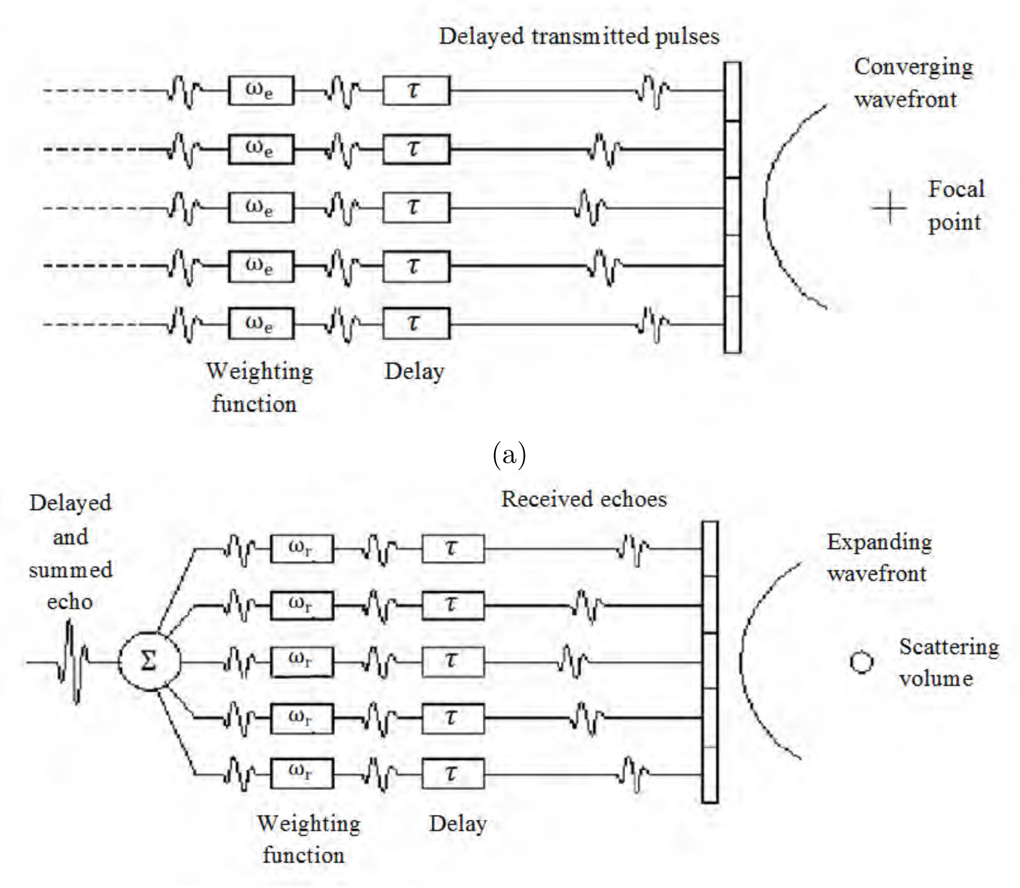

(a)

(b)

FIGURE 1.2 – Principle of delay and sum beamforming (a) in emission and (b) in reception.

Image resolution

The quality of an ultrasound system depends strongly on both axial and lateral resolutions of the acquisition system.

Axial resolution The axial resolution refers to the ability to distinguish two different structures that lie in the direction of the propagation (i.e. parallel) of the ultrasound beam as separate and distinct. This resolution depends on the shape and length of the ultrasound wave, on the wave-length and the band-width of the probe. The frequencies used in echography usually range from 1 to 20 MHz. However, the attenuation of the sound wave is increased at higher frequencies, so in order to have better penetration of deeper tissues, a lower frequency (3-5 MHz) is used. At about 3-3.5 Mhz, the axial resolution is about 0.2 mm.

Lateral resolution The lateral resolution refers to the ability to distinguish two structures lying side by side (i.e., perpendicular to the beam axis). Lateral resolution is directly related to the transducer beam width, which in turn is inversely related to the ultrasound frequency : the thinner the beam, the better the lateral resolution will be. The lateral resolution depends on the geometry of the transducer, the frequency and the focal distance which corresponds to the distance between the probe and the point where the beam is the finest. Using the beamforming technique, the focusing can be modified during the exam by the operator to give an optimal resolution in the region of interest. It can be noted that using dynamic focusing, it is also possible to focus on multiple points along a certain direction.

1.1.2 Fundamental physical concepts

Ultrasound imaging relies on the physical interaction between an ultrasound wave and the tissues of the human body. As the acoustic wave travels through the body, it is changed and distorted by the physical properties of the tissues it encounters. Part of the wave is reflected whenever the wave travels through an interface between two media with different acoustical properties (acoustic impedance mismatch). Furthermore, the ultrasound wave transfers energy to the medium as it travels, which is converted to heat. The main interaction forms are absorption, reflection and refraction, while the reflection may be classified as specular or diffuse, the latter yielding to the well-known speckle phenomenon.

Medium	Density $[kg \cdot m^{-1}]$	Speed of sound $[m \cdot s^{-1}]$	Characteristic acoustic impedance $[kg \cdot m^{-2} \cdot s^{-1}]$	Attenuation α at 1 MHz $[dB \cdot cm^{-1}]$
Air	1.2	333	0.40×10^3	12
Blood	1.06×10^3	1566	1.66×10^6	0.2
Bone	$1.38 - 1.81 \times 10^3$	2070 - 5350	$3.75 - 7.38 \times 10^6$	10
Brain	1.03×10^3	1505 - 1612	$1.55 - 1.66 \times 10^6$	0.6
Fat	0.92×10^3	1446	1.33×10^6	0.48
Kidney	1.04×10^3	1567	1.62×10^6	
Lung	0.40×10^3	650	0.26×10^6	40
Liver	1.06×10^3	1566	1.66×10^6	0.5
Muscle	1.07×10^3	1542 - 1626	$1.65 - 1.74 \times 10^6$	1.09
Spleen	1.06×10^3	1566	1.66×10^6	0.0022
Water	1.00×10^3	1480	1.48×10^6	
Soft Tissues		1540 (average)	1.63×10^6	0.54 (average)

TABLE 1.1 – Approximate densities, sound speeds, characteristic acoustic impedances and attenuation of human tissues.

Absorption

As the ultrasonic wave propagates, the particle oscillations that it causes require energy, causing the wave to lose energy mostly in the form of heat. This phenomenon is characterized by the attenuation coefficient. This coefficient is specific to each medium and increases with the wave frequency, see Table 1.1.

Reflection and transmission

As a plane ultrasonic wave encounters an interface between two media of different mechanical properties, a part of the energy is carried into the second medium and a part of it is reflected as an echo at places where there are discontinuities in the acoustical properties between the two media. This phenomenon is dependent of the incident angle and the differences of acoustic impedances of the media (see Table 1.1). Acoustic reflexions are of two kinds depending of the size of the interface : specular and diffuse reflection.

Specular reflection (see Figure 1.3) appears when the transmitted ultrasound wave meets interfaces where the size of the inhomogeneities in acoustical impedance is larger than the wavelength of the acoustical signal. Thus, specular reflections allow to visualize boundaries of two different media, like those which separate blood and tissue.

Diffuse reflection type occurs at an interface whose dimensions are comparable to the wavelength or smaller. The diffuse reflection phenomenon is responsible for the "noisy" nature of ultrasound images (also known as "speckle") and gives information about spatial properties of the point scatterers as illustrated in Figure 1.4.

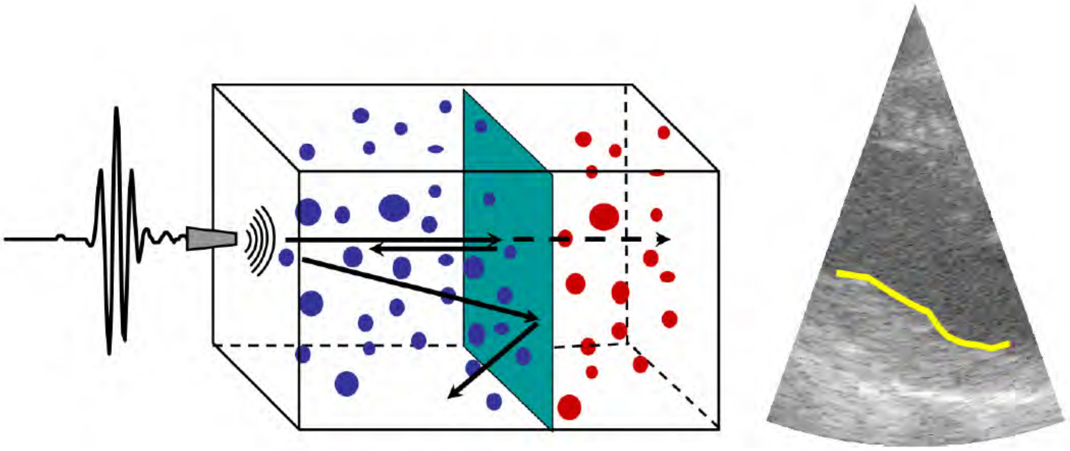
(a) diagram

(b) real image

FIGURE 1.3 – Illustration of specular reflection. (a) principle of specular reflection. (b) Specular interface that separates blood pool from tissue region (yellow line). Reproduced with permission from [Bernard, 2006].

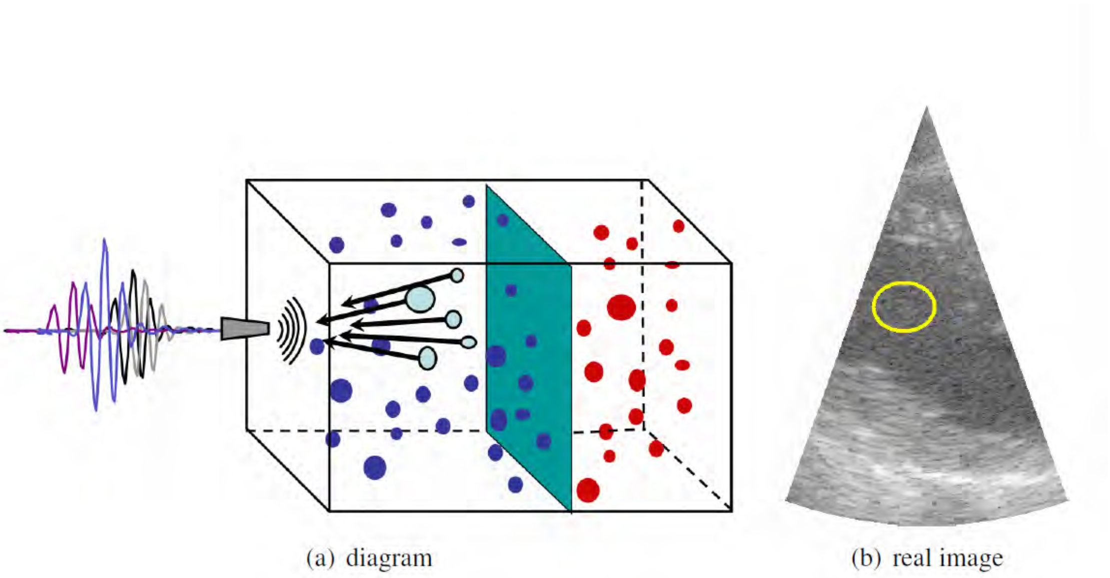

FIGURE 1.4 – Illustration of diffuse reflection. (a) principle of diffuse reflection. (b) A region where we can found some diffuse reflections from blood (yellow delimitation). Reproduced with permission from [Bernard, 2006].

Speckle

The speckle phenomenon corresponds to the granular appearance of homogeneous tissues in ultrasound images and is a result of the scattering of the ultrasound wave as it propagates through a medium with small point scatterers, as illustrated in Figure 1.4. This texture arises from the diffuse reflexion and is a results of both constructive and destructive interferences of the back-scattered acoustic waves. A constructive (resp. destructive) interference yields a bright (resp. dark) region in the echographic image.

The speckle nature depends on the spatial resolution of the ultrasound equipment, which is mathematically defined as the point spread function (PSF). The local size of the PSF is denominated as resolution cell. The scatterers within a resolution cell contribute locally to the speckle interference pattern. Given the shape of the ultrasound beam that converges to the focal point and diverges afterward, the size of the resolution cell varies with depth. This phenomenon is limited in practice through the use of dynamic focusing inside the acquisition systems.

As a consequence, the spatial distribution, density and echogeneity of the scatterers within a resolution cell of these scatterers influence the speckle pattern. Speckle can be both seen as a noisy component of the image or as a characteristic feature of the tissues. In order to enhance the homogeneity of image appearance within the same tissue, several authors have proposed speckle-suppressing filtering techniques [Yu and Acton, 2002, Michailovich and Tannenbaum, 2006]. Nevertheless, the speckle pattern can also be seen as a tissue fingerprint, as it arises deterministically from the distribution of the scattering sites from the underlying tissue architecture, although not representing their true spatial arrangement (i.e. the observed speckle does not directly correspond to underlying tissue microstructure). Furthermore, it has been shown that the speckle pattern keeps its shape under small motion/deformation, making it extremely useful for tracking problems. Thus, while on a still frame it can be seen as spatial noise, thus making automatic image segmentation more difficult, the coherent motion of the speckle patterns is of great value for motion estimation algorithms.

1.2 Ultrasound signal representations

The obtained ultrasound signal on the receiving transducer elements needs to be processed in order to highlight the pertinent information and display it as a classic ultrasound image. The steps of the image formation process are illustrated in Figure 1.5 and described below.

1.2.1 Radio-frequency signal (RF)

The transducer converts the acoustical reflected wave into an electrical signal. The radio-frequency signal corresponds to the signal obtained after the beamforming operation. This signal contains a lot of microinformations on the structures that the transmitted sound-wave insonified. In order to cover a region of the patient's body, several ultrasound beams are emitted in different directions and the corresponding RF signals are gathered to form an RF image (Figure 1.5.(a) and (b)).

1.2.2 Complex envelope signal (IQ)

The complex envelope (usually called IQ signal for In phase Quadrature signal) is obtained through demodulation of the analytic signal according to its central frequency f0. The resulting signal is complex with a spectrum having a maximum frequency value lower than the one of the RF and analytical signals. Thus, the IQ signal has the same amount of useful information but implies a lower sampling frequency than the RF signal.

1.2.3 Envelope signal

The envelope signal is used for the display of the echographic image. This signal corresponds to the envelope of the RF signal and can be derived either from the RF or the IQ signal (see Fig. 1.5.(c) and (d)). A logarithmic compression is applied to the envelope signal in order to compensate for the high dynamics of the image. This last operation allows to obtain the final gray levels used for the display of the image (see Fig. 1.5.(e) and (f)). If the image was acquired using a sectorial probe, the image is also converted from polar coordinates (ρ, θ) to cartesian coordinates (x, y).

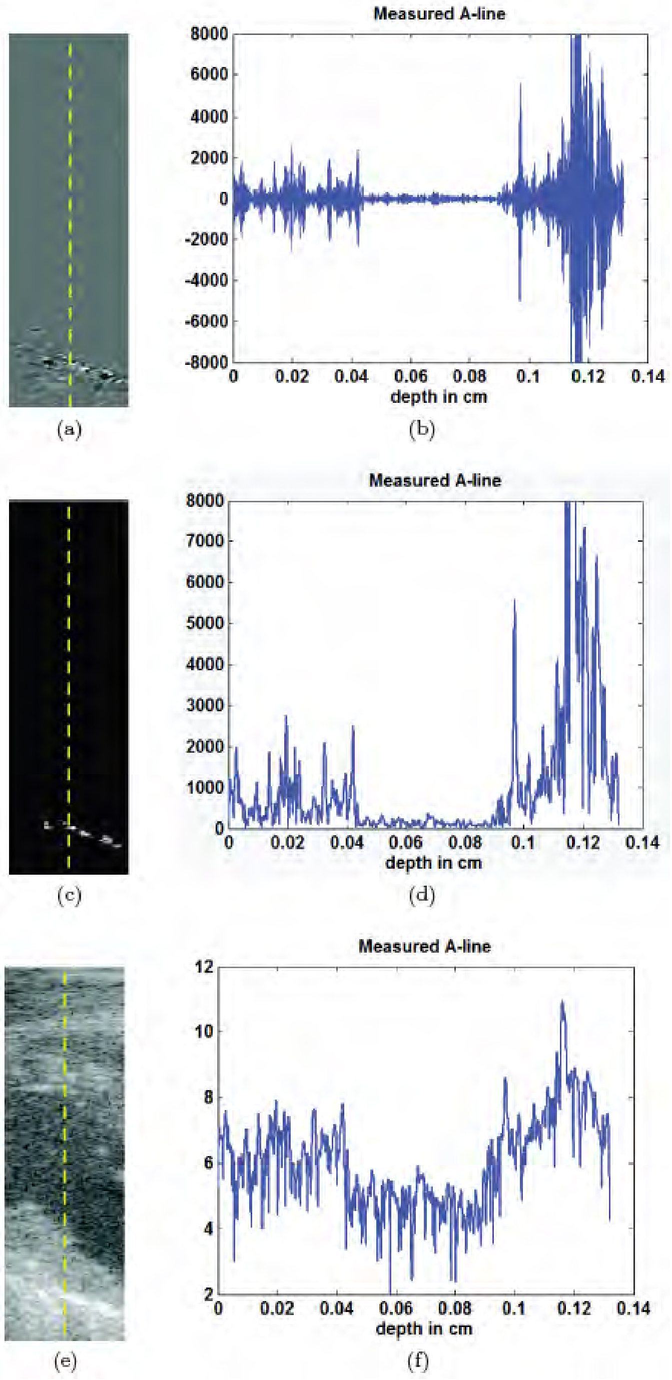

FIGURE 1.5 – Illustration of the ultrasound image formation. Radio-frequency image ((a), (b)), envelope image ((c), (d)) and envelope image with logarithmic compression ((e), (f)) are successively derived. The final image (e) corresponds to the image displayed on the screen of the ultrasound equipment. For each image, we give the A line signal corresponding to the yellow curve. Reproduced with permission from [Bernard, 2006].

1.3 Imaging modes

Three imaging modes are usually used in clinical routine : the M-mode, the B-mode and the Doppler mode.

1.3.1 M-mode echography

The M-mode, where the M stands for motion, consists in continuously observing over time the echoes generated by one ultrasound beam, whose orientation is fixed. The movement of the organs crossed by the beam induce a variation of the position and intensity of the echoes received by the probe. Since only one spatial dimension is used, the time resolution is much higher than in B-mode imaging (typically tens of Hertz in B-mode imaging over KHz in M-mode imaging) and thus allows the observation of very fast movements. For instance, M-mode is often used in echocardiography to observe the movements of heart walls and valves.

1.3.2 B-mode echography

The B-mode is the most frequently used imaging mode. It can be either 2-dimensional or 3-dimensional (due to the recent advances in echographic probes) and thus allows to image both depth and width (in 2D) or thickness (in 3D).

2D imaging

The 2D B-mode imaging is the most widespread mode in clinical routine. It consists in scanning a plane through the body and displaying the received echoes in a two-dimensional image. To do so, many emissions are done successively, each time with a different beam orientation. The position of an echo on the image is determined by its travel time and the corresponding beam orientation. The acquisition process is quite fast and generally allows a framerate of 20 to 30 images per second.

3D imaging

Even though, 2D ultrasound imaging systems are useful diagnostic imaging techniques as they are highly flexible, fast, cheap and noninvasive, they also suffer from several limitations [Fenster et al., 2011] :

- Conventional ultrasound images are 2D, though the anatomy is 3D, thus the user needs to combine mentally several 2D images in order to obtain a 3D representation of the organ anatomy or pathology. This is time-consuming and inaccurate as it may result in an inter-observer variability and incorrect diagnoses.
- Accurate measurements and delineations of organs or lesions volumes can be variable and sometimes inaccurate on 2D acquisitions.

- Monitoring the progression of a pathology or lesion is challenging since it is particularly difficult to place the 2D US imaging transducer at the same location and orientation on the patient at different time intervals.
- It does not permit the viewing of planes that are parallel to the skin.

In order to overcome these limitations, three-dimensional ultrasound imaging systems have been developed. The first three-dimensional US images were demonstrated in the 1970s and the first commercial system was made available in 1989 by Kretz, Zipf, Austria. Over the past decades, researchers and commercial companies concentrated efforts in order to develop efficient three-dimensional US imaging systems. However, development of 3D US systems require real-time or near real-time scanning techniques, with accurate volumetric geometry on inexpensive and mobile systems. A wide range of systems has been developed to obtain 3D US images, that comprise the use of linear arrays in mechanical and free-hand scanning and the use of 2D arrays.

Mechanical 3D US scanning systems These systems perform a mechanical scanning sweep of the volume of interest through the motion (rotation, translation, tilt) of a 2D transducer and then post-process the data acquired to form a 3D image. Because the scanning geometry is predefined and mechanically controlled, the positions and orientation of the acquired 2D US images are accurately known. These types of systems exist either under the form of integrated 3D US transducers where a linear US transducer is moved inside the housing or use external fixtures to move a conventional 2D transducer. The advantage of the first type is that they are easier to use and have more mobility than the systems using fixtures but they require special US machines. While US machines using fixtures can adapt to any type of transducer but are cumbersome. Generally, mechanical 3D scanners can be heavy, bulky and inconvenient to use on the body depending of the location or the organ.

Free-hand scanning with position sensing Another approach uses a conventional US transducer generating 2D images and uses sensors to allow tracking of the transducer as it moved over the body in order to reconstruct an accurate 3D volume [Fargier-Voiron et al., 2014]. The 3D imaging system can be formed from a conventional 2D transducer whose position and orientation is tracked. This can be achieved by mounting a sensor on the transducer to obtain its position and orientation as it is moved over the body. As this techniques is not mechanical the transducer has to be swept over the anatomy by an operator at an adequate speed to ensure the necessary spatial sampling and that the set of 2D images doesn't have any gaps.

3D US scanning systems using 2D arrays In order to cover an anatomy volume of interest, the mechanical and free-hand techniques require a large number of US acquisition lines. However there is a fundamental limit corresponding to the trade-off between temporal and spatial resolution : the ultrasound wave must travel into the body and the echoes need to propagate back to the transducer. Thus, the average framerate achievable by these systems is of about 2/3 volumes per second which is not sufficient in some cases, as for example, the case of a beating heart that beats at around 60-75 beats per minute. To overcome the speed limitations and the need to move by hand the transducer, transducers generating real-time 3D volumes have been recently developed. These transducers use a 2D phased array, allow to remain stationary and use the phased array to electronically sweep a pyramid-shaped volume. This approach in which the echoes are received by a 2D array matrix provides the acquisition and display of real time 3D images. The main challenge of this technique is physically connecting all the elements to wires and activating them on transmission/reception modes, and thus, a solution is activating only a fraction of them, leading to naturally sparse RF data. Since the technology for developing 2D matrix arrays transducers is complexe, few companies provide it and these systems are not yet common in the clinical routine.

The types of 3D acquisition strategies using linear and matrix arrays described in this section are presented in Figure 1.6.

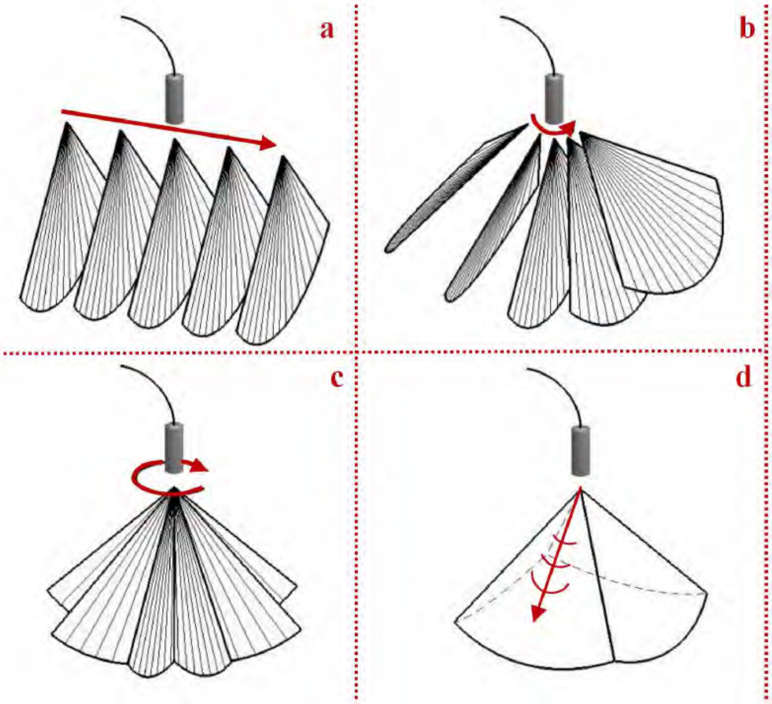

FIGURE 1.6 – Different acquisition strategies for 3D ultrasound images : (a), (b), (c) present mechanical scanning approaches with linear, tilt and rotational motions and (d) shows an electronic 2D phased array approach. Reproduced with permission from [Barbosa, 2013].

1.3.3 Doppler echography

Medical US systems can also be used to estimate and visualize the blood flow coming through blood vessels by using Doppler systems. These systems can be used to detect, measure and image blood flow or any other movement at a position in the body and find its velocity over time. The measurements are obtained by repeatedly sending pulses in the same direction and then using the correlation between each of these pulses to calculate the velocity.

The principle of the Doppler effect

Doppler velocimetry is based on the fact that the frequency of ultrasound reflected by a moving particle is different from the frequency of the emitted ultrasound. Let us consider a target in motion relative to an ultrasound transmitter and receiver (Figure 1.7), where f_e is the frequency of an emitted ultrasound wave, c its propagation speed and the target forms an angle θ with the axis of the ultrasound beam. The frequency of the wave emitted by the particle moving at velocity v is no longer f_e but a new frequency f_d which is caused by the Doppler effect. This variation in frequency is due to the movement of the target while the wave is not modified, its wave length being preserved. The Doppler frequency corresponding to he shift in relation to the frequency of the US emission is given by : $f_d = \frac{2f_e|v|\cos\theta}{c}$.

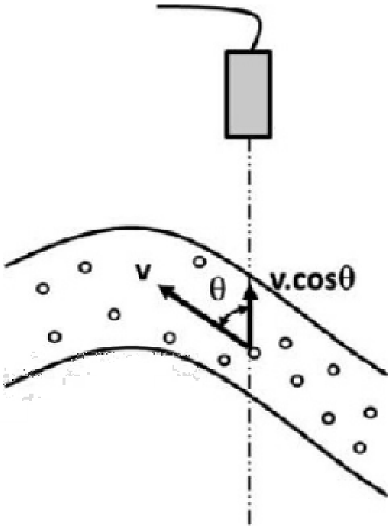

FIGURE 1.7 – Principle of velocity measurement with Doppler ultrasound effect. Reproduced with permission from [Vray et al., 2014].

Continuous wave (CW) Doppler

The CW Doppler system consists of a transmitter which emits continuously a sinusoidal wave and in a receiver constantly detecting the backscattered waves. The ultrasound wave, after reflection from the moving particles , is collected by the receiving transducer and the electrical signal is amplified. Then a complex demodulation allows to obtain after filtering the signal at the Doppler frequency that is proportional to the velocity of the blood. However, the speed of the moving elements is deducted without any axial resolution, i.e. the information from all the inhomogeneities located in the targeted volume is superposed.

Pulsed wave Doppler

The CW Doppler systems are non-invasive and easy to use systems but they lack the possibility to detect the depth in tissue of the vessel. It is possible that two different vessels that are at different depths, will be interrogated at the same time and thus, yielding a wrong frequency due to the superposition of the back-scattered waves. Thus, the PW Doppler was created to overcome the problems of the CW Doppler. Here, the emission is not continuous anymore, but the transmitter emits a series of ultrasound pulses that propagate and interact with the blood and tissue. The returning echoes are received by the same transducer and amplified. In the case of the PW Doppler, it is not the shift in emitted frequency that is detected but the shift in position of the scatterers, as shown in Figure 1.8. The left side of the figure shows the series of echoes received by the transducer. These received signals are shown on top of each other. The right part of the figure shows the Doppler signal, formed by taking one sample value from each received signal at a given time (thus associated to a given depth) indicated by the dashed line in the left graph. The Doppler signal will thus be constant if there is no motion and will correspond to a sinusoid in the case of a stationary flow (i.e. with constant velocity). To reduce errors speed is generally calculated on an averaged signal corresponding to 128 emissions. The emission pulse frequency repetition is called PRF (Pulse Frequency Repetition) and it is proportional to the depth of exploration since we must wait for the returning echoes before a new emission. It has been shown that the Doppler frequency can not be greater than PRF / 2.

Using a number of pulse-echo lines and sampling at the depth of interest, thus, gives a digital signal with a frequency proportional to velocity. Having a movement of a collection of scatterers with different velocities then gives a superposition of the contribution from the individual scatterers and gives rise to a spectral density reflecting the density of the velocities. Applying a Fourier transform to the received signal will thus directly reveal the velocity distribution for a given time. Often a B-mode image is presented along with the sonogram in a duplex Doppler system, and the area of investigation is shown on the image. In order to show the blood velocity in vessels, one point is selected on the B-mode image and the evolution of the velocity at the given point is shown as function of time on a pulsed Doppler spectrogram. If both modes B-mode imaging and pulsed Doppler spectrogram, need to be used in the same imaging sequence then the acquisition time must be shared between the two imaging systems and a strategy for alternating them is required.

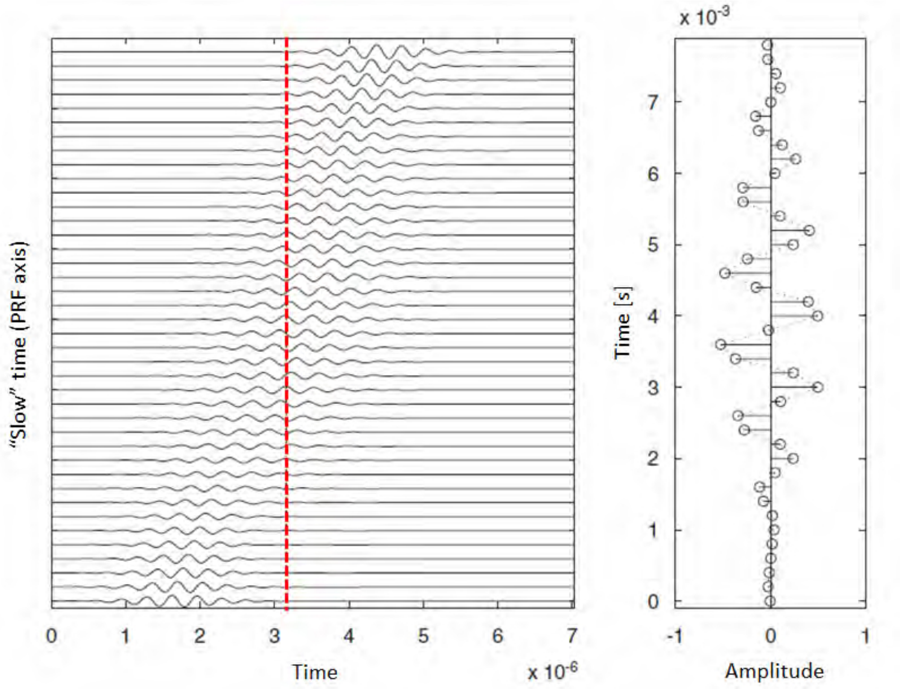

FIGURE 1.8 – PW Doppler. The left graph shows the RF line series received from the successive emitted pulses. The right graph shows the Doppler signal corresponding to a given depth, materialized by the dotted line on the left graph. Modified with permission from [Jensen, 1996b]

An example we show in Figure 1.9 the duplex scan for a carotid artery. The left part shows the B-mode ultrasound image of the artery with the placement of the range gate or measurement site. The right side shows the spectrogram, which gives the velocity distribution over time.

Challenges

As we have seen throughout this chapter, ultrasound image processing poses several challenges. Indeed, ultrasound image quality is strongly affected by the acquisition conditions, especially in 3D imaging and duplex acquisitions. The main challenge in 3D imaging for using the promising matrix arrays in acquiring real-time 3D volumes is of technical nature and consists in the difficulty of connecting all the elements and activating them at will. On the other hand, in duplex imaging, B-mode imaging and pulsed Doppler spectrogram, need to be used in the same imaging sequence, thus, the acquisition time must be shared between the two imaging systems and a strategy for alternating them is required. In both cases, a better acquisition strategy is needed and a possible solution is based on the compressed sensing framework that we will present in the next chapter.

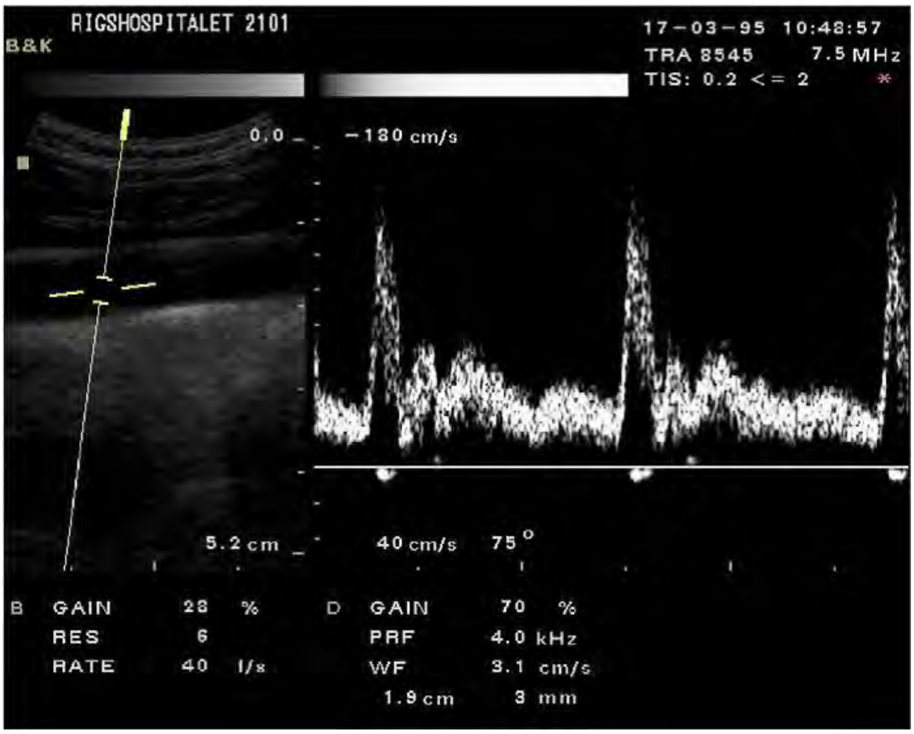

FIGURE 1.9 – Duplex scan showing both B-mode image and spectrogram of the carotid artery. Reproduced with permission from [Jensen, 1996b]

Chapitre 2

Compressed sensing theory

In this chapter we intend to summarize the main aspects of the relatively novel theory of compressed sensing theory (CS), which provides a fundamentally new approach to data acquisitions by suggesting that it is possible to surpass the limits of traditional sampling. The interested reader will find in [Duarte and Eldar, 2011, Eldar and Kutyniok, 2012] a more detailed presentation of the CS framework and properties. First, we will give a general introduction about the CS theory, followed by the mathematical formulation of the main theorems and the illustration and analysis of the associated assumptions. This leads us to a discussion on the reconstruction techniques. We then focus on the Bayesian CS which gives a novel formulation of the problem. The last chapter focuses on the learning of the sparsifying dictionaries, more specifically the general context and the main algorithms found in literature.We finish the chapter on the CS theory by presenting the application of CS in signals and image reconstruction.

2.1 Introduction

In the midst of nowadays technological revolution where the amount of data collected and generated by sensors and sensing systems is exploding, it is becoming difficult to handle all this information. In many emerging applications, the acquisition or processing of the generated data is posing a tremendous challenge. This may be due to several difficulties :

- high sampling bound implied by the Nyquist-Shannon sampling theorem,
- physical impossibility to build devices capable of acquiring samples at the necessary rate (e.g. seismic sensors, ultrasound matrix probes),

- the cost of designing or using the acquisition systems,
- time and economic constraints demanded by the existing devices (e.g. MRI acquisitions should be quick enough to avoid any movement of the patient's organs)
- health risks for the users (e.g. radiation exposure related to the image acquisition duration in certain imaging fields such as CT-scans)

In order to address the challenges raised by dealing with such high-dimensional data, the usual approach often relies on compression. This compression-based approach aims at representing the signal in a basis or a frame in which it has a sparse or at least a compressible representation. The original signal can be recovered by preserving only the values of the largest coefficients of the signal, the rest of the coefficients being discarded and thus their acquisition can be considered wasteful. A common example of this approach are digital images, videos or audio signals which concentrate most of their energy on very few wavelet coefficients, and it is exploited by the PEG, JPEG2000, MPEG, and MP3 compression standards.

In this context, compressed sensing provided a fresh and effective approach of data acquisition. Rather than store all the measurements imposed by the Shannon-Nyquist limit and then discard much of the information, it would be more efficient to directly acquire only the usefu part of thel signal to begin with. Such approach is at the heart of compressed sensing, thus allowing to simultaneously perform measurement and compression. The benefits of this method are obvious since it permits by design to get around the above mentioned problems.

In this chapter we address the fundamental concepts of the compressed sensing theory (CS), that can also be called compressive sampling or or compressive sensing. We will present a brief review of the mathematical formalization, its key concepts, the main algorithms for sparse recovery and some basic results.

2.2 Problem formulation

2.2.1 Formalization

Compressive sensing (CS) [Candés and Wakin, 2008] allows the reconstruction of a signal $x \in \mathbb{R}^n$ from a linear combination of a small number of random measurements $y \in \mathbb{R}^m, m < n$. In a general setting, the measurements y may be acquired in the so-called "sensing basis" Φ , which depends on the acquisition device. For example, in MRI, Φ is the Fourier basis and in ultrasound, Φ simply consists in the usual delta functions. We then have :

$$y = R\Phi x \tag{2.1}$$

where $R\Phi$ is thus a $m \times n$ matrix. The columns of R have an entry one at random positions and zero elsewhere, thereby modeling the random selection of the measurements.

The CS theory assumes that x has a sparse representation in some model basis Ψ, which can be an orthonormal basis, a frame or an overcomplete dictionary, such that :

$$x = \Psi v \tag{2.2}$$

where v has only $k < m < n$ non zero coefficients. The vector of coefficients v is then said to be k-sparse. CS theory shows that this sparsity allows an exact recovery of v with overwhelming probability for a certain class of matrices $\Phi\Psi$ [Candés and Wakin, 2008]. In particular, the sensing basis Φ has to be incoherent with the model basis Ψ [Candés and Romberg, 2007]. Finally, the problem can be written as follows :

$$y = R\Phi\Psi v = Av \tag{2.3}$$

where A is a $m \times n$ full rank matrix (i.e. the m rows of A are independent).

In these settings, the CS problem thus amounts to solve (2.3) for v , under the constraint that v is sparse. Once v is estimated, the signal x , can then be computed from (2.2).

Formally, the CS problem may be solved through the following l_0-minimization problem P_0 :

$$P_0 : \quad \hat{v} = arg \min_{v \in \mathbb{R}^n} \|v\|_0 \quad \text{subject to} \quad y = Av \tag{2.4}$$

where the l_0 norm of v is $\|v\|_0 = \# \{i, v_i \neq 0\}$.

P_0 implies that from all the possible solutions of (3), we seek the sparsest one. In general, solving (4) is NP-hard. Iterative greedy algorithm attempt to solve this problem by successively adding nonzero components to a sparse approximation of v (see [Tropp and Gilbert, 2007]).

An alternative way of tackling the CS problem is to replace the l_0 norm by the l_1 norm, i.e. considering the convex relaxation of (2.4) and solving the following basis pursuit problem P_1 [Candés, 2008, Candés and Tao, 2005] :

$$P_1 : \quad \hat{v} = arg \min_{v \in \mathbb{R}^n} \|v\|_1 \quad \text{subject to} \quad y = Av \tag{2.5}$$

where the l_1 norm of v is $\|v\|_1 = \sum_{i=1}^{n} |v_i|$. The conditions yielding the equivalence of problems P_0 and P_1, based on the so-called restricted isometry property (RIP), have been presented by Candès in [Candés, 2008] (see also [Candés and Wakin, 2008]).

The interest of using the l_1 norm over the conventional l_2 norm to promote sparsity can be easily explained using a geometrical interpretation. Figure 2.1, shows l_1 and l_2 minimizations for the 2 dimensional data case. The line represents the set of solutions to $y = \Phi x$. The unit circle for the l_1 norm is a square with axis aligned corners, while the l_2 ball is the well known unit circle. In this example, the solution we search lies on one of the two axes which in the case of the l_2 ball can be found only in the case the solution line is vertical or horizontal, i.e. $\Phi = 0$. Thus, for the l_2 minimization, the solution line will choose points far from the coordinate axis which are non-sparse while in the case of the l_1 ball the line will intersect a corner giving a sparse solution.

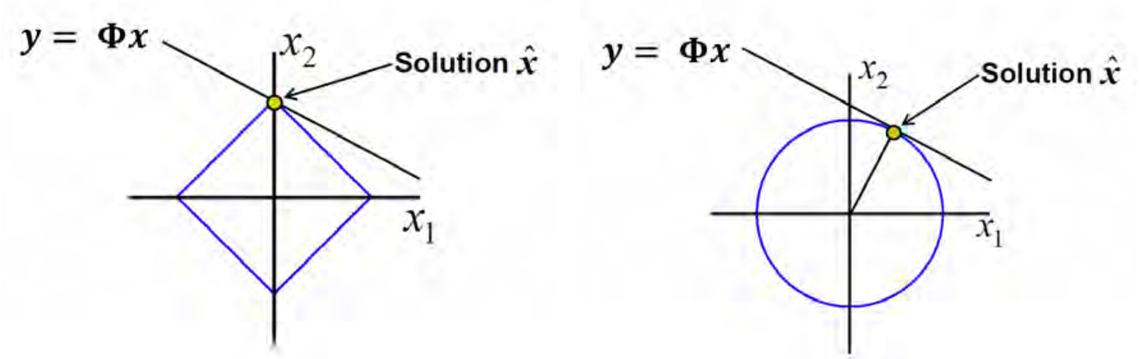

(a) l_1 ball (b) l_2 ball

FIGURE 2.1 – (a) Solving the l_1 minimization problem in $\mathbb{R}^2$ and (b) l_2 minimization problem in $\mathbb{R}^2$. The l_1 ball intersects the line of solutions to give the sparsest solution but the l_2 ball does not.

The framework described above assumes that we are given exact samples of the signal to be recovered. This is seldom the case in practice, since the measurements are very often corrupted by noise. For reconstruction of measurements with additive noise, we have :

$$y = Av + e \tag{2.6}$$

where e represents a noise term of bounded energy $\|e\|_2 \leq \varepsilon$. The original basis pursuit problem P_1 can be recast as the following problem [Candés, 2008] :

$$P_2 : \quad \hat{v} = arg \min_{v \in \mathbb{R}^n} \|v\|_1 \quad \text{subject to} \quad \|y - Av\|_2 \leq \varepsilon \tag{2.7}$$

In practical applications the signal is generally not exactly sparse but most of its coefficients in (2) are small. When signal coefficients v decays exponentially in absolute value, the signal is said to be compressible. The solution found by P1 (2.5) or P2 (2.7) gives the approximation of v by keeping its largest entries.

2.2.2 Sparsity

Signals may often be expressed as a linear combination of just a few significant elements from a known basis, frame or dictionary. When this representation is exact we say that the signal is sparse. However, true sparsity is almost never reachable due to the presence of noise but they are often compressible. For example, if a digital natural image is taken, it is well known that wavelets provide a sparse approximation. This is illustrated in Figure 2.2, which shows a wavelet decomposition of Lena, a reconstruction of the image using only 5% of the highest wavelet coefficients and the original Lena image. We observe that most of the wavelet coefficients are close to zero. Thus, we can obtain a good approximation of the signal by setting the small coefficients to zero.

The notion of sparsity, illustrated here above, states that a vector is k-sparse when it has at most k non-zero coefficients. This is measured by the l_0 norm, as following :

$$\|v\|_0 = \# \{i, v_i \neq 0\} \tag{2.8}$$

In most cases, the signal is not sparse itself but has a sparse representation in some basis, frame or dictionary. This signal can be expressed in this basis, denoted Ψ, as $x = \Psi v$ where $\|v\|_0 \leq k$.

In the context of compressed sensing sparsity is the prior information of the signal we intend to efficiently sense. If the signal itself is not sparse, we will try to sparsify it by considering its expansion in a representation domain. In this case, two possibilities can be envisaged. If certain characteristics of the signal are known, the representation basis can be chosen amongst the known basis and frames such as the Fourier basis, wavelets, etc. The advantages of such a representation are that the fast associated transforms are known as well as their mathematical properties. Otherwise, we can choose adaptive dictionaries that allow for sparser representations since they are optimized for the signals in question. This is done through dictionary learning. In this case, the mathematical structure of these transforms is unknown.

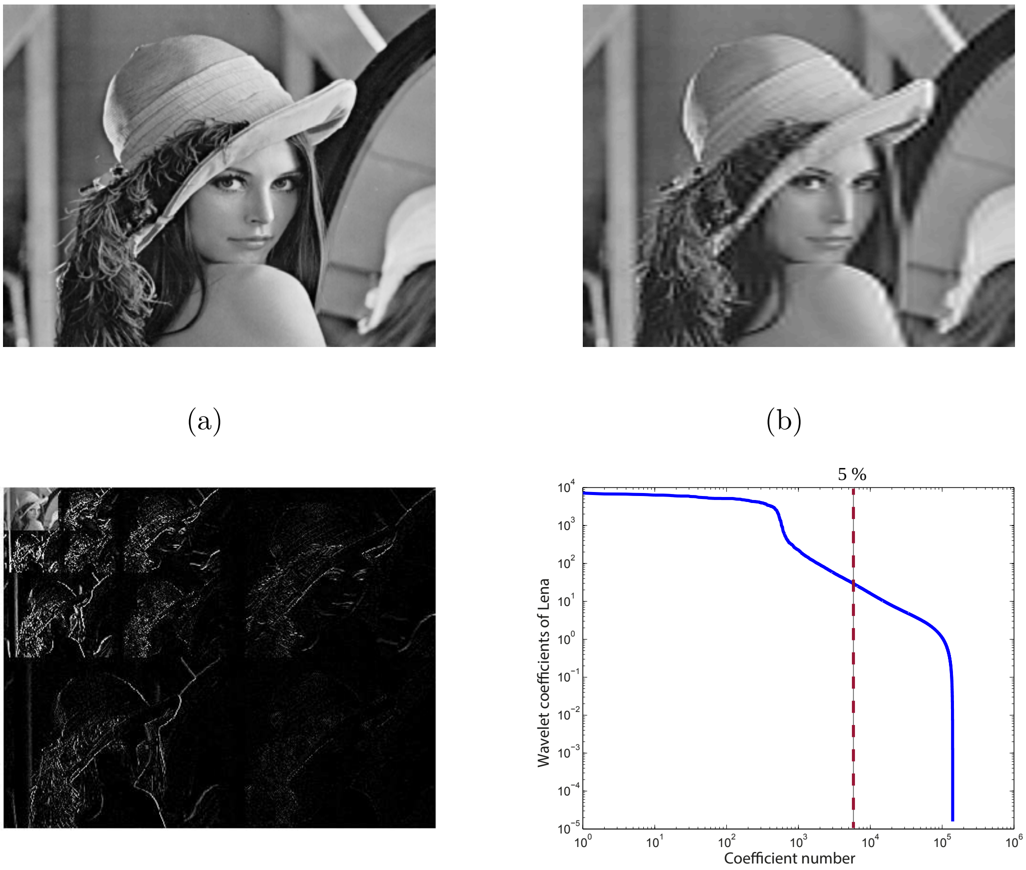

(a) (b)

(c) (d)

FIGURE 2.2 – (a) Original 512 × 512 Lena image. (b) Image reconstructed from 5% of the wavelet coefficients of the original image. Only the largest coefficients were kept. The others were set to zero. (c) Wavelet decomposition. Large coefficients are represented by white pixels, while small coefficients are represented by black pixel. (d) Sorted wavelet coefficients of the original image on a log-scale.

2.2.3 Incoherence

We consider a pair of orthobases $(\Phi, \Psi) \in \mathbb{R}^n$, corresponding respectively to the so called sensing basis and sparsifying basis. The coherence between Φ and Ψ is then defined as :

$$\mu(\Phi, \Psi) = \sqrt{n} \cdot \max_{1 \leq k,j \leq n} |\langle \phi_k, \psi_j \rangle| \tag{2.9}$$

The coherence measures the largest correlation between any two elements of Φ and Ψ [Donoho and Huo, 2001]. If Φ and Ψ contain correlated elements, the coherence is large, otherwise, is small and is comprised in $[1, \sqrt{n}]$. Compressed sensing concentrates on pairs that have low coherence, also called incoherence. This means that the information carried by the few sparse coefficients of v in (2.2) is spread all over the entries of y in (2.3). An example of a pair of bases that has low coherence is the Dirac basis and the Fourier basis.

This time-frequency pair gives a maximal incoherence since $\mu(\Phi, \Psi) = 1$.

Theorem 1. *Fix* $x \in \mathbb{C}^n$ *and suppose that the coefficient* v *of* x *in the basis* Ψ *is k-sparse. Select* m *measurements in the* Φ *domain uniformly at random. Then if*

$$m \geqslant C \cdot \mu^2(\Phi, \Psi) \cdot k \cdot log(n) \tag{2.10}$$

for some positive constant C*, the solution to* (2.5) *is exact with overwhelming probability.*

Details are available in [Candés and Romberg, 2007]. From this theorem we deduce that the greater the incoherence, the fewer samples are needed for exact reconstruction. This theorem is illustrated in Figure 2.3. The simulated signal x is of length $n = 64$ and is built from a k-sparse vector with $k = 4, 8, 16, 32$. The magnitude of the k non-zero coefficients follows a Gaussian distribution centered at zero with a standard deviation of 1. The simulated acquired signal y consisted of randomly picking m samples of x. For each value of the parameter k, 500 different signals were generated, sampled and reconstructed. The reconstruction was done using the SPGL1 (see Section 2.3.2) algorithm with default settings. From 500 trials, the probability of exact reconstruction can thus be estimated. The reconstructed signal is considered to be exact if the PSNR is higher than 70 dB. In this Figure we reconstruct the signal using a sensing matrix and sparsifying matrix that are maximally incoherent (2.3.(a) Φ = Dirac, Ψ = Fourier) and that are maximally coherent (2.3.(b) Φ = Dirac, Ψ = Dirac). As expected, the probability of recovery using the pair that has low incoherence is very low, while with the pair that has high incoherence the probability of exact reconstruction is much higher. Is can also be noticed that less sparse signals require more measurements to be efficiently reconstructed.

Interestingly, it has been shown that random matrices are largely incoherent with any fixed basis [Kutyniok, 2012]. Thus, linear projection of the data on sub-Gaussian random matrices (e.g. with i.i.d. Gaussian, Rademacher or Bernoulli entries) provides incoherent measurements allowing for exact reconstruction with a minimal number of samples. Figure 2.4 shows an example of such improvement using the pair of matrices Φ = Gaussian random matrix and Ψ = Dirac. As shown in [Kutyniok, 2012] the projection on the Gaussian matrix allows exact reconstruction with a number of samples much smaller than in the case on coherent matrices.

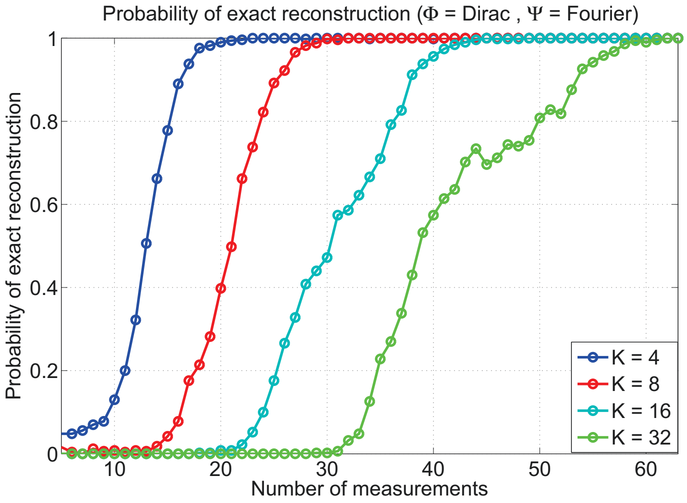

(a)

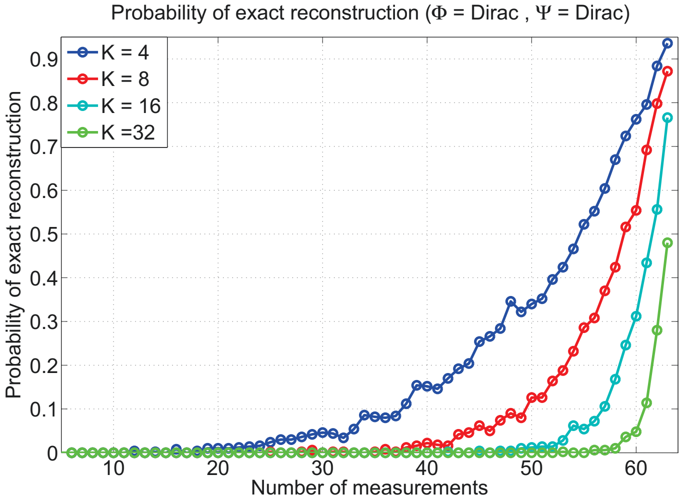

(b)

FIGURE 2.3 – Empirical estimation of the probability of recovery of x for different values of K and m (number of measurements) for (a) Φ = Dirac, Ψ = Fourier and (b) Φ = Dirac, Ψ = Dirac.

2.2.4 The Restricted Isometry Property (RIP)

We have seen that we can recover sparse signals from just a few measurements for noiseless and exactly sparse signals. However, for data corrupted by noise or a signal that is approximatively sparse, which is the case of most signals, the CS needs stronger and more general conditions. In this context, Candès, Tao and others introduced the so-called restricted isometry property which allows to study the general robustness of CS and provides a mean to evaluate the precision of the reconstruction [Candés et al., 2006a, Candés et al., 2006b, Baraniuk et al., 2007, Candés and Tao, 2005].

Theorem 2. *Let A be an $m \times n$ matrix. Then A approximately has the Restricted Isometry*

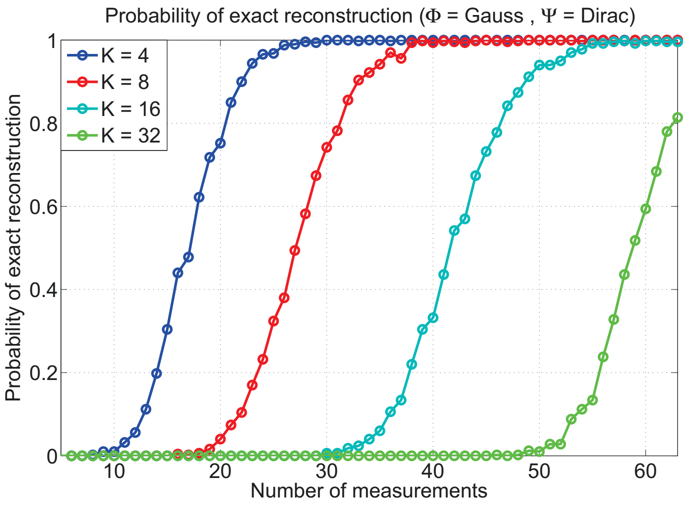

FIGURE 2.4 – Empirical estimation of the probability of recovery of x for different values of K and m (number of measurements) for Φ = Gauss, Ψ = Dirac.

Property (RIP) of order k, if there exists a $\delta_k \in (0,1)$ *such that*

$$(1-\delta_k)\|v\|_2^2 \leq \|Av\|_2^2 \leq (1+\delta_k)\|v\|_2^2 \tag{2.11}$$

for all k-sparse vectors v.

This theorem implies, if satisfied, that A preserves the distance of the k-sparse vectors.

In the case of the noiseless recovery, it has been proven [Candés et al., 2006b, Candés and Tao, 2005, Candés and Wakin, 2008] that if the RIP holds, the P_1 problem gives an exact reconstruction :

Theorem 3. *Assume that* $\delta_{2k} < \sqrt{2}-1$. *Then the solution v to* (P_1) *obeys :*

$$\begin{aligned}\|v^* - v\|_{l_2} &\leq \frac{C_0}{\sqrt{k}}\|v - v_k\|_{l_1} \quad \textit{and}\\ \|v^* - v\|_{l_1} &\leq C_0\|v - v_k\|_{l_1}\end{aligned} \tag{2.12}$$

for some constant C_0 *and* v_k *is the vector v with all but his k largest coefficients pout to* 0. *In particular, if v is k-sparse, the recovery is exact.*

In the case of noisy reconstruction, the next theorem assesses a stable reconstruction of the signal [Candés et al., 2006b]. In this context, the reconstruction error is proportional to the noise level of the measurements.

Theorem 4. *Assume that* $\delta_{2k} < \sqrt{2}-1$. *Then the solution v to* (P_2) *obeys :*

$$\|v^* - v\|_{l_2} \leq \frac{C_0}{\sqrt{k}}\|v - v_k\|_{l_1} + C_1\epsilon \tag{2.13}$$

for some constant C_0 *and* C_1*.*

The next step is finding which matrices A and how many measurements are needed for the RIP condition to be achieved. The RIP condition has been demonstrated in two situations. In the first situation, RIP can be achieved with overwhelming probability for pairs of random sensing matrices (i.e. Gauss, Bernoulli) and orthonormal basis [Rudelson and Vershynin, 2008,Mendelson et al., 2008]. The minimal number of measurements needed to reconstruct the signal is :

$$m \geq C \cdot k \cdot \log(\frac{n}{k}) \tag{2.14}$$

where C is some constant.

The second situation in which the RIP can be established is for pairs of orthonormal bases [Candés and Tao, 2006]. It is sufficient to have :

$$m \geq C \cdot k \cdot (\log n)^4 \tag{2.15}$$

measurements in order to be able to reconstruct the signal.

2.3 Sparse signal recovery algorithms

In this section, we will provide a brief overview of the different types of algorithms typically used for sparse recovery. The sparse recovery problem was formulated in Section 2.2.1 and aims to minimize an objective function, subject to a constraint. In order to solve (2.4) , (2.5) and (2.7) different optimization strategies have been introduced. The corresponding algorithms are very numerous and are still the topic of a very active research (see [Tan et al., 2015a,Tan et al., 2015b,Fountoulakis et al., 2014,Dinh and Cevher, 2014]), it is therefore highly difficult to cover them in a single section of a thesis chapter. We thus propose to classify the different algorithms based on their approach of the problem, then present a brief explanation and the application of these algorithms. The algorithms that we decided to use during this thesis are explored in more details.

The reconstruction methods can be classified into the following groups, based on their approaches to the CS problem :

- l_0 norm minimization solved by greedy algorithms.
- l_1 norm minimization based on convex optimization algorithms.
- l_p norm with $0 \leq p \leq 1$ minimization handled by non-convex optimization approaches.

2.3.1 l_0-norm reconstruction

If we choose to solve the CS through the following l_0-minimization problem P_0 :

$$P_0 : \ \hat{v} = arg \min_{v \in \mathbb{R}^n} \|v\|_0 \ \text{ subject to } \ y = Av \tag{2.16}$$

then we have to consider greedy algorithms to attempt solving this problem, since this is, in general, a NP-hard problem.

Greedy algorithms iteratively approximate the coefficients and the support of the original signal. They have the advantage of being very fast and easy to implement. There are a high number of greedy methods for solving such problems [Blumensath and Davies, 2008a, Blumensath and Davies, 2009, Cohen et al., 2008, Dai and Milenkovic, 2009, Davenport and Wakin, 2010, Donoho et al., 2012, Needell and Tropp, 2009, Needell and Vershynin, 2010].We only briefly describe some of the most common methods. The first and most used greedy approaches are the matching pursuit methods and iterative thresholding method.

Matching Pursuit (MP) methods

The most well-known greedy approach is Orthogonal Matching Pursuit (OMP), which is introduced in [Pati et al., 1993] as an improved extension of Matching Pursuit [Mallat and Zhang, 1993]. Other examples of greedy algorithms are stagewise OMP (StOMP) [Donoho et al., 2012], regularized OMP (ROMP) [Needell and Vershynin, 2010], and compressive sampling MP (CoSamp) [Needell and Tropp, 2009].

Orthogonal Matching Pursuit : We first consider here the OMP algorithm, which is an iterative greedy approach that selects at each step the column of A that is is the most correlated with the signal residuals. Then its contribution is subtracted from the original measurement vector and the algorithm iterates on the residual (see Algorithm 1). The hope is that after a certain number of iterations the OMP identified the correct set on columns. The stopping rule can consist of either a limit on the number of iterations or a requirement that the residual of $y = Av$ tends to 0. Tropp and Gilbert [Tropp and Gilbert, 2007] proved that OMP can be used to recover a sparse signal with high probability using CS measurements.

```
Data: CS matrix/dictionary A, measurement vector y
Initialization : $\hat{v_0} = 0, r_0 = y, \Lambda_0 = \emptyset, i = 1$;
repeat
    Find the index $\lambda_i$ that solves the optimization problem :
    $\lambda_i = arg\max_{j=1...N} |\langle r_{i-1}, a_j \rangle|$;
    $\Lambda_i \leftarrow \Lambda_{i-1} \cup \{\lambda_i\}$ : add entry corresponding to largest correlation to support;
    Augment the matrix with chosen atoms : $\tilde{A_i} = [\tilde{A_{i-1}}, a_{\lambda_i}]$ ;
    Update signal estimate : $v_i = arg\min_v \left\| \tilde{A_i} v - y \right\|$;
    Update the residual : $r_i = y - Av_i$;
    $i = i + 1$;
until $\|r_i\|_{l_2} < \epsilon \; or \; i \leq ITER\_MAX$;
Result: Sparse representation $\hat{v}$
```

Algorithm 1: Orthogonal Matching Pursuit

Iterated hard thresholding

In the case of the iterated hard thresholding method, we start from an initial signal estimate $\hat{v_0} = 0$, the algorithm iterates a gradient descent step followed by hard thresholding until a convergence criterion is met. These types of algorithms and their properties, in particular, the performance guarantees and convergence speed have been studied in detail in [Blumensath and Davies, 2008b, Blumensath and Davies, 2009].

```
Data: CS matrix/dictionary A, measurement vector y, sparsity level k
Initialization : $\hat{v_0} = 0, i = 0$;
repeat
    $\hat{x_{i+1}} = H_K(\hat{x_i} + A^T(y - A\hat{x_i}))$;
    Where $H_K(a)$ is the non-linear operator that sets all but the largest (in
    magnitude) $K$ elements of A to zero.;
    $i = i + 1$;
until $\|r_i\|_{l_2} < \epsilon \; or \; i \leq ITER\_MAX$;
Result: Sparse representation $\hat{v}$
```

Algorithm 2: Iterated Hard Thresholding

Conclusion

The principal advantage of the greedy algorithms is that they are quite straightforward and easy to understand and code. However, the principal disadvantage is that in many cases there is no guarantee that finding the locally optimal solution yields the optimal global solution. Greedy algorithms compute the support of the sparse signal x iteratively instead of doing a exhaustive search that would lead to a combinatorial explosion. Once the support of the signal is obtained, the pseudo-inverse of the measurement matrix restricted to the corresponding columns can be used to reconstruct the actual signal x. A clear advantage to this approach is speed, even though as we said, its guarantees are not as strong as those of Basis Pursuit. It is also important to consider the size of the signals we want to recover which, in our case, is very high. As the greedy algorithms require explicit matrices for inversions and decompositions they cannot be used for large scale problems when the matrices are not stored as implicit operators.

Though we will not use the greedy algorithms for the CS reconstruction problem because of the disadvantages described above, we will, however, use them for the sparse recovery step in the dictionary learning problem described in Section 3.1. In this case, greedy algorithms are more frequently used since they are the most efficient from a runtime point of view.

The greedy algorithms are numerous and interested readers can refer to [Tropp and Wright, 2010] for a more detailed review. In the next section, some of the methods for minimizing the relaxed sparse approximation problems are explored.

2.3.2 l_1 norm reconstruction

In this section we present some of the most used algorithms that solve the (2.7) problem. This formulation, recalled hereunder, comes to finding the solution with minimum l_1 norm and is also called "Basis Pursuit" method. This sparse recovery problem is solvable using linear programming.

For reconstruction of measurements with additive noise, we have :

$$y = Av + e \tag{2.17}$$

where e represents a noise term of bounded energy $\|e\|_2 \leq \varepsilon$. In this setting, reconstruction can be performed by solving the following minimization problem [Candés, 2008] :

$$\min_{v \in \mathbb{R}^n} \|v\|_1 \quad \text{subject to} \quad \|y - Av\|_2 \leq \varepsilon \tag{2.18}$$

The convex optimization problem (2.18) can also be formulated as the following convex optimization problem proposed by Chen et al. [Chen et al., 1998] :

$$\min_{v \in \mathbb{R}^n} \|Av - y\|_2^2 + \lambda \|v\|_1 \tag{2.19}$$

This formulation is closely related to convex quadratic programming, for which many algorithms are available. The parameter λ is a Lagrange multiplier which is related to the l_2 norm of the data misfit and to the l_1 norm of the constrained solution. Another formulation of the optimization problem is the LASSO problem [Tibshirani, 2011], which minimizes the l_2 norm of the data misfit such that the l_1 norm of the solution is less than a fixed threshold :

$$\min_{v\in\mathbb{R}^n} \|Av - y\|_2^2 \text{ subject to } \|v\|_1 \leq \tau \tag{2.20}$$

In the last few years numerous algorithms have been proposed for solving the aforementioned l_1 problems that have arisen in CS. Standard methods, such as the interior-point algorithms [Candés and Romberg, 2005] for linear and quadratic programming can be used to solve (2.18) but need explicit matrices in order to be effective which is not always the case in CS. First-order algorithms, which are able to handle encoding matrices that are not explicit, lead to better performance. In this category, we find most of the l_1 norm reconstruction algorithms. One of the earliest methods is the gradient projection method suggested in [Figueiredo et al., 2007], the most studied methods are the iterative shrinkage-thresholding (IST) method [Daubechies et al., 2004, Elad, 2006] and derivatives (fixed-point continuation (FPC) [Hale et al., 2008], fast IST [Beck and Teboulle, 2009], SpaRSA [Wright et al., 2009] algorithms). We can also find in the literature the homotopy approaches [Efron et al., 2004, Osborne et al., 2000, Osborne et al., 1999], which are based on repeatedly solving 2.19 for all values of λ and in this way, finding the right value that recovers the solution of (2.18). However, these approaches can easily become computationally expensive. There are also algorithms that solve the constrained l_1 problems such as the Bregman iteration, the spectral projection gradient method [van den Berg and Friedlander, 2009c], the NESTA algorithm [Becker et al., 2009], the alternating direction method (ADM) based algorithms [Yang and Zhang, 2011a].

The literature of the algorithms proposed to solve the (2.18), (2.19) and (2.20) problems is overwhelming and it is not possible to summarize all the existing algorithms in the limited space of this chapter. We thus, focus on two algorithms that we will use in the next chapters of this study : the spectral projected gradient and the alternating direction method.

Spectral projected gradient (SPGL1)

In 2008, Friedlander and van den Berg [van den Berg and Friedlander, 2009c] proposed a method which consists in solving a sequence of the problem (2.20) by using the spectral projected gradient algorithm introduced in [Birgin et al., 1999]. They use the fact that the dual solution of (2.20) can be used to determine how to update τ so that the next solution of (2.20) is much closer to the solution of (2.18).

Let x_τ denote the optimal solution of 2.20. The function ϕ gives the optimal solution to this problem for each $\tau \geq 0$ and is defined as :

$$\phi(\tau) = \|y - Av\|_2 \tag{2.21}$$

The graph of the ϕ function traces the optimal trade-off between $\|v\|_1$ and $\|Av - y\|_2$, which defines the Pareto curve. Figure 2.5 gives an example of such a curve.

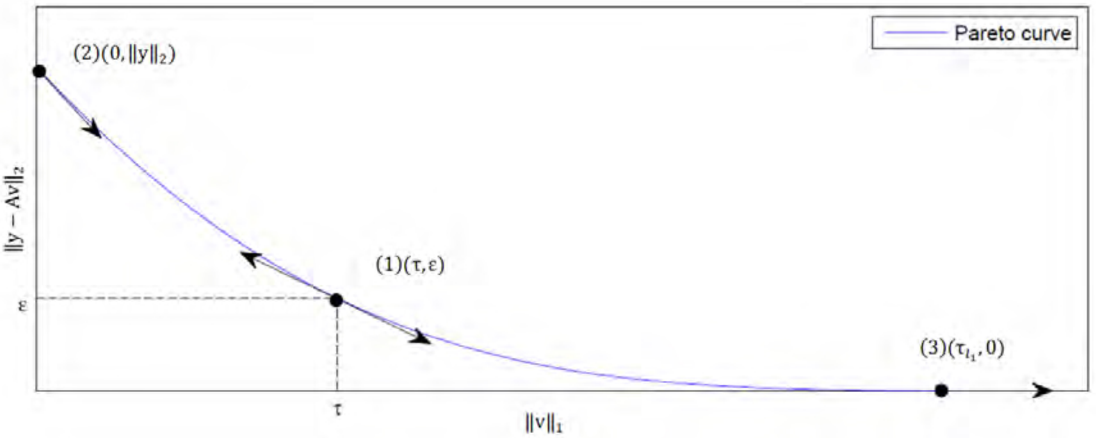

FIGURE 2.5 – Illustration of a Pareto curve. Point (1) shows the connection between the parameters of (2.18), 2.20 and 2.19. Point (3) corresponds to a solution of P_1.

Point (1) shows the connection between the three parameters of (2.18), 2.20 and 2.19. Coordinates of a point on the curve are (τ, ε) and the slope of the tangent at this point is $-\lambda$. End points of the curve correspond to two special cases. When $\tau = 0$ (Point (2)), the solution of 2.20 is $v = 0$, which corresponds to the solutions of (2.18) with $\varepsilon = \|y\|_2$ and 2.19 with $\lambda = \left\|A^H y\right\|_\infty / \|y\|_2$. When $\varepsilon = 0$ (Point (3)), the solutions of (2.18) corresponds to the solutions of 2.20, where τ is the l_1 norm of the solution.

As shown in [van den Berg and Friedlander, 2009c], the ϕ function is a convex and continuously differentiable in τ. The derivative of ϕ is, thus given by $-\lambda_\tau$, where $\lambda_\tau \geq 0$ is the unique dual solution of problem 2.20. The SPGL1 approach is then based on applying Newton's method to find a root of the nonlinear equation :

$$\phi(\tau) = \varepsilon \tag{2.22}$$

which defines a sequence of regularization parameters $\tau_k \to \tau_\varepsilon$, where v_{τ_ε} is a solution to the noisy basis pursuit problem (2.18). In other words, τ_ε is the parameter that causes (2.20) and (2.18) to share the same solution. As shown in [van den Berg and Friedlander, 2009c] a crucial aspect is that the sequence of solutions can be efficiently solved (O(nlog(n) complexity)) using an adapted projected gradient method. The code of SPGL1 is available online [van den Berg and Friedlander, 2009a].

Alternating Direction Method

Yang and Zhang [Yang and Zhang, 2011a] introduced the idea of using the alternating direction method (ADM) for solving the l_1 minimization problem. This group of first-order primal-dual algorithms based on the ADM technique proposes to solve the problems (2.5), (2.18), (2.20) and (2.19). An open source Matlab package called YALL1 is available online [Yang and Zhang, 2011b] and it can solve eight different l_1 minimization models, i.e. (2.5), (2.18), (2.20), (2.19) and their nonnegative counterparts.

The principle of the algorithms consists of two main steps : the first step is to reformulate the l_1 problem into one having partially separable objective functions by adding new variables and constraints ; and the second step consists in applying an exact or inexact alternating direction method to the resulting problem. The derived alternating direction algorithms can be regarded as first-order primal-dual algorithms because both primal and dual variables are updated at each and every iteration.

In practice,the derived ADM algorithms follow the general ADM framework that considers the structured optimization problem :

$$\min_{x,y} f(x) + g(y) \quad \text{subject to} \quad Ax + By = b \tag{2.23}$$

where $f(x) : \mathbb{R}^m \to \mathbb{R}$ and $g(y) : \mathbb{R}^n \to \mathbb{R}$ are convex functions, x and y are separate in the objective and coupled in the constraint. The augmented Lagrangian function of this problem is given by :

$$\mathcal{L}_{\mathcal{A}}(x, y, \lambda) = f(x) + g(y) - \lambda^T(Ax + By - b) + \frac{\beta}{s}\|Ax + By - b\|^2 \tag{2.24}$$

where λ is the Lagrangian multiplier and β is a penalty term. The ADM iterates as follows :

$$\begin{cases} x^{k+1} = arg\min_x \mathcal{L}_{\mathcal{A}}(x, y^k, \lambda^k) \\ y^{k+1} = arg\min_y \mathcal{L}_{\mathcal{A}}(x^{k+1}, y, \lambda^k) \\ \lambda^{k+1} = \lambda^k - \gamma\beta(Ax^{k+1} + By^{k+1} - b) \end{cases} \tag{2.25}$$

Applied to l_1 minimization this framework gives ADM-like algorithms. For example, if we apply this approach to the (2.18) minimization problem we obtain :

$$\min_{v,r} \|v\|_1 \quad \text{subject to} \quad Av + r = y,\ \|r\| \le \delta \tag{2.26}$$

which is equivalent to the 2.23 form and thus has an augmented Lagrangian subproblem of the form :

$$\min_{x,r} \|v\|_1 - u^T(Av + r - y) + \frac{\beta}{s}\|Av + r - y\|^2 \quad \text{subject to} \quad \|r\| \le \delta \tag{2.27}$$

Applying the ADM framework to the previous Lagrangian subproblem gives the following iteration scheme :

$$\begin{cases} r^{k+1} = \mathcal{P}_{B_\delta}(u^k/\beta - (Av^k - y)) \\ v^{k+1} = Shrink(v^k - \tau A^T(Av^k + r^{k+1} - y - u^k/\beta), \tau/\beta) \\ u^{k+1} = u^k - \gamma\beta(Av^{k+1} + r^{k+1} - y) \end{cases} \tag{2.28}$$

The details of the calculations and of the variables are given in [Yang and Zhang, 2011a] and each ADM based algorithm follows the same framework but has a different formulation which we will not detail here.

Conclusion

As we said previously, the literature of the algorithms proposed to solve the convex optimization problem is overwhelming and up to this day there is no review classifying and comparing all the existing algorithms, as far as we know. It seems that there is no clear winner that always achieves the best performance in terms of both speed and accuracy and that the choice of the algorithm is done in function of the sparse recovery problem that is treated.

Our choice was oriented towards the SPGL1 and YALL1 algorithms based on several criteria. First of all, both these algorithms were developed for large-scale applications. In our application, the data sets are large and the matrix A in the CS problem is often available only as an operator due to its size. For example, 3D ultrasound signals can contain up to $512^2 = 262,144$ elements, which means that the matrix A can have on the order of $512^4 = 68.7 \cdot 10^9$ elements which represents 550 GB of data in double precision. It is thus necessary to store A as an operator. Many algorithms have been therefore excluded because they required explicit matrices and could not be used for large-scale problems. Another advantage of these two algorithms is that both have a fast and optimized implementation available online and a detailed user guide. It is also worth to notice that both are representative algorithms of the l_1 minimization literature and are very often considered as a reference in comparisons with other algorithms (see e.g [Dinh and Cevher, 2014, Fountoulakis et al., 2014]). SPGL1 has been cited more than 800 times since its appearance and YALL1 almost 500 times [Yang and Zhang, 2011c, van den Berg and Friedlander, 2009b].

2.3.3 l_p-norm reconstruction

In this section we consider briefly the family of non-convex minimization algorithms. Specifically, if we replace the l_1 norm by the l_p norm in (2.5), where $0 < p < 1$, it has been shown in [Chartrand, 2007, Mourad and Reilly, 2009, Chartrand and Staneva, 2008] that l_p norm will produce exact reconstruction with a smaller number of measurements.

Mathematically, the minimization problem can be written as following :

$$P_p : \quad \hat{v} = arg \min_{v \in \mathbb{R}^n} \|v\|_p^p = arg \min_{v \in \mathbb{R}^n} \sum_i |v_i|^p \quad \text{subject to} \quad y = Av \tag{2.29}$$

One class of algorithms that can be used for finding the sparse solution vector of the l_p norm optimization problem is called Iterative Re-weighted Least Squares (IRLS) [Gorodnitsky and Rao, 1997,Chartrand and Yin, 2008,Daubechies et al., 2010,Li, 1993,Rao and Kreutz-Delgado, 1999].

Iterated reweighted least-squares algorithms

IRLS algorithms use the simplicity of the least squares solution and perform at least as well as, or even better than, the l_1 norm. All IRLS algorithms have the general form :

$$\min_{v \in \mathbb{R}^n} \left\| W^{-1} v \right\|_2^2 \quad \text{subject to} \quad y = Av \tag{2.30}$$

where W is a diagonal weighting matrix that may reflect some priors of the solution vector v. These algorithms are iterative and the estimated solution at the kth iteration can be expressed as : $v_k = W_x(AW_k)^{\dagger} y$, where the † sign represents the Moore-Penrose inverse. The IRLS algorithms differ in function of the way the diagonal matrix is defined.

For example, the authors in [Gorodnitsky and Rao, 1997] set $W_k = diag(v_{k-1})$ which is equivalent to minimizing $\sum_i |v_i|^p$. Iterative reweighted l_1 has also been used for sparse representation with the relaxed logarithmic sparsity measure $\sum_i log(|v_i|)$ in [Candés and Boyd, 2008]. Another approach is to replace the l_p objective function by a weighted l_2 norm :

$$arg \min_{v \in \mathbb{R}^n} \sum_i w_i v_i^2 \quad \text{subject to} \quad y = Av$$

where the weights are computed from the previous iterate, so that $w_k = |v_{k-1}|^{p-2}$. This approach results in choosing the weighting matrix as $W_k = 1/w_k = diag(|v_{k-1}|^{2-p})$ with $p \leq 1$ as suggested in [Rao and Kreutz-Delgado, 1999, Chartrand and Yin, 2008].

2.4 Bayesian CS

The sparse reconstruction problem of compressed sensing can be reformulated as an estimation problem solved in a Bayesian framework. If we reformulate the CS problem given in (2.6) assuming the A matrix is known and that the noise ϵ is approximated by an additive Gaussian noise with a zero mean and unknown variance σ^2, the quantities that remain to be estimated based on the CS measurements are the sparse coefficients v and the noise variance σ^2. Thus, the associated Gaussian likelihood model is given by :

$$p(y|v,\sigma^2) = (\pi\sigma^2)^{-n} \exp(-\frac{1}{\sigma^2} \|y - Av\|_2^2) \tag{2.31}$$

The sparsity is then modeled by introducing an a priori on the coefficients to be recovered, $p_0(v)$:

$$p_0(v) \propto \exp(-\|v\|_0) \tag{2.32}$$

This Bayesian approach transforms the CS problem of recovery of the sparse coefficients v into a linear-regression problem with the prior constraint that v is sparse. The Bayesian approaches that have been developed to solve the previous linear-regression problem can be divided into several categories :

1. Bayesian pursuit algorithms that are Bayesian counterparts of the greedy method described in section 2.3.1, [Schniter et al., 2008, Zayyani et al., 2009],
2. Bayesian approaches that replace the prior $p_0(v)$ with a fixed and computationally convenient family of priors [Figueiredo and Nowak, 2001, Figueiredo, 2002, Ji et al., 2008, Tibshirani, 2011] , the most common being the Laplace distributions, the scale-invariant Jeffreys prior or the α-stable distribution.
3. Sparse Bayesian learning (SBL) algorithms that use a prior that is learned from the data [Tipping, 2001, Tan and Li, 2009, Wipf and Rao, 2007, Figueiredo, 2003].

Though each of these approaches has its advantages and drawbacks, here we will focus our attention on the sparse Bayesian learning algorithms (SBL) which have been often derived for and applied to sparse signal recovery and compressed sensing.

2.4.1 Sparse Bayesian learning (SBL) framework

We briefly introduce the methodology behind the sparse Bayesian learning which is more extensively described in [Tipping, 2001, Wipf and Rao, 2007, Wipf and Rao, 2004]. In this framework, each coefficient v_i is assumed to satisfy a Normal distribution :

$$p(v_i,\gamma_i) \sim \mathcal{N}(0,\gamma_i) \tag{2.33}$$

where γ_i is an unknown variance hyperparameter thus controlling the sparsity of v_i. In practice, a high number of the estimated γ_i tend to zero and thus leading to sparse solutions. Assuming the coefficients v_i are independently and identically distributed, the overall distribution is $p(v,\gamma) = \prod_{i=1}^{N} p(v_i,\gamma_i)$ where the coefficients are characterized by the parameter vector $\gamma = [\gamma_1, ...\gamma_N]^T$. Given γ and by combining likelihood and prior, it has been shown in [Tipping, 2001] that the posterior density of v becomes :

$$p(v|y,\gamma) = \frac{p(v,y;\gamma)}{\int p(v,y;\gamma)dv} = \mathcal{N}(\mu,\Sigma) \tag{2.34}$$

with mean and covariance given by :

$$\begin{aligned} \Sigma &= \Gamma - \Gamma A^T \Sigma_t^{-1} A \Gamma \\ \mu &= \Gamma A^T \Sigma_t^{-1} y \end{aligned} \tag{2.35}$$

where $\Gamma = diag(\gamma)$ and $\Sigma_t = \sigma^2 I + \Phi \Gamma \Phi^T$.

The parameters γ and hence the sparsity of v are generally estimated using the Type II maximum likelihood procedure [Tipping, 2001, MacKay, 1992] which is equivalent to maximizing the marginal likelihood with respect to the hyperparameters γ. This is equivalent to minimizing the following :

$$\begin{aligned} \mathcal{L}(\gamma) &= -2 \log \int p(y|v) p(v, \gamma) dv = -2 \log p(y, \gamma) \\ &= \log |\Sigma_t| + y^T \Sigma_t^{-1} y \end{aligned} \tag{2.36}$$

Once the hyperparameters γ are learned, the MAP estimate of v, that we denoted $\hat{v}$, can be directly obtained from the mean of the posterior, $\hat{v} = \mu$.

2.4.2 Block sparse Bayesian learning (BSBL) framework

This algorithm is an extension of the previously presented algorithm and it was proposed by Zhang [Zhang and Rao, 2012, Zhang and Rao, 2013a]. In this framework, the SBL approach is adapted to a block-wise model that learns and exploits intra-block correlation, i.e. correlation between the elements within each block. Even though this type of correlation exists in signals and images, there are few algorithms that take into account this intra-block correlation. As we will see, this gives the resulting algorithm several nice properties in terms of signal recovery capacity.

Our sparse model expressed in (2.7) can be seen as a block sparse model. Its mathematical expression is the same as in (2.6) but v has a block structure :

$$v = [\underbrace{v_1, \ldots . v_{d_1}}_{\mathbf{v}_1^T}, \ldots, \underbrace{v_{d_{g-1}+1}, \ldots ., v_{d_g}}_{\mathbf{v}_g^T}]^T \tag{2.37}$$

where the $d_i, i = 1, \ldots g$ are not necessarily identical. Among these blocks, only a few are nonzero and thus a signal with this structure is a block sparse signal.

In the BSBL framework, each block $\mathbf{v}_i \in \mathbb{R}^{d_i}$ is assumed to follow a parametrized multivariate Gaussian distribution :

$$p(\mathbf{v}_i, \gamma_i, B_i) \sim \mathcal{N}(0, \gamma_i B_i), \ i = 1, \ldots g \tag{2.38}$$

with the unknown hyperparameters γ_i and B_i. As previously, γ_i controls the sparsity of each block and when $\gamma_i = 0$ the corresponding block becomes zero. $B_i \in \mathbb{R}^{d_i \times d_i}$ is a positive definite matrix that captures the intra-block correlation structure of block i. The approach assumes that the blocks are mutually uncorrelated and thus, the prior of v becomes :

$$p(v, \{\gamma_i, B_i\}_i) \sim \mathcal{N}(0, \Sigma_0) \tag{2.39}$$

where Σ_0 is a block-diagonal matrix of $\gamma_i B_i$ such that :

$$\Sigma_0 = \begin{bmatrix} \gamma_1 B_1 & & & \\ & \gamma_2 B_2 & & \\ & & \ddots & \\ & & & \gamma_g B_g \end{bmatrix}$$

By assuming that the noise vector follows the parametrized multivariate Gaussian distribution : $p(\epsilon, \sigma^2) \sim \mathcal{N}(0, \sigma^2 I)$. The posterior density of v can be written by applying Bayes' rule and is given by :

$$p(v|y, \sigma^2, \{\gamma_i, B_i\}_{i=1}^g) \sim \mathcal{N}(\mu_x, \Sigma_x) \tag{2.40}$$

with mean and covariance given by :

$$\begin{aligned} \Sigma_x &= (\Sigma_0^{-1} + \frac{1}{\sigma^2} A^T A)^{-1} \\ \mu_x &= \Sigma_0 A^T (\sigma^2 I + A \Sigma_0 A^T)^{-1} y \end{aligned} \tag{2.41}$$

The parameters $\sigma^2, \{\gamma_i, B_i\}_{i=1}^g$ are estimated by the Type II maximum likelihood procedure [Tipping, 2001, MacKay, 1992] which amounts to minimizing the following negative log likelihood with respect to each parameter :

$$\begin{aligned} \mathcal{L}(\Theta) &= -2 \log \int p(y|v, \sigma^2) p(v, \{\gamma_i, B_i\}_i) dv \\ &= \log |\sigma^2 I + A \Sigma_0 A^T| + y^T (\sigma^2 I + A \Sigma_0 A^T)^{-1} y \end{aligned} \tag{2.42}$$

where $\Theta = \{\sigma^2, \{\gamma_i, B_i\}_{i=1}^g\}$ denotes all the parameters ensemble. This minimization can be solved using different methods, each resulting in a different learning rule of the hyperparameters. Zhang presented three learning rules for the hyperparameters : the Expectation-Maximization (EM) method, the Bound-Optimization (BO) method and a hybrid method between BSBL and Group-Lasso type algorithms [Zhang and Rao, 2012, Zhang and Rao, 2013a]. Once the hyperparameters are learned, the maximum a posteriori of v can be estimated from the mean of the posterior density, μ_x.

The first method for minimizing $\mathcal{L}(\Theta)$ treats the v as hidden data and minimizes this expression over γ using a simple EM algorithm for covariance estimation. Computing the derivatives with respect to γ_i and σ^2 and then setting them to zero gives the learning rules for γ_i and σ^2. Though this method benefits from the general convergence properties of the EM algorithm and has a good recovery, this update rule is computationally slow. Thus, Zhang developed derived a much faster learning rule for γ_i based on the Bound-Optimization method (BO) also known as the Majorization-Minimization method [Elad, 2010,Stoica and Babu, 2012]. The method is denoted BSBL-BO and not only has a greater speed than the BSBL-EM method but has also a good performance on noisy data. The last method introduced by Zhang is denoted BSBL-l_1 and is a hybrid between BSBL and group-LASSO algorithms. On one hand, this method adaptively learns and exploits intra-block correlation to obtain better performance, as BSBL-EM and BSBL-BO. On the other hand, it is much faster and is especially suited for large data sets since it needs only few iterations that can be implements by any group-LASSO type algorithm. In terms of recovery speed, BSBL-BO is generally a bit slower than BSBL-l_1 but faster than BSBL-EM. While, in terms of recovery performance, its recovery performance is slightly poorer than BSBL-EM but better than BSBL-l_1. Among these three algorithms, only BSBL-EM and BSBL-BO have the ability to recover non-sparse signals or with non-sparse representations if they have correlation structures while BSBL-l_1 does not give satisfactory results in this type of application. In chapter IV, for the application to Doppler US data we will use the BSBL-BO algorithm due to its clear advantages over the other two algorithms.

Conclusion

Concentrating on the SBL framework offers several advantages over the other algorithms :

- The reconstruction performance is robust to the features of the sensing matrix Φ. It has been demonstrated that SBL still provides a good performance even if the columns of Φ are highly coherent while other methods based on convex relaxation give highly degraded performances [Wipf, 2011]. Experiments also showed that SBL algorithms maintain a good performance when the sensing matrix is a non-random matrix which is very interesting for the ultrasound area that uses sensing matrices that are not random and that can have correlated columns.
- Its structure provides a large adaptability to model and exploit different types of signals and the structure within.
- This group of algorithms provides better terms of local and global convergence than than convex relaxation algorithms. For example, it has been shown that SBL provides a sparser solution that LASSO algorithms [Wipf and Nagarajan, 2010].
- It provides scale-invariant solutions.

The main drawback of SBL is that it is computationally expensive and thus, more efficient strategies to diminish the computational load are needed.

More precisely, among all the SBL algorithms we focused on the block SBL framework [Zhang and Rao, 2013b] that has the particularity of being able to recover true non-sparse signals if the solution signals are correlated [Zhang et al., 2013b, Zhang et al., 2013c]. This is a highly desired characteristic, since real signals are not exactly sparse and their representation in a sparsifying basis or dictionary may not be sufficiently sparse. It is also important to note that the BSBL algorithms exploit the correlation structures in sparse signals. In [Zhang et al., 2013b, Zhang et al., 2013c], it has been shown that exploiting the correlation structure can significantly improve the reconstruction performance and that it is critical for the recovery of real signals that are not sparse or do not have a sparse representation.

2.5 Applications of compressed sensing

Compressed sensing is a promising tool for all applications where acquiring the whole set of measurements necessary using the usual information theory paradigm for the formation of the signal or image is difficult or even impossible. Although its application to practical systems is relatively new, it can clearly be expected to see CS applied more and more in the future, as the technological evolution demands devices that are cheaper, faster and efficient. In the following, we will review in summary a few of the many applications to apply the CS framework [Qaisar et al., 2013].

Compressive cameras

Compressive sensing can has been used for efficient and inexpensive compressive imaging systems and cameras. The first application was the single pixel camera (SPC) imagined by Rice university [Duarte et al., 2008, Wakin et al., 2006]. This compressed imaging camera collects incoherent measurements using a micro-mirror matrix and thus needs a single photon detector instead of millions. This application allows reducing the number of measurements and thus, building a cheaper, smaller and simpler camera without degrading the spatial resolution.

Seismic imaging

Seismic data that is usually very large and has high-dimensionality. This is due to the seismology techniques that rely on the gathering of massive data collections which is represented in five dimensions ; two for sources, two for receivers and one for time. However, because of high measurement and computational cost, it is desirable to reduce the number of sources and receivers which could reduce the number of samples. Since the size and desired resolution of the investigated areas by seismologists continues to increase, it is necessary to reduce the number of samples acquired. CS is able to solve this problem and a successful reconstruction theory was developed with a randomized dimensionality-reduction approach that decreases the acquisition cost and the processing

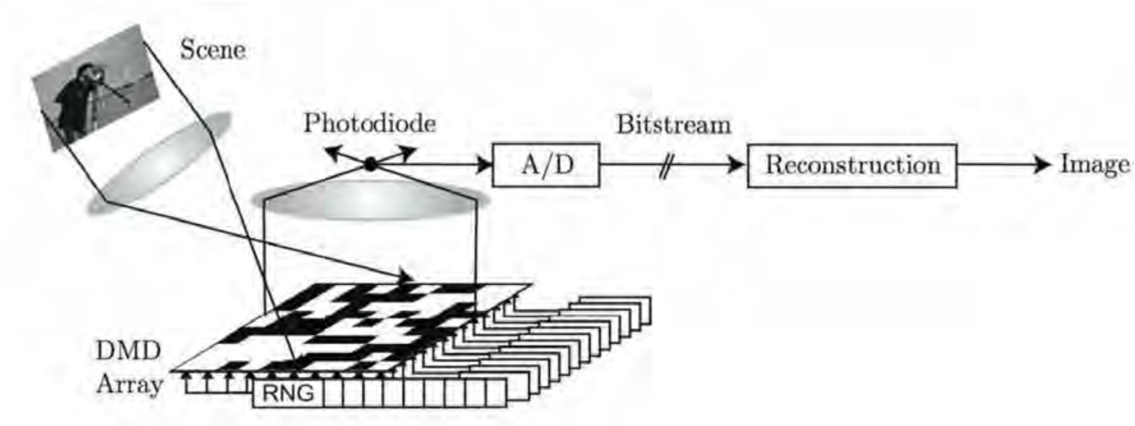

FIGURE 2.6 – Block diagram of Compressive Imaging Camera [Wakin et al., 2006]

significantly [Herrmann et al., 2012]. For example, in [Herrmann et al., 2012] remarkably good results are obtained with a significantly reduced computational cost using only 17 simultaneous shots opposed to 350 sequential shots needed for the simulation of the original synthetic data.

Compressive communications networks

CS can be exploited in the different layers of communication networks. In the physical layer, there are many instances where a large amount of information should be processed and CS can be used on sparse physical signals such as ultra-wide-band (UWB) signals, wide-band cognitive radio signals. The advantage is that the information is sparse though the size of input information is huge. At the Media Access Control (MAC) layer, CS can be used to implement multi-access channels. At the network layer, CS can be used for data collection in wireless sensor networks, where the sensory signals are usually sparse in certain representations. At the application level, CS can be used to monitor the network itself, where network performance metrics are sparse in some transform domains. In Wireless Sensor Networks (WSNs) an approach of using compressive data gathering (CDG) helps in overcoming the challenges of high communication costs and uneven energy consumption by sending 'm' weighted sums of all sensor readings to a sink which recovers data from these measurements [Luo et al., 2009], as shown in Figure 2.7. A recent review of these applications can be found in [Huang et al., 2013].

Radar systems

There are many applications of CS to the various radar systems. The application to the radar system design is the most straightforward where CS can be applied in pulse compression for temporal sampling. It has also been applied to multiple-input/multiple-output (MIMO) radar systems that are well adapted for the use of CS since all signals are related to the transmitted and received pulses and the radar scene is sparse. CS has also been effectively applied to synthetic aperture radar (SAR), ultra-wide-band (UWB) radar

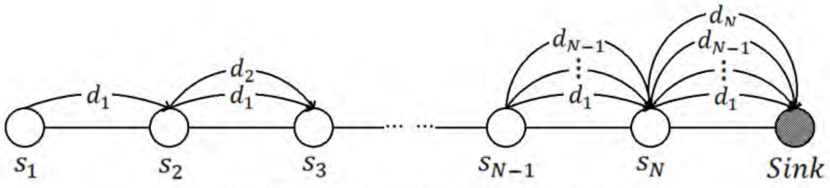

(a) Baseline data collection

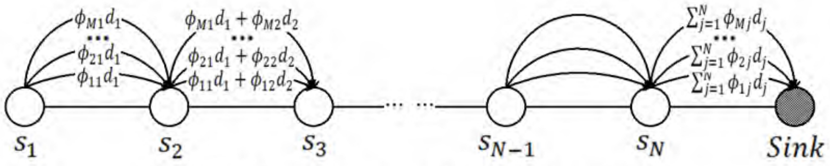

(b) Compressive data gathering

FIGURE 2.7 – Comparing baseline data collection and compressive data gathering in a multi-hop route [Luo et al., 2009]

or ground Penetrating radars (GPRs). Figure 2.8 shows an example of a recent application of CS to inverse synthetic aperture radar (ISAR) images where the image is successfully reconstructed from only 25% of the samples [Feng et al., 2014]. A more complete review of the state of the art of CS in the various radar systems is given in [Ender, 2013].

Medical imaging

The CS theory has seen an increasing success over the past years and in particular in medical imaging applications, where reducing the acquisition times can diminish the costs and acquisition times, thus making the equipment available for more patients, it may reduce the health risks (e.g. radiation risks in CT) and improve diagnostics by avoiding organ motion artifacts. For example, in CT the radiation exposure is related to the image acquisition duration, MRI acquisitions should be fast to avoid movement from the patient and in 3D ultrasound the spatial resolution should be improved without sacrificing the frame rate. The first and most widespread applications of CS is MRI due to the properties of this imagery type : firstly, these MRI images have sparsity properties in the wavelet domain and secondly, the MRI scanners acquire naturally samples encoded in the frequency domain. These properties made MRI one of the most successful applications of CS in medical imaging. A review of several examples of applications of CS in this field was given in [Wang et al., 2011]. CS applications in MRI have been the earliest but research in this domain is still ongoing and giving promising results as it can give ten-fold faster acquisitions with almost no loss in information [Chen and Huang, 2014, L. Weizman, 2015] and Figure 2.9 gives an example of such an application.

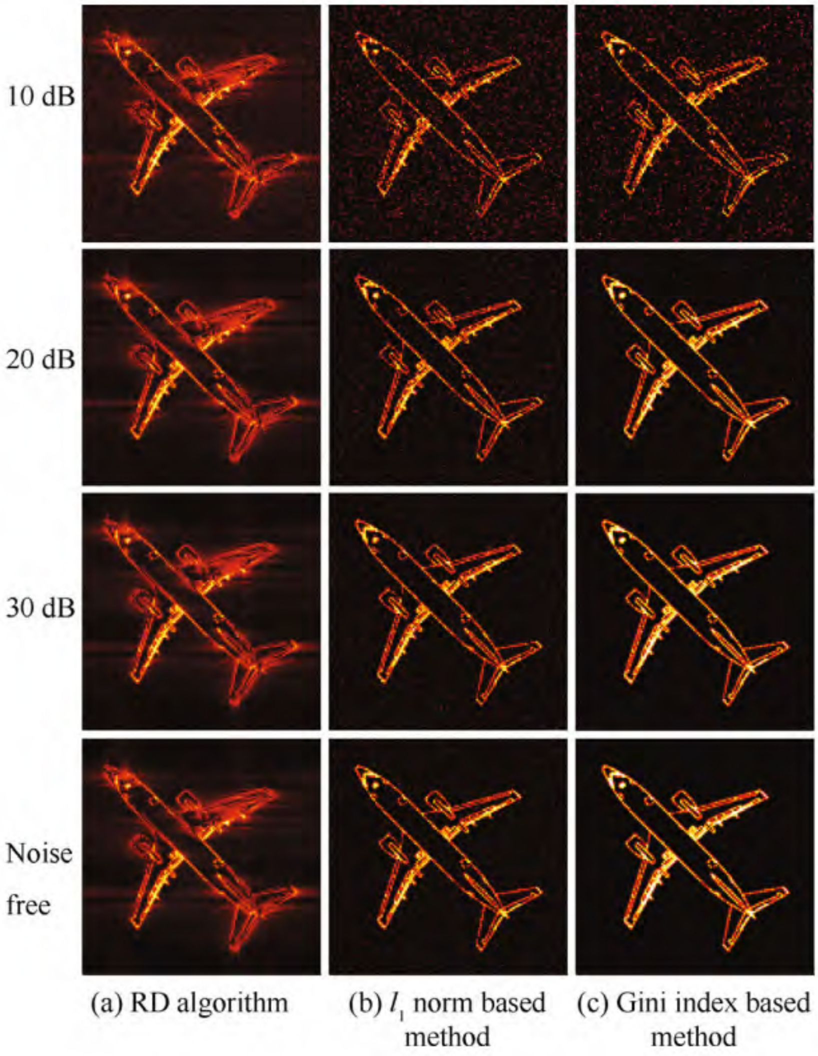

FIGURE 2.8 – Images reconstructed by different approaches versus SNR using 25% of the samples [Feng et al., 2014]

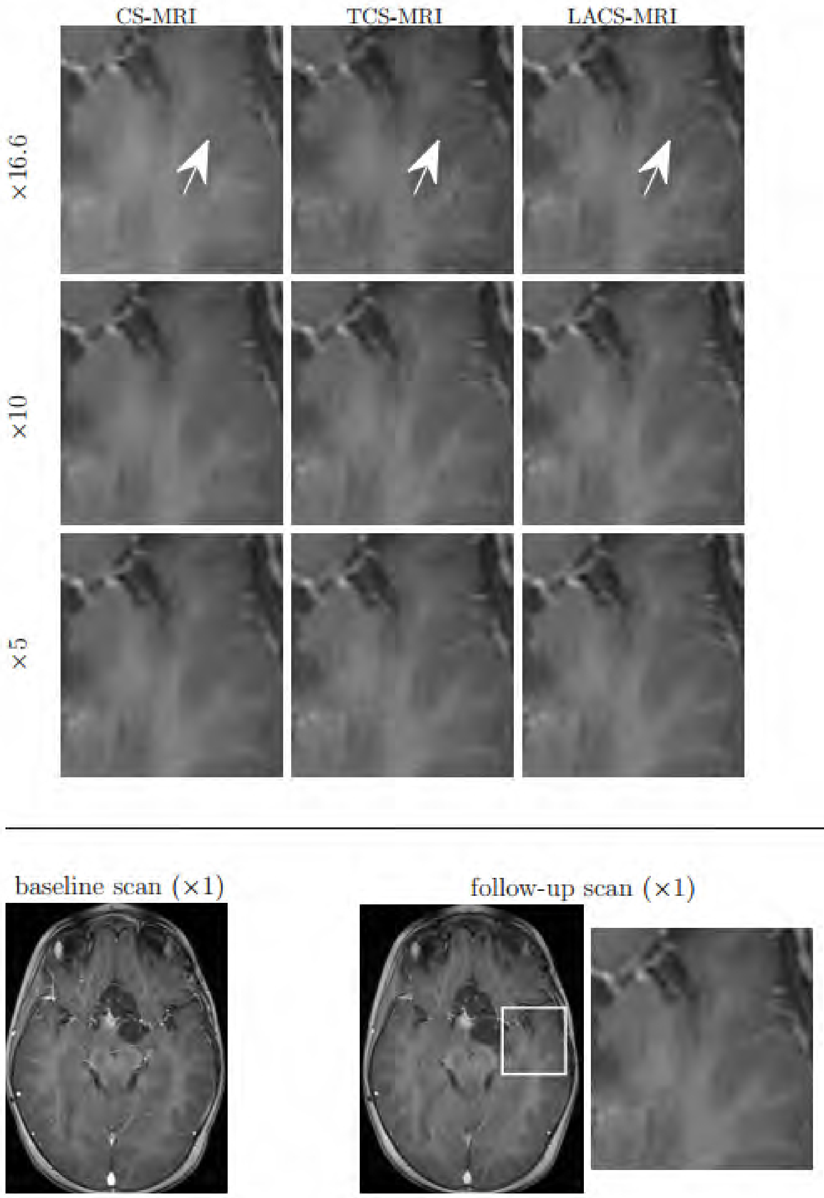

FIGURE 2.9 – 3D reconstruction results at 16.6-fold acceleration, at 10-fold acceleration and at 5-fold acceleration with methods proposed in [L. Weizman, 2015].

Chapitre 3

Dictionary learning : sparsifying dictionaries

3.1 Introduction

A fundamental choice in the application of the CS framework is choosing the right sparsifying dictionary. There are two different ways for choosing this dictionary : either using a fixed bases or using a learning-based approach, in which the dictionary is trained to fit a given set of signal examples. The first type of dictionary has an analytic formulation and a fast transform but do not necessarily best sparsify the signals that they are supposed to handle. While the second type of dictionary has the ability to adapt to a specific family of signals of interest. Such dictionaries allow for much sparser representations of the signals since they are optimized for a family of signals that are of interest such as US images. Even more, it has been observed that learning a dictionary directly from training rather than using a predetermined dictionary (such as wavelet or Fourier) usually leads to better representation and hence can provide improved results in many practical image processing applications such as restoration and classification [Rubinstein et al., 2010]. However, using learned dictionaries comes at the price of a higher computational load and using them in the CS application involves more computations, compared to the fixed dictionaries.

In this section, we shall present how to learn dictionaries for a specific set of signals, some of the algorithms proposed by the literature and finally focus on the K-SVD method, as it shows good results in many applications, and has a less complex implementation.

3.2 Dictionary learning formulation

Dictionary learning uses a set of training samples $X = \{x_i\}_{i=1}^N$, which contains N samples, to find an optimal dictionary D of $\mathbb{R}^{n \times K}$ containing K atoms of size n that will best sparsify them. This can be formulated as the following minimization problem :

$$\min_{D,\Theta} \|X - D\Theta\|_F^2 \ \ s.t. \ \forall i, \|\theta_i\|_0 \leq T_0 \tag{3.1}$$

where $\|\|_F$ is the Frobenius norm defined as the square root of the sum of the absolute squares of its elements. T_0 is the number of non-zero entries, which is expected to be very small, X contains all the training samples as columns and Θ contains the corresponding coefficients.

Solving the dictionary learning problem is also NP-hard and numerous algorithms have been proposed, the literature on this topic being vast and fast growing.

3.3 Dictionary learning algorithms

3.3.1 K-Means

The K-Means method is part of the clustering family methods, in which the descriptive vectors $\{d_k\}_{k=1}^K$ are learned and each training sample is represented by the vector $d_i \in \{d_k\}_{k=1}^K$ that is closest to it (using the l_2 distance measure). Thus, we can see the clustering problem as a specific sparse representation in which only one atom is allowed in the signal decomposition. The difference between this method and the sparse representation is that in the latter one example can be represented as a linear combination of several atoms. In that sense, the sparse representation can be interpreted as a generalization of the clustering problem.

Each iteration of the corresponding training algorithm comprises two steps [Gersho and Gray, 1991] :

1. Assign each training sample to their nearest neighbor in $\{d_k\}_{k=1}^K$.
2. Given the previous assignment, update the vectors $\{d_k\}_{k=1}^K$ such that they better represent their assigned training samples.

This two-steps approach inspired many other algorithms, that usually only differ in the way they calculate the coefficients or in the procedure to update the dictionary's atoms. The first and simplest approach to perform this step is to replace each vector in $\{d_k\}_{k=1}^K$ by the mean of its assigned training samples.

3.3.2 Method of Optimal Directions (MOD)

The Method of Optimal Directions (MOD) was introduced by Engan et al. in 1999 [Engan et al., 1999, K. Engan and Kreutz-Delgado, 1999], and follows the K-means model, also called the sparsification process. This process is composed by two steps : the first is the sparse coding step which is performed using any pursuit algorithm (usually OMP) and thus allows computing Θ while D is fixed. The second stage is the dictionary update. The main contribution of MOD concerns this dictionary update step.

If we assume the sparse coding step is done, then we can define the residual error as $e_i = x_i - D\theta_i$. Thus, the overall sparse representation mean square error is given by :

$$\|E\|_F^2 = \|e_1, e_2, ...e_N\|_F^2 = \|X - D\Theta\|_F^2 \tag{3.2}$$

Assuming that Θ is fixed, we can seek an update to D such that the above error is minimized. Since $p >> K$, this corresponds to a least-square minimization problem and then this update step can be performed by :

$$D^{n+1} = X\Theta^{nT} \cdot (\Theta^n \Theta^{nT})^{-1} \tag{3.3}$$

3.3.3 K-SVD Dictionary Learning

The K-SVD method solves iteratively the optimization problem using two steps : the sparse-coding step and the dictionary update step. In the sparse-coding stage we assume the knowledge of D and we find Θ using any pursuit algorithm.

The KSVD approach differs from the MOD method in that the update of D is done one column at a time. Assuming Θ is fixed, the kth column d_k in the dictionary D is updated with its corresponding representation coefficients denoted as θ_T^k. The penalty term of the objective function in (3.1) can be rewritten as :

$$\begin{aligned} \|X - D\Theta\|_F^2 &= \left\| X - \sum_{j=1}^{K} d_j \theta_T^j \right\|_F^2 \\ &= \left\| \left(X - \sum_{j \neq k} d_j \theta_T^j \right) - d_k \theta_T^k \right\|_F^2 \\ &= \left\| E_k - d_k \theta_T^k \right\|_F^2 \end{aligned} \tag{3.4}$$

The error matrix E_k is restricted by choosing only the columns corresponding to those elements that initially used d_k in their representation. The restricted matrix is denoted by E_k^R. The penalty term is then minimized directly via singular value decomposition (SVD) such that the restricted matrix E_k^R is decomposed to $E_k^R = U\Delta V^T$. The solution for d_k is defined as the first column of U, and the coefficient vector θ_R^k as the first column of V multiplied by $\Delta(1,1)$. Note that, in this solution, we necessarily have that i) the columns of D remain normalized and ii) the support of all representations either stays the same or gets smaller by possible canceling of terms.

This algorithm is called K-SVD as it obtains the updated dictionary by SVD computations, each determining one column. The algorithm iterates between the two steps until convergence. K-SVD algorithm and variations can be seen in detail in [Aharon et al., 2006,Smith and Elad, 2013]. In this study, the implementation of the approximate K-SVD presented by Rubinstein [Rubinstein et al., 2006] were used with the improvements proposed in [Smith and Elad, 2013] for the learning of the overcomplete dictionary.

```
Data: The set of training samples $X = \{x_i\}_{i=1}^N$, $T_0$
Initialization : $D_0 \in \mathbb{R}^{p \times K}$ with $l_2$ normalized columns, J = 1;
repeat
    – Sparse coding step :
      Use any pursuit algorithm to compute the representation vectors $\theta_i$ for each example
      $x_i$, by approximating the following solution : ;
      $\min_{\theta_i} \|x_i - D\theta_i\|_2^2$ s.t. $\|\theta_i\|_0 \leq T_0$, for $i = 1, 2, .., N$ ;
    – Dictionary update step :
      Each column $k = 1, 2, ..., K \in D^{J-1}$ is updated as follows : ;
        1. Define the set of training samples that use the atom $d_k$ :
           $\omega_k = \left\{ i | 1 \leq i \leq N, x_T^k(i) \neq 0 \right\}$
        2. Compute the error matrix $E_k = X - \sum_{j \neq k} d_j \theta_T^j$ :
        3. Restrict $E_k$ by choosing the columns that correspond to $\omega_k$ and obtain $E_k^r$
        4. Apply SVD decomporition : $E_k^R = U \Delta V^T$
        5. Choose the updated atom $d_k$ to be the first column of U : $d_k = U_1$
        6. Update the coefficient vector $\theta_R^k$ as the first column of $V$ multiplied by $\Delta(1, 1)$
    – $J = J + 1$;
until $\|X - D\Theta\|_{l_2} < \epsilon$ or $J \leq ITER\_MAX$;
Result: Dictionary D
```

Algorithm 3: K-SVD algorithm

3.3.4 Other Dictionary Learning Methods

Maximum Likelihood

The methods reported in [Lewicki and Olshausen, 1999,Hyvrinen et al., 2009,Olshausen and Field, 1997,Lewicki et al., 1998] use probabilistic reasoning in the construction of D. They assume that for every sample x we have the following relationship :

$$x = D\theta + v \tag{3.5}$$

with θ a sparse representation and v a Gaussian white noise with zero mean and variance σ^2.

Given the samples $X = \{x_i\}_{i=1}^N$, all these works seek the dictionary that maximizes the likelihood function $P(X|D)$. The overall problem can be written as :

$$D = arg\max_D \sum_{i=1}^N \max_{\theta_i} P(x_i, \theta_i|D) = arg\min_D \sum_{i=1}^N \min_{\theta_i} \|D\theta_i - x_i\|^2 + \lambda \|\theta_i\|_1 \tag{3.6}$$

As shown in [Olshausen and Field, 1997], the problem 3.6 can be solved using an iterative method which includes two main steps in each iteration : (1) the first step calculates the coefficients θ_i using a gradient descent method and (2) the second step updates the dictionary using :

$$D^{j+1} = D^j - \mu \sum_{i=1}^N (D^j\theta_i - x_i)\theta_i^T \tag{3.7}$$

Maximum A Posteriori

In [Figueiredo and Nowak, 2001, Figueiredo, 2002] a probabilistic point of view is adopted that is very similar to the Maximum Likelihood method discussed above. In this framework rather than working with the likelihood function $P(X|D)$, as above, the posterior $P(D|X)$ is used. Using Bayes rule, we get $P(D|X) \propto P(X|D)P(D)$, and thus we can use the likelihood expression as before, and add a prior on the dictionary as a new ingredient. These works considered several priors $P(D)$ and per each proposed an update formula for the dictionary.

When no prior is chosen, the update formula is the same as (3.8) proposed in [Olshausen and Field, 1997]. When a prior constrains D to have a Frobenius unit norm, the update formulas is :

$$D^{j+1} = D^j - \mu E X^T + \mu \cdot tr(XE^T D^j)D^j \tag{3.8}$$

In this case different columns of D can have different norm values and as a consequence, columns with small values are under-used, as the coefficients needed are larger and thus more penalized. Another choice of prior constrains the columns of D to have an unit l_2 norm. The update formula is given by :

$$d_i^{j+1} = d_i^j + \mu(I - d_i^j {d_i^j}^T) \cdot Ex_i^t \tag{3.9}$$

Simulations in [Figueiredo and Nowak, 2001, Figueiredo, 2002] report that the training algorithms are slower than the MOD but with promising results.

Union of Orthonormal Bases

This work introduced by Elad [Elad and Bruckstein, 2002] and generalized by Gribonval [Gribonval and Nielsen, 2003] considers the dictionary as an union of orthonormal bases. This method exploits the fact that a signal $x \in \mathbb{R}^n$ has an unique representation in several orthonormal bases, $D = [D^1, ...D^L]$ where $D^i \in \mathbb{R}^{n \times n}, j = 1, ...L$. The coefficients of the sparse representations Θ such that $\|X - D\Theta\|_F$ is reduced, can be decomposed into L pieces, each piece θ_i being the sparse representation of y in the bases D^i.

The sparse coding step can be solved using a simple pursuit algorithm. Once the coefficients are known, this algorithm updates each orthonormal basis D^i by first computing a residual matrix : $E_i = X - \sum_{i \neq j} D_i \Theta_i$. Then by solving a constrained least squares problem with $\|E_i - D_i \Theta_i\|_F^2$ and fixed Θ_i and E_j. Unfortunately, experimental results reported in [Lesage et al., 2005] show weak performance compared to previous methods.

Conclusion

Almost all the previously presented methods can be interpreted as a generalization of the K-means algorithm. There are however several noticeable differences between these procedures that make them more or less adapted for the training of a dictionary. Adaptability is one of the researched properties, meaning that any pursuit algorithm can be used by the training algorithm. This is possible only if the sparse coding stage is independent from the dictionary update stage. This property allows one to choose an adequate balance between recovery performance and speed. Only MAP, MOD and K-SVD based methods propose it. Another crucial property is the efficiency of the algorithm that can be measured by the training speed. Almost all of the described methods are quite slow. For example, MOD algorithm cannot be applied to large dimension problems due to the matrix inversion step. The K-SVD algorithm is the most efficient among the presented algorithms, with an effective sparse coding step and an accelerated dictionary update stage. Moreover, the K-SVD algorithm is simple to implement and understand with a clear objective function. Although there are many more dictionary learning algorithms, we choose to use the K-SVD algorithm due to its numerous properties, its robustness and its popularity in the dictionary learning community that proves its reliability.

III Contribution1 : Compressed sensing in US imaging using dictionary learning

Chapitre 4

Compressed sensing in US imaging

4.1 Introduction

In this chapter we introduce a new approach based on the use of learned overcomplete dictionaries in the CS context for the reconstruction of 3D ultrasound images. We begin by giving in section 4.2 a detailed state of the art of compressed sensing in 2D and 3D ultrasound imaging. Section5 shows preliminary results obtained by the application of the proposed methos to 2D US images. The sections 6.1.2, 6.1.3 and 6.1.1 then presents the conditions of application of the proposed approach to the 3D simulated and experimental data. It details in particular the sampling patterns and reconstruction scheme used in this study. Section 6.2 presents the results obtained from numerical simulations. It details the influence of the sampling pattern and of several parameters of the dictionary learning algorithm such as training patches size, subsampling rate and redundancy of the dictionary on the reconstruction accuracy. Section 6.3 describes the results obtained from acquisitions performed *ex vivo* on animal brains, hearts and kidneys and section 6.4 provides the results obtained from *in vivo* liver and kidney data. The accuracy associated to the learned dictionary is assessed and compared to the accuracy associated to fixed sparsifying transforms such as the Fourier or discrete cosine. Moreover, the generality of the approach is studied by reconstructing the 3 types of organs from a unique dictionary. In each case, the accuracy is evaluated as a function of the subsampling rate. Finally, section 7 concludes this contribution.

4.2 State of the art of CS in US imaging

As described in Chapter 1, ultrasound imaging system is a useful diagnostic imaging technique as it is highly flexible, fast, cheap and noninvasive. Although the conventional two-dimensional ultrasound systems present several advantages, they also suffer from the following limitations :

- The user needs to combine mentally several 2D images in order to obtain a 3D representation of the organ anatomy or pathology. This is time-consuming and inaccurate as it may result in an inter-observer variability.
- Accurate measurements and delineations of organs or lesions can be variable and some times inaccurate on 2D acquisitions.
- Monitoring the progression of a pathology or lesion is challenging since it is particularly difficult to place the 2D US imaging transducer at the same location and orientation on the patient at different time intervals.
- It does not permit the viewing of planes that are parallel to the skin.

In order to overcome these limitations, three-dimensional ultrasound imaging systems have been developed. Most of the 3D US imaging systems are based on one of the following techniques : mechanical scanning, free-hand scanning with or without position sensing and electronic steering based on 2D matrix array transducers. The systems performing a mechanical scanning sweep of the volume of interest through the motion (rotation, translation) of a 2D transducer and then post-process the data acquired to form a 3D image. However, the associated probes can be heavy, bulky and difficult to use on the body depending of the location or the organ. Another approach uses a conventional US transducer generating 2D images and uses sensors to allow tracking of the transducer as it moved over the body in order to reconstruct an accurate 3D volume [Fargier-Voiron et al., 2014]. The mechanical and free-hand techniques limit the speed of volume acquisition to about 2/3 volumes per second. To overcome the speed limitations and the need to move by hand the transducer, transducers generating real-time 3D volumes have been recently developed. These transducers use a 2D phased array, allow to remain stationary and use the phased array to electronically sweep a pyramid-shaped volume. The main challenge of this technique is physically connecting all the sensors and thus, only a fraction can be activated, leading to naturally sparse RF data.

The application of compressed sensing to this field of imaging techniques seems natural and applications such as the 3D imaging using matrix arrays is an excellent candidate all the more since 3D US systems require a significant increase in computation speed for acquiring, reconstructing and viewing the US volumes in real time.

In the following section, we will give an overview of the recent approaches applying CS in medical ultrasound. The application of compressed sensing techniques to US imaging has motivated research efforts only recently, since the first works were published in

2010 [Friboulet et al., 2010, Quinsac et al., 2010a, Quinsac et al., 2010b] and therefore few studies have been devoted to this topic to date. A key element in CS is that the data to be reconstructed should have a sparse expansion in some basis or dictionary (e.g. Fourier basis, wavelet basis, dictionary learned from data,...). As a consequence, one important feature of the existing studies is the choice of the representation where the US data are assumed to be sparse. Moreover, US echographic data may be considered at various stages of the image formation pipeline. Let us recall here that US image acquisition starts with the transmission of a series of pulses from the transducers towards the scanned environment. The returning echoes are then processed to get a series of raw channel signals available from the probe elements, which are then beamformed to form the radio-frequency (RF) signals. Detection of the envelope of each RF signal and juxtaposition yields the so-called envelope image. Log transformation finally provides the usual B-mode image. As a consequence, one of the main features of the existing studies is the type of signal/image to be reconstructed and the choice of the sparse representation basis in which the US data is assumed to be sparse.

4.2.1 Sparsity assumption

Sparse distribution of scatterers

Several works [Schiffner et al., 2012, Schiffner and Schmitz, 2011, Wagner et al., 2012, Wagner et al., 2011, Tur et al., 2011, Chernyakova and Eldar, 2014, Zhang et al., 2013a, Zhuang et al., 2012] assume a sparse distribution of scatterers in the direct, spatial domain. In [Schiffner et al., 2012, Schiffner and Schmitz, 2011], the authors aim at producing an image using only one single plain wave that has the spatial resolution of an image obtained convention US imaging. The idea behind this method is to produce images at the highest temporal resolution, i.e. one image per transmitted pulse so the acquisition time would be the time for the wave to make a round-trip at the speed of sound. In order to apply this approach, they propose writing the direct scattering reconstruction problem under the constraint that the scatterer distribution is sparse, as follows :

$$p^{sc}(e_\theta) = G(e_\theta)\gamma_k$$

with $p^{sc}(e_\theta)$ being the scattered acoustic pressure received by the transducer elements after emission of a plane wave in direction θ. $G(e_\theta)$ is a matrix representing the interaction with the scatterers and γ_k is the approximation of point scatterers located on a regular lattice. This ill posed problem is a CS problem under the constrained that γ_k is sparse and the authors perform the reconstruction using l_1 minimization. This approach gave good results on images composed of few, strong scatterers, as shown in Figure 4.1, since the sparsity hypothesis is verified.

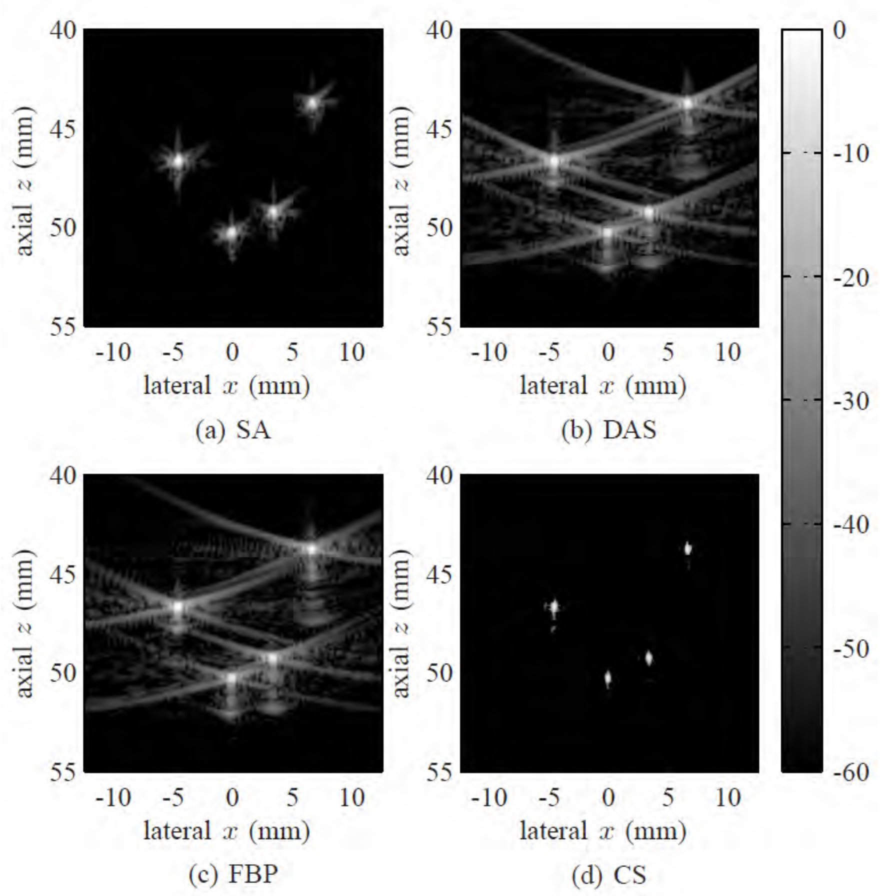

(a) SA (b) DAS (c) FBP (d) CS

FIGURE 4.1 – Result from [Schiffner et al., 2012] obtained from a phantom consisting in four isolated scatterers. The CS result (d) is compared with synthetic aperture (a), delay and sum (b) and Fourier propagation (c)

The same sparsity hypothesis is proposed in a different framework in [Wagner et al., 2012, Wagner et al., 2011, Tur et al., 2011, Chernyakova and Eldar, 2014] based on the finite rate of innovation model and the Xampling technique. These techniques allows reducing the number of samples needed for the reconstruction of an image composed of strong reflectors. However, a drawback of this approach is the inability of reconstructing the speckle which is of a significant importance for the ultrasound imaging [Chernyakova and Eldar, 2014] . This loss is consistent with the hypothesis of the scatterer map sparsity since it tends to eliminate the small echoes and keep only the highest ones. The method has been recently extended to a more general context where the speckle is better preserved through a l_1 norm reconstruction as it can be observed in Figure 4.2.

Sparse signal assumption

Most of the previous works however consider that the signal is sparse in a given basis or frame such as Fourier [Basarab et al., 2013, Dobigeon et al., 2012, Friboulet et al., 2010, Liebgott et al., 2013, Quinsac et al., 2011], wavelets [Chuo et al., 2013, Friboulet et al.,

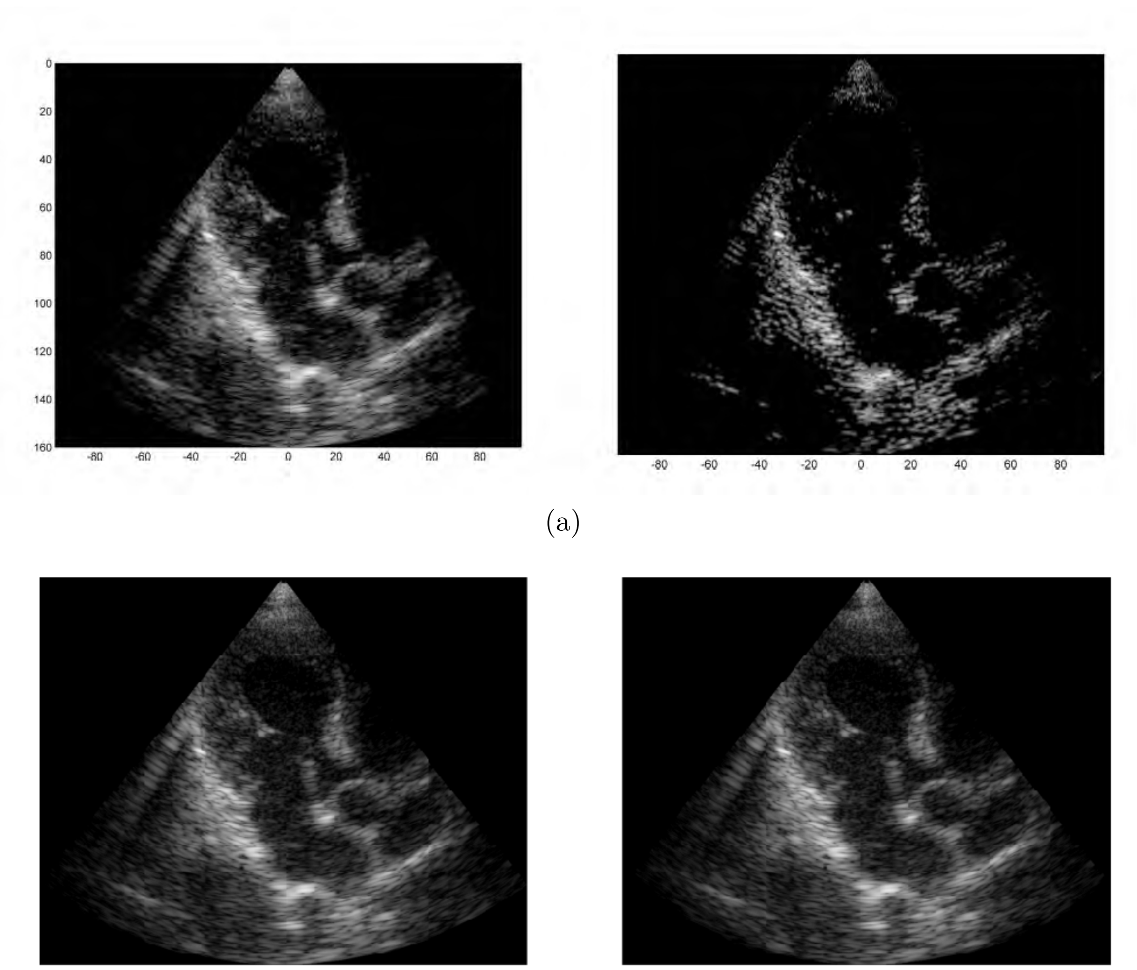

(a)

(b)

FIGURE 4.2 – (a) Result from [Wagner et al., 2012] : original image and image obtained by CS with l_0 optimization. (b) Result from [Chernyakova and Eldar, 2014] : original image and image obtained by CS with l_1 optimization.

2010, Liebgott et al., 2013, Quinsac et al., 2010b], Discrete Cosine [Quinsac et al., 2010b] or wave atoms [Friboulet et al., 2010, Liebgott et al., 2013]. The signal that is considered to be sparse is either the raw channel data available from the probe elements or the signal obtained after the beamforming of the raw channel data.

Sparse raw RF signals In this case the raw RF channels are considered to be sparse is a fixed basis. The objective of applying the CS framework at this point of the US image construction is to reduce the quantity of acquired data and thus the number of raw signal channels. In [Friboulet et al., 2010, Liebgott et al., 2013] the raw data measurements were reconstructed using l_1 minimization and three sparsifying fixed basis were tested : Fourier, wavelets and wave atoms. The obtained results showed the wave atoms give a good reconstruction with a reconstruction error two times smaller than with the Fourier basis and high quality B-mode images are obtained using only 20% of the original measurements. However, this approach uses an uniform random sampling as a measurements setup which is difficultly implementable in practice.

Sparse beamformed RF signals In this case the sparsity assumption is made on the beamformed RF signals. In [Chuo et al., 2013] these signals are considered to be sparse in the wavelet domain, while in [Quinsac et al., 2010a, Quinsac et al., 2011, Basarab et al., 2013, Dobigeon et al., 2012] the 2D Fourier transform of the beamformed 2D RF images is assumed to be sparse. Thus, in the context of the CS formulation, the sensing matrix is the spatial acquisition mask where spatial samples are measured at random positions and the sparsifying matrix is the inverse 2D Fourier transform. The resulting inverse problem has been solved in [Quinsac et al., 2010a] by a nonlinear conjugate gradient descent method. However, more accurate results are given in [Quinsac et al., 2011, Basarab et al., 2013,Dobigeon et al., 2012] using a Bayesian framework. Figure 4.3 gives a simulation result extracted from [Dobigeon et al., 2012], showing the original image and the reconstructions using a reweighted l_1 minimization by conjugate gradient and the Bayesian framework.

In [Achim et al., 2010, Achim et al., 2014], the authors assume that the ultrasound RF echoes are sparse and characterized through α-stable distributions. The reconstruction was based on the l_p norm minimization approach that employed the iteratively reweighted least squares (IRLS) algorithm adapted for the alpha-stable distributed data. Their results showed a significant increase of the reconstruction quality when compared with some l_1 minimization algorithms.

4.2.2 Measurement sensing

The second important feature for ensuring a successful CS reconstruction is the way the measurement of the data is performed. While most of the studies rely on conventional CS performed in the discrete domain, the works in [Tur et al., 2011, Wagner et al., 2012] are particular as they use an analog-to-digital version of CS based on the so-called Xampling mechanism [Mishali et al., 2011] and considering the US data as Finite Rate of Innovation signals [Vetterli et al., 2002]. As far as discrete CS is considered, early works showed that linear projection of the data on sub-Gaussian random matrices (e.g. with i.i.d. Gaussian, Rademacher or Bernoulli entries) provides incoherent measurements allowing for exact reconstruction. In practice however, the use of random sensing matrices is not straightforward, since it implies dedicated acquisition hardware. Such sensing matrices have been thus mostly used in simulation studies, such as [Achim et al., 2010, Achim et al., 2014, Zhang et al., 2013a] with Gaussian matrices and [Zhuang et al., 2012] with a Rademacher matrix.

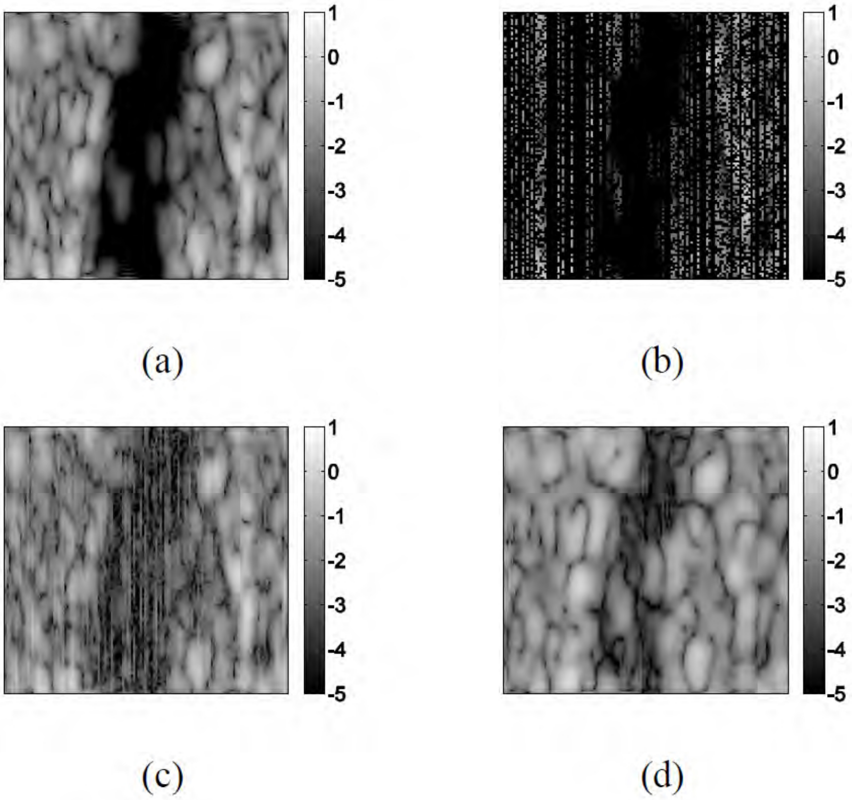

Figure 4.3 – Result from [Dobigeon et al., 2012] : (a) Original US image, (b) measured samples, (c) image reconstructed using reweighted conjugate gradient optimization and (d) image reconstructed using the proposed Bayesian method

Since using random sensing matrices is difficult in practice, it is often preferred to resort to deterministic, structured sensing matrices. More generally, the physics of acquisition often imposes a deterministic sensing matrix, e.g. Fourier in MRI. Since US acquisition is performed in the direct domain, the sensing matrix is simply the identity. In this case, successful CS reconstruction of US images implies uniform random sampling of the data. The specificities of US acquisition then yield two possible strategies. In the first strategy each of the acquired RF line is sampled according to a distinct random pattern and the full US acquisition (corresponding to the juxtaposition of the N acquired RF lines) then forms the RF image. Overall, this strategy can thus simply be seen as directly sampling the full RF image with a point-wise 2D or 3D random pattern and many studies devoted to CS in US uses such scheme [Achim et al., 2010, Achim et al., 2014, Basarab et al., 2013, Dobigeon et al., 2012, Zhang et al., 2013a, Zhuang et al., 2012]. Let us note however that while this sampling strategy is desirable for CS reconstruction, its practical implementation is far from obvious. First, such implementation implies a dedicated hardware allowing for the desired random sampling. Moreover, RF lines are nowadays obtained by beamforming in the digital domain and the sampling has thus to be performed at the level of raw data. This is taken into account in the study by Liebgott [Liebgott et al., 2013], which performs CS reconstruction of pre-beamformed RF signals. The second strategy corresponds to a line-wise random pattern : it simply consists in randomly skipping the acquisition of several RF lines, thus yielding a RF image with missing lines. The main interest of this strategy relies on the fact that it is by design much easier to implement in practice and it has thus been used in several studies [Basarab et al., 2014, Chuo et al., 2013, Quinsac et al., 2011].

4.3 Contributions

Let us end this chapter by noting that there are very few studies dealing with 3D US data. In [Quinsac et al., 2010b, Quinsac et al., 2012] pointwise and line-wise sampling patterns have been proposed and compared on one experimental RF image using Daubechies wavelets, finite differences and discrete cosine as sparsifying bases. Very recently Birk et al. [Birk et al., 2014] extended the analog-to digital Xampling mechanism to 3D acquisitions.

The objective of this chapter is to investigate in details the feasibility of compressive sensing 3D ultrasound. We will present here some preliminary results but also some main novelties and contributions :

- First, we propose a CS framework using learned overcomplete dictionaries since they can be optimized for a particular class of images such as US images and thus allow for sparser representations. Initially, we test this framework as a preliminary validation on 2D US data.
- Secondly, we address the reconstruction of 3D US data and more particularly, we show that the learned dictionary approach yields better performances than conventional sparsifying dictionaries based on fixed transforms such as Fourier or discrete cosine. To the best of our knowledge, this aspect has never been investigated for 3D ultrasound. The only study in the literature that might be compared to our work is reported in [Tosic et al., 2010], which deals with US tomography. The technique that we propose is different as we work on 3D ultrasound echography.
- Then, we evaluate the generality of the learned dictionary approach. Indeed this approach may be hampered by over-learning, yielding a learned dictionary providing satisfying reconstruction only for images very close to the learning set. We show that it is possible to build a dictionary allowing to reliably reconstruct different volumes of different *ex vivo* organs.
- Finally, we also focus our attention on the measurement sensing setup. We chose to concentrate on the line-wise sampling of entire RF lines which results in an increase of the frame rate since we work on the reconstruction of the envelope image. We study the influence of the sampling strategy on simulated data, by comparing in each case the 2 most common sampling patterns, i.e. point-wise and line-wise ran-

dom patterns. We show in particular that although not fully uniform, the line-wise sampling results in an accuracy comparable to the conventional point-wise sampling, using the dictionary based strategy we propose. As previously mentioned, this indicates that CS acquisition of 3D data is feasible in practice in a relatively simple setting.

Chapitre 5

Application to 2D US imaging

The main purpose of this section is to show the feasibility of reconstructing high quality US images from less elements or sampled data using CS theory using an overcomplete dictionary. We test this approach on 2D US images.

5.1 Application of CS and dictionary learning to 2D US images

5.1.1 CS reconstruction scheme

The experimental beamformed RF signals produced by experimental acquisition on phantom data were gathered and formed the original data, x to imitate acquisition. The data acquisition in US imaging is performed in the direct space so the acquisition basis Φ is the Dirac basis. These original beamformed images were then subsampled by removing varying amounts of samples. The spatial position of the removed samples was selected according to a uniform random law. CS reconstruction was then performed from the subsampled data sets where 25% to 75% of the original samples were removed.

CS reconstruction using an overcomplete dictionary was performed using a block-wise approach. Let x_i of $\mathbb{R}^p, p < n$, be a patch of an image x and D of $\mathbb{R}^{p\times K}$ be an overcomplete dictionary, with $p < K$, such that $x_i = Dv_i$. We can rewrite the classical CS algorithms to reconstruct each patch x_i from the linear measurements y_i :

$$\begin{aligned} &\hat{v}_i = arg \min_{v_i \in \mathbb{R}^K} \|v_i\|_1 \quad \text{subject to} \quad \|y_i - R\Phi D v_i\|_2 \leq \varepsilon \\ &\hat{x}_i = D\hat{v}_i \end{aligned} \tag{5.1}$$

After reconstructing all the $\hat{x}_i$, the patches are recombined by shifting and summing in order to get the full 2D US image $\hat{x}$. The 2D CS reconstruction problem (5.1) was solved in this case using the greedy orthoghonal mathching pursuit algorithm OMP described in section 2.3.1 [Pati et al., 1993].

5.1.2 Learning overcomplete dictionaries from 2D US images

Application of CS implies learning D such that v_i is a sparse representation of the patch i in D. We will then be able to recover the original image patches from the linear measurements y_i. Dictionary learning uses a set of training samples $X = \{x_i\}_{i=1}^N$, which contains N samples, to find an optimal dictionary D of $\mathbb{R}^{p \times K}$ containing K atoms of size p that will best sparsify them. This can be formulated as the following minimization problem :

$$\min_{D,\Theta} \|X - D\Theta\|_F^2 \;\; s.t. \; \forall i, \|\theta_i\|_0 \leq T_0 \tag{5.2}$$

T_0 is the number of non-zero entries, which is expected to be very small, X contains all the training samples as columns and Θ contains the corresponding coefficients. The training data consisted of patches extracted from the original beamformed RF image.

Solving the dictionary learning problem is also NP-hard and numerous algorithms have been proposed. We have chosen the implementation of the approximate K-SVD presented by Rubinstein [Rubinstein et al., 2006] with the improvements proposed in [Smith and Elad, 2013] for the learning of the overcomplete dictionary and the OMP algorithm was used for the block-wise CS reconstruction. All these algorithms were described in Chapter 3.1. Besides the K-SVD dictionary, we include two other bases in our experiments for comparison : the Fourier basis and the Daubechies db5 wavelets.

5.1.3 Reconstruction quality evaluation

The accuracy of the results was quantified by comparing the CS reconstruction to the original data through the normalized root mean square error (NRMSE) which is defined as

$$\text{NRMSE} = \frac{\|x - \hat{x}\|_2}{\|x\|_2} \tag{5.3}$$

where x is the original image and $\hat{x}$ is the reconstructed image.

5.2 Results

5.3 Experimental acquisition setup

The experimental channel RF data were acquired using the Ultrasonix MDP research platform (Richmond, BC, Canada) equipped with the parallel channel acquisition system SonixDaq. The data consisted in 128 single element received signals of a linear L14-5W/60 Prosonic (Korea) probe. The central frequency of the probe was 7 MHz and the signals were collected using a 40-MHz sampling rate. The medium imaged was a general-purpose ultrasound phantom CIRS Model 054GS (Virginia, USA). The beamformed data are calculated using the delay and sum beamformer using a constant Hanning apodization over the 128 receive elements.

5.3.1 Dictionary learning

The training data consisted of 8 × 8 patches extracted from the original beamformed RF image and the testing data consisted of the very same image. We use typical values for the algorithm parameters : sparsity $T_0 = 8$; patch dimension $p = 64$ (i.e. 8×8) ; and overcompleteness of $q = 4$ where the size of the dictionary is given by $K = q \times p$ (i.e. $K = 4 \times 64 = 256$). Figure 5.1 shows examples of such learned dictionaries for different numbers of atoms.

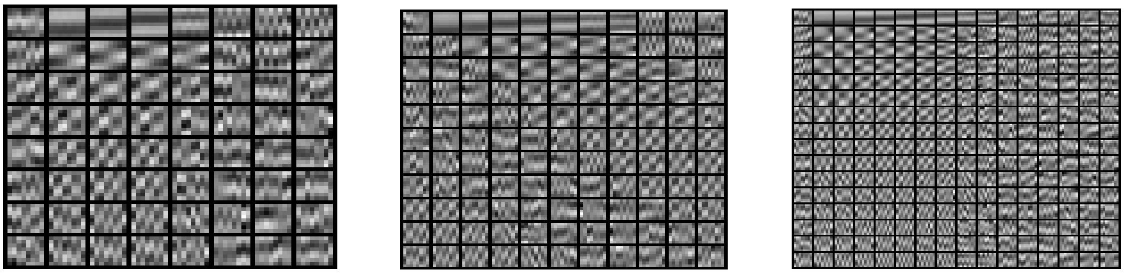

(a) 64 8 × 8 atoms (b) 128 8 × 8 atoms (c) 256 8 × 8 atoms

FIGURE 5.1 – Examples of dictionaries learned using K-SVD on patches extracted from the original beamformed image. Different setup are illustrated, with the number of atoms varying.

5.3.2 Sparsity of US images

In order to apply the CS theory we made the assumption of sparsity in a given basis Ψ. The concept of sparsity can be illustrated by plotting the coefficients in a given basis in order of magnitude. If they decay rapidly, then the compressed signal containing the s largest coefficients will be close to the original signal and this percentage of transform coefficients will be sufficient to get reliable reconstructions. If in addition to sparsity we

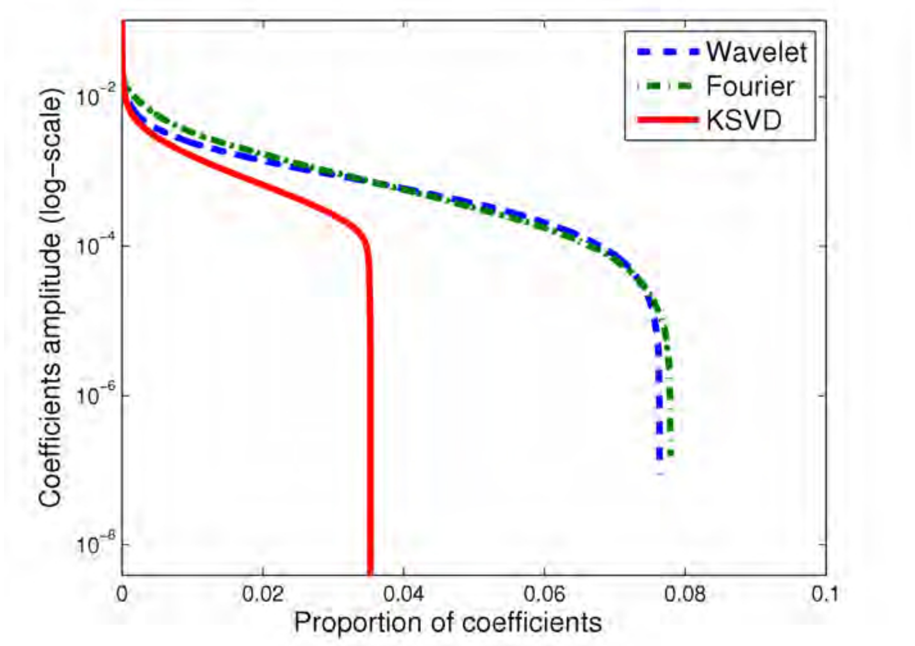

FIGURE 5.2 – Ordered relative values of the K-SVD dictionary, Fourier and wavelet transform coefficients, for an US image.

satisfy the hypothesis of incoherence then the original signal can be recovered exactly with overwhelming probability.

Figure 5.2 illustrates the concept of sparsity in the domain of three transforms : Daubechies wavelets, Fourier basis and K-SVD dictionary. The transform coefficients decay very rapidly, indicating a sparse representation of the image. Because the sparse representation in the K-SVD dictionary decays the fastest in comparison to the other transforms, it is possible to have a higher quality reconstruction using only 2% of its largest coefficients.

5.3.3 Reconstruction results

Figure 5.3 shows the reconstruction NRMSE error as a function of the subsampling rate and for each of the transforms used for reconstruction. It can be observed that the error increases with the number of removed samples, whatever the reconstruction basis. The error corresponding to the wavelets takes the largest values, and the error associated to the Fourier basis shows intermediate values. The K-SVD dictionary gives the smallest error, whatever the subsampling rate.

Figure 5.4.(a) shows the original beamformed RF data and the images obtained from CS reconstruction using wavelets, Fourier and K-SVD dictionary and Figure 5.4.(b) shows the associated error. In this example, the reconstructions have been performed after remo-

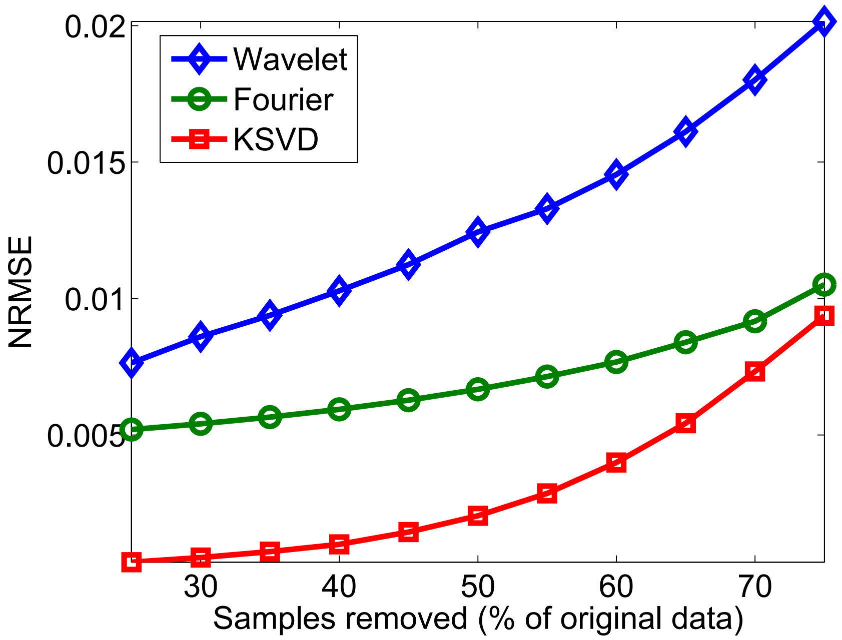

FIGURE 5.3 – NRMSE as a function of the number of removed samples. The error is computed on the RF beamformed images after CS reconstruction using K-SVD dictionary, Fourier and wavelets.

ving 75% of the original data. These images suggest that the higher errors are associated with the wavelet and Fourier reconstructions. The K-SVD preserves the details of the RF beamformed data while the Fourier based reconstruction smoothens the data and wavelet based reconstruction provides a poor result.

Whatever the reconstruction sparsifying basis, Figure 5.4.(b) indicates that the higher error values are located in the hyperechoic cyst and the different high-intensity scatterers areas associated to large signal amplitude.

Figure 5.5.(a) shows the log-envelope images corresponding to the reconstructed RF data, for better visibility and figure 5.5.(b) the corresponding error images. Due to the log operation, which performs amplitude compression, the error is now less localized and appears to be more evenly spread over the image. The performance of the reconstruction may be better observed on the top part of the images that is almost completely lost with wavelets. The K-SVD dictionary also seems to better reproduce the speckle.

5.4 Conclusion

This study demonstrates the high potential of learned overcomplete dictionaries for CS in US imaging. Experiments performed on experimental RF data with the K-SVD

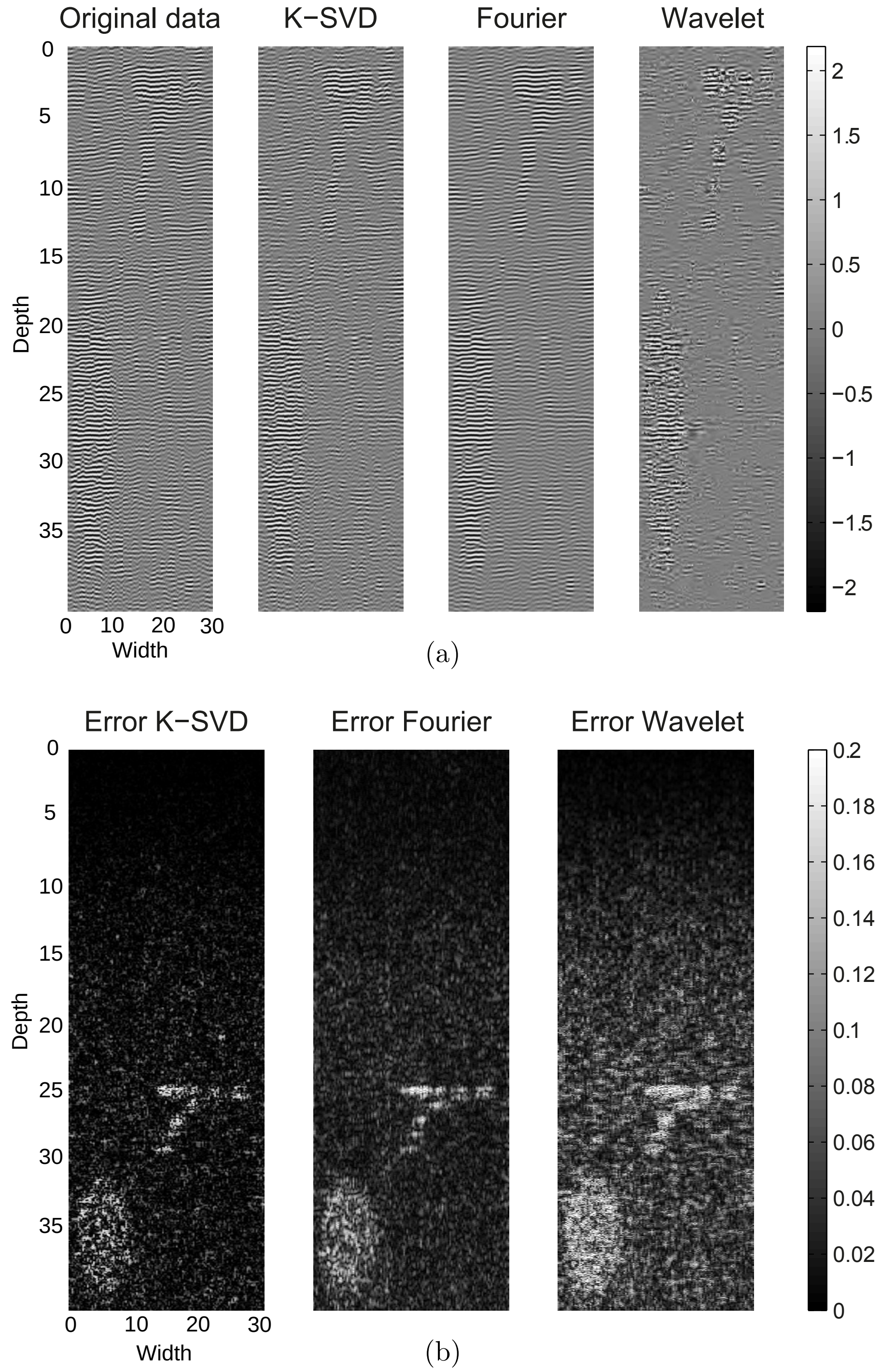

(a)

(b)

FIGURE 5.4 – (a) Original and reconstructed RF data using wavelets, Fourier, and K-SVD dictionary. (b) Absolute error between original image and reconstructed RF data using K-SVD dictionary, Fourier and wavelets. Data were reconstructed using 75% subsampling. The colormaps were rescaled for better visibility.

based CS reconstruction using only 25% of the initial samples resulted in US images close to the original, with minimal loss of information. Thereby, compressive sensing (CS)

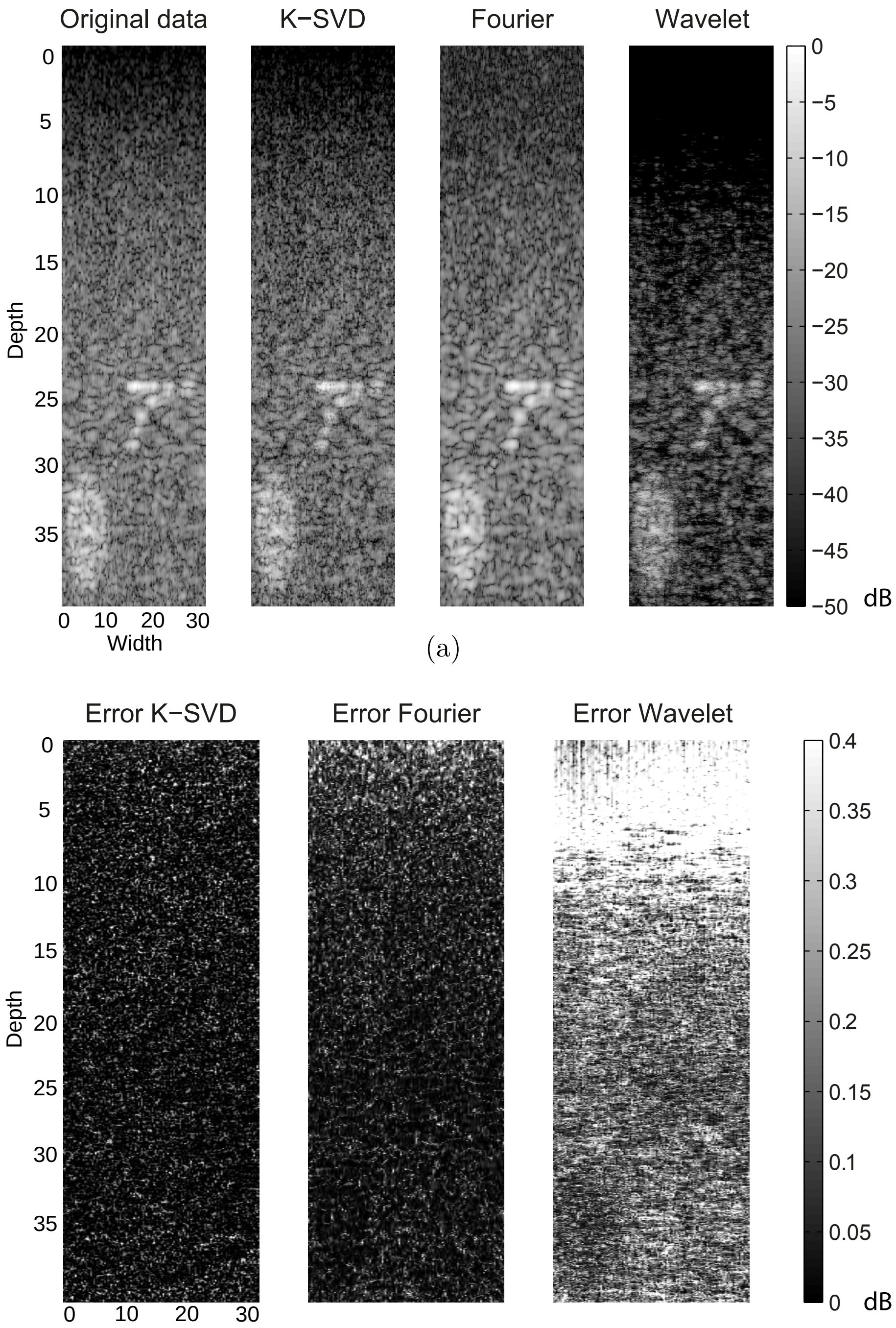

(a)

(b)

FIGURE 5.5 – (a) Log-envelope beamformed images computed from the original data and from CS reconstruction using K-SVD dictionary, Fourier and wavelets. (b) Absolute error between beamformed log-envelope image computed from the original data and CS reconstruction using K-SVD dictionary, Fourier and wavelets. Data were reconstructed using 75% subsampling. The colormaps were rescaled for better visibility.

reconstruction with overcomplete dictionaries is feasible in medical ultrasound.

Chapitre 6

Application to 3D US imaging

The objective of this chapter is to investigate in detail the feasibility of compressive sensing 3D ultrasound.

6.1 Application of CS and dictionary learning to 3D US images

6.1.1 CS reconstruction scheme

The CS reconstruction was applied on subsampled envelopes of normalized volumes before log-compression of simulation, *ex vivo* and *in vivo* experimental 3D ultrasound volumes. The volume that is used in the CS reconstruction was excluded from the training set of the overcomplete dictionary. In the experiments, where sectorial probes are used, we work only on the polar data before scan conversion to the Cartesian data. CS reconstruction was then performed on a sub-sampled dataset by removing varying amounts of samples. In the results presented, $20 - 80\%$ of the original samples were removed.

CS reconstruction using an overcomplete dictionary was performed using a block-wise approach. The patches extracted from the volume can be overlapping with an overlap rate r and are of size p. Let x_i of $\mathbb{R}^p, p \ll n$ where n is the total size of volume x, be a 3D patch of the volume to be reconstructed and D of $\mathbb{R}^{p \times K}$ be the overcomplete dictionary, where K is the number of atoms of size p, $p < K$. For this patch (2.7) then writes $x_i = Dv_i$ where v_i thus contains the coefficients of the expansion of x_i in D as in (5.1). By solving (5.1), we can then recover x_i from the linear measurements y_i of $\mathbb{R}^m$. The 3D CS reconstruction problem for each 3D patch was solved in our case through the l_1 minimization using the spectral projected-gradient algorithm SPGL1 describd in section 2.3.2 [van den Berg and Friedlander, 2009c].

The accuracy of the results was quantified by comparing the CS reconstruction to the original data through the normalized root mean square error (NRMSE) defined as in 5.1.3.

6.1.2 Sampling patterns in 3D US imaging

The sampling protocols in US imaging have to be designed to fulfill both the requirements of CS and of the US devices. On one hand, according to the CS theory the sampling basis has to be incoherent with the sparsifying basis. On the other hand as mentioned in section 4.2.2, the US imaging devices have a limited number of sampling strategies that can be adopted due to the physical constraints of the ultrasound devices. Of course, specific hardware could be developed but this is beyond the scope of this work which aims at using CS with minimal modifications of the US equipment. An uniform random point-wise sampling is desirable for CS reconstruction but is of limited practical interest, whereas the line-wise random sampling is easy to implement in practice but does not correspond to the standard CS settings.

In this context, two different sampling schemes R_1 and R_2 are proposed and evaluated. R_1 is a uniform random point-wise sampling pattern in the three directions. R_2 consists of uniformly random sampling the same set of RF lines on each consecutive slice of the volume in the axial direction. This sampling pattern simply consists in randomly skipping the acquisition of several RF lines, thus yielding a RF image with missing lines. These two sampling schemes are represented in Figure 6.1.

6.1.3 Reconstruction bases

The quality of the reconstruction depends on the sparsity of its representation in the sparsifying basis Ψ which can be an orthonormal basis, a frame or an overcomplete dictionary. RF data represent a specific challenge, because they do not easily lend themselves to a sparse representation in fixed basis or frames. We thus propose using learned overcomplete dictionaries to represent them. Indeed, such a dictionary is optimized for a given family of signals of interest and allow theoretically for much sparser representations of these signals.

The dictionary was learned using the K-SVD approach described in Section 5.1. The dictionary that was learned over a subset of 3D patches extracted from the envelope of US volumes. The performance of the K-SVD method is affected by the following parameters of the dictionary learning algorithm : patch size (p), overcompleteness (q, where the size

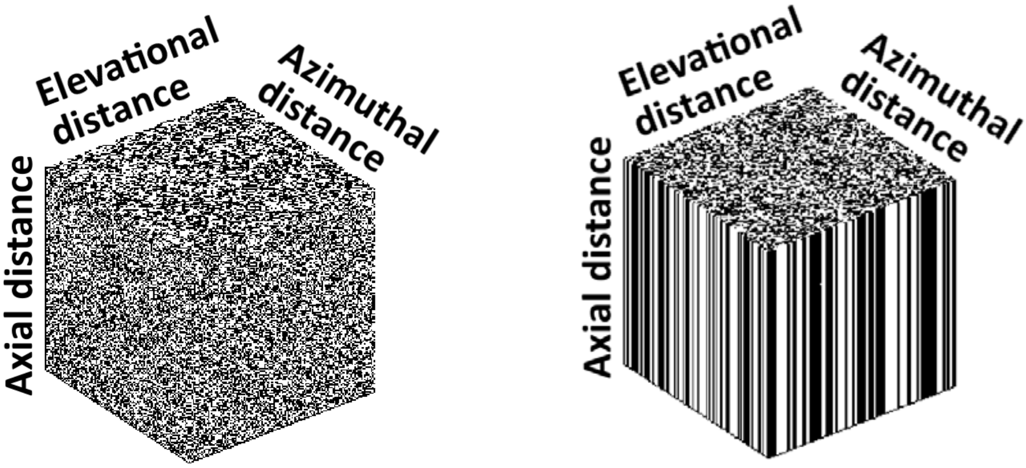

(a) R_1 : 3D random sampling (b) R_2 : 3D line-wise sampling

FIGURE 6.1 – Sampling masks R_1 and R_2 adapted to a spatial sampling of 3D US volumes. The black pixels correspond to the samples used for CS. The proportion of samples here is 50% of the original volume.

of the dictionary is given by $K = q \times p$), and overlap of patches (r, overlapping percentage rate between two consecutive patches).

In order to quantify the interest of learned dictionary for CS reconstruction of US data, it will be informative to compare this reconstruction with the one obtained with standard bases. In this study, we have selected two bases for this comparison : the first is the Fourier basis (i.e. standard DFT), since it is maximally incoherent with the sensing Dirac basis and it has been shown to provide reasonable results. The second basis is the discrete cosine transform (DCT), since it has better coefficients concentration properties than the Fourier transform and thus should provide a more compressible representation.

6.2 Simulation results

6.2.1 Simulation setup

We evaluate our algorithm on simulated 3D echocardiographic images generated according to the framework recently proposed in [Alessandrini et al., 2015, Craene and *et al.*, 2013]. In synthesis they are obtained by combining an electromechanical model of cardiac contraction [Sermesant et al., 2001] with an ultrafast ultrasound simulator (COLE, [Gao et al., 2009] and Field II, [Jensen and Svendsen, 1992]). The framework was used to simulate the ultrasound scan of one cardiac cycle of a healthy heart and have been obtained with a similar approach as in [**Lorintiu, O.** et al., 2015].[1]

---

[1] The corresponding data is made publicly available at the following link : http ://bit.ly/3dstraus.

TABLE 6.1 – Dictionary learning parameters

Parameters	Default value	Tested values
p	$\mathbf{8^3}$	$4^3, 6^3, 10^3, 12^3$
r (%)	**50**	0, 25, 75
q	**4**	1, 2, 3

We note that the so obtained sequences, despite synthetic, look extremely realistic and in terms of image properties are fully representative of what is expected from real ultrasound recordings (see Figure 6.7(a)).

The simulated US system was equipped with a cardiac phased array transducer of center frequency 3.3 MHz transmitting a Gaussian weighted pulse with a -6 dB relative bandwidth of 65%.The raw RF signals were sampled at 50 MHz and a symmetric transverse two-way beam profile was assumed, focusing at 80 mm when transmitting and dynamically focusing on receive.

The simulated RF images consisted of 107×80 beamlines in azimuthal and elevational direction and 6782 samples in axial direction over an angle of 80×80 degrees, resulting in a frame rate of 30 Hz due to the use of parallel beamforming. More details on the ultrasound model can be found in [Craene and *et al.*, 2013]. After envelope calculation the final data sets were downsampled at 2.2 MHz and consisted of 296 samples in axial direction and 107×80 beamlines .

Using this protocol we simulated two data sequences for this paper with two different scatterer distributions which produce two different speckle patterns. The data was divided in two groups : the training group consisting of five volumes coming from the first simulated sequence and a testing group consisting of one volume of the second simulated sequence. The training data was used for the learning of the overcomplete dictionary while the testing data was reconstructed using the CS theory. Appendix A shows how the percentage of subsampling rates relates to the Nyquist sampling for the simulated dataset.

6.2.2 Influence of dictionary learning parameters

Our first objective is to evaluate the performance of our method by acting on the following parameters of the dictionary learning algorithm : patch size (p), overcompleteness (q, where the size of the dictionary is given by $K = q \times p$), and overlap of patches (r, overlapping percentage rate between two consecutive patches).

We measure the influence of each parameter separately, by making one of them vary in the range specified in the Table I "Tested values" column, while all others are set to their default value. The performance is measured by comparing the CS reconstruction to the original data through the NRMSE as a function of the number of removed samples. We present in the following, the results obtained using the sampling pattern R_2 (line-wise sampling) since the sampling mask R_1 is of limited interest for US acquisitions. The influence of the sampling patterns R_1 and R_2 is then tested on the reconstruction of simulation data using a learned dictionary with default parameters.

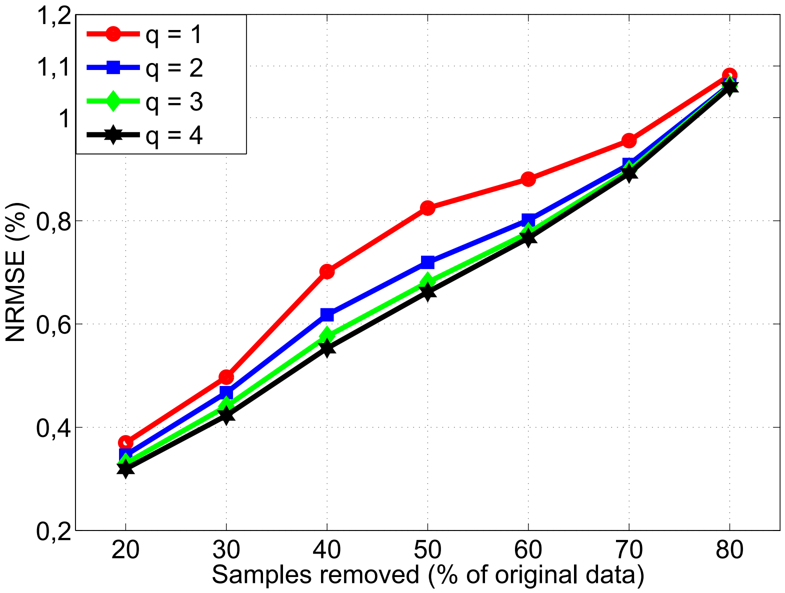

FIGURE 6.2 – Influence of the overcompleteness q on the resulting NRMSE as a function of the number of removed samples using the sampling mask R_2. Other parameters are $p = 8^3, r = 50\%$.

Influence of the overcompleteness

In Figure 6.2 we present the reconstruction errors obtained for four tested redundancy values $q = 1, 2, 3, 4$. As can be seen, for any subsampling rate the increase of the number of dictionary elements generally improves the results, although this improvement becomes small when the dictionary is at least three times overcomplete.

Influence of the overlapping percentage

As shown in Figure 6.3, a high overlapping rate means that more patches y_p contribute to the reconstruction of the same patch, which leads to a lower statistical reconstruction error. However, having an overlapping rate that is too close to 1 is not favorable in terms

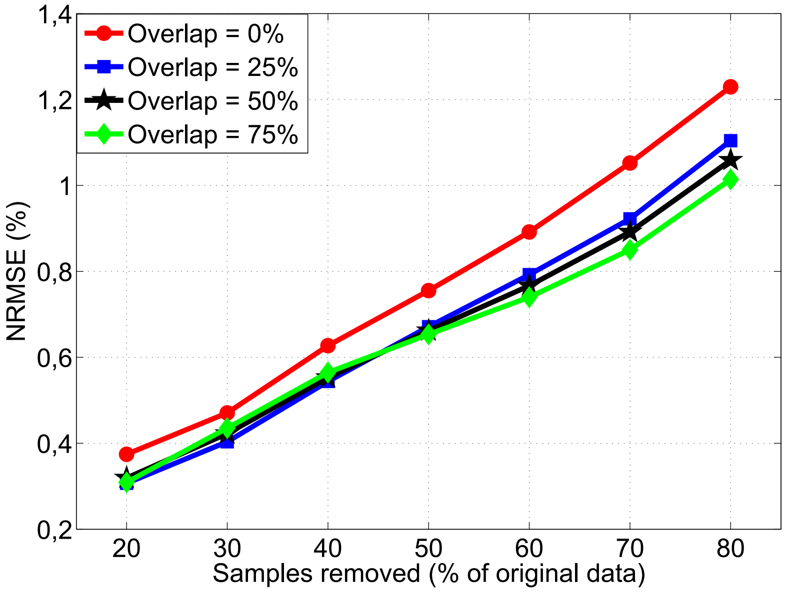

FIGURE 6.3 – Influence of the overlap percentage on the resulting NRMSE as a function of the number of removed samples using the sampling mask R_2. Other parameters are $p = 8^3, q = 4$.

of computational load : indeed increasing the overlap rate increases the number of patch reconstructions. Moreover, we can observe from Figure 6.3 that the improvement is very small when the overlap is larger than 25%.

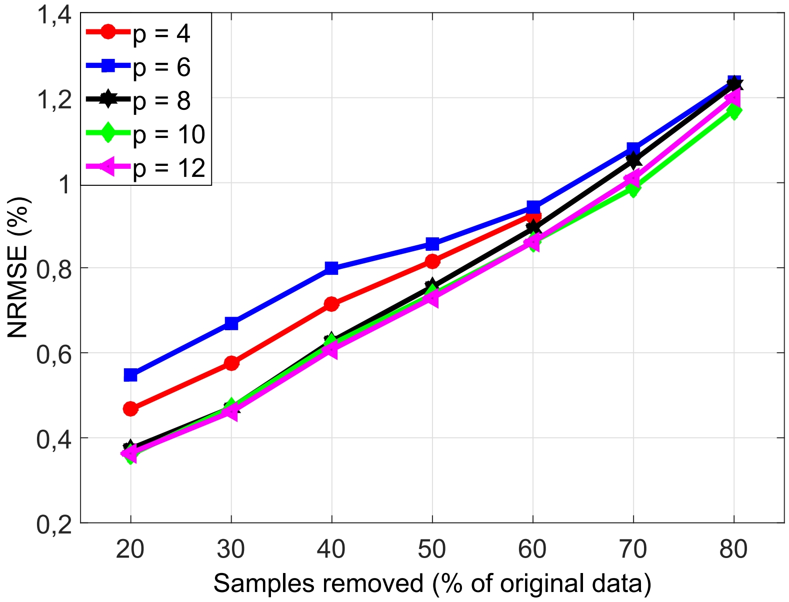

FIGURE 6.4 – Influence of the patch size n on the resulting NRMSE as a function of the number of removed samples using the sampling mask R_2. Other parameters are $q = 4, r = 0\%$.

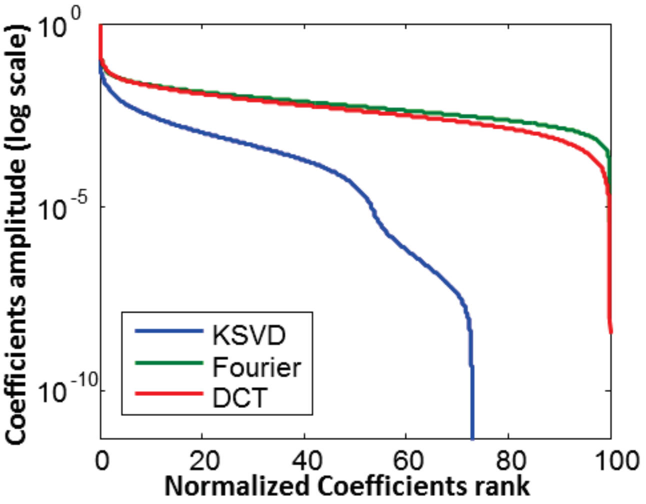

FIGURE 6.5 – Ordered relative values of the K-SVD dictionary, Fourier and DCT coefficients, for a 3D US simulation volume.

Influence of the patch size

Figure 6.4 shows the accuracy obtained for different patch sizes. Note that this experiment was made independent of the overlap factor by setting r=0% (i.e. no overlap) since the average that is introduced by the overlapping factor may bias the reconstruction error. We notice on Figure 6.4 that the reconstruction NRMSE is close for patches of size equal to or larger than 8, thus we might be tempted to choose a high patch size in order to reduce the number of total patch reconstructions. However, the higher the patch, the larger the reconstruction computational load. A patch size of 8 is the good compromise between a good NRMSE and a reasonable amount of computations.

6.2.3 Sparsity of 3D simulation US images

We extend here the assumption that 2D US data is sparse in a given basis Ψ to 3D US volumes. The concept of sparsity is illustrated by plotting the sparse coefficients in a given basis in order of magnitude. In Figure 6.5 we illustrate the concept of sparsity of 3D data in the domain of three transforms : K-SVD dictionary, Fourier basis and DCT. The sparse representation in the K-SVD dictionary decays the fastest in comparison to the other transforms,meaning that it is possible to have a higher quality reconstruction using this representation coefficients. While the coefficients in the Fourier and DCT representation start to slowly decay only from 80% of the total number of coefficients, the coefficients in the K-SVD dictionary decay fast from 50-60%. Given that the largest coefficients represent 70% of the total number of coefficients in the K-SVD dictionary, then this percentage of transform coefficient will be sufficient to get reliable reconstruction.

6.2.4 Comparison of simulation US data reconstruction results

Using the default parameters, we compare the reconstruction results that we obtain using the K-SVD dictionary with compressed sensing reconstructions using the Fourier basis and the DCT. This comparison is performed for the two proposed sampling patterns R_1 and R_2. Figure 6.6 shows the reconstruction NRMSE error as a function of the subsampling rate and for each of the transforms used for reconstruction and using the sampling patterns R_1 and R_2. It can be observed that the error increases with the number of removed samples, for every transform and whatever the sampling pattern. The error corresponding to the DCT takes the largest values, and the distance between the error curves corresponding to each transform is relatively constant. The K-SVD dictionary clearly gives the smallest error, whatever the subsampling rate and performs particularly well for high subsampling rates. We note that for any transform, the reconstruction error associated with the line-wise sampling pattern R_2 is close and slightly larger than the error obtained with the point-wise subsampling scheme R_1, which is from a theoretical point of view the most incoherent with the representation basis/dictionary. This is interesting since it shows that CS acquisition of 3D data is feasible in a relatively simple setting. Overall, these results show that the default parameters previously chosen for the K-SVD dictionary perform well on simulated volumes.

Figure 6.7 shows the log-envelope images corresponding to the reconstructed non-log envelope 3D US volume in Polar and Cartesian coordinates. The reconstructions have been performed for the subsampling rates 50% and 80%, and allow to visually evaluate the significance of the NRMSE plotted in Figure 6.6. We focus our attention on the sampling mask R_2 since the sampling mask R_1 is of limited interest for US acquisitions. We do not show the results obtained with the DCT since they are similar to the ones obtained with the Fourier basis and the reconstruction error is higher. Figure 6.7(a) represents the original volume and the reconstruction at 50% and 80% subsampling in Polar coordinates and 6.7(b) in Cartesian coordinates. It can be observed that the K-SVD CS reconstruction provides the best results using 50% of the initial data while with the Fourier CS reconstruction the missing sample lines can be observed on the reconstructions. Even though the reconstruction produced by the K-SVD dictionary using a 80% subsampling rate are better than with the Fourier basis, the results deteriorate and the missing sample lines can be seen on the reconstructions. In the case of the Fourier reconstruction the missing lines are clear distinguishable in both Polar or Cartesian coordinates while for the K-SVD reconstruction we can see the effect of the reconstruction only on the 80% subsampling case.

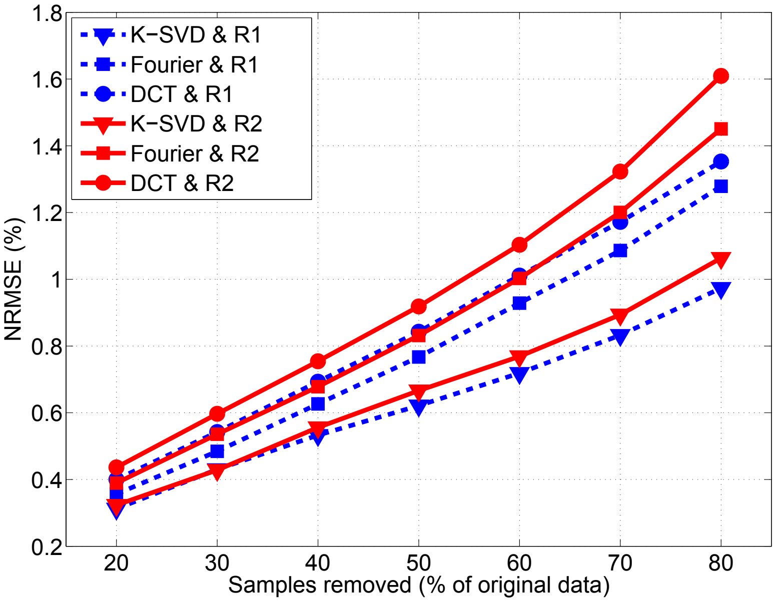

FIGURE 6.6 – NRMSE as a function of the number of removed samples using the sampling mask R_1 and R_2. The error is computed on the envelope of the 3D US volume after CS reconstruction using K-SVD dictionary, Fourier basis and DCT.

6.2.5 Speckle reconstruction

We evaluated the speckle reconstruction characteristics by considering all $8 \times 8 \times 8$ distinct patches contained in the simulated 3D US volumes and line-wise random subsampling scheme R_2. The correlation coefficient between the reconstructed patches and the initial patches was then measured. Figure 6.8 below shows the distribution of the correlation coefficient for all the patches of the 3D volumes for a reconstruction performed at 50% subsampling rate. We notice that, in the case of the K-SVD reconstruction, the correlation between initial patches and reconstructed patches is high except in seven localized, regularly spaced areas where this correlation is much lower. After further investigation we found that these regions correspond to the corners of the volume where there are no scatterers (i.e. no scatterers were placed in these regions in the no simulation setup), and thus only reconstruction noise is present. On the other hand, the CS Fourier reconstruction gives much lower correlations, with most values comprised between 0.8 and 0.2.

Figure 6.9 provides a more global perspective on the results, by showing the mean and variance of the correlation as a function of the subsampling rate, for Fourier and KSVD-based reconstructions. It may be observed that from 20% to 50% subsampling the correlation using the KSVD dictionary CS reconstruction is high (ranging from 1 to 0.9) whereas it decreases to 0.8 for a sampling rate of 80%. On the opposite, Fourier-based reconstruction gives lower correlation values, from 0.6 to 0.3 with a higher variance.

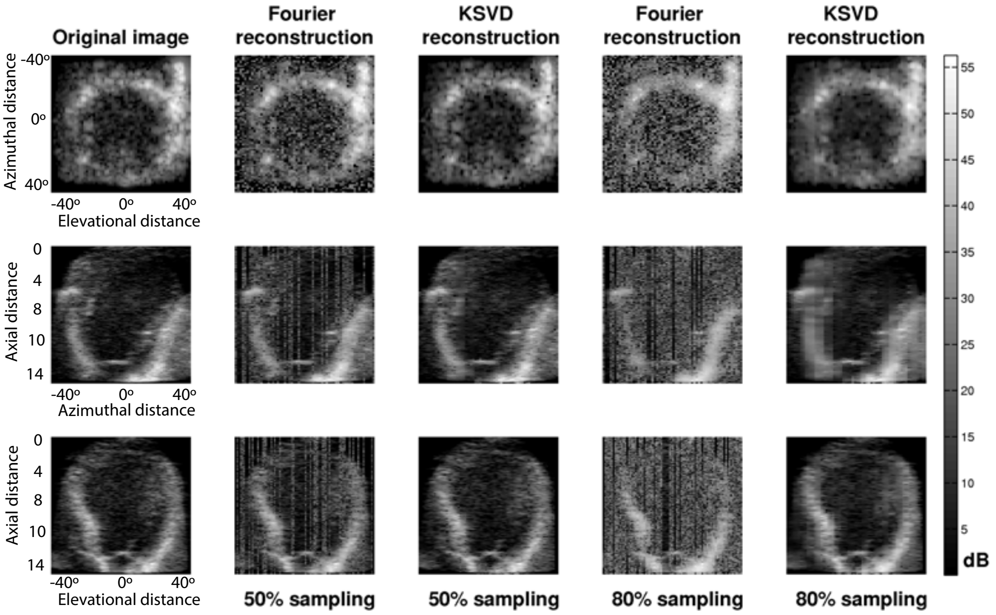

(a) Polar coordinates

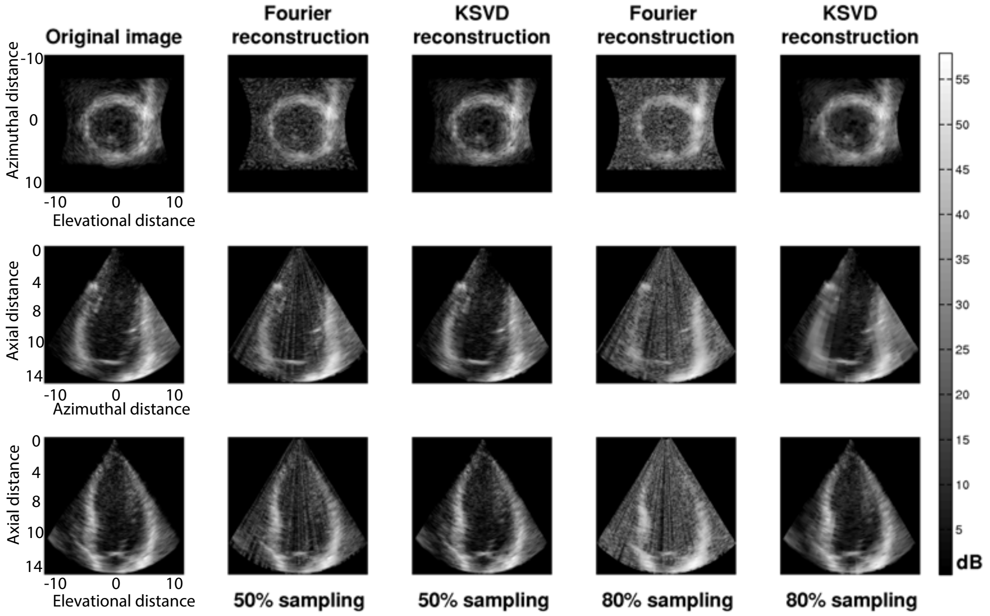

(b) Cartesian coordinates

FIGURE 6.7 – Visualization of 3D CS reconstructions of a simulated US volume using the sampling mask R2 in (a) Polar coordinates and (b) Cartesian coordinates. Original data, Fourier based reconstruction using a 50% subsampling rate, K-SVD based reconstruction using a 50% subsampling rate, Fourier based reconstruction using a 80% subsampling rate and K-SVD based reconstruction using a 80% subsampling rate.

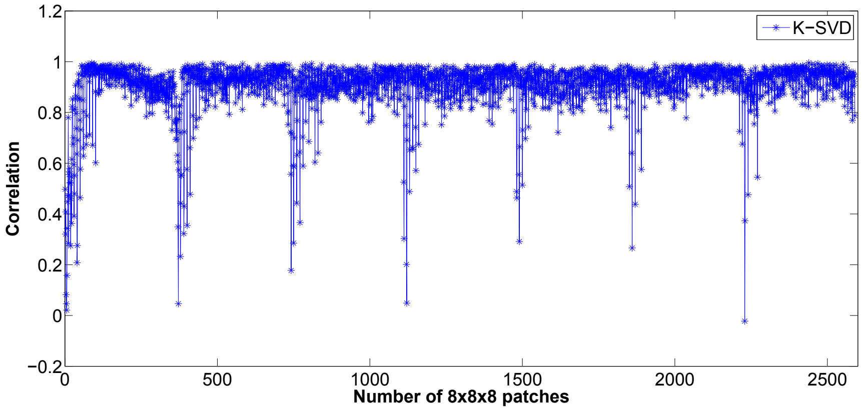

(a)

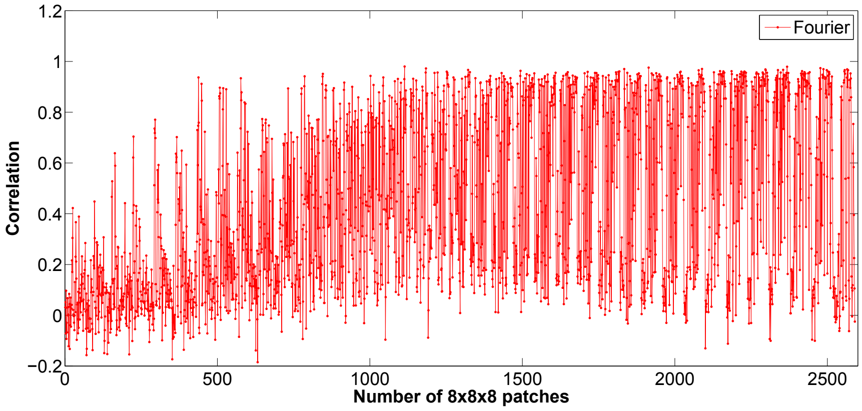

(b)

FIGURE 6.8 – Correlation as a function of the patch number between original volume and the (a) CS KSVD reconstruction and the (b) CS Fourier reconstruction at 50% subsampling using the line-wise R_2 scheme.

6.3 *Ex vivo* experimental results

6.3.1 *Ex vivo* experimental acquisition setup

For the acquisition of the volumes we use the Ultrasonix MDP research platform equipped with the 4DC7-3/40 Convex 4D transducer. Using this imaging system we imaged the following *ex vivo* organs purchased from the store : 3 pig brains, 3 sheep hearts and 2 sheep kidneys. The central frequency of the probe was of 5 MHz for the 3 organs and the signals were collected using a 40 MHz sampling rate. The transmitted beams, as well as the received signals, were focused at 56 mm depth. The field of view (FOV) varied between 55 and 65 degrees. For each organ we acquired the non-log envelope. As previously, we only use the non-log envelope volumes to perform the CS reconstruction.

The acquired images consisted of 128×47 beamlines (azimuthal and elevational direction) for the brains, 96×43 beamlines for the hearts and 96×41 for the kidneys. The

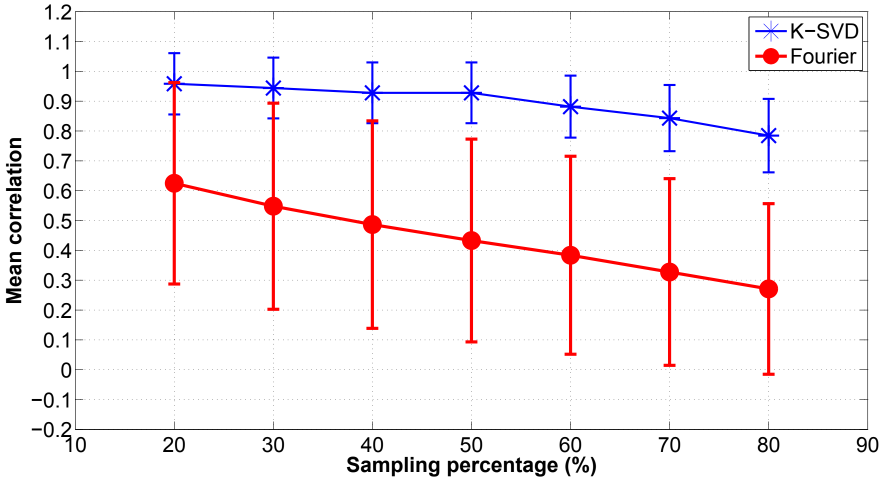

FIGURE 6.9 – Mean correlation and standard deviation between the original volume and the KSVD or Fourier reconstruction at different subsampling rates line-wise R_2 scheme.

number of samples in the axial direction was 1792, 2304 and 1792 samples respectively. After non-log envelope calculation the final data sets were downsampled at 5 MHz and consisted of $128 \times 47 \times 224$, $96 \times 43 \times 288$ and $96 \times 41 \times 224$ voxels for the brains, hearts and kidneys respectively.

6.3.2 *Ex vivo* reconstruction results using organ-dependent dictionaries

Ex vivo US images reconstruction

The CS reconstruction using organ-specific dictionaries was tested on sets composed of US acquisitions of two different organs : *ex vivo* brain and heart. The training and testing data consisted of different acquisitions of the same kind of organ. According to the reconstruction scheme and the previously chosen default parameters the training data was composed of patches extracted from the volumes belonging to the training dataset.

The training data consisted of $8 \times 8 \times 8$ patches extracted from the volumes belonging to the training dataset. We use typical values for the algorithm parameters : patch dimension $p = 512$ (i.e. 8^3) ; overlap of patches $r = 50\%$ and overcompleteness of $q = 4p$ (i.e. $K = 4 \times 512$). For both organs the training sets were composed of random patches extracted from two acquired volumes of two distinct brains or hearts and the testing data corresponded to the acquisition of a third brain or heart. The testing data consisted in both cases of approximatively 20000 patches, that is 70% of the total number of patches. Appendix A shows how the percentage of subsampling rates relates to the Nyquist sampling for the experimental dataset.

Figures 6.10.(a) and 6.10.(b) show the reconstruction NRMSE errors as a function of the number of removed samples using the sampling masks R_1 and R_2 for the *ex vivo* brain and heart US volumes. In both cases, the errors increase with the number of samples removed for all the reconstruction transforms. The DCT always gives the highest reconstruction error, closely followed by the Fourier basis. The values of the NRMSE of these two transforms are relatively close : in the case of the random subsampling scheme R_1 the mean difference is of 0.23×10^{-2} and 0.22×10^{-2} and in the case of the line-wise subsampling R_2 of 0.27×10^{-2} and 0.2×10^{-2} for the brain and respectively heart reconstruction.

The K-SVD dictionary gives the smallest error, whatever the subsampling rate. The difference, in terms of NRMSE error between the CS reconstruction using the Fourier basis and the K-SVD dictionary is in the range $[0.26 - 1.4] \times 10^{-2}$ for R_1 and $[0.35 - 2.2] \times 10^{-2}$ for R_2 for both organs. It is interesting to notice that the error of reconstruction using the K-SVD dictionary and a line-wise sampling mask R_2 is smaller than the error obtained with the Fourier basis and random subsampling scheme R_1, which is from a theoretical point of view the most incoherent.

The results obtained for the two organs are close and the curves exhibit the same tendencies. The differences between the K-SVD CS reconstructions of the two different organs are in the range $[0.25 - 0.49] \times 10^{-2}$ for the R_1 subsampling and $[0.34 - 0.42] \times 10^{-4}$ for the R_2 subsampling. This indicates that the dictionary performs as well for different organs with organ-specific dictionaries.

Figures 6.11 and 6.12 show the log-envelope images corresponding to the reconstructed non-log envelope 3D US volume of the *ex vivo* brain and heart in Polar and Cartesian coordinates., for better visibility. We show only one axial-azimuthal slice on which we can better see the effects of the sampling and the quality of the reconstruction. We do not show the results obtained with the DCT since they are similar to the ones obtained with the Fourier basis. The left image represents the original data before subsampling and reconstruction, followed by the Fourier and K-SVD CS reconstruction at 50% and 80% subsampling rates.

Overall we notice that the CS method provided good reconstructions of the whole volume except in the case of the 80% subsampling where we can clearly start to see the missing RF samples and lines, particularly in the case of the Fourier-based reconstruction. At 50% subsampling, CS with the K-SVD dictionary reconstructs better the fine details such as the walls of the chambers in the heart and the speckle pattern. At 80% subsampling, even though the reconstruction produced by the K-SVD dictionary are better than with the Fourier basis, the quality of the results is lower and the missing sample channels and artifacts due to the patch-wise reconstruction start to be seen.

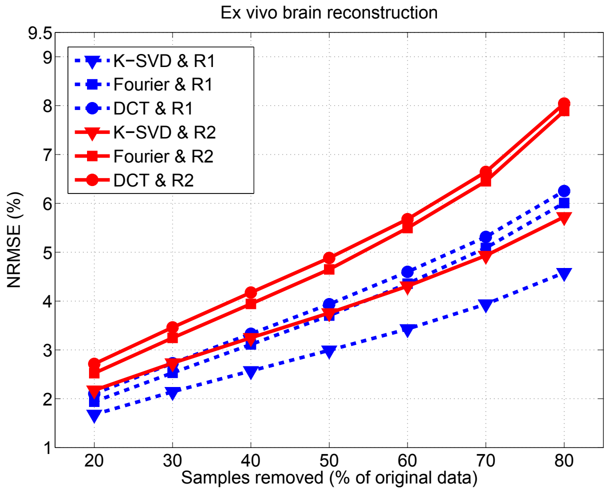

(a) *ex vivo* brain

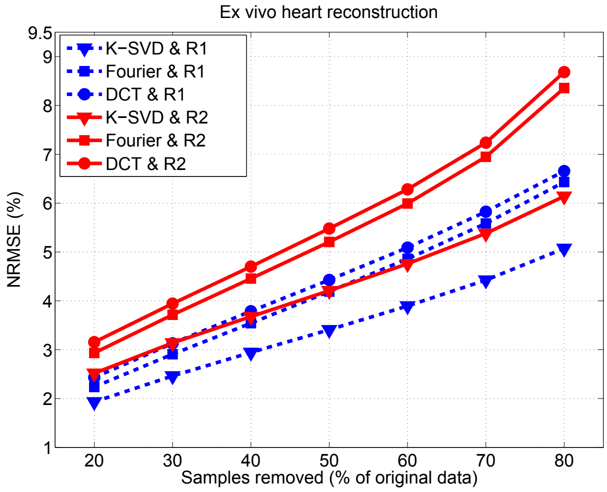

(b) *ex vivo* heart

FIGURE 6.10 – NRMSE as a function of the number of removed samples using the sampling masks R_1 and R_2. The error is computed for the CS reconstruction of the *ex vivo* : (a) brain and (b) heart using organ-dependent K-SVD dictionary, Fourier basis and DCT.

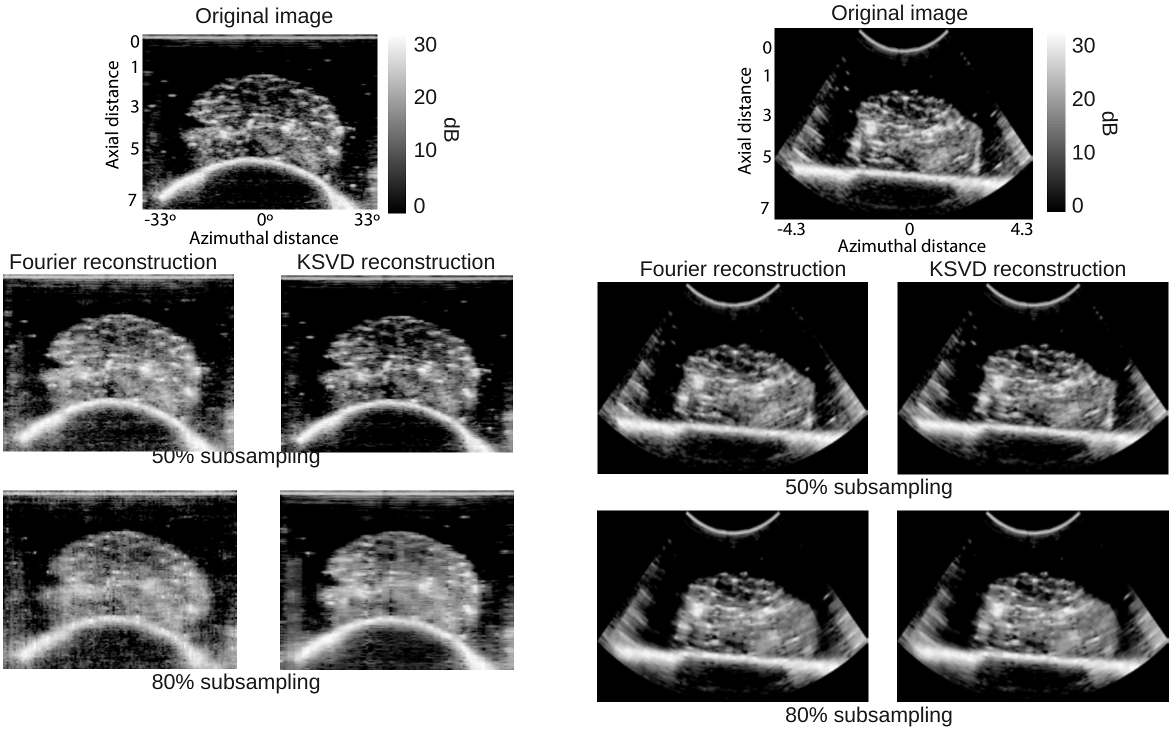

(a) Polar coordinates

(b) Cartesian coordinates

FIGURE 6.11 – Visualization of 3D CS reconstructions of an *ex vivo* brain US volume using the sampling mask R_2 in (a) Polar coordinates and (b) Cartesian coordinates. Reconstructions using the K-SVD dictionary for 50 and 80% subsampling rates.

6.3.3 Generality : Reconstruction results using a single dictionary

In order to test the generality of the CS reconstruction using an overcomplete dictionary learned with the K-SVD algorithm, we trained the dictionary on a set composed of US acquisitions of three different organs. The training data is thus composed of US volumes of two brains, two hearts and one kidney. The testing dataset is composed of one brain, one heart and one kidney that are not included in the training dataset. The dictionary learning parameters remain the same as previously and we focus our attention on the sampling mask R_2 since the sampling mask R_1 is of limited interest for US acquisitions and yields similar results.

Figure 6.13 shows the reconstruction error NRMSE for the beamformed non-log envelope images as a function of the subsampling rate, for each of the transforms used for reconstruction and for each of the reconstructed US organ volumes i.e. : brain, heart and kidney. We can notice that the results obtained for the three organs are very close and the curves exhibit the same tendencies. Interestingly, the differences between the reconstructions performed using the specific dictionaries of the previous section (Figures 6.10) and the ones performed using the general dictionaries are very small : in the range $[4.8-6.4]\times10^{-4}$ for the brain reconstruction and $[1.1-7.4]\times10^{-4}$ for the heart reconstruction. This indi-

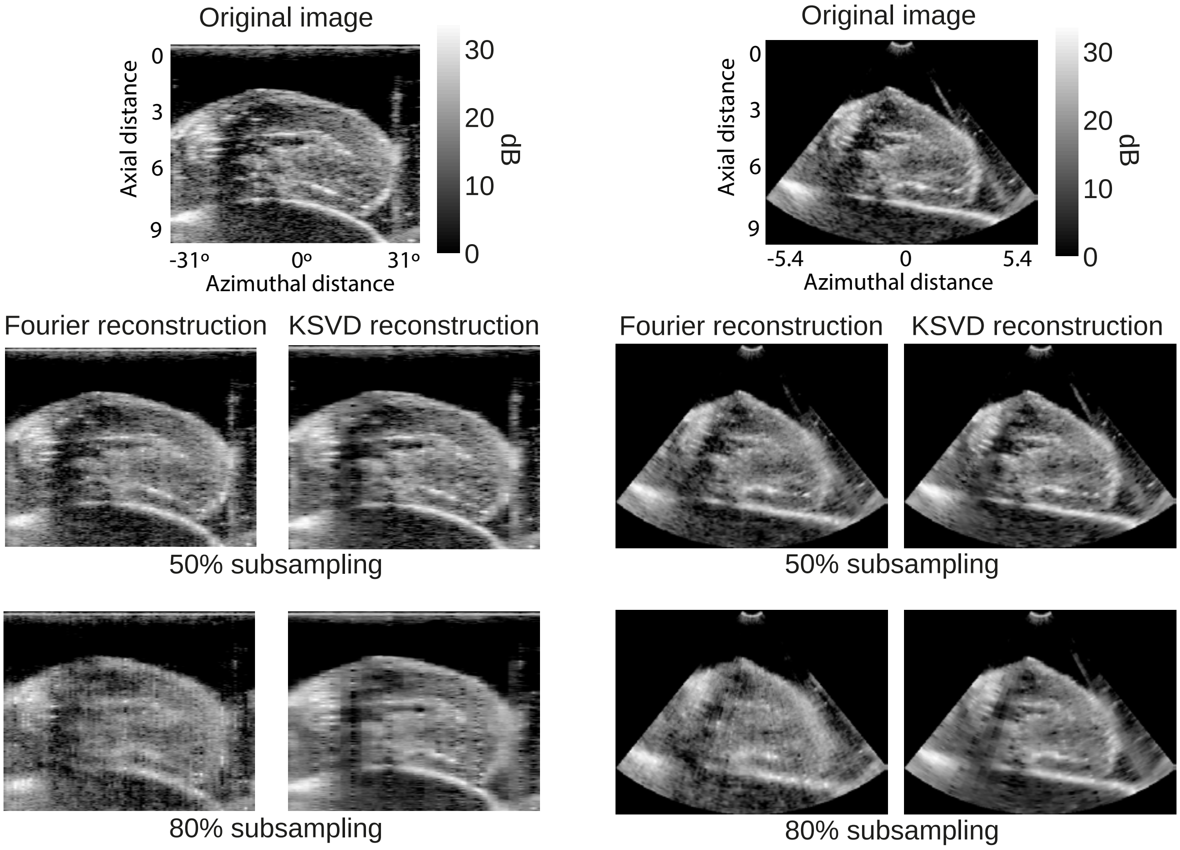

(a) Polar coordinates

(b) Cartesian coordinates

FIGURE 6.12 – Visualization of 3D CS reconstructions of an *ex vivo* heart US volume using the sampling mask R_2 in (a) Polar coordinates and (b) Cartesian coordinates. Reconstructions using the K-SVD dictionary for 50 and 80% subsampling rates.

cates that the general dictionary performs as well as the organ-specific dictionaries.

Figure 6.14 shows the log-envelope images corresponding to the reconstructed non-log envelope 3D US volume of the *ex vivo* kidney in Polar and Cartesian coordinates. We show only one axial-azimuthal slice on which we can see the effects of the sampling and the quality of the reconstruction. We do not show the results obtained with the DCT since they are similar to the ones obtained with the Fourier basis and the reconstruction error is higher. We do not show either the reconstructions of the *ex vivo* heart and brain since the results in terms of reconstruction errors are similar. The left image represents the original data before subsampling and reconstruction followed by the CS reconstruction using the K-SVD dictionary and the CS reconstruction using the Fourier basis at 50% and 80% subsampling.

The first observation to make is that for all the subsampling rates, the CS method provided good reconstructions of the whole volume except in the case of the 80% subsampling where we can clearly start to see the missing columns, particularly in the case of the Fourier-based reconstruction. It can be observed that the K-SVD CS reconstruction provides the best results, as previously, while with the Fourier CS reconstruction the missing sample lines can always be seen on the reconstructions. Even though the reconstruction produced by the K-SVD dictionary using 20% of the initial data are better than with the Fourier basis, the quality of the results decreases when removing more samples and the missing samples start to be visible on the reconstructions. At 50% subsampling CS with the dictionary reconstructs better the fine details such as the vessel ramifications in the kidney. At 80% subsampling, even though the reconstruction produced by the K-SVD dictionary are better than with the Fourier basis, the quality of the results is lower and the missing sample channels start to be seen on the reconstructions. At such subsampling rate, the CS reconstruction with the Fourier basis loses almost completely the fine details and the resulting image is much deteriorated while with the K-SVD these structures are still preserved.

Overall we observe that the reconstructions performed with experimental data are consistently worse than with the simulated data. In terms of NRMSE the error is indeed five times higher in the case of the experimental volumes. This is easily explained by the quality of the original samples. The comparison of Figure 6.7 (simulated data) and the Figures 6.14 (experimental data) shows clear differences : the simulated images have a better resolution and less speckle regions than the experimental volumes.

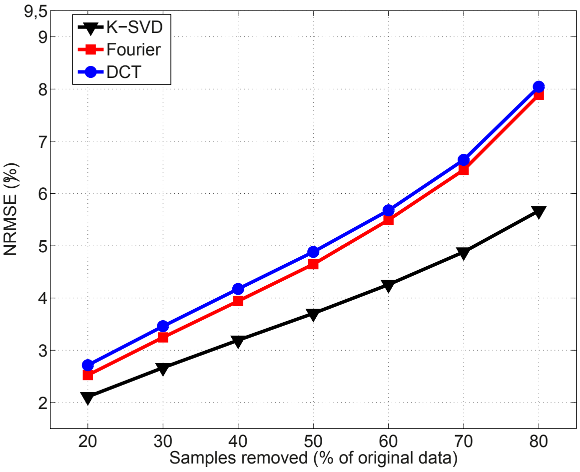

(a) brain

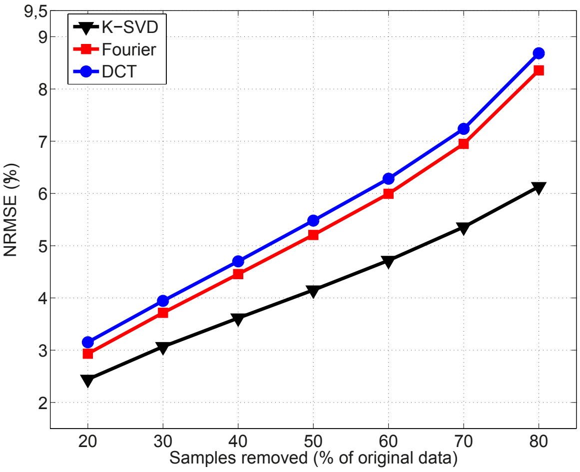

(b) heart

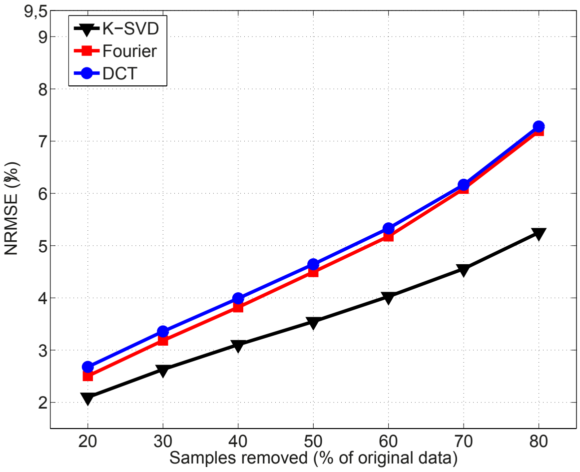

(c) kidney

FIGURE 6.13 – NRMSE as a function of the number of removed samples using the line-wise sampling mask R_2. The error is computed for the CS using the general K-SVD dictionary, Fourier basis and DCT for the CS reconstruction of : (a) brain, (b) heart and (c) kidney.

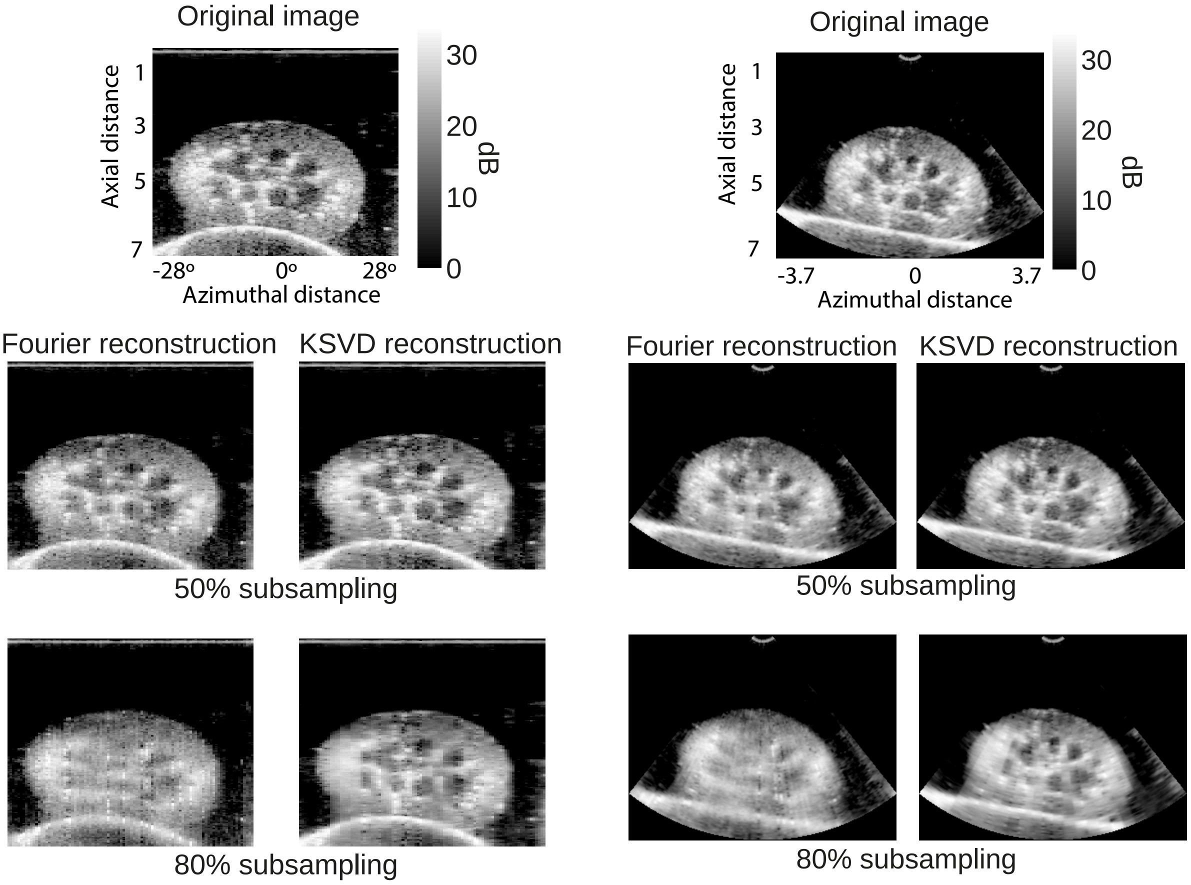

(a) Polar coordinates

(b) Cartesian coordinates

FIGURE 6.14 – Visualization of 3D CS reconstructions of an *ex vivo* kidney US volume using the sampling mask R_2 in (a) Polar coordinates and (b) Cartesian coordinates. Reconstructions using the K-SVD dictionary for 50 and 80% subsampling rates.

6.3.4 Speckle reconstruction

We evaluated the speckle reconstruction characteristics by measuring the correlation coefficient between the initial and reconstructed patches of all $8 \times 8 \times 8$ distinct patches contained in the *ex vivo* kidney US volumes and the line-wise random subsampling R_2 scheme. Figure 6.15 shows the distribution of the correlation coefficients for all the patches reconstructed with the K-SVD dictionary and the Fourier basis at a subsampling rate of 50%. Compared to the correlations found for the simulation US reconstruction in Figure 6.8, the CS K-SVD reconstruction gives slightly lower correlation values and has a particular region that is affected in terms of correlation situated between the 300th and 400th patch. The speckle reconstruction correlations obtained with the K-SVD dictionary are still higher than with the Fourier basis. The CS Fourier reconstruction gives much lower correlations, with most values comprised between 1 and 0.4 and with a quite large region where they get close to 0 correlation, whereas with the K-SVD reconstruction most correlation values situate between 1 and 0.6.

Figure 6.16 shows the mean and variance of the correlation as a function of the subsam-

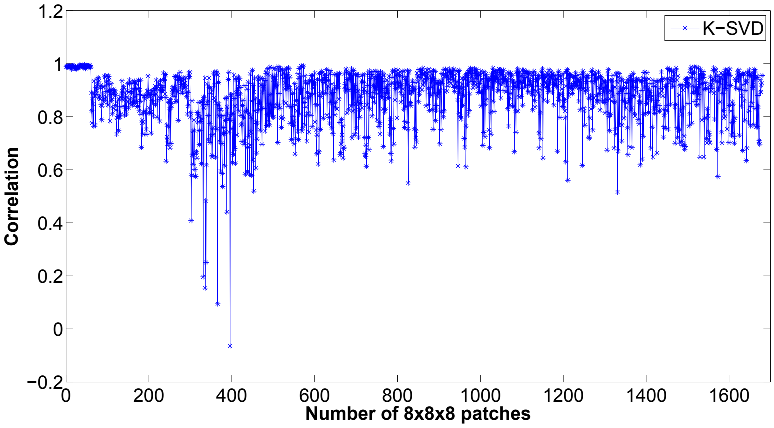

(a)

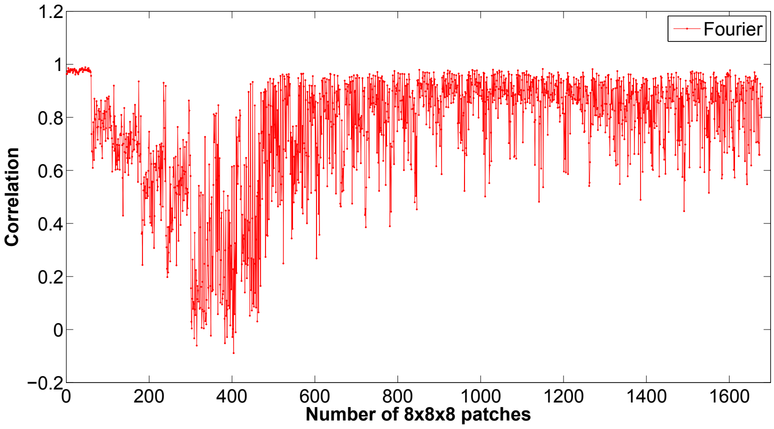

(b)

FIGURE 6.15 – Correlation as a function of the patch number between original volume and the (a) CS KSVD reconstruction and the (b) CS Fourier reconstruction at 50% subsampling.

pling rate, for Fourier and KSVD-based reconstructions. We can observe that the K-SVD dictionary always provides a higher correlation than the reconstructions using the Fourier basis. Up to 40% subsampling the correlation with K-SVD is is high (ranging from 1 to 0.9) and it degrades down to 0.75 for a 80% subsampling. The Fourier-based reconstruction gives a good correlation at 20% subsampling but rapidly deteriorates, decreasing to 0.55 at 80% subsampling. It is also interesting to notice that the correlations obtained with the dictionary give variances two times lower than with the Fourier basis.

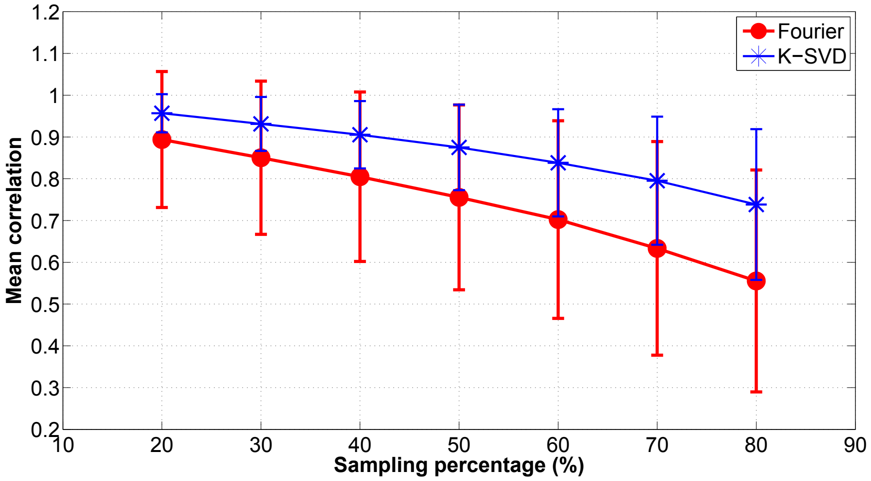

FIGURE 6.16 – Mean correlation and variance between the original volume and the KSVD or Fourier reconstruction at different subsampling rates.

6.4 *In vivo* experimental results

6.4.1 *In vivo* experimental acquisition setup

For the acquisition of the volumes we use the Ultrasonix MDP research platform equipped with the 4DC7-3/40 Convex 4D transducer. Using this imaging system we imaged the liver and the kidney of two healthy subjects. All subjects provided written informed consent. The central frequency of the probe was of 4 MHz for all the acquisitions. The transmitted beams, as well as the received signals, were focused at 76 mm depth. Other parameters of the probe were : field of view (FOV) = 45 degrees, frame rate = 2 Hz and gain = 50% for all the acquisitions. For each subject and organ we acquired the non-log envelope. As previously, we only use the non-log envelope volumes to perform the CS reconstruction. After non-log envelope calculation and down-sampling, the final data sets were sampled at 5MHz and consisted of volumes of 33 × 128 × 512 voxels.

6.4.2 *In vivo* reconstruction results non organ-dependent dictionaries

The CS reconstruction of *in vivo* US organs was tested in a general context using the dictionary described in the previous section, i.e. learned from a set of 3 different *ex vivo* animal organs (two brains, two hearts and one kidney). The testing dataset is composed of one liver and one kidney that were acquired *in vivo*. We focus our attention on the sampling mask R_2 and on the Fourier basis, used as a reference.

Figure 9.12 shows the reconstruction error NRMSE for the non-log envelope images as a function of the subsampling rate, for each of the transforms used for reconstruction and for each of the reconstructed US organ volumes i.e. liver and kidney. We can notice that the results obtained for the two organs are very close and the curves exhibit the same tendencies. The differences between the reconstructions performed using the same dictionary for the reconstruction of *ex vivo* volumes (Figure 6.13) and the ones performed on *in vivo* US volumes are very small : in the range $[4.5 - 7.6] \times 10^{-3}$ for the kidney reconstruction. This indicates that the general dictionary performs well for both *ex vivo* or *in vivo* 3D acquisitions.

Figure 6.18 shows the log-envelope images corresponding to the reconstructed non-log envelope 3D US volume of an *in vivo* liver, in Polar and Cartesian coordinates for better visibility. We show only one axial-azimuthal slice on which we can see the effects of the sampling and the quality of the reconstruction. We do not show the results obtained with the DCT since they are similar to the ones obtained with the Fourier basis and the reconstruction error is higher. The left image represents the original data before subsampling and reconstruction followed by the CS reconstruction using the *ex vivo* K-SVD dictionary and the CS reconstruction using the Fourier basis at 50% and 80% subsampling. We observe that we do not see anymore the subsampled beamlines on the reconstruction. The Fourier reconstruction still has visually a poorer quality than the K-SVD reconstruction, the images are covered with noise and the finer details are lost. At 50% subsampling, CS using the dictionary gives satisfying results and both small and big structures are preserved. At 80% subsampling, even though the reconstruction produced by the K-SVD dictionary is better than with the Fourier basis, the quality of the results is lower and some regions are deteriorated.

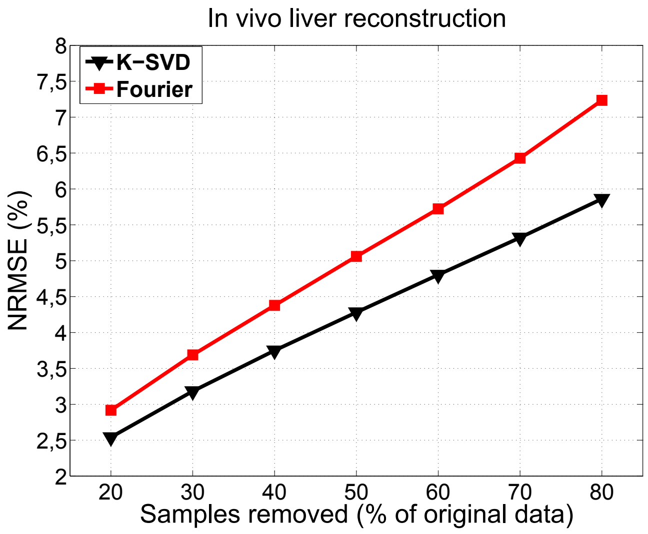

(a) liver

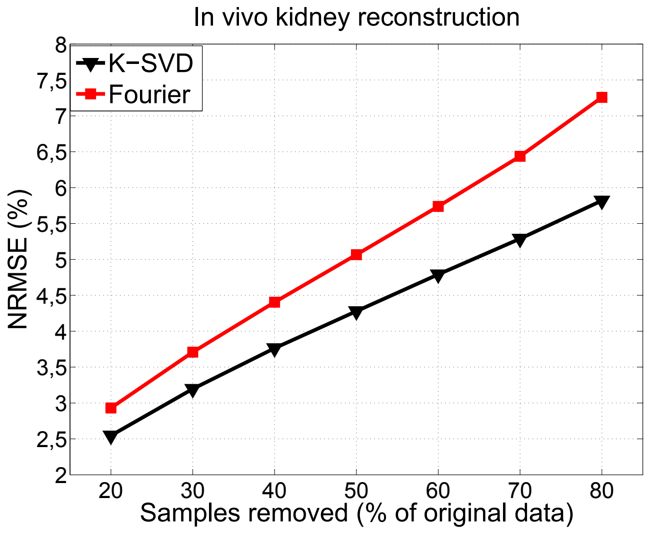

(b) kidney

FIGURE 6.17 – NRMSE as a function of the number of removed samples using the line-wise sampling mask R_2. The error is computed for the CS using the general K-SVD dictionary and the Fourier basis for the CS reconstruction of : (a) liver and (b) kidney.

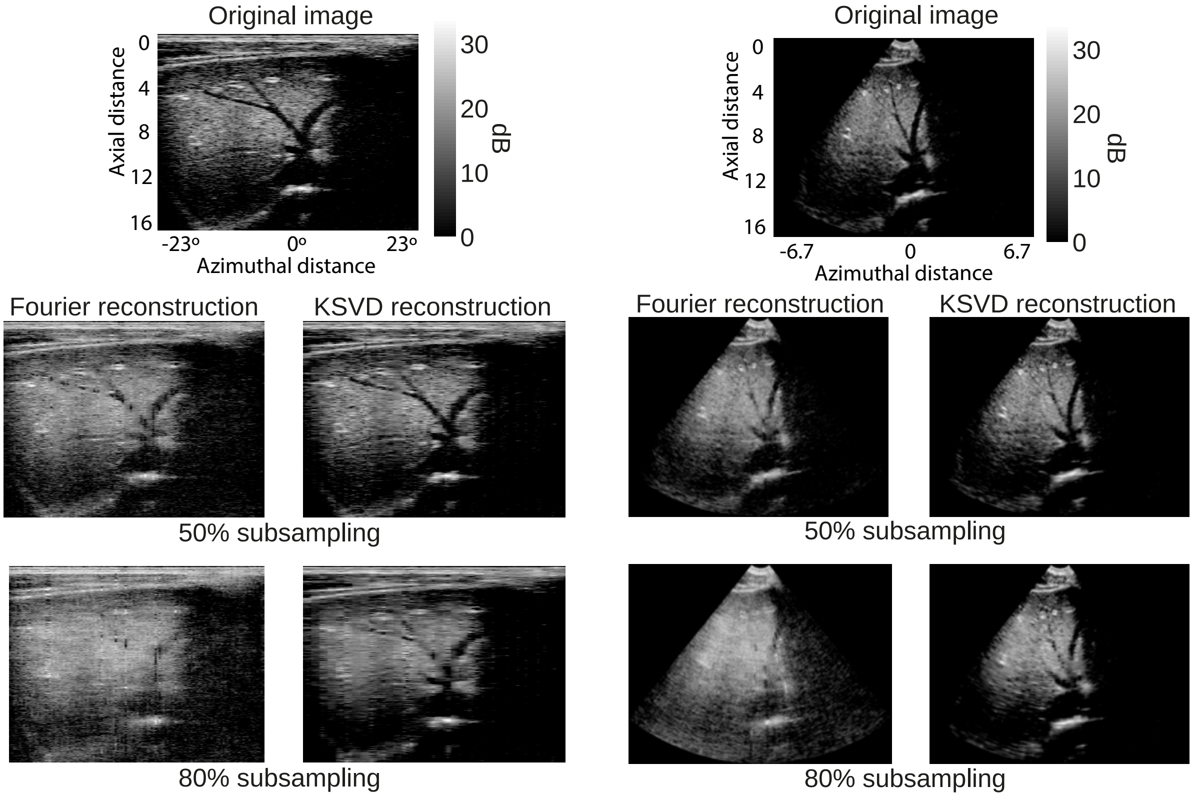

(a) Polar coordinates

(b) Cartesian coordinates

FIGURE 6.18 – Visualization of 3D CS reconstructions of an *in vivo* liver US volume using the sampling mask R_2. Reconstructions using the K-SVD dictionary for 50 and 80% subsampling rates.

Chapitre 7

Conclusion and perspectives

This study demonstrates that the CS theory using overcomplete learned dictionaries can be applied to 3D ultrasound imaging to reduce the volume of data needed for the reconstruction and speed up the acquisitions. We showed in particular that the learned dictionary approach yields lower errors (NRMSE) than conventional sparsifying dictionaries based on fixed transforms such as Fourier or discrete cosine, meaning that the US images have a sparser representation in learned dictionaries. Experiments performed on simulated and experimental 3D US volumes with the K-SVD based CS reconstruction using a subsampling rate up to 60% resulted in US volumes close to the original, with minimal loss of information and seem to confirm our sparsity hypothesis.

In addition, a sampling protocol suited to US imaging was proposed here by randomly subsampling full RF lines. The obtained results using this line-wise sampling strategy showed that we can recover 3D ultrasound signals of high quality using only 60% of the initial data. This shows in particular that although not fully uniform, the line-wise sampling yields results with an accuracy comparable to the conventional point-wise random subsampling. This indicates that CS acquisition of 3D data is thus feasible in practice in a relatively simple setting.

Finally, we evaluated the generality of the learned overcomplete dictionary by training it on 3D US volumes of different *ex vivo* and *in vivo* organs. This approach showed that the dictionary is not hampered by overlearning and provides satisfying reconstructions for images coming from different organs. The difference between the reconstruction error obtained with a specific dictionary and the one obtained with the general dictionary is minimal (on the order of 10^{-4}).

In this contribution we showed the powerful potential of CS to reduce data volume and speed up acquisitions with the proposed sampling protocol. However, the learned dictionary cannot be represented as an implicit operator neither does it have an explicit inverse, then, since the sparse coefficients have to be decomposed in the learned dictionary by solving a minimization problem, the overall computational time is highly increased. Considering that the dictionary is learned in advance, using dedicated circuits (GPU type) for the CS reconstruction could allow a great improvement in processing times and overall increase the imaging rate, keeping the real-time nature of US imaging.

Future work will include an investigation of adaptive sparse learning routines providing on the fly dictionaries as well as an optimization of the processing and reconstruction times. Various applications will also be considered (3D imaging using matrix arrays and duplex ultrasonography (B-mode/Doppler)).

IV Contribution 2 : Compressed sensing in Doppler ultrasound using block sparse Bayesian learning

Chapitre 8

Compressed sensing in Doppler ultrasound

8.1 Introduction

In this chapter we focus on developing a framework for using duplex Doppler ultrasound systems. As explained in chapter 1.3.3, these type of systems need to interleave the acquisition and display of a B-mode image and of the pulsed Doppler spectrogram. Thus, a framework for alternating Doppler and US emissions is proposed here by using a CS based framework for randomly interleaving the two types of emissions. The proposed method reconstructs the Doppler signal segment by segment using the block sparse Bayesian learning (BSBL) algorithms (see chapter 2.4.2). It is worth emphasizing that the success of BSBL algorithms in this application clearly show their unique ability to exploit block-correlated signals and to recover non-sparse signals.

The remaining of this chapter is structured as follows. In section 8.2 we briefly review the state of art techniques used for alternating the two kinds of acquisitions. In section 9.1 we give in detail the framework of application of the standard CS and BSBL based reconstructions to Doppler signals. In section 9.2 we give the simulation results and discuss in particular the choice of all the parameters used by both methods. Our BSBL based method is compared to the method proposed in [Richy et al., 2013]. Finally, the experimental feasibility is presented in section 9.3.

8.2 State of the art of CS in Doppler imaging

As explained in section 1.3.3, duplex Doppler is an echographic mode that allows visualizing at the same time a B-mode image and the blood flow. In order to show the blood velocity in vessels, one point is selected on the B-mode image and the evolution of the velocity at the given point is shown as function of time on a pulsed Doppler spectrogram (also called pulsed wave (pw)-spectrogram). If both modes, B-mode imaging and pulsed Doppler spectrogram, need to be used in the same imaging sequence then the acquisition time must be shared between the two imaging systems and a strategy for alternating them is required.

The first possibility that can be considered is alternating the two kinds of acquisitions. However, this halves the pw-spectrogram pulse repetition frequency (PRF) and thus divides the maximum measurable velocity by two. Another possible approach is to regularly interrupt the Doppler emissions to acquire a full B-mode image. This gives pw-spectrogram with gaps in the signal. The methods by Kristoffersen and Angelsen [Kristoffersen and Angelsen, 1988] or Klebaek et al. [Klebaek et al., 1995] were proposed to fill in the gaps produced by the acquisition the US image. However these methods assume that the blood flow can be predicted or is stable, which is not true in the case of abrupt variations and leads to inaccurate estimations. The only studies that investigate the reconstruction of the missing samples in duplex ultrasound systems were developed by Jensen in [Jensen, 2006] and further investigated in [Mollenbach and Jensen, 2008]. The proposed technique is based on the use of filter banks to reconstruct the missing samples and was tested for regularly and randomly subsampled sequences.

In the context of the novel compressed sensing technique, described in detail in chapter 2, there are only few studies that treat the problem of duplex acquisitions [Zobly and Kakah, 2011, Zobly and Kadah, 2013, Richy et al., 2011, Richy et al., 2013]. Zobly et al. apply conventional basis pursuit in [Zobly and Kakah, 2011] and a multiple measurement vector (MMV) techniques in [Zobly and Kadah, 2013] to reconstruct the Doppler signal. However it is difficult to draw conclusions from these works to the extent that the sensing basis and the model basis (dictionary) are not specified.

In the recent studies [Richy et al., 2011, Richy et al., 2013], it has been shown shown that compressed sensing-based reconstruction of Doppler signal allowed reducing the number of Doppler emissions and yielded better results than traditional interpolation. The particularity of this work is the decomposition of the signal to be reconstructed in several segments of same length which reduces the computation times since the reconstruction algorithm is applied only to a reduced number of measurements. This method has been evaluated on both simulated and real sonograms. However, in this study the reduction of Doppler emission has to be limited to 60% in order to produce satisfying reconstruction (i.e. a PSNR $>$ 20 dB).

We thus propose here to improve over the study in [Richy et al., 2013] using the BSBL framework to reconstruct Doppler signals. Given the characteristics of the BSBL framework described in section 2.4.2, it seems that the Doppler signal provides the ideal conditions for applying this method. Indeed, BSBL exploits the intra-correlation structure within a signal. Knowing that the sequence of Doppler samples is provided by a continuous temporal evolution of a region of scatterers over a lapse of time, it seems reasonable to assume that Doppler samples will be correlated over a given time period, yielding the intra-correlation structure that is exploited by BSBL. Moreover, the results shown in [Richy et al., 2013] show that the Doppler signals are only moderately sparse. The BSBL framework is well-adapted to deal with this difficulty, since it is able to recover non-sparse true solutions to inverse problems with sufficiently small errors, as long as the entries in solution vectors or solution matrices are correlated.

As we will see in the sequel, the developed method reconstructs the Doppler signal segment by segment from data sets where flow and B-mode emissions are randomly interleaved. Each segment is reconstructed in the context of compressive sensing theory described in chapter 2 using the block sparse Bayesian learning framework described in section 2.4.2.

Chapitre 9

CS Doppler ultrasound reconstruction using block sparse Bayesian learning

9.1 Application of the BSBL framework to Doppler signals

9.1.1 Acquisition and reconstruction scheme

The principle of the method developed here is based of the acquisition of a sparse sequence of sub-sampled data in order to alternate the Doppler and B-mode emissions. We remind here that the type of ultrasound pulses that are sent out by the probe when B-modeimaging is done is different from the one sent out for flow imaging. The pulsed Doppler spectrogram is obtained by selectiong one point in the B-mode image and showing the evolution of the velocity at that given depth as a function of time. The original Doppler signal is denoted by $x \in \mathbb{C}^n$. CS reconstruction was performed on a fully sampled dataset that we samples randomly much below the conventional sampling rate. The subsampling rate, r, is the ratio of the number of kept Doppler samples to the total number of samples, n. The time saved by ignoring the other samples is used for B-mode imaging. The Doppler signal is supposed to be available in real time, which leads us to a segment-by-segment reconstruction strategy, whose principle is summarized in Figure 9.1. The segments extracted from the signal may be overlapping with an overlap rate r and are of size p.

Let x_i of $\mathbb{R}^p, p \ll n$, be a segment of the Doppler signal to be reconstructed and Ψ of $\mathbb{R}^{p \times p}$ be the sparsifying transform. For this segment the CS formulation writes $x_i = \Psi v_i$ where v_i thus contains the coefficients of the expansion of x_i in Ψ.

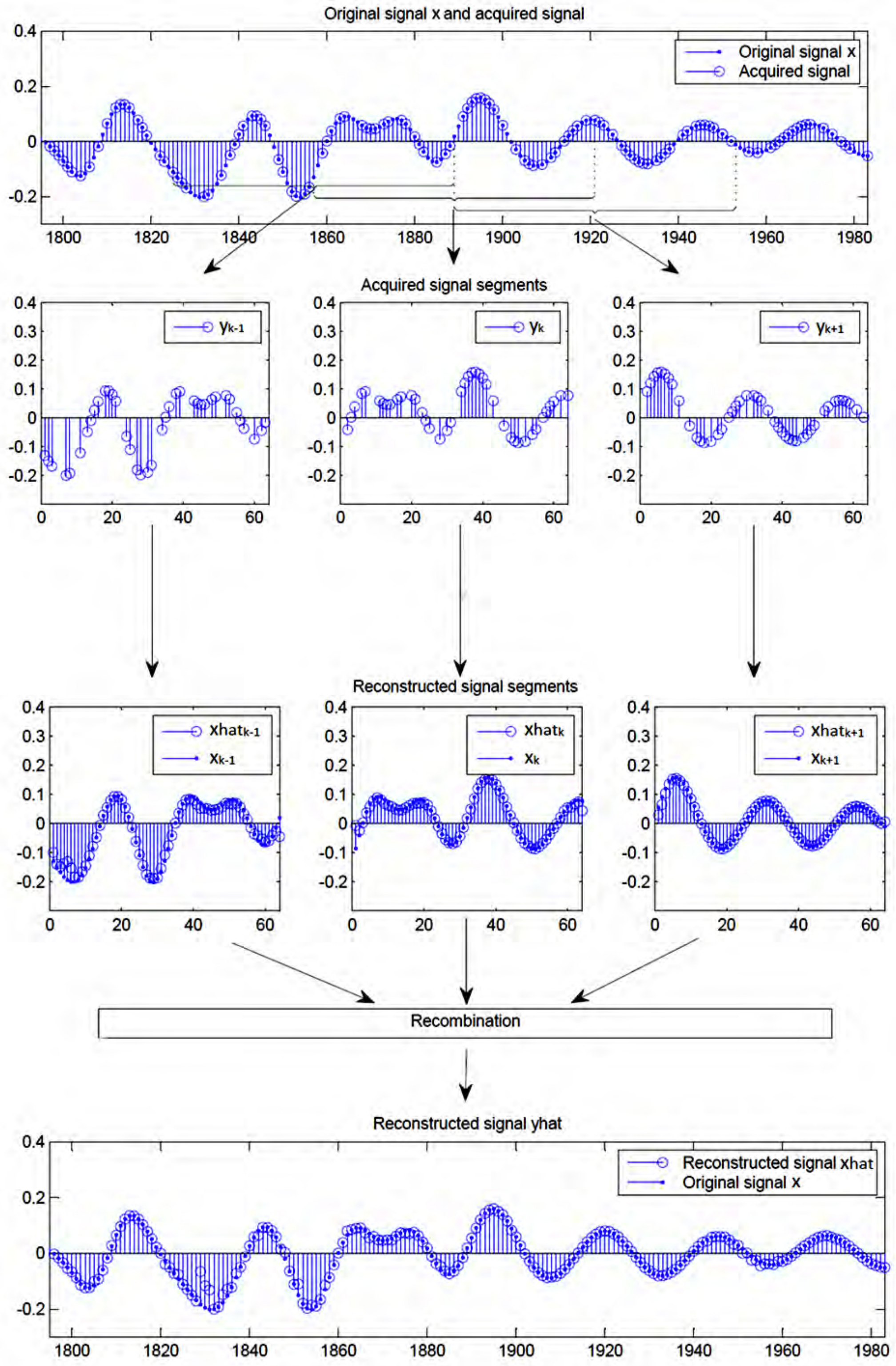

FIGURE 9.1 – Principle of the method. Modified with permission from [Richy et al., 2013].

Classical CS reconstruction applied to Doppler signals

The data acquisition in Doppler as in US imaging is performed in the direct space so the acquisition basis Φ is the Dirac basis and the sample selection is done randomly. From here, we can rewrite the classical CS algorithms to reconstruct each segment x_i from the linear measurements y_i of $\mathbb{R}^m$:

$$\begin{aligned} &\hat{v}_i = arg \min_{v_i \in \mathbb{R}^p} \|v_i\|_1 \quad \text{subject to} \quad \|y_i - R\Phi\Psi v_i\|_2 \leq \varepsilon \\ &\hat{x}_i = \Psi \hat{v}_i \end{aligned} \tag{9.1}$$

After reconstructing all the $\hat{x}_i$, the segments are recombined by shifting and summing in order to get the full Doppler signal $\hat{x}$, see Figure 9.1.

The CS reconstruction method considered in [Richy et al., 2013] and based on a classical basis pursuit approach is used here as a reference to compare with. The reconstruction is applied segment by segment to Doppler measurements and the calculation of each $\hat{x}_i$ by solving (9.1) is carried out by an iterative algorithm taken from YALL1, a solver developed by Zhang et al. [Yang and Zhang, 2011a, Yang and Zhang, 2011b] based on the alternating direction method and described in section 2.3.2.

BSBL framework applied to Doppler signals

The above sparse reconstruction scheme can be reformulated as an estimation problem solved in a Bayesian framework. If we reformulate the CS problem given in (9.1) and assuming that the noise ϵ is approximated by an additive Gaussian noise with a zero mean and unknown variance σ^2, the quantities that remain to be estimated based on the measurements segments are the sparse coefficients v_i and the noise variance σ^2. Thus, the associated Gaussian likelihood model is given by :

$$p(y_i|v_i, \sigma^2) = (\pi\sigma^2)^{-p} \exp(-\frac{1}{\sigma^2} \|y_i - R\Phi\Psi v_i\|_2^2) \tag{9.2}$$

The coefficients corresponding to each reconstructed segment $\hat{v}_i$ are estimated using the BSBL framework described in section 2.4.2 and the corresponding segment $\hat{x}_i$ is obtained from $\hat{x}_i = \Psi \hat{v}_i$. The full Doppler signal $\hat{x}$ is reconstructed according to Figure 9.1.

9.1.2 Reconstruction bases

As explained in section 2, the choice of the representation and sensing domains is decisive for the efficiency of CS signal recovery. In ultrasound and Doppler imaging, the signal is acquired in the direct domain, which means that $\Phi = I$. As for the sparsity domain Ψ, we consider several transforms for the classical CS reconstruction framework described above. In this study, we have selected two bases for this comparison : the first is the Fourier basis (i.e. standard DFT), since it is maximally incoherent with the sensing Dirac basis, it is fast to compute and it has been shown to provide reasonable results. The second basis is represented by the directional wave atoms, which were recently introduced by Demanet and Ying [Demanet and Ying, 2007] and used for comparison with [Richy et al., 2013]. Let us note that, directional wave atoms do not form a basis but a tight Parseval frame with redundancy two.

In the case of the BSBL framework we only focus on the Fourier basis for the transformation basis of the Doppler signals.

9.1.3 Reconstruction quality evaluation

To measure the quality of the reconstructions for a given parameter set, we use the average PSNR, defined as

$$\text{PSNR} = 10 \log_{10} \frac{\max \hat{x}^2}{MSE} \tag{9.3}$$

where MSE is the mean-squared error calculated using the following equation : $MSE = \frac{\sum_i (x_i - \hat{x}_i)^2}{p}$.

Pw-spectrograms of the reconstructed signals are also used to evaluate qualitatively the results of the Doppler reconstruction. For a given parameter setting, if the number of repetitions (n_{rep}) of the reconstruction is higher than one, the reconstructed signal that is chosen among the n_{rep} results to compute the pw-spectrogram is the one that corresponds to the median PSNR.

9.2 Simulation results

In the following sections we explore how the performance of the BSBL algorithm with Doppler data is affected by various experimental factors.

9.2.1 Simulated Doppler data

Using the FIELD II program [Jensen and Svendsen, 1992], and the example given at [Jensen, 1996a] we simulated the blood flow in a femoral artery. First the scatterers contained in an artery of radius 2 mm are generated. It consists of a list of random coordinates spatially uniformly distributed and a list of random amplitudes following a Gaussian distribution. Then, the scatterers are moved in order to obtain their position at each time instance according to the Womersley model [Jensen, 1996b]. The PRF was set to 5 kHz for a mean velocity of 0.15 m/s and a beam/flow angle of 60°. The 128-element probe had a center frequency of 3 MHz. We focus on the reconstruction of a Doppler signal that corresponds to a complete cardiac cycle of about 1 s. The resulting pw-spectrogram is presented in Figure 9.2.

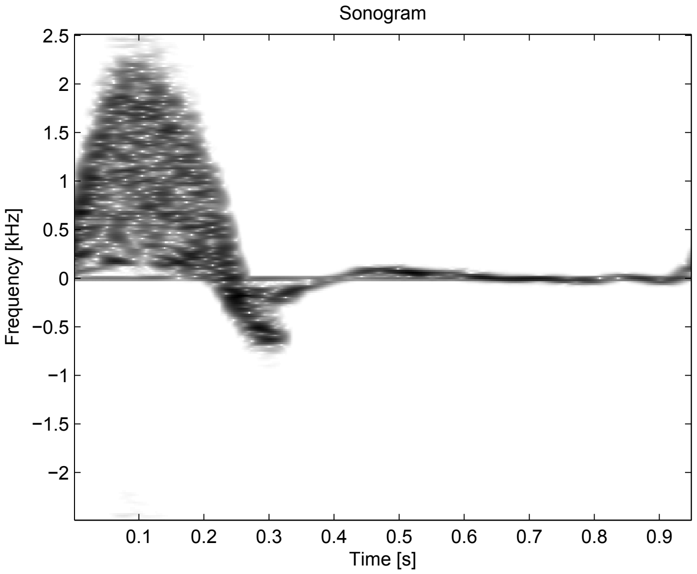

FIGURE 9.2 – Pw-spectrogram of the signal generated with FIELD II

9.2.2 Influence of BSBL method parameters

Our first objective is to evaluate the performance of the BSBL method on Doppler data by acting on the block partition. To examine this we compared two versions of the Bound-Optimization based algorithm proposed by Zhang [?, ?] and described in section 2.4.2. The first version corresponds simply to original method BSBL-BO and uses a fixed block partition. The second version, EBSBL-BO, corresponds to an extension where the block partition is assumed to be unknown and thus, to be determined during the reconstruction process. For the BSBL-BO algorithm the block partition was designed as follows : the location of the first element of each block was 1, $1+b$, $1+2b$, ..., where the block size is b.

In the EBSBL-BO framework, all the blocks are also of equal size b, but all possible blocks that overlap each other with an overlap step of size one are now considered. The block i starts at the element i of v_i and ends at the element $(i+b-1)$. All the nonzero elements of v_i lie in some of these blocks. Similar to the framework described in section 2.4.2, the block i is assumed to satisfy a multivariate Gaussian distribution with 0 mean and covariance matrix given by $\sigma_i B_i$. So, as previously, we have $p(v_i) \sim \mathcal{N}(0, \Sigma_0)$ but Σ_0 is no longer a block diagonal matrix. Now in Σ_0 each $\sigma_i B_i$ lies along the principal diagonal and overlaps the adjacent $\sigma_j B_j$. The previous BSBL framework can thus not be used. As a consequence, the covariance matrix Σ_0 is expanded as follows : $\hat{\Sigma_0} = diag\left\{\sigma_1, ..., \sigma_{(n-b+1)} B_{(n-b+1)}\right\}$ and from this an expanded model is derived for the BSBL-BO algorithm, which is called EBSBL-BO. The details of this algorithm can be found in [Zhang and Rao, 2012, Zhang and Rao, 2013a] and the expansion representation can be examined in Figure 9.3.

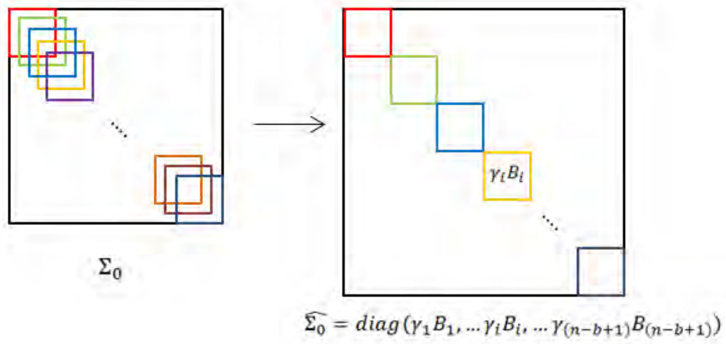

FIGURE 9.3 – Structures of the original Σ_0 and the expanded $\hat{\Sigma_0}$. Each color block corresponds to a possible nonzero block $\sigma_i B_i$.

In our case, the size of the blocks is to be determined, thus we tested both methods for different block sizes (b) and at several subsampling rates (S) given in Table 9.1. The performance is measured by comparing the CS reconstruction to the original data through the PSNR as a function of the number of removed samples. As shown in Figures 9.4.(a) and 9.4.(b) the block size is a determining factor for the quality of the reconstruction. We notice that the BSBL algorithms are slightly more sensitive to the size of b than EBSBL algorithms, especially when the partition size is high. Thus, the block sizes of 20 and 40 are not suitable for these algorithms and block sizes of 5, 10 and 20 give similar results. Lastly, the pw-spectrograms shown in Figure 9.5 confirm that these three block sizes give very close reconstruction results with a slightly better reconstruction for block sizes 5 and

TABLE 9.1 – Dictionary learning parameters

Parameters	Tested values
b	$5, 10, 20, 40, 60$
S (%)	20, 30, 40, 50, 60, 70, 80

10. Indeed, in the case $b = 20$ there are some small reconstruction errors at a subsampling rate of 80% that are introduced in the areas pointed by arrows on Figure 9.5. Since the $b = 5$ requires more calculations due to the higher number of partition per block, we will use $b = 10$ for the following reconstruction using the BSBL and ESBL algorithms.

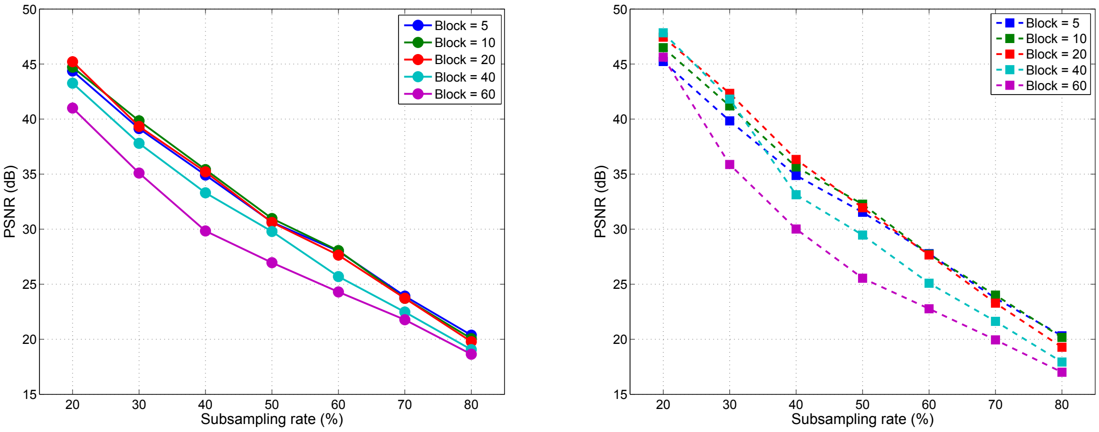

(a) BSBL reconstruction

(b) EBSBL reconstruction

FIGURE 9.4 – Influence of the block size b on the resulting PSNR as a function of the subsampling rate (S %), for (a) the BSBL algorithm and (b) the EBSBL algorithm. The other parameters are set to default values : r = 50%, p =256, $\Psi = Fourier$

9.2.3 Influence of CS reconstruction parameters

Another objective is to evaluate here the performance of our method by acting on the parameters related to the CS reconstruction of the pw-spectrogram. The parameters that will vary are : the segment size (p), the sampling rate (S), the overlap of segments (r, overlapping percentage rate between two consecutive segments) and the sparsifying transform (Ψ).

We measure the influence of each parameter separately, by making one of them vary in the range specified in the Table 9.2 "Tested values" column, while all others are set to their default value. The performance is measured by comparing the CS reconstruction to the original data through the PSNR as a function of the number of removed samples.

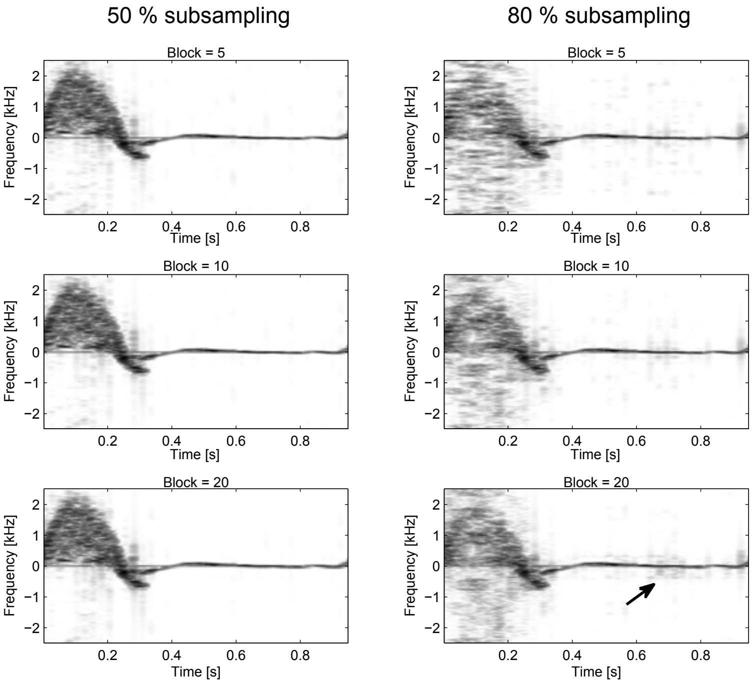

(a) BSBL reconstruction

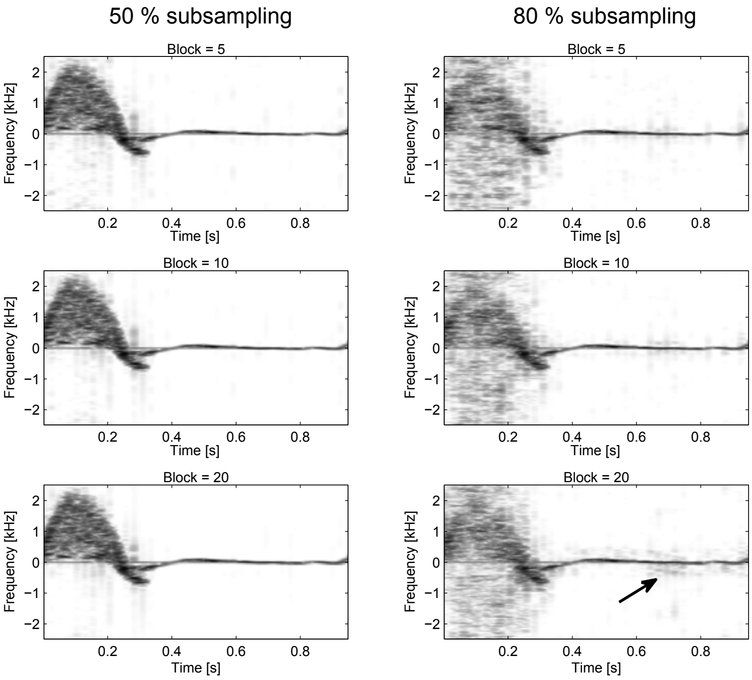

(b) EBSBL reconstruction

FIGURE 9.5 – Pw-spectrograms of (a) BSBL and (b) EBSBL algorithms based reconstructions for $b = 5, 10, 20$ at $S = 50$ and 80% subsampling rates. (The other parameters are set to default values : r = 50%, p =256, $\Psi = Fourier$)

TABLE 9.2 – Dictionary learning parameters

Parameters	Default value	Tested values
p	$\mathbf{2^8}$	$2^5, 2^6, ..., 2^{10}$
r (%)	**50**	0, 25, 50, 75
S (%)	**50**	20, 30, 40, 50, 60, 70, 80
Ψ	**Fourier**	Fourier, Wave atoms

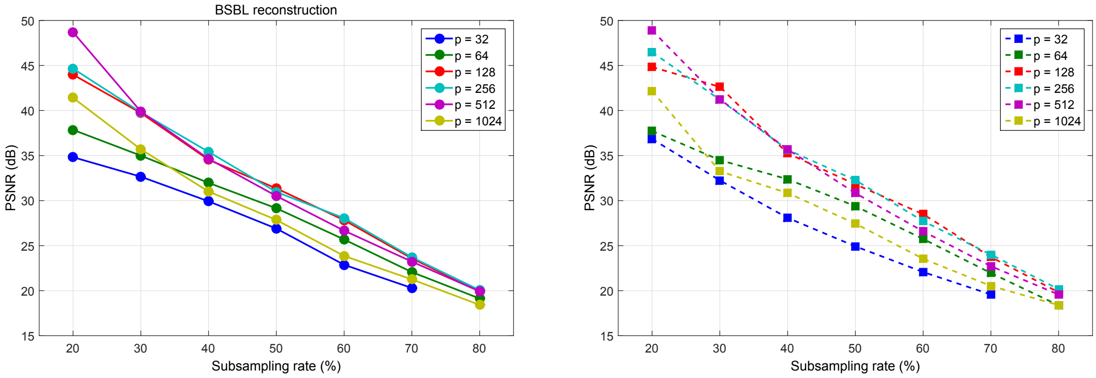

(a) BSBL reconstruction (b) EBSBL reconstruction

FIGURE 9.6 – Influence of the segment size n on the resulting PSNR as a function of the subsampling rate (S %), for (a) the BSBL algorithm and (b) the EBSBL algorithm. The other parameters are set to default values r = 50%, b = 10, Ψ = *Fourier*

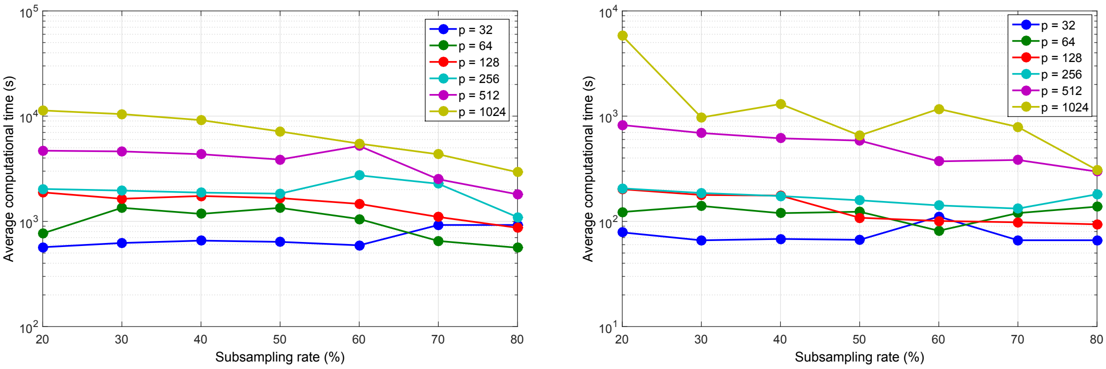

(a) BSBL reconstruction (b) EBSBL reconstruction

FIGURE 9.7 – Influence of the segment size p on the average computation time as a function of the subsampling rate (S %), for (a) the BSBL algorithm and (b) the EBSBL algorithm. The other parameters are set to default values r = 50%, b = 10, Ψ = *Fourier*

Influence of the segment length

The choice of the segment length when using the BSBL framework amounts to finding a compromise between time and frequency resolution. If p is too large, the blood flow may vary too much within the time frame corresponding to one segment, thus leading to a less sparse spectra and therefore to more reconstruction noise. On the other hand, if the segments contain too few samples, the frequency components of the signal cannot be recovered accurately. Figure 9.6 shows the validity of these assumptions as the poorest results are obtained for the segments of smallest sizes $32, 64$ and 1024 which is too large and thus yielding large variations of the blood flow. The optimal values are obtained for segment lengths of 128 and 256 as a with a segment length of 512 there is a small loss in PSNR starting from the 40% subsampling rate. Figure 9.7 represents the average computational time for the two methods, that we show in a logarithmmic scale for a better representation of the results. We notice that the EBSBL method is at least 2 times faster than the BSBL method. In the cases of segment lengths of $p = 32, 64, 128, 256$ the EBSBL method is ten times faster than the BSBL method. Since the computation times increase with the segment size, we would be inclined to choose $p = 128$ but in order to compare our results to the results obtained in previous studies, we choose the same segment length as in [Richy et al., 2013], $p = 256$.

Influence of the overlapping rate

The influence of overlapping is depicted in Figure 9.8. It may be first observed that the influence of the overlap rate is limited : the maximum difference between any two overlap rates is indeed less than 2 dB. The lowest PSNR is achieved with non-overlapping segments (r=0) which is expected since this type of reconstruction can introduce border errors. The best reconstruction is obtained for a 25% overlapping rate and the reconstruction quality then slightly decreases for higher overlapping rate. This phenomenon is best seen for low subsampling rates.

Figure 9.9 shows the average computation time for each overlap percentage and subsampling rate. We notice that the computation time clearly increases with the overlap. Indeed, the overlapping rate should not be too close to 100%, as the time allowed for each segment reconstruction and therefore the number of iterations per segment increases with the number of segment reconstructions. Again, the EBSBL framework can be 10 times faster than the BSBL framework and is at least 5 times faster. The most efficient overlap rate both in terms of PSNR error and computation times is 25%.

Comparison of Doppler reconstruction methods

As CS is based on random sampling, the reconstruction quality may vary depending on the sample set retained from the original data. To allow statistical analysis, for each parameter setting, the simulation is repeated using $n_{rep} = 20$ independent random sampling sets.

Using the default parameters ($p = 256, r = 50\%, b = 10$), we compare the reconstruction results that we obtain using the BSBL and EBSBL algorithms with classical,

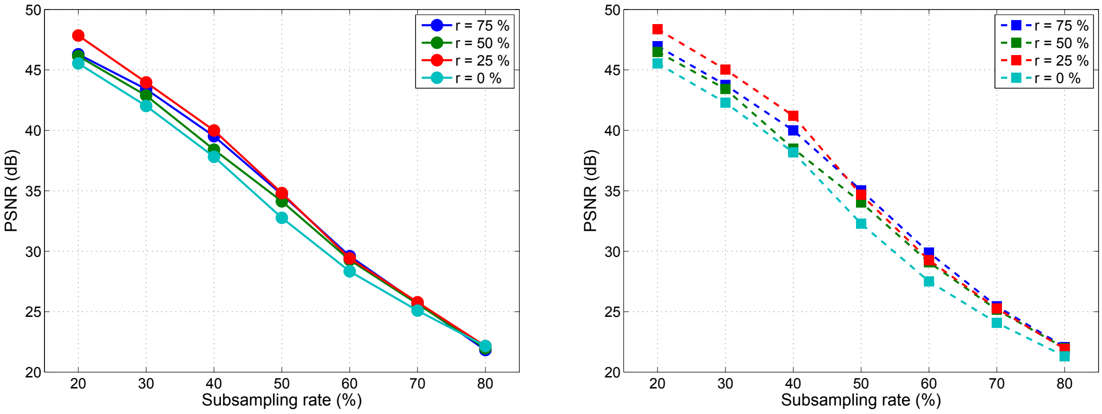

(a) BSBL reconstruction (b) EBSBL reconstruction

FIGURE 9.8 – Influence of the overlap percentage r on the resulting PSNR as a function of the subsampling rate (S %), for (a) the BSBL algorithm and (b) the EBSBL algorithm. The other parameters are set to default values p = 256, b = 10, Ψ = *Fourier*

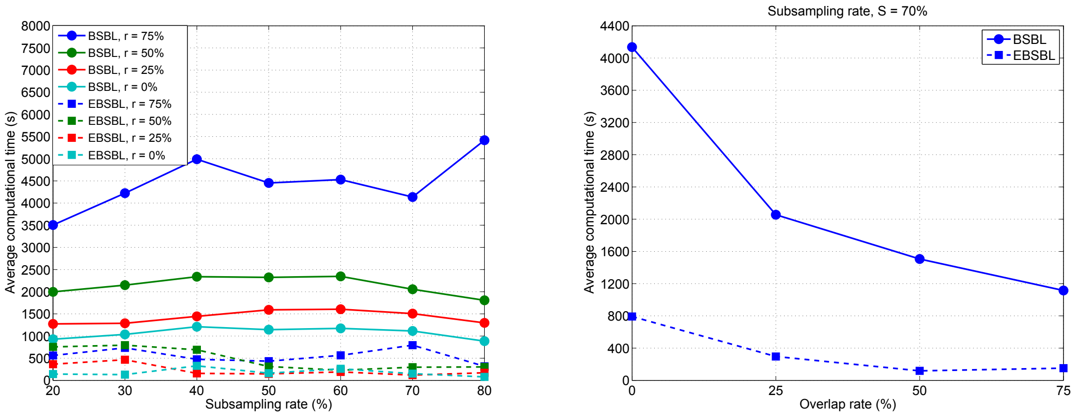

(a) (b)

FIGURE 9.9 – Influence of the overlap percentage r on the average computation time (a) as a function of the subsampling rate (S %) and (b) for S = 70%. The other parameters are set to default values p = 256, b = 10, Ψ = *Fourier*

basis pursuit based CS reconstructions using the Fourier basis and the wave atoms as proposed in the previously mentioned study [Richy et al., 2013]. Figure 9.10.(a) shows the reconstruction PSNR as a function of the subsampling rate for each transform and reconstruction approach. It can be observed that the PSNR decreases with the number of removed samples for every transform. The BSBL and EBSBL algorithms give equivalent results, the mean difference between the PSNRs being of 0.25 dB. The proposed algorithms clearly give the highest PSNR whatever the subsampling rate and perform well even for high subsampling rates. The difference between the standard CS reconstruction and the BSBL frameworks is of about 7 dB up to a subsampling rate of 60%. Overall, these results show that the default parameters previously chosen for the BSBL approaches perform well on simulated Doppler data. Figure 9.10.(b) presents the average computation time for the entire Doppler segment as a function of the subsampling rate for all the transforms and approaches. We notice that the computation time of the BSBL algorithm is approximatively 100 higher than the one of the EBSBL algorithm for an equivalent reconstruction error. Since the EBSBL gives the same performance in terms of reconstruction both with $p = 128, r = 25\%$ and $p = 256, r = 50\%$, we tend to prioritize the fastest approach which is, as it can be seen on Figure 9.10.(b), EBSBL with $p = 128, r = 25\%$.

Figure 9.11 shows the pw-spectrograms obtained with the BSBL, EBSBL approaches and the Fourier and wave atom based CS reconstructions for high subsampling rates, $S = 50, 60, 70, 80\%$. We can see that the performance using the classical CS reconstruction is strongly corrupted by noise starting at subsampling rates of $S = 50 - 60\%$. Over this threshold, the signal gets extremely noisy, especially in the first third of the cycle, which corresponds to the portion where the signal is the least sparse. The remaining part of the signal, being sparser, is well reconstructed up to $S = 80\%$. The performance using BSBL and EBSBL is highly improved compared to the classical CS as the reconstructed sonograms are exploitable up to subsampling rate of 80%. We notice that with the proposed framework we gain a compression level at acquisition of 10% : for example, at a subsampling rate of 70% with the BSBL based methods we obtain a higher PSNR than with the standard Fourier or wave atom based CS method at a subsampling rate Of 60%.

Overall, the results thus show that the proposed BSBL methods clearly provides better reconstruction than the conventional basis pursuit CS used in [Richy et al., 2013]. This can be linked to the basic properties of the BSBL framework, i.e. its ability to take into account intra-block correlation and to deal with only approximately sparse signals.

Signal acquisition and reconstruction time delay

Let us consider, the reconstruction of a single segment of the Doppler signal x_k in which each sample corresponds to one Doppler emission. Therefore before the reconstruction of this segment, all the Doppler samples must be acquired. The delay of acquisition between the first and last sample is incompressible and equal to $(n-1)/f_{PRF}$, which in the case of a PRF set to 5 KHz and using the default segment size (p=256) is 51 ms.

In addition to this incompressible delay, the computation time needed for the reconstruction has to be taken into account. The reconstruction time, which we denote Δt_r, is calculated as a function of function of the overlapping rate, the segment length and the PRF which equals to $\Delta t_r = \frac{\delta}{f_{PRF}}$ in the case of real time reconstruction, where $\delta = (1 - r/100)p$. At the limit of real-time reconstruction, we have $\Delta t_{r_1} =$ 25,6 ms in our default settings $(r = 50\%, p = 256)$ and $\Delta t_{r_2} =$ 19,2 ms for $r = 25\%, p = 128$. As it can be

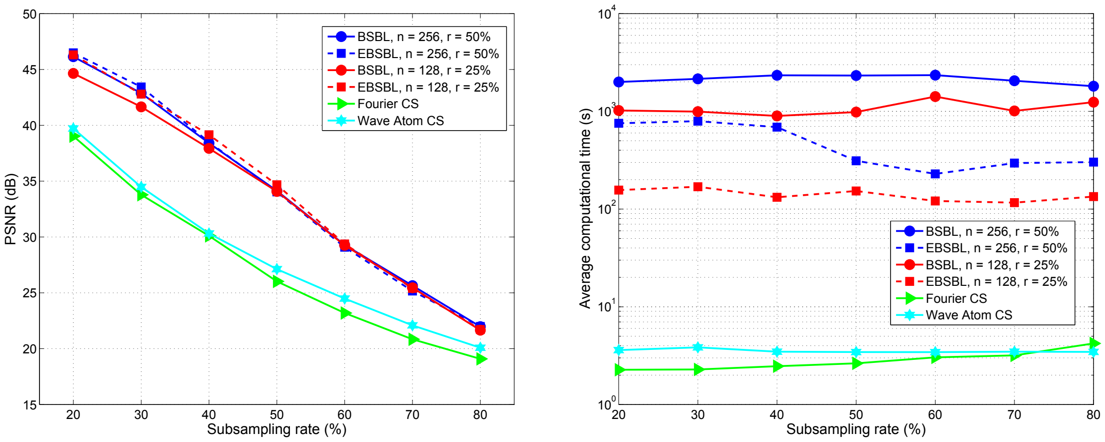

(a) (b)

FIGURE 9.10 – (a) PSNR and (b) Average computation time comparison of BSBL framework based algorithms with DFT- and wave-atom-based CS reconstructions as a function of the subsampling rate (S %).

seen on Figure 9.10.(b) the reconstruction of one segment takes approximatively between 26 and 53 ms for the Fourier CS based reconstructions and between 80 and 100 ms for the wave atom CS reconstruction, which is close to the delay of reconstruction needed for real-time reconstruction. For the moment the reconstruction time of one segment is between 2 and 3 seconds for the EBSBL framework with $r = 25\%, p = 128$ and between 8 and 10 seconds with $r = 50\%, p = 256$ which are values too high to have a real-time reconstruction. A possible track to reduce these computation times down to values compatible with real-time would consist in using parallel or GPU- based implementation.

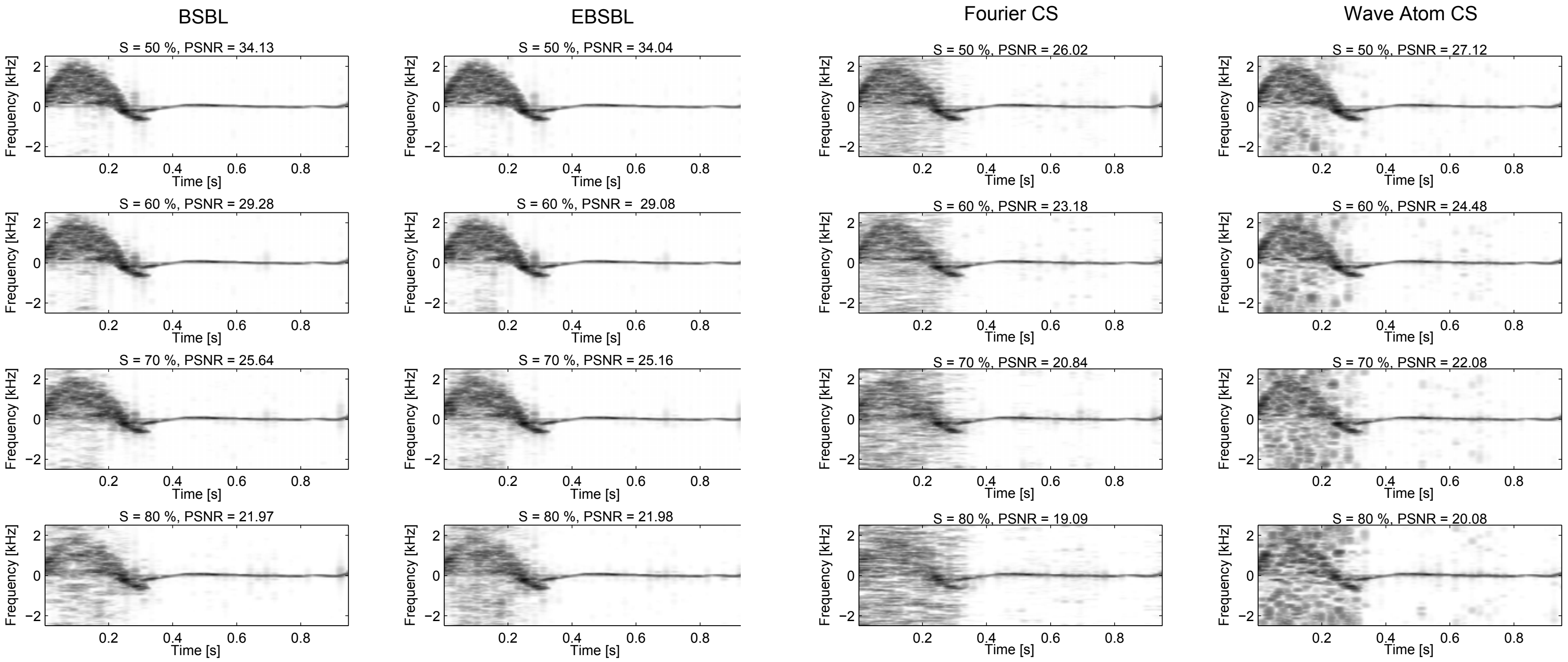

(a) BSBL and EBSBL algorithms

(b) Fourier and Wave atom CS

FIGURE 9.11 – Pw-spectrograms of (a) BSBL and EBSBL reconstruction and (b) Fourier and wave atom CS reconstructions for subsampling rates of $S = 50, 60, 70, 80\%$. (The other parameters are set to default values : r = 50%, p =256)

9.3 Experimental results

Finally, we propose to test this technique on experimental in vivo data acquisitions. This experiment was performed using a conventional approach, i.e. all Doppler RF lines were acquired in a row at a sufficient PRF. Then, samples were removed randomly at different sample selection rate in order to imitate the CS acquisition. This was done in order to have a reference signal to compare our reconstruction with and evaluate quantitatively our technique.

9.3.1 In vivo experimental Doppler data

The data were acquired using the advanced open platform for ultrasound research, Ula-Op, described by Tortoli et al. in [Tortoli et al., 2009]. The femoral artery of a 23 year old male healthy volunteer was scanned at $f_{prf} = 5$ kHz using a L523 linear array from Esaote (Esaote Spa, Genoa, Italy). Figure 9.12 shows the original pw-spectrogram.

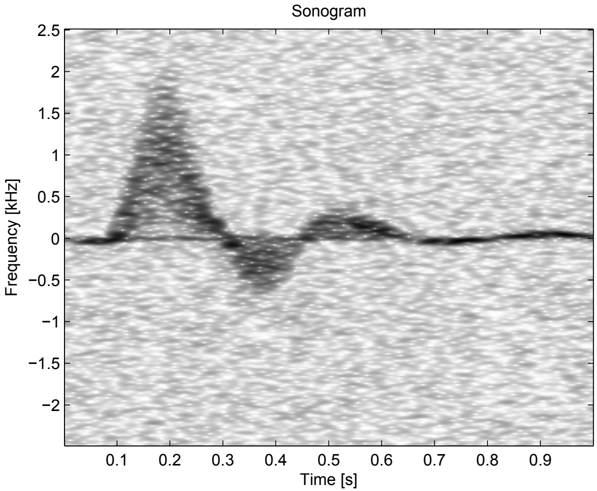

FIGURE 9.12 – Pw-spectrogram of a femoral artery acquired with the Ula-Op system

9.3.2 Reconstruction results with *in vivo* Doppler data

Figure 9.13.(a) shows the reconstruction PSNR as a function of the subsampling rate for each transform and reconstruction approach. It may be first observed that the PSNR is overall smaller than in the case of simulation, whatever the method. The interesting fact is however that, as in simulation, the BSBL reconstructions yields better results than the classical CS, with a difference in PSNR of about 2 dB on average. Another way to look at this result consists in noting that the proposed BSBL framework allows to increase the subsampling rate by about 10% while maintaining the same reconstruction quality (e.g. BSBL yields approximately the same PSNR at 70% subsampling as classical CS at 60%). In terms of computational time, the BSBL and EBSBL give the same performances as obtained on the reconstruction on simulation Doppler data. EBSBL with r = 25% and p

= 128 gives the best performance with a minimal loss in terms of PSNR.

In Figure 9.14 we show the pw-spectrograms obtained with the BSBL, EBSBL approaches and the Fourier and wave atom based CS reconstructions for high subsampling rates, $S = 50, 60, 70, 80\%$. On these figures we can observe that the BSBL and EBSBL methods give also visually a better reconstruction quality than the basis pursuit Fourier and wave atom CS reconstructions for all the shown subsampling rates. The background noise is poorly restored for all the methods but with a behavior depending of the reconstruction method. We can observe that with the BSBL and EBSBL methods the noise is eliminated on some areas corresponding to partitions in the reconstructed segments while the Doppler signal is still well reconstructed even at a subsampling rate of 80%. In the BSBL framework the partition of the blocks in a segment is non-overlapping and thus less blocks are found to be correlated and reconstructed which translates in the noise free areas that we see on the reconstructed spectrograms. While with the EBSBL approach the partition of the blocks within a segment is overlapping and thus the background noise is better reconstructed. Using the classical CS reconstruction we start to completely lose the Doppler signal after a subsampling rate of 70% as it is drowned in the background noise. We deduce that the BSBL based methods allocate in an efficient way the sparse coefficients to the frequencies corresponding to the highest magnitudes and thus reconstruct well the Doppler signal but lose blocks of the background noise. On the opposite, with the Fourier and wave atom basis pursuit based CS the coefficients are more uniformly distributed resulting in an uniform reconstruction of the noise but also to the loss of the Doppler signal at high subsampling rates.

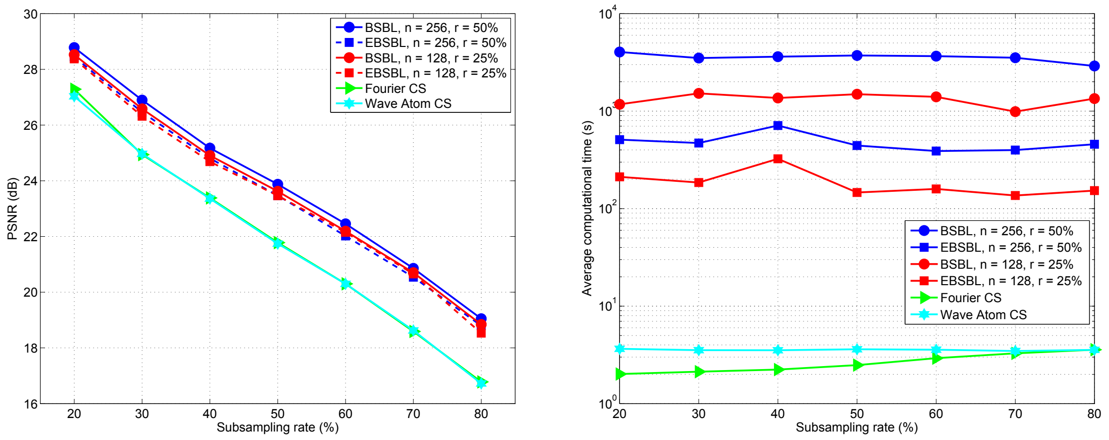

(a) (b)

FIGURE 9.13 – (a) PSNR and (b) Average computation time comparison of BSBL framework based algorithms with DFT- and wave-atom-based CS reconstructions as a function of the subsampling rate (S %)

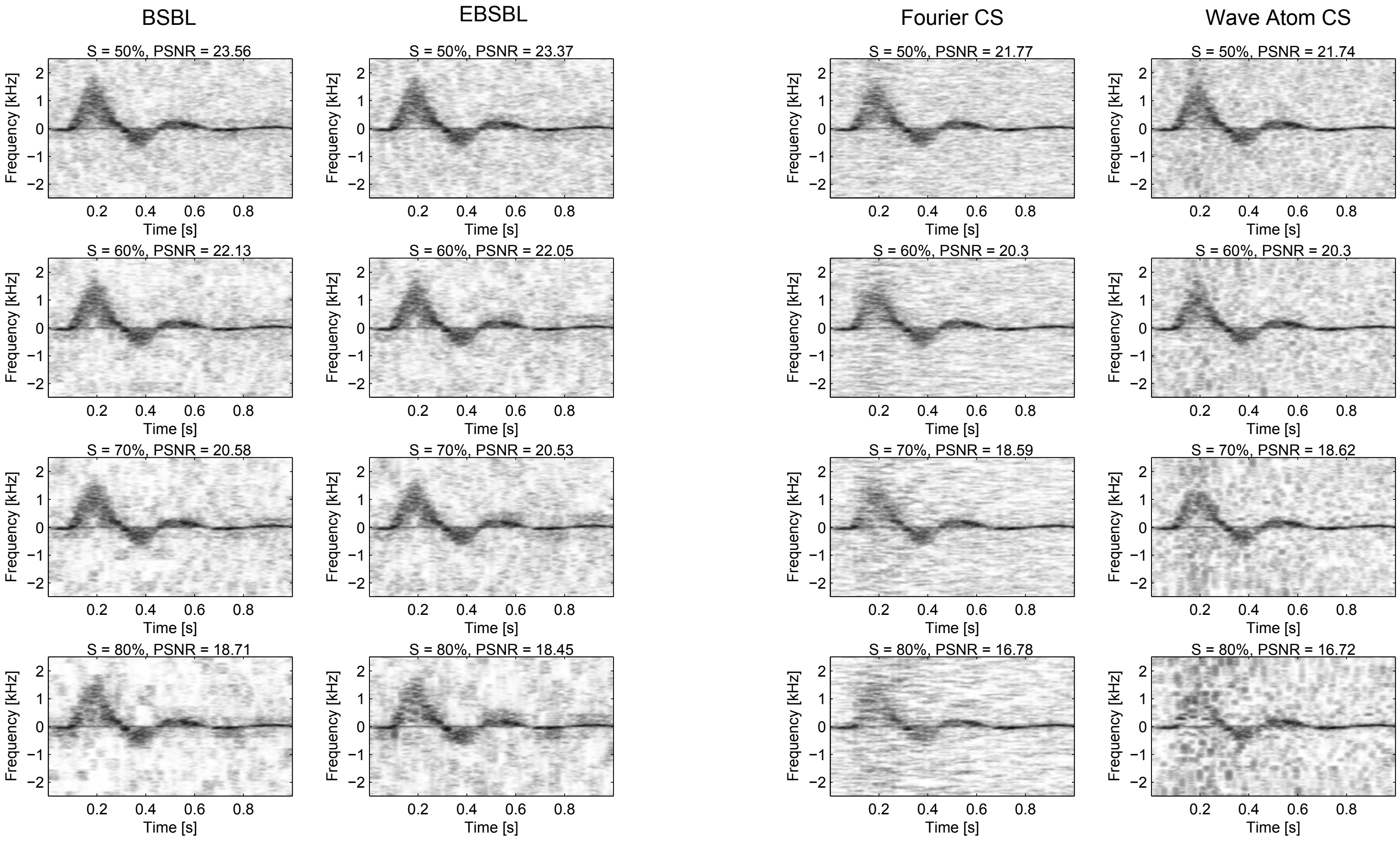

(a) (b)

FIGURE 9.14 – Pw-spectrograms of (a) BSBL and EBSBL reconstructions and (B) Fourier and wave atom CS reconstructions for subsampling rates of $S = 50, 60, 70, 80\%$. (The other parameters are set to default values : r = 25%, p =128)

Chapitre 10

Conclusion and perspectives

In this contribution, we have proposed an ultrasound technique for blood flow estimation based on a Bayesian compressive sensing framework. The technique proposed has a high potential for application in duplex modes, where the acquisition time needs to be shared between the different modes. The proposed technique shows improved results compared to the previously proposed study based on the classical basis pursuit-based CS reconstruction [Richy et al., 2013]. With this approach, the results are improved for all subsampling rates and sparsifying transforms proposed by the previous study.

Another important remark is that the properties of the BSBL approach provide the good conditions for CS in the context of Doppler signals reconstruction. Indeed, Doppler signals have correlated samples since their acquisitions is performed over the same region during continuous lapses of time. This feature is exploited by the BSBL algorithms that are based on the assumption that there exists an intra-block correlation structure within the signal. Moreover, the BSBL framework has been proven to recover non-sparse signals, which is the case of Doppler signals that are moderately sparse as shown in [Richy et al., 2013].

A downside of this method is the average computation time per segment which is too high for a real-time implementation of duplex Doppler ultrasound systems. In practice, we would need to reduce the computation times by a factor of 100. However, distributed parallel computing, GPU implementation or a more detailed optimization and vectorization of the BSBL and EBSBL frameworks will most probably allow reaching the necessary speed rates required for real-time reconstruction.

V General conclusions and perspectives

10.1 Goals and contributions

The goal of this work was to propose CS based methods for reconstructing and representing ultrasound signals that could greatly benefit from reducing the amount of data to be acquired. As we have seen, 3D ultrasound imaging is an excellent candidate that could greatly benefit from the application of the CS theory, all the more since it requires a significant increase in computation speed for acquiring, reconstructing and viewing the US volumes in real-time. This type of imaging system using transducers generating real-time 3D volumes have been recently developed and their technology is so complex that they are not yet common in clinical routine. Another type of US imaging technique interesting for the use of a compressed acquisition is duplex Doppler ultrasound imaging where the acquisition time must be shared between two imaging modes and therefore a technique is needed for reconstructing the missing samples.

We first focused on the compressed acquisition and reconstruction of 3D US images. We proposed a CS framework based on the use of learned overcomplete dictionaries to sparsely reconstruct 3D US images. Knowing that a fundamental choice in the application of the CS framework is choosing the right sparsifying dictionary, we focused on dictionaries that have the ability to fit to our specific class of signals. This type of dictionaries allow for much sparser representations which is a valuable quality in the context of CS reconstructions. This approach was initially tested as a preliminary validation on 2D US data. We showed the high potential of learned dictionaries for CS in US imaging by testing this approach on experimental RF data and we obtained US images with minimal loss of information using only 25% of the initial samples of the acquisition.

In a second step, we addressed the reconstruction of 3D US data. More particularly, we showed that the learned dictionary based approach yields better performances than conventional sparsifying dictionaries based on fixed transforms. Then, we evaluated the generality of the learned dictionary CS approach as it might have been hampered by over-learning thus providing a dictionary capable of satisfyingly reconstructing only images close to the learning set. We proved that this is not the case and the constructed dictionaries reliably reconstruct different *ex vivo* and *in vivo* organ volumes. We also focused on the measurement sensing setup and especially on a sampling strategy that does not imply a fundamental modification of the existing US hardware. Thus, we concentrated on a line-wise sampling scheme that is implementable in practice in a relatively simple setting and results in an increase of the frame-rate. This approach was validated on simulation, *ex vivo* and *in vivo* experimental 3D images and for all the previous types of acquisitions it provided satisfying reconstructions and better results than existing conventional CS methods.

Our last contribution was to develop a framework for using duplex Doppler US systems that need to share the acquisition and display of a B-mode US image and of the Doppler spectrogram. The proposed CS reconstruction technique applies a Bayesian CS framework exploiting Doppler signal properties. Since Doppler acquisitions are performed over the same region and during continuous lapses of time, their samples are temporally correlated. This property is exploited by the proposed BSBL CS framework as it is based on the assumption that the reconstructed signal has an internal correlation structure. Moreover, the BSBL framework has been proven to recover signals that are only approximatively sparse, which is the case of Doppler signals as shown in [Richy et al., 2013].

10.2 Perspectives

Our research on the feasibility of CS using learned dictionaries in 3D US imaging and CS using block sparse Bayesian learning for duplex Doppler systems has however some limitations and thus opens several research perpectives.

One of the limitations of this study comes from the usage of learned dictionaries. Although these provide much sparser and adapted representation of our data, the downside is that they have no explicit inverse or fast transform and thus for each reconstruction a minimization problem has to be solved. This increases the computational load and the associated computation times (several hours with our unoptimized Matlab code), so dictionary-based CS method cannot currently be used for real-time 3D acquisitions. A solution to this problem could come from GPU or adapted parallel implementations. As an illustrative example, in MRI [Li et al., 2014] have designed parallel algorithms implemented on GPU for dictionary learning algorithm (K-SVD algorithm) and reconstruction and the experimental results showed that more than 325 times of speed up is achieved as compared to non-optimized CPU codes.

An alternative to this approach could consist in using Deep Learning techniques, that jointly trains the dictionary and an efficient non-linear regressor that maps any input to its sparse representation, i.e. to the sparse set of dictionary coefficients [Qian and Shi, 2014, Gregor and LeCun, 2010]. In this case, the CS framework will be given an adapted and sparsity-optimal dictionary for our class of signals and the learned inverse transform that speeds up the reconstruction process. This approach has been successfully tested on the CS reconstruction of MRI images very recently and showed promising results [Majumdar, 2015]. Though the deep learning technique used in this study requires huge amounts of data and large training times, once the nonlinear mapping is learned the reconstruction time is very fast since it only requires a few matrix vector products.

It would also be interesting to study the CS reconstruction of dynamic US images. Indeed, in the context of dynamic imaging we can assume that the motion of a major part of the scanned anatomy has a slow movement and only a few portions have a rapid motion. Thus, the difference between two temporally consecutive frames will give a sparse difference image since the slow motion zones will cancel each other and the high motion zones will give the difference image. The assumption that the difference between two consecutive US frames is sparse makes dynamic US an ideal candidate for CS recovery under a temporal sparsity assumption. In this context, it would be interesting to test several algorithms that take into account the time-varying sparsity model, such as the Kalman Filtered Based Compressed Sensing (KF-CS) [Vaswani, 2009], the Least-Squares Compressed-Sensing (LS-CS) [Vaswani, 2010] and the Spatio-Temporal Sparse Bayesian Learning (STSBL) [Zhang et al., 2014] algorithms. All these algorithms consider that the support is changing slowly but STSBL makes an additional assumption on the spatial correlation within the signals which is very interesting for the reconstruction of dynamic US signals.

In duplex Doppler imaging, a 2D tracking Doppler is proposed as an alternative to PW Doppler, in which the sample volume follows the trajectory of the blood scatterers over time [Avdal et al., 2014]. This alternative to PW Doppler reduces Doppler spectral broadening and provides spectrograms that are sparser in the Fourier domain. This can be exploited in the CS context in order to obtain better reconstruction results, since, as we previously noticed the spectrograms are well reconstructed when the velocity range is narrow while the segments that have a broad spectrum require more samples for an equivalent reconstruction quality.

Finally it can be noted that the validation of the proposed methods was performed on healthy subjects. It is thus important to also evaluate the performances on pathological cases and see if our methods still provides accurate results.

Appendix

Annexe A

Relationship between Nyquist and CS sampling

A.1 Simulated data

In the case of the synthetic data set, the raw RF signals were acquired with a simulated transducer having a central frequency of 3.3 MHz and sampled at 50 MHz so this sampling rate is indeed higher than the one corresponding to 4 times the central frequency, as typically used on clinical scanners. However, we do not work on the RF signals but on the envelope of the beamformed RF data, which were sampled at 2.2 MHz. Figure A.1 below shows the mean spectrum of envelope signal corresponding to the beamlines of the simulated data. The magnitude of the spectrum can be considered as negligible after $f_{max} = 0.55$ MHz, so the sampling frequency approximately corresponds to 4 times f_{max}.

The percent random subsampling rates can be related to an equivalent regular sampling frequency (i.e. regular sampling that would provide the same amount of samples). The maximum frequency component f_c (i.e. the maximum frequency component that could be reliably acquired using this regular sampling frequency) can then be estimated using the suggested conservative rule, i.e $f_c = f_s/4$. The corresponding calculations are given in the table below A.1. As an example, at 80% subsampling the maximum frequency component can be estimated at $f_c = 0.11$ MHz for a regular sampling frequency of 0.44 MHz, which would clearly be too low in a regular subsampling setup.

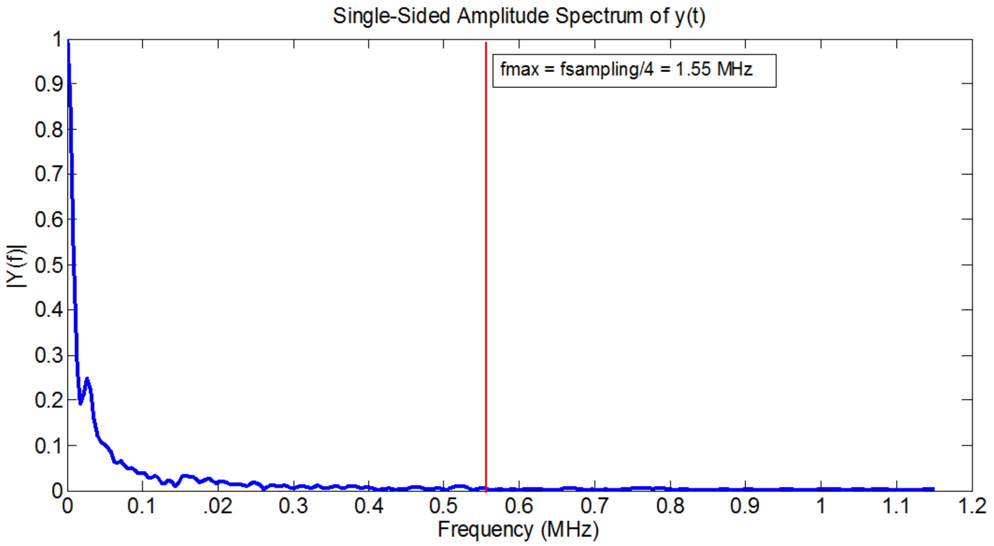

FIGURE A.1 – Mean spatial spectrum for all the beamlines in the envelope of the simulated data

TABLE A.1

CS random subsampling rate	0 %	20 %	30 %	40 %	50 %	60 %	70 %	80 %
Equivalent regular sampling frequency (f_s) MHz	2.2	1.76	1.54	1.32	1.1	0.88	0.66	0.44
Estimated max frequency component ($f_c = f_s/4$) MHz	0.55	0.44	0.385	0.33	0.275	0.22	0.165	0.11

A.2 Experimental data

In the case of the experimental acquisitions, the central frequency of the probe was of 5 MHz for the 3 organs and the RF signals were collected using a 40 MHz sampling rate. The derived envelope signals were then sampled at 5 MHz. Figure A.2 below shows the mean spectrum of envelope signal associated to the beamlines of the experimental data correponding to the *ex vivo* kidney acquisition. The magnitude of the spectrum can be considered as negligible after $f_{max} = 1.3$ MHz, so the sampling frequency approximately corresponds to 4 times f_{max}.

As for the simulated data, the maximum frequency component f_c has been estimated using the suggested conservative rule, i.e. $f_c = f_s/4$ and the corresponding calculations are presented in table A.2. For the experimental data, at 80% subsampling the maximum frequency component corresponds to $f_c = 0.25$ MHz for a regular sampling frequency of 1 MHz, which would be too low in a regular subsampling setup.

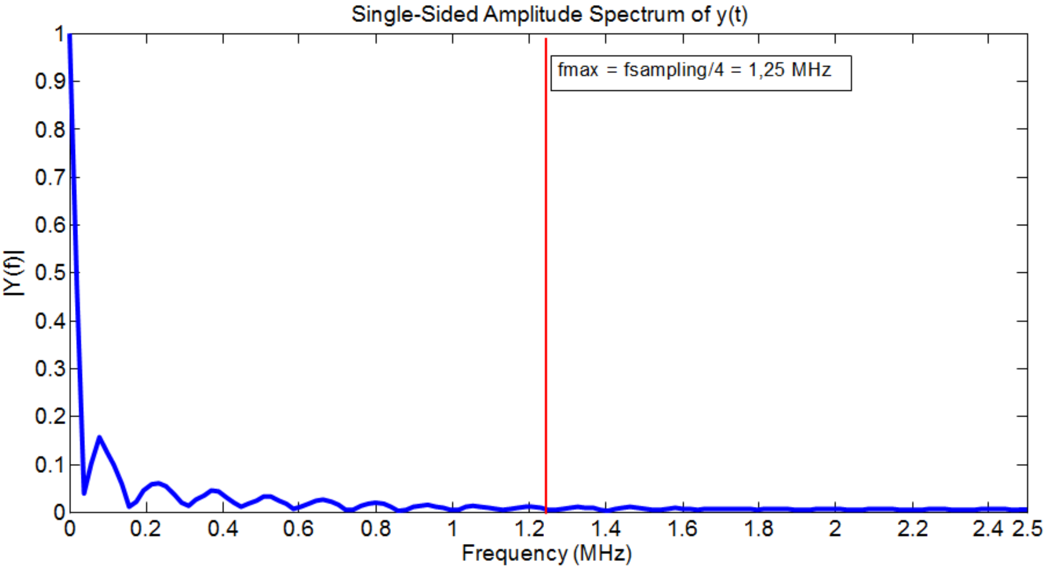

FIGURE A.2 – Mean spatial spectrum for all the beamlines in the envelope of the experimental data correponding to the *ex vivo* kidney acquisition

TABLE A.2

CS random subsampling rate	0 %	20 %	30 %	40 %	50 %	60 %	70 %	80 %
Equivalent regular sampling frequency (f_s) MHz	5	4	3.5	3	2.5	2	1.5	1
Estimated max frequency component ($f_c = f_s/4$) MHz	1.25	1	0.875	0.75	0.625	0.5	0.375	0.11

Personal bibliography

International journal

[Lorintiu O. et al., 2015a] **Lorintiu O.**, Liebgott H., Alessandrini M., Bernard O., and Friboulet D., "Compressed sensing reconstruction of 3D ultrasound data using dictionary learning and line-wise subsampling", IEEE Transactions on Medical Imaging, accepted, 2015.

International conferences

[Lorintiu O. et al., 2015b] **Lorintiu O.**, Liebgott H., Bernard A., Bernard O., and Friboulet D., "Compressed sensing reconstruction of line-wise sub-sampled 3D echographic images based on dictionary learning : an experimental study", IEEE International Ultrasonics Symposium, accepted, Taipei, Taiwan, 2015.

[Lorintiu O. et al., 2015c] **Lorintiu O.**, Liebgott H., Bernard O., and Friboulet D., "Sub-sampled Doppler ultrasound reconstruction using block sparse Bayesian learning", IEEE International Ultrasonics Symposium, accepted, Taipei, Taiwan, 2015.

[Lorintiu O. et al., 2014] **Lorintiu O.**, Liebgott H., Alessandrini M., Bernard O., and Friboulet D., "Compressed sensing reconstruction of 3D ultrasound data using dictionary learning", IEEE International Conference on Image Processing (ICIP'14, pp. 1317-1321, Paris, France, 2014.

[Lorintiu O. et al., 2013] **Lorintiu O.**, Liebgott H., Bernard O., and Friboulet D., "Compressive Sensing Ultrasound Imaging using Overcomplete Dictionaries", IEEE International Ultrasonics Symposium, pp. 45-48, Prague, Czech Republic, 2013.

Miscellaneous

[Lorintiu O. et al., 2012] **Lorintiu O.**, Bernard O., Friboulet D. and Liebgott H., "Compressive sensing reconstruction in ultrasound medical imaging", Journées Imagerie du Vivant, Lyon, France, 2012.

Bibliographie

[Achim et al., 2014] Achim, A., Basarab, A., Tzagkarakis, G., Tsakalides, P., and Kouamé, D. (2014). Reconstruction of compressively sampled ultrasound images using dual prior information. In *IEEE International Conference on Image Processing (ICIP)*, page in press.

[Achim et al., 2010] Achim, A., Buxton, B., Tzagkarakis, G., and Tsakalides, P. (2010). Compressive sensing for ultrasound rf echoes using a-stable distributions. In *International Conference of the IEEE Engineering in Medicine and Biology Society (EMBC)*, pages 4304–4307.

[Aharon et al., 2006] Aharon, M., Elad, M., and Bruckstein, A. (2006). k -svd : An algorithm for designing overcomplete dictionaries for sparse representation. *Signal Processing, IEEE Transactions on*, 54(11) :4311–4322.

[Alessandrini et al., 2015] Alessandrini, M., De Craene, M., Bernard, O., Giffard-Roisin, S., Allain, P., Weese, J., Saloux, E., Delingette, H., Sermesant, M., and D'hooge, J. (2015). A pipeline for the generation of realistic 3d synthetic echocardiographic sequences : Methodology and open-access database. *Medical Imaging, IEEE Transactions on*, PP(99) :1–1.

[Angelsen, 2000] Angelsen, B. A. J. (2000). Ultrasound imaging. waves, signals and signal processing. *Emantec AS, Trondheim, Norway.*

[Avdal et al., 2014] Avdal, J., Ekroll, I., Fadnes, S., Lovstakken, L., and Torp, H. (2014). 2d tracking doppler for cardiac jet flow velocity estimation. In *Ultrasonics Symposium (IUS), 2014 IEEE International*, pages 1718–1721.

[Baraniuk et al., 2007] Baraniuk, R., Davenport, M., Devore, R., and Wakin, M. (2007). A simple proof of the restricted isometry property for random matrices. *Constr. Approx*, 2008.

[Barbosa, 2013] Barbosa, D. (2013). *Automated assessment of cardiac morphology and function : An integrated B-spline framework for real-time segmentation and tracking of the left ventricle*. PhD thesis. PhD thesis, Lyon, INSA 2013. Available from : `http://www.theses.fr/2013ISAL0111`.

[Basarab et al., 2014] Basarab, A., Achim, A., and Kouamé, D. (2014). Medical ultrasound image reconstruction using compressive sampling and lp norm minimization. In *SPIE Medical Imaging*.

[Basarab et al., 2013] Basarab, A., Liebgott, H., Bernard, O., Friboulet, D., and Kouamé, D. (2013). Medical ultrasound image reconstruction using distributed compressive sampling. In *IEEE International Symposium on Biomedical Imaging (ISBI)*, pages 624–627.

[Beck and Teboulle, 2009] Beck, A. and Teboulle, M. (2009). A fast iterative shrinkage-thresholding algorithm for linear inverse problems. *SIAM Journal on Imaging Sciences*, 2(1) :183–202.

[Becker et al., 2009] Becker, S., Bobin, J., and Candés, E. (2009). NESTA : A Fast and Accurate First-order Method for Sparse Recovery. *ArXiv e-prints.*

[Bernard, 2006] Bernard, O. (2006). *Segmentation in echocardiographic imaging using parametric level set model driving by the statistics of the radiofrequency signal.* PhD thesis. PhD thesis, INSA Lyon.

[Birgin et al., 1999] Birgin, E. G., Martínez, J. M., and Raydan, M. (1999). Nonmonotone spectral projected gradient methods on convex sets. *SIAM J. on Optimization*, 10(4) :1196–1211.

[Birk et al., 2014] Birk, M., Burshtein, A., Chernyakova, T., Eilam, A., Choe, J., Nikoozadeh, A., Khuri-Yacoub, P., and Eldar, Y. C. (2014). Compressed 3d ultrasound imaging with 2d arrays. In *IEEE International Conference on Acoustics, Speech and Signal Processing (ICASSP).*

[Blumensath and Davies, 2008a] Blumensath, T. and Davies, M. (2008a). Gradient pursuits. *Signal Processing, IEEE Transactions on*, 56(6) :2370–2382.

[Blumensath and Davies, 2008b] Blumensath, T. and Davies, M. (2008b). Iterative thresholding for sparse approximations. *Journal of Fourier Analysis and Applications*, 14(5-6) :629–654.

[Blumensath and Davies, 2009] Blumensath, T. and Davies, M. E. (2009). Iterative hard thresholding for compressed sensing. *Applied and Computational Harmonic Analysis*, 27(3) :265 – 274.

[Candés and Romberg, 2005] Candés, E. and Romberg, J. (2005). l_1-magic : Recovery of sparse signals via convex programming.

[Candés and Romberg, 2007] Candés, E. and Romberg, J. (2007). Sparsity and incoherence in compressive sampling. *Inverse Problems*, 23(3) :969.

[Candés et al., 2006a] Candés, E., Romberg, J., and Tao, T. (2006a). Robust uncertainty principles : exact signal reconstruction from highly incomplete frequency information. *Information Theory, IEEE Transactions on*, 52(2) :489–509.

[Candés and Tao, 2005] Candés, E. and Tao, T. (2005). Decoding by linear programming. *Information Theory, IEEE Transactions on*, 51(12) :4203–4215.

[Candés and Tao, 2006] Candés, E. and Tao, T. (2006). Near-optimal signal recovery from random projections : Universal encoding strategies ? *Information Theory, IEEE Transactions on*, 52(12) :5406–5425.

[Candés and Wakin, 2008] Candés, E. and Wakin, M. (2008). An introduction to compressive sampling. *Signal Processing Magazine, IEEE*, 25(2) :21–30.

[Candés, 2008] Candés, E. J. (2008). The restricted isometry property and its implications for compressed sensing. *Comptes Rendus de l'Academie des Sciences*, 346(9 - 10) :589 – 592.

[Candés et al., 2006b] Candés, E. J., Romberg, J. K., and Tao, T. (2006b). Stable signal recovery from incomplete and inaccurate measurements. *Communications on Pure and Applied Mathematics*, 59(8) :1207–1223.

[Candés and Boyd, 2008] Candés, E.J., W. M. B. and Boyd, S. P. (2008). Enhancing sparsity by reweightes l1 minimization. *Journal of Fourier Analysis and Applications*, 14 :629–654.

[Chartrand, 2007] Chartrand, R. (2007). Exact reconstruction of sparse signals via nonconvex minimization. *Signal Processing Letters, IEEE*, 14(10) :707–710.

[Chartrand and Staneva, 2008] Chartrand, R. and Staneva, V. (2008). Restricted isometry properties and nonconvex compressive sensing. *Inverse Problems*, 24(035020) :1–14.

[Chartrand and Yin, 2008] Chartrand, R. and Yin, W. (2008). Iteratively reweighted algorithms for compressive sensing. In *Acoustics, Speech and Signal Processing, 2008. ICASSP 2008. IEEE International Conference on*, pages 3869–3872.

[Chen and Huang, 2014] Chen, C. and Huang, J. (2014). Exploiting the wavelet structure in compressed sensing mri. *Magnetic Resonance Imaging*, 32(10) :1377 – 1389.

[Chen et al., 1998] Chen, S. S., Donoho, D. L., and Saunders, M. A. (1998). Atomic decomposition by basis pursuit. *SIAM Journal on Scientific Computing*, 20(1) :33–61.

[Chernyakova and Eldar, 2014] Chernyakova, T. and Eldar, Y. (2014). Fourier-domain beamforming : the path to compressed ultrasound imaging. *Ultrasonics, Ferroelectrics, and Frequency Control, IEEE Transactions on*, 61(8) :1252–1267.

[Chuo et al., 2013] Chuo, Y., Chan, T.-H., and Li, M.-L. (2013). Ultrasound compressed sensing : Performance study of reconstruction on different ultrasound imaging data. In *IEEE International Ultrasonics Symposium*, pages 903–905.

[Cohen et al., 2008] Cohen, A., Dahmen, W., and Devore, R. (2008). Instance optimal decoding by thresholding in compressed sensing. *Proc 8th Int Conf Harmonic And Partial Differential Equations*, pages 1–28.

[Craene and *et al.*, 2013] Craene, M. D. and *et al.*, S. M. (2013). 3d strain assessment in ultrasound (straus) : A synthetic comparison of five tracking methodologies. *Medical Imaging, IEEE Transactions on*, 32(9) :1632–1646.

[Dai and Milenkovic, 2009] Dai, W. and Milenkovic, O. (2009). Subspace pursuit for compressive sensing signal reconstruction. *Information Theory, IEEE Transactions on*, 55(5) :2230–2249.

[Daubechies et al., 2004] Daubechies, I., Defrise, M., and De Mol, C. (2004). An iterative thresholding algorithm for linear inverse problems with a sparsity constraint. *Communications on Pure and Applied Mathematics*, 57(11) :1413–1457.

[Daubechies et al., 2010] Daubechies, I., DeVore, R., Fornasier, M., and Güntürk, C. S. (2010). Iteratively reweighted least squares minimization for sparse recovery. *Communications on Pure and Applied Mathematics*, 63(1) :1–38.

[Davenport and Wakin, 2010] Davenport, M. and Wakin, M. (2010). Analysis of orthogonal matching pursuit using the restricted isometry property. *Information Theory, IEEE Transactions on*, 56(9) :4395–4401.

[Demanet and Ying, 2007] Demanet, L. and Ying, L. (2007). Wave atoms and sparsity of oscillatory patterns. *Applied and Computational Harmonic Analysis*, 23(3) :368–387.

[Dinh and Cevher, 2014] Dinh, Q. T. and Cevher, V. (2014). A primal-dual algorithmic framework for constrained convex minimization. Available from : `http://arxiv.org/abs/14065403`.

[Dobigeon et al., 2012] Dobigeon, N., Basarab, A., Kouamé, D., and Tourneret, J.-Y. (2012). Regularized bayesian compressed sensing in ultrasound imaging. In *European Signal and Image Processing Conference (EUSIPCO)*.

[Donoho et al., 2012] Donoho, D., Tsaig, Y., Drori, I., and Starck, J.-L. (2012). Sparse solution of underdetermined systems of linear equations by stagewise orthogonal matching pursuit. *Information Theory, IEEE Transactions on*, 58(2) :1094–1121.

[Donoho and Huo, 2001] Donoho, D. L. and Huo, X. (2001). Uncertainty principles and ideal atomic decomposition. *IEEE Transactions on Information Theory.*

[Duarte et al., 2008] Duarte, M., Davenport, M., Takhar, D., Laska, J., Sun, T., Kelly, K., and Baraniuk, R. (2008). Single-pixel imaging via compressive sampling. *Signal Processing Magazine, IEEE*, 25(2) :83–91.

[Duarte and Eldar, 2011] Duarte, M. and Eldar, Y. (2011). Structured compressed sensing : From theory to applications. *Signal Processing, IEEE Transactions on*, 59(9) :4053–4085.

[Efron et al., 2004] Efron, B., Hastie, T., Johnstone, I., and Tibshirani, R. (2004). Least angle regression. *Annals of Statistics*, 32 :407–499.

[Elad, 2006] Elad, M. (2006). Why simple shrinkage is still relevant for redundant representations ? *Information Theory, IEEE Transactions on*, 52(12) :5559–5569.

[Elad, 2010] Elad, M. (2010). *Sparse and Redundant Representations : From Theory to Applications in Signal and Image Processing.* Springer Publishing Company, Incorporated, 1st edition.

[Elad and Bruckstein, 2002] Elad, M. and Bruckstein, A. (2002). A generalized uncertainty principle and sparse representation in pairs of bases. *Information Theory, IEEE Transactions on*, 48(9) :2558–2567.

[Eldar and Kutyniok, 2012] Eldar, Y. and Kutyniok, G. (2012). *Compressed Sensing : Theory and Applications.* Compressed Sensing : Theory and Applications. Cambridge University Press. Available from : http://books.google.fr/books?id=Gm3ihcJwN0YC.

[Ender, 2013] Ender, J. (2013). A brief review of compressive sensing applied to radar. In *Radar Symposium (IRS), 2013 14th International*, volume 1, pages 3–16.

[Engan et al., 1999] Engan, K., Aase, S., and Hakon Husoy, J. (1999). Method of optimal directions for frame design. 5 :2443–2446 vol.5.

[Fargier-Voiron et al., 2014] Fargier-Voiron, M., Presles, B., Pommier, P., Rit, S., Munoz, A., Liebgott, H., Sarrut, D., and Biston, M. C. (2014). Impact of probe pressure variability on prostate localization for ultrasound-based image-guided radiotherapy. *Radiotherapy and Oncology*, 111(1).

[Feng et al., 2014] Feng, C., Xiao, L., and Wei, Z.-H. (2014). Compressive sensing inverse synthetic aperture radar imaging based on gini index regularization. *Int. J. Autom. Comput.*, 11(4) :441–448.

[Fenster et al., 2011] Fenster, A., Parraga, G., and Bax, J. (2011). Three-dimensional ultrasound scanning. *Interface Focus*, 1(4) :503–519.

[Figueiredo, 2002] Figueiredo, M. (2002). Adaptive sparseness using jeffreys prior. *Advances in Neural Information Processing Systems*, 14.

[Figueiredo, 2003] Figueiredo, M. (2003). Adaptive sparseness for supervised learning. *Pattern Analysis and Machine Intelligence, IEEE Transactions on*, 25(9) :1150–1159.

[Figueiredo and Nowak, 2001] Figueiredo, M. and Nowak, R. (2001). Wavelet-based image estimation : an empirical bayes approach using jeffrey's noninformative prior. *Image Processing, IEEE Transactions on*, 10(9) :1322–1331.

[Figueiredo et al., 2007] Figueiredo, M., Nowak, R., and Wright, S. (2007). Gradient projection for sparse reconstruction : Application to compressed sensing and other inverse problems. *Selected Topics in Signal Processing, IEEE Journal of*, 1(4) :586–597.

[Fountoulakis et al., 2014] Fountoulakis, K., Gondzio, J., and Zhlobich, P. (2014). Matrix-free interior point method for compressed sensing problems. *Mathematical Programming Computation*, 6(1) :1–31.

[Friboulet et al., 2010] Friboulet, D., Liebgott, H., and Prost, R. (2010). Compressive sensing for raw rf signals reconstruction in ultrasound. In *IEEE International Ultrasonics Symposium*, pages 367–370.

[Gao et al., 2009] Gao, H., Choi, H. F., Claus, P., Boonen, S., Jaecques, S., Van Lenthe, G., Van der Perre, G., Lauriks, W., and D'hooge, J. (2009). A fast convolution-based methodology to simulate 2-dd/3-d cardiac ultrasound images. *Ultrasonics, Ferroelectrics and Frequency Control, IEEE Transactions on*, 56(2) :404–409.

[Gersho and Gray, 1991] Gersho, A. and Gray, R. M. (1991). *Vector Quantization and Signal Compression*. Kluwer Academic Publishers, Norwell, MA, USA.

[Gorodnitsky and Rao, 1997] Gorodnitsky, I. and Rao, B. (1997). Sparse signal reconstruction from limited data using focuss : a re-weighted minimum norm algorithm. *Signal Processing, IEEE Transactions on*, 45(3) :600–616.

[Gregor and LeCun, 2010] Gregor, K. and LeCun, Y. (2010). Learning fast approximations of sparse coding. In *Proceedings of the 27th International Conference on Machine Learning (ICML-10), June 21-24, 2010, Haifa, Israel*, pages 399–406. Available from : `http://www.icml2010.org/papers/449.pdf`.

[Gribonval and Nielsen, 2003] Gribonval, R. and Nielsen, M. (2003). Sparse representations in unions of bases. *Information Theory, IEEE Transactions on*, 49(12) :3320–3325.

[Hale et al., 2008] Hale, E. T., Yin, W., and Zhang, Y. (2008). Fixed-point continuation for l_1-minimization : Methodology and convergence. *SIAM Journal on Optimization*, 19(3) :1107–1130.

[Herrmann et al., 2012] Herrmann, F., Friedlander, M., and Yilmaz, O. (2012). Fighting the curse of dimensionality : Compressive sensing in exploration seismology. *Signal Processing Magazine, IEEE*, 29(3) :88–100.

[Huang et al., 2013] Huang, H., Misra, S., Tang, W., Barani, H., and Al-Azzawi, H. (2013). Applications of Compressed Sensing in Communications Networks. *ArXiv e-prints*.

[Hyvrinen et al., 2009] Hyvrinen, A., Hurri, J., and Hoyer, P. O. (2009). *Natural Image Statistics : A Probabilistic Approach to Early Computational Vision*. Springer Publishing Company, Incorporated, 1st edition.

[Jensen, 1996a] Jensen, J. (1996a). Calculation of pulsed wave phantom data for arteria femoralis. Available from : `http://server.elektro.dtu.dk/www/jaj/field/?examples/pw_example/example_pw_phantom.html`.

[Jensen and Svendsen, 1992] Jensen, J. and Svendsen, N. (1992). Calculation of pressure fields from arbitrarily shaped, apodized, and excited ultrasound transducers. *IEEE Trans. Ultrason., Ferroelectr., Freq. Control*, 39(2) :262–267.

[Jensen, 1996b] Jensen, J. A. (1996b). Estimation of blood velocities using ultrasound, a signal processing approach.

[Jensen, 2006] Jensen, J. A. (2006). Spectral velocity estimation in ultrasound using sparse data sets. *The Journal of the Acoustical Society of America*, 120(1).

[Ji et al., 2008] Ji, S., Xue, Y., and Carin, L. (2008). Bayesian compressive sensing. *Signal Processing, IEEE Transactions on*, 56(6) :2346–2356.

[K. Engan and Kreutz-Delgado, 1999] K. Engan, B. D. R. and Kreutz-Delgado, K. (1999). Frame design using focuss with method of optimal directions (mod). page 65–69.

[Klebaek et al., 1995] Klebaek, H., Jensen, J., and Hansen, L. (1995). Neural network for sonogram gap filling. In *Ultrasonics Symposium, 1995. Proceedings., 1995 IEEE*, volume 2, pages 1553–1556 vol.2.

[Kristoffersen and Angelsen, 1988] Kristoffersen, K. and Angelsen, B. (1988). A time-shared ultrasound doppler measurement and 2-d imaging system. *Biomedical Engineering, IEEE Transactions on*, 35(5) :285–295.

[Kutyniok, 2012] Kutyniok, G. (2012). Compressed sensing : Theory and applications. *CoRR*, abs/1203.3815.

[L. Weizman, 2015] L. Weizman, Y.C. Eldar, D. B. B. (2015). Compressed sensing for longitudinal mri : An adaptive-weighted approach. *Preprint submitted to Medical Image Analysis*, 29(3) :88–100.

[Lesage et al., 2005] Lesage, S., Gribonval, R., Bimbot, F., and Benaroya, L. (2005). Learning unions of orthonormal bases with thresholded singular value decomposition. In *Acoustics, Speech, and Signal Processing, 2005. Proceedings. (ICASSP '05). IEEE International Conference on*, volume 5, pages v/293–v/296 Vol. 5.

[Lewicki and Olshausen, 1999] Lewicki, M. S. and Olshausen, B. A. (1999). A probabilistic framework for the adaptation and comparison of image codes. *J. Opt. Soc. Am. A*, 16 :1587–1601.

[Lewicki et al., 1998] Lewicki, M. S., Sejnowski, T. J., and Hughes, H. (1998). Learning overcomplete representations. *Neural Computation*, 12 :337–365.

[Li et al., 2014] Li, J., Sun, J., Song, Y., Xu, Y., and Zhao, J. (2014). Accelerating the reconstruction of magnetic resonance imaging by three-dimensional dual-dictionary learning using cuda. In *Engineering in Medicine and Biology Society (EMBC), 2014 36th Annual International Conference of the IEEE*, pages 2412–2415.

[Li, 1993] Li, Y. (1993). A globally convergent method for $l_p $ problems. *SIAM Journal on Optimization*, 3(3) :609–629.

[Liebgott, 2005] Liebgott, H. (2005). *Synthèse de réponse impulsionnelle en imagerie ultrasonore pour l'estimation vectorielle du déplacement*. PhD thesis. Thèse de doctorat dirigée par Delachartre, PhilippeVray, Didier et Wilhjelm, Jens E. Acoustique Villeurbanne, INSA 2005. Available from : http://www.theses.fr/2005ISAL0076.

[Liebgott et al., 2013] Liebgott, H., Prost, R., and Friboulet, D. (2013). Pre-beamformed rf signal reconstruction in medical ultrasound using compressive sensing. *Ultrasonics*, 53(2) :525–533.

[Luo et al., 2009] Luo, C., Wu, F., Sun, J., and Chen, C. W. (2009). Compressive data gathering for large-scale wireless sensor networks. In *Proceedings of the 15th Annual International Conference on Mobile Computing and Networking*, MobiCom '09, pages 145–156, New York, NY, USA. ACM.

[MacKay, 1992] MacKay, D. J. (1992). The evidence framework applied to classification networks. *Neural Computation*, 4 :720–736.

[Majumdar, 2015] Majumdar, A. (2015). Real-time dynamic MRI reconstruction using stacked denoising autoencoder. *CoRR*, abs/1503.06383. Available from : http://arxiv.org/abs/1503.06383.

[Mallat and Zhang, 1993] Mallat, S. and Zhang, Z. (1993). Matching pursuits with time-frequency dictionaries. *Signal Processing, IEEE Transactions on*, 41(12) :3397–3415.

[Mendelson et al., 2008] Mendelson, S., Pajor, A., and Tomczak-Jaegermann, N. (2008). Uniform uncertainty principle for bernoulli and subgaussian ensembles. *Constructive Approximation*, 28(3) :277–289.

[Michailovich and Tannenbaum, 2006] Michailovich, O. and Tannenbaum, A. (2006). Despeckling of medical ultrasound images. *Ultrasonics, Ferroelectrics, and Frequency Control, IEEE Transactions on*, 53(1) :64–78.

[Mishali et al., 2011] Mishali, M., Eldar, Y. C., Dounaevsky, O., and Shoshan, E. (2011). Xampling : Analog to digital at sub-nyquist rates. *IET Circuits, Devices & Systems*, 5(1) :8–20.

[Mollenbach and Jensen, 2008] Mollenbach, S. and Jensen, J. (2008). Duplex scanning using sparse data sequences. In *Ultrasonics Symposium, 2008. IUS 2008. IEEE*, pages 5–8.

[Mourad and Reilly, 2009] Mourad, N. and Reilly, J. P. (2009). lP minimization for sparse vector reconstruction. pages 3345–3348.

[Needell and Tropp, 2009] Needell, D. and Tropp, J. (2009). Cosamp : Iterative signal recovery from incomplete and inaccurate samples. *Applied and Computational Harmonic Analysis*, 26(3) :301 – 321.

[Needell and Vershynin, 2010] Needell, D. and Vershynin, R. (2010). Signal recovery from incomplete and inaccurate measurements via regularized orthogonal matching pursuit. *Selected Topics in Signal Processing, IEEE Journal of*, 4(2) :310–316.

[Olshausen and Field, 1997] Olshausen, B. A. and Field, D. J. (1997). Sparse coding with an overcomplete basis set : A strategy employed by v1 ? *Vision Research*, 37(23) :3311 – 3325.

[Osborne et al., 2000] Osborne, M., Presnell, B., and Turlach, B. (2000). A new approach to variable selection in least squares problems. *IMA Journal of Numerical Analysis*, 20(3) :389–403.

[Osborne et al., 1999] Osborne, M. R., Presnell, B., and Turlach, B. A. (1999). On the lasso and its dual. *Journal of Computational and Graphical Statistics*, 9 :319–337.

[Pati et al., 1993] Pati, Y., Rezaiifar, R., and Krishnaprasad, P. (1993). Orthogonal matching pursuit : recursive function approximation with applications to wavelet decomposition. pages 40–44 vol.1.

[Qaisar et al., 2013] Qaisar, S., Bilal, R., Iqbal, W., Naureen, M., and Lee, S. (2013). Compressive sensing : From theory to applications, a survey. *Communications and Networks, Journal of*, 15(5) :443–456.

[Qian and Shi, 2014] Qian, L. and Shi, X. (2014). Denoising predictive sparse decomposition. In *Big Data and Smart Computing (BIGCOMP), 2014 International Conference on*, pages 223–228.

[Quinsac et al., 2010a] Quinsac, C., Basarab, A., Girault, J., and Kouamé, D. (2010a). Compressed sensing of ultrasound images : sampling of spatial and frequency domains. In *IEEE Workshop on Signal Processing Systems*, pages 231–236.

[Quinsac et al., 2010b] Quinsac, C., Basarab, A., Gregoire, J.-M., and Kouamé, D. (2010b). 3d compressed sensing ultrasound. In *IEEE International Ultrasonics Symposium*, pages 363–366.

[Quinsac et al., 2012] Quinsac, C., Basarab, A., and Kouamé, D. (2012). Frequency domain compressive sampling for ultrasound imaging. *Advances in Acoustics and Vibration*, 12 :1–16.

[Quinsac et al., 2011] Quinsac, C., Dobigeon, N., Basarab, A., Kouamé, D., and Tourneret, J.-Y. (2011). Bayesian compressed sensing in ultrasound imaging. In *IEEE International Workshop on Computational Advances in Multi-Sensor Adaptive Processing (CAMSAP)*, pages 101–104.

[Rao and Kreutz-Delgado, 1999] Rao, B. and Kreutz-Delgado, K. (1999). An affine scaling methodology for best basis selection. *Signal Processing, IEEE Transactions on*, 47(1) :187–200.

[Richy et al., 2013] Richy, J., Friboulet, D., Bernard, A., Bernard, O., and Liebgott, H. (2013). Blood velocity estimation using compressive sensing. *IEEE Transactions on Medical Imaging*, 32(11) :1979–1988.

[Richy et al., 2011] Richy, J., Liebgott, H., Prost, R., and Friboulet, D. (2011). Blood velocity estimation using compressed sensing. In *Ultrasonics Symposium (IUS), 2011 IEEE International*, pages 1427–1430.

[Rubinstein et al., 2010] Rubinstein, R., Bruckstein, A., and Elad, M. (2010). Dictionaries for sparse representation modeling. *Proceedings of the IEEE*, 98(6) :1045–1057.

[Rubinstein et al., 2006] Rubinstein, R., Zibulevsky, M., and Elad, M. (2006). Efficient implementation of the k-svd algorithm using batch orthogonal matching pursuit. Available from : `http://www.cs.technion.ac.il/%7Eelad/software/`.

[Rudelson and Vershynin, 2008] Rudelson, M. and Vershynin, R. (2008). On sparse reconstruction from fourier and gaussian measurements. *Communications on Pure and Applied Mathematics*, 61(8) :1025–1045.

[Schiffner et al., 2012] Schiffner, M., Jansen, T., and Schmitz, G. (2012). Compressed sensing for fast image acquisition in pulse-echo ultrasound. *Biomedical Engineering*, 57(SI-1) :192–195.

[Schiffner and Schmitz, 2011] Schiffner, M. and Schmitz, G. (2011). Fast pulse-echo ultrasound imaging employing compressive sensing. In *Ultrasonics Symposium (IUS), 2011 IEEE International*, pages 688–691.

[Schniter et al., 2008] Schniter, P., Potter, L., and Ziniel, J. (2008). Fast bayesian matching pursuit. In *Information Theory and Applications Workshop, 2008*, pages 326–333.

[Sermesant et al., 2001] Sermesant, M., Coudière, Y., Delingette, H., Ayache, N., and Désidéri, J. (2001). An electro-mechanical model of the heart for cardiac image analysis. In *Medical Image Computing and Computer-Assisted Intervention - MICCAI*, volume 2208, pages 224–231.

[Smith and Elad, 2013] Smith, L. and Elad, M. (2013). Improving dictionary learning : Multiple dictionary updates and coefficient reuse. *Signal Processing Letters, IEEE*, 20(1) :79–82.

[Stoica and Babu, 2012] Stoica, P. and Babu, P. (2012). Spice and likes : Two hyperparameter-free methods for sparse-parameter estimation. *Signal Processing*, 92(7) :1580 – 1590.

[Tan et al., 2015a] Tan, M., Tsang, I., and Wang, L. (2015a). Matching pursuit lasso part i : Sparse recovery over big dictionary. *Signal Processing, IEEE Transactions on*, 63(3) :727–741.

[Tan et al., 2015b] Tan, M., Tsang, I., and Wang, L. (2015b). Matching pursuit lasso part ii : Applications and sparse recovery over batch signals. *Signal Processing, IEEE Transactions on*, 63(3) :742–753.

[Tan and Li, 2009] Tan, X. and Li, J. (2009). Computationally efficient sparse bayesian learning via belief propagation. In *Signals, Systems and Computers, 2009 Conference Record of the Forty-Third Asilomar Conference on*, pages 1566–1570.

[**Lorintiu, O.** et al., 2015] **Lorintiu, O.**, Liebgott, H., Alessandrini, M., Bernard, O., and Friboulet, D. (2015). Compressed sensing reconstruction of 3d ultrasound data using dictionary learning and line-wise subsampling. *IEEE Transactions on Medical Imaging*, accepted.

[Tibshirani, 2011] Tibshirani, R. (2011). Regression shrinkage and selection via the lasso : a retrospective. *Journal of the Royal Statistical Society : Series B (Statistical Methodology)*, 73(3) :273–282.

[Tipping, 2001] Tipping, M. E. (2001). Sparse bayesian learning and the relevance vector machine. *J. Mach. Learn. Res.*, 1 :211–244.

[Tortoli et al., 2009] Tortoli, P., Bassi, L., Boni, E., Dallai, A., Guidi, F., and Ricci, S. (2009). Ula-op : an advanced open platform for ultrasound research. *Ultrasonics, Ferroelectrics, and Frequency Control, IEEE Transactions on*, 56(10) :2207–2216.

[Tosic et al., 2010] Tosic, I., Jovanovic, I., Frossard, P., Vetterli, M., and Duric, N. (2010). Ultrasound tomography with learned dictionaries. In *Acoustics Speech and Signal Processing (ICASSP), 2010 IEEE International Conference on*, pages 5502–5505.

[Tropp and Gilbert, 2007] Tropp, J. and Gilbert, A. (2007). Signal recovery from random measurements via orthogonal matching pursuit. *Information Theory, IEEE Transactions on*, 53(12) :4655–4666.

[Tropp and Wright, 2010] Tropp, J. and Wright, S. (2010). Computational methods for sparse solution of linear inverse problems. *Proceedings of the IEEE*, 98(6) :948–958.

[Tur et al., 2011] Tur, R., Eldar, Y. C., and Friedman, Z. (2011). Innovation rate sampling of pulse streams with application to ultrasound imaging. *IEEE Transactions on Signal Processing*, 59(4) :1827–1842.

[van den Berg and Friedlander, 2009a] van den Berg, E. and Friedlander, M. (2009a). Spgl1 : A solver for large-scale sparse reconstruction. Available from : `http://www.cs.ubc.ca/labs/scl/spgl1`.

[van den Berg and Friedlander, 2009b] van den Berg, E. and Friedlander, M. (2009b). Spgl1 : A solver for large-scale sparse reconstruction. Available from : `https://scholar.google.fr/citations?view_op=view_citation&hl=en&user=m0gIIH4AAAAJ&citation_for_view=m0gIIH4AAAAJ:u5HHmVD_uO8C`.

[van den Berg and Friedlander, 2009c] van den Berg, E. and Friedlander, M. P. (2009c). Probing the pareto frontier for basis pursuit solutions. *SIAM Journal on Scientific Computing*, 31(2) :890–912. Available from : `http://dx.doi.org/10.1137/080714488`.

[Vaswani, 2009] Vaswani, N. (2009). KF-CS : compressive sensing on kalman filtered residual. *CoRR*, abs/0912.1628. Available from : `http://arxiv.org/abs/0912.1628`.

[Vaswani, 2010] Vaswani, N. (2010). Ls-cs-residual (ls-cs) : Compressive sensing on least squares residual. *Signal Processing, IEEE Transactions on*, 58(8) :4108–4120.

[Vetterli et al., 2002] Vetterli, M., Marziliano, P., and Blu, T. (2002). Sampling signals with finite rate of innovation. *Signal Processing, IEEE Transactions on*, 50(6) :1417–1428.

[Vray et al., 2014] Vray, D., Brusseau, E., Detti, V., Varray, F., Basarab, A., Beuf, O., Basset, O., Cachard, C., Liebgott, H., and Delachartre, P. (2014). *Ultrasound Medical Imaging*, page 1–72. John Wiley & Sons, Inc. Available from : http://dx.doi.org/10.1002/9781118761236.ch1.

[Wagner et al., 2011] Wagner, N., Eldar, Y. C., Feuer, A., Danin, G., and Friedman, Z. (2011). Xampling in ultrasound imaging.

[Wagner et al., 2012] Wagner, N., Eldar, Y. C., and Friedman, Z. (2012). Compressed beamforming in ultrasound imaging. *IEEE Transactions on Signal Processing*, 60(9) :4643–4657.

[Wakin et al., 2006] Wakin, M., Laska, J., Duarte, M., Baron, D., Sarvotham, S., Takhar, D., Kelly, K., and Baraniuk, R. (2006). An architecture for compressive imaging. In *Image Processing, 2006 IEEE International Conference on*, pages 1273–1276.

[Wang et al., 2011] Wang, G., Bresler, Y., and Ntziachristos, V. (2011). Guest editorial compressive sensing for biomedical imaging. *Medical Imaging, IEEE Transactions on*, 30(5) :1013–1016.

[Wipf, 2011] Wipf, D. (2011). Sparse estimation with structured dictionaries. *Advances in Neural Information Processing Systems (NIPS)*. Available from : http://research.microsoft.com/apps/pubs/default.aspx?id=167599.

[Wipf and Nagarajan, 2010] Wipf, D. and Nagarajan, S. (2010). Iterative reweighted l_1 and l_2 methods for finding sparse solutions. *Selected Topics in Signal Processing, IEEE Journal of*, 4(2) :317–329.

[Wipf and Rao, 2004] Wipf, D. and Rao, B. (2004). Sparse bayesian learning for basis selection. *Signal Processing, IEEE Transactions on*, 52(8) :2153–2164.

[Wipf and Rao, 2007] Wipf, D. and Rao, B. (2007). An empirical bayesian strategy for solving the simultaneous sparse approximation problem. *Signal Processing, IEEE Transactions on*, 55(7) :3704–3716.

[Wright et al., 2009] Wright, S., Nowak, R., and Figueiredo, M. (2009). Sparse reconstruction by separable approximation. *Signal Processing, IEEE Transactions on*, 57(7) :2479–2493.

[Yang and Zhang, 2011a] Yang, J. and Zhang, Y. (2011a). Alternating direction algorithms for l_1-problems in compressive sensing. *SIAM Journal on Scientific Computing*, 33(1) :250–278.

[Yang and Zhang, 2011b] Yang, J. and Zhang, Y. (2011b). Yall1. Available from : http://yall1.blogs.rice.edu/.

[Yang and Zhang, 2011c] Yang, J. and Zhang, Y. (2011c). Yall1. Available from : https://scholar.google.fr/citations?view_op=view_citation&hl=en&user=KNaIT2kAAAAJ&citation_for_view=KNaIT2kAAAAJ:u-x6o8ySG0sC.

[Yu and Acton, 2002] Yu, Y. and Acton, S. (2002). Speckle reducing anisotropic diffusion. *Image Processing, IEEE Transactions on*, 11(11) :1260–1270.

[Zayyani et al., 2009] Zayyani, H., Babaie-Zadeh, M., and Jutten, C. (2009). Bayesian pursuit algorithm for sparse representation. In *Acoustics, Speech and Signal Processing, 2009. ICASSP 2009. IEEE International Conference on*, pages 1549–1552.

[Zhang et al., 2013a] Zhang, Q., Li, B., and Shen, M. (2013a). A measurement-domain adaptive beamforming approach for ultrasound instrument based on distributed compressed sensing : Initial development. *Ultrasonics*, 53 :255 – 264.

[Zhang et al., 2014] Zhang, Z., Jung, T., Makeig, S., Pi, Z., and Rao, B. D. (2014). Spatiotemporal sparse bayesian learning with applications to compressed sensing of multichannel physiological signals. *CoRR*, abs/1404.5122. Available from : `http://arxiv.org/abs/1404.5122`.

[Zhang et al., 2013b] Zhang, Z., Jung, T.-P., Makeig, S., and Rao, B. (2013b). Compressed sensing for energy-efficient wireless telemonitoring of noninvasive fetal ecg via block sparse bayesian learning. *Biomedical Engineering, IEEE Transactions on*, 60(2) :300–309.

[Zhang et al., 2013c] Zhang, Z., Jung, T.-P., Makeig, S., and Rao, B. (2013c). Compressed sensing of eeg for wireless telemonitoring with low energy consumption and inexpensive hardware. *Biomedical Engineering, IEEE Transactions on*, 60(1) :221–224.

[Zhang and Rao, 2012] Zhang, Z. and Rao, B. (2012). Recovery of block sparse signals using the framework of block sparse bayesian learning. pages 3345–3348.

[Zhang and Rao, 2013a] Zhang, Z. and Rao, B. (2013a). Extension of sbl algorithms for the recovery of block sparse signals with intra-block correlation. *Signal Processing, IEEE Transactions on*, 61(8) :2009–2015.

[Zhang and Rao, 2013b] Zhang, Z. and Rao, B. (2013b). Extension of sbl algorithms for the recovery of block sparse signals with intra-block correlation. *Signal Processing, IEEE Transactions on*, 61(8) :2009–2015.

[Zhuang et al., 2012] Zhuang, X., Zhao, Y., Dai, Z., Wang, H., and Wang, L. (2012). Ultrasonic signal compressive detection with sub-nyquist sampling rate. *Journal of Scientific and Industrial Research*, 71(3) :195–199.

[Zobly and Kadah, 2013] Zobly, S. and Kadah, Y. (2013). Multiple measurements vectors compressed sensing for doppler ultrasound signal reconstruction. In *Computing, Electrical and Electronics Engineering (ICCEEE), 2013 International Conference on*, pages 319–322.

[Zobly and Kakah, 2011] Zobly, S. and Kakah, Y. (2011). Compressed sensing : Doppler ultrasound signal recovery by using non-uniform sampling amp ; random sampling. In *Radio Science Conference (NRSC), 2011 28th National*, pages 1–9.

TITRE EN FRANCAIS

Reconstruction par acquisition compressée en imagerie ultrasonore medicale 3D et Doppler.

RESUME EN FRANCAIS

L'objectif de cette thèse est le développement de techniques adaptées à l'application de la théorie de l'acquisition compressée en imagerie ultrasonore 3D et Doppler. En imagerie ultrasonore 3D une des principales difficultés concerne le temps d'acquisition très long lié au nombre de lignes RF à acquérir pour couvrir l'ensemble du volume. Afin d'augmenter la cadence d'imagerie une solution possible consiste à choisir aléatoirement des lignes RF qui ne seront pas acquises. La reconstruction des données manquantes est une application typique de l'acquisition compressée. Une autre application d'intérêt correspond aux acquisitions Doppler duplex où des stratégies d'entrelacement des acquisitions sont nécessaires et conduisent donc à une réduction de la quantité de données disponibles. Dans ce contexte, nous avons réalisé de nouveaux développements permettant l'application de l'acquisition compressée à ces deux modalités d'acquisition ultrasonore. Dans un premier temps, nous avons proposé d'utiliser des dictionnaires redondants construits à partir des signaux d'intérêt pour la reconstruction d'images 3D ultrasonores. Une attention particulière a aussi été apportée à la configuration du système d'acquisition et nous avons choisi de nous concentrer sur un échantillonnage des lignes RF entières, réalisable en pratique de façon relativement simple. Cette méthode est validée sur données 3D simulées et expérimentales. Dans un deuxième temps, nous proposons une méthode qui permet d'alterner de manière aléatoire les émissions Doppler et les émissions destinées à l'imagerie mode-B. La technique est basée sur une approche bayésienne qui exploite la corrélation et la parcimonie des blocs du signal. L'algorithme est validé sur des données Doppler simulées et expérimentales.

TITRE EN ANGLAIS

Compressed sensing reconstruction for 3D and Doppler medical ultrasound.

RESUME EN ANGLAIS

This thesis is dedicated to the application of the novel compressed sensing theory to the acquisition and reconstruction of 3D US images and Doppler signals. In 3D US imaging, one of the major difficulties concerns the number of RF lines that has to be acquired to cover the complete volume. The acquisition of each line takes an incompressible time due to the finite velocity of the ultrasound wave. One possible solution for increasing the frame rate consists in reducing the acquisition time by skipping some RF lines. The reconstruction of the missing information in post processing is then a typical application of compressed sensing. Another excellent candidate for this theory is the Doppler duplex imaging that implies alternating two modes of emission, one for B-mode imaging and the other for flow estimation. Regarding 3D imaging, we propose a compressed sensing framework using learned overcomplete dictionaries. Such dictionaries allow for much sparser representations of the signals since they are optimized for a particular class of images such as US images. We also focus on the measurement sensing setup and propose a line-wise sampling of entire RF lines which allows to decrease the amount of data and is feasible in a relatively simple setting of the 3D US equipment. The algorithm was validated on 3D simulated and experimental data. For the Doppler application, we proposed a CS based framework for randomly interleaving Doppler and US emissions. The proposed method reconstructs the Doppler signal using a block sparse Bayesian learning algorithm that exploits the correlation structure within a signal and has the ability of recovering partially sparse signals as long as they are correlated. This method is validated on simulated and experimental Doppler data.

INTITULE ET ADRESSE DE L'U.F.R. OU DU LABORATOIRE

Université de Lyon, CREATIS ; CNRS UMR5220 ; Inserm U1044 ; INSA-Lyon ; Université Lyon 1, 7 Av. Jean Capelle, 69621 VILLLEURBANNE, France.